Ordering and Defects in Artificial Magnetic Square Ice: Thermodynamic and Field-Driven Processes

Jason Phillip Morgan

School of Physics and Astronomy

University of Leeds

Submitted in accordance with the requirements for the degree of

Doctor of Philosophy

September 2011

The candidate confirms that the work submitted is his own, except where work which has formed part of jointly-authored publications has been included. The contribution of the candidate and the other authors to this work has been explicitly indicated below. The candidate confirms that appropriate credit has been given within the thesis where reference has been made to the work of others.

Work contained in chapters 4 and 6 of this thesis have been published in the following jointly authored manuscripts respectively.

J. P. Morgan, A. Stein, S. Langridge and C. H. Marrows "Magnetic reversal of an artificial square ice: dipolar correlation and charge ordering" *New Journal of Physics, (at press), (2011).*
Sample fabrication was conducted by A. Stein. Experimental procedures, data collection and data analysis were conducted by J. P. Morgan. The work was supervised by S. Langridge and C. H. Marrows.

J. P. Morgan, A. Stein, S. Langridge and C. H. Marrows "Thermal ground-state ordering and elementary excitations in artificial magnetic square ice" *Nature Physics* **7***, 75-79, (2011).*
Sample fabrication was conducted by J. P. Morgan and A. Stein. Data collection, data analysis and calculations were conducted by J. P. Morgan. The work was supervised by S. Langridge and C. H. Marrows.

Acknowledgements

I would like to begin by thanking my supervisors Dr Chris Marrows and Prof Sean Langridge for their direction and support over the last four years. I am also very grateful for the insightful guidance of Dr Gavin Burnell and Prof Bryan Hickey.

All samples studied in this thesis were fabricated by, or under the supervision of, Dr Aaron Stein (CFN), who deserves a great deal of thanks for making this work possible. Thanks to Dr Dario Arena (NSLS) for assistance with the experiment of chapter 4, paper proof-reading, and for knowing the best places to eat on Long Island. Thanks to Dr Christy Kinane, Dr Ray Fan and Dr Tim Charlton (ISIS) and Dr Cecilia Sanchez-Hanke (NSLS) for their help and for always going above and beyond.

Thanks to Zoe Budrikis and Prof Bob Stamps (UWA/Glasgow) for many useful discussions, proof-readings and the included simulation results in chapter 5. I am also very grateful for the efforts of Johanna Akerman (ISOM) who made substantial contributions to the data collection for chapter 5 and data processing for sections 6.3 and 6.4.

Dr Mike Evans should be thanked for his valuable help in understanding the statistical mechanical analysis discussed and employed in sections 6.4 and 6.4.1.

A big thanks to the members of the Condensed Matter group, past and present, for making my time at Leeds both interesting and fun, particularly Mark Elkin and Dr David “Super-Salad” Ciudad.

Finally, I would like to thank my parents, my brother and Raffaela for their love and support. Diolch yn fawr iawn i bawb!

Abstract

This thesis addresses the behaviour of artificial magnetic square spin ice patterns in response to applied magnetic fields and thermal activation. Two main points of focus are the access of well-defined statistical states and the properties of fractionalised "monopole" charge defects. Experimental investigations are conducted using magnetic force microscopy of athermal remanent states.

Magnetic reversal of a square ice subject to magnetic fields applied slightly off a diagonal symmetry axis is found to mediate via incremental sublattice-independent processes. Dipolar correlations manifest as charge defect propagation and ordering, along and between adjacent flipped moment chains respectively. Quenched disorder, while allowing for bulk defect nucleation, is responsible for strongly suppressing correlations.

A constant magnitude rotating field protocol is investigated. The acquisition of strong ground state ordering via highly correlated edge-nucleated reversal processes, as recently predicted, is not found, attributable to the enhancement of bulk processes by quenched disorder. An optimally tuned field allows for efficient demagnetisation towards the ground state.

A study of as-fabricated states is presented, magnetically self-ordered following formation of magnetic elements via evaporative vacuum deposition. Compelling evidence is presented, in a case study of a sample closely approaching the ground state, for superparamagnetism during early deposition stages which is subsequently arrested. Large ground state domains are observed sustaining Boltzmann factor weighted monopole excitations. Evidence is present for monopole interactions

playing a role in thermal ordering, as excitations explore a dipolar energy band structure. Further, order is found to increase with interaction strength, and preliminary results suggest that quenched disorder acts to suppress it. Statistical mechanical calculations show that states achieved correspond closely to arrested thermal equilibrium. Consideration of an effective thermodynamic model presented for ac field demagnetised states is given. Comparison allows for discussion of the general role of quenched disorder and the effective temperature of a "frozen" state.

Contents

Abbreviations

AFM	Atomic force microscopy
DPS	Diagonally polarised state
E	Energy
EBL	Electron beam lithography
GS	Ground state
k_{B}	Boltzmann's constant
$k_{\mathrm{B}}T$	Thermal energy
L-TEM	Lorenz Transmission Electron Microscopy
MFM	Magnetic force microscopy
μ_0	Free space magnetic permeability
μ_{B}	Bohr magneton
Py	Permalloy
R	Molar constant
RS	Random state
SEM	Scanning electron microscopy
SPM	Scanning probe microscopy
T_i	Vertex type i
V_i	Vertex configuration i
YPS	y-axis polarised state

List of Figures

List of Tables

Chapter 1

Introduction

1.1 Overview

Recent years have seen a prominent research movement in which the physics of geometrical frustration and resultant emergent phenomena have been extensively explored via model systems. Frustration arises when no configuration of a system can simultaneously minimise all pairwise interactions between its components, an effect which is found throughout the field condensed matter and beyond [1; 2]. A great deal of this work appears to have been instigated and inspired by the realisation of an "artificial spin ice", as reported by Wang et al. in 2006 [3], an experimental 2D vertex array of Ising-like nanomagnets designed to exhibit analagous frustrated interactions to those found in 3D bulk crystalline spin ice materials at low temperatures [4], a modern paradigm of geometrical frustration and a magnetic analogue of the classic frustrated material, water ice [5]. These 3D ice systems posses macroscopic ground state degeneracy and extensive zero-temperature entropy.

A much earlier example of such work is the study of 2D artificial Ising antiferromagnets using arrays of superconducting current rings, some 15 years ago [6; 7], in which an important interplay between inter-elemental interactions and quenched disorder in the patterns was identified. With the advent of artificial spin ice, this field has matured beyond the study of systems which only previously existed as theoretical models, the artificial kagome spin ice for example [8; 9] being a very close analogue of the dipolar kagome ice phase found in crystalline

spin ice under a (111)-direction magnetic field [10; 11; 12]. Analogous physics is hence directly accessible and observable via magnetic microscopies, and the great convenience and ease of constructing such artificial systems via modern nanofabrication tools [13] is currently being rigorously exploited.

To date, essentially all artificial spin ices studied experimentally posses a crucial dissimilarity to their crystalline counterpart - when studied, they are athermal at all accessible temperatures. A large proportion of work has hence focussed on field ordering and the direct resolution of local configurations using microscopy under remanent conditions. Following an ac demagnetisation "field-anneal" process, short range magnetic correlations and "icy" local configurations are found in the artificial lattices [3; 9; 12; 14; 15; 16; 17; 18], similar to the properties of crystalline spin ice.

The excitment surrounding these system was only further reinforced by the more recent realisation of quasi-particle excitations within the crystalline spin ice systems which resemble and interact like Coulombic magnetic monopoles, arising due to fractionalisation [19]. This naturally triggered the invocation of analogous treaments of similar topological charge defects which exist on the artificial lattices [18; 20; 21; 22; 23; 24; 25; 26; 27; 28; 29], generated and manipulated experimentally using magnetic fields on field-prepared "icy" background states.

The aim of this thesis is to present significant contributions to the ever-growing volume of work on artificial spin ices, focussing exclusively on the square ice system. Both the generation of icy states and the propagation and control of charged monopole defects will be addressed. Further, recent progress in understanding the effects of true thermalisation of these 2D ice lattices will be presented. More generally, the work addresses means by which to prepare well-defined background states on the square ice lattice and to understand the behaviour and properties of charge defects which occur on top.

The remainder of this chapter will overview some key information regarding nanomagnetism and statistical mechanics that underlie the subject matter of the thesis.

Chapter 2 will present a brief review of spin ice materials, and a more detailed discussion of artificial spin ices, as well as publications key to understanding the

results later presented, and signifying the place of these results within the context of the current state-of-the-art.

Chapter 3 will summarise the techniques and methods used to fabricate, characterise and experimentally study the patterned ice arrays.

Chapter 4 will discuss results of an incremental magnetic reversal experiment, as reported in reference [29]. By preparation of a well known long range ordered polarised state [30], charge propagation is mediated on this ice-like background via correlated dipolar cascade chains, similar to those previously observed on the kagome ice system [24]. Only short range chain correlation are found as quenched pattern disorder acts to randomise behaviour. Further, the first observation of the effects of charge interactions are made, which are manifested through the dipolar ordering.

Chapter 5 presents an experimental realisation of an alternative "field-anneal" routine recently predicted to yield strong square ice ground state ordering in finite area arrays [21]. The effects of edges are found to have been strongly suppressed, which can be understood by the enhancement of bulk processes by quenched disorder in the patterned systems.

In chapter 6, work addressing the first ever experimental studies of thermalisation of an artificial spin ice, via states and configurations "frozen-in" during sample fabrication, will be presented, as recently reported in reference [25]. Long range ground state ordering is observed experimentally for the first time. Strong qualitative and quantitative evidence for thermalsiation is presented, and a monopole-string excitation dipolar energy band structure is shown to exist, in which defects observed above the groundstate can explore as well-defined elementary excitations. Order is found to be controllable via inter-elemental interaction strength as well as interfacial roughness in the elemental thin film structures. Further a simple mean field description based on the canonical ensemble shows that close-to-equilibrium states are achieved, as well as providing insight in to the opposing influence on the "effective temperature" of the system by coupling and quenched disorder in both thermal and field anneal processes.

To close, in chapter 7 an overview of the key results of the work will be given as well as a discussion of potential directions for future work.

1.2 Nanoscale Magnetic Behaviour

In this section, an overview of the various competing energetic contributions influencing the behaviour of ferromagnetic materials will be given, and their consequences on the behaviour of nanoscale magnetic elements [13; 31]. These contributions are exchange energy E_{ex} which acts to align spins with each other, magnetocrystalline anisotropy energy E_{K} which acts to align spins along preferred crystallographic axes, demagnetising energy E_{demag} associated with the presence of demagnetising fields, Zeeman energy E_{Z} which acts to align spins with an externally applied field, and thermal energy E_{T} which acts to randomise the direction of spins. As the size of a magnetic element is reduced, the relative magnitudes of these energies changes, significantly altering the material's behaviour.

At the surface of a magnetic material, any component of magnetisation, $\mathbf{M}$, normal to the surface will come to an abrupt end, meaning that $\nabla \cdot \mathbf{M} \neq 0$. As the divergence of magnetic flux $\nabla \cdot \mathbf{B} = \mu_0 \nabla \cdot (\mathbf{H} + \mathbf{M}) = 0$ [32], where μ_0 is the free space magnetic permeability, diverging magnetisation is accompanied by and equal and opposite divergence of magnetic field $-\nabla \cdot \mathbf{H}$. This is as if the surface of the material holds a distribution of magnetic charges, sources and sinks of what is referred to as the demagnetising field, $\mathbf{H}_{\text{demag}} = -\underline{\mathbf{D}}\mathbf{M}$, where $\underline{\mathbf{D}}$ is a shape dependent demagnetising tensor, generally a complicated function of position within the material. Only an ellipsoidally shaped material has an uniform $\mathbf{H}_{\text{demag}}$ and hence a simple scalar demagnetising factor D. External to the material, the surface charge distribution creates a stray magnetic field.

$\mathbf{H}_{\text{demag}}$ carries with it an energy density given by $E_{\text{demag}} = -\frac{\mu_0}{2}\int(\mathbf{H}_{\text{demag}} \cdot \mathbf{M})dV = \frac{\mu_0}{2}\int(\underline{\mathbf{D}}M^2)dV$, where the integral is taken over the material volume V. In order to reduce demagnetising fields, stray fields, and the associated energy, magnetic material will often form magnetic domain structures - small regions of uniform $\mathbf{M}$ (reaching saturation magnetisation, $|\mathbf{M}| = M_{\text{s}}(T)$, which is generally a function of temperature T) randomly arranged to minimise out of plane magnetisation, figure 1.1, separated by regions of rotating $\mathbf{M}$ called domain walls, which cost less energy than the cost of sustaining a demagnetising field. Demagnetising effects are balanced at short range by exchange interactions between

spins, described by $E_{\text{ex}} = -2J\mathbf{S}_1 \cdot \mathbf{S}_2$ under the Heisenberg Hamiltonian approximation, where J is the exchange constant, positive for ferromagnetic interactions, between spins with vectors $\mathbf{S}_1$ and $\mathbf{S}_2$. Magnetisation is typically uniform over at least the exchange length, ($\sim$ nanometers), the length scale over which exchange dominates. Usually, domains are very many exchange lengths in size.

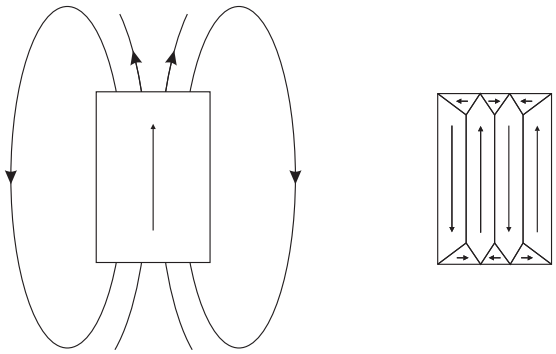

Figure 1.1: A single domain and multidomain state of a magnetic element. With magnetisation represented by arrows, the magnetic state on the left would cost a large amount of energy in demagnetisation fields. The state on the right has minimal demagnetising field by the formation closure domains.

For a Bloch wall (a domain wall with a planar magnetisation rotation) in a simple cubic crystal of lattice constant a the areal energy density can be shown to be equal to $JS^2\pi^2/N_{\text{s}}a^2$, where N_{s} is the number of spins (of magnitude S) in a chain forming/crossing a wall, with a total rotation π between domains. The unwinding of a wall, increasing N_{s}, hence appears energetically favourable, however this unravelling is balanced by the effect of magnetocrystalline anisotropy. Within a magnetic material there are preferred axes for the magnetisation to align with, dependent on crystal structure. Domains will tend to align locally with the crystalline "easy" axes, however, a domain wall cannot avoid having magnetisation components along the crystalline "hard" axes. For a Bloch wall this produces an areal energy density contribution equal to $N_{\text{s}}Ka/2$, where K is an anisotropy constant describing the strength of this effect, acting to tighten the domain wall. The resultant equilibrium surface energy density of a Bloch wall can be shown to be equal to $\pi\sqrt{AK}$, where $A = 2JS^2/a$.

Ultimately, in large bulk magnetic materials, states of reduced energy can be achieved by the formation of magnetic domains, the exact characteristics being dependent largely on material [33]. Magnetically hard materials tend to have large crystalline anisotropies - they are hard to magnetise, hard to demagnetise and therefore make good permanent magnets, e.g. NdFeB. The contrary is true for magnetically soft materials, such as polycrystalline permalloy (Py), an alloy of Ni(80%) and Fe(20%). Polycrystalline materials possesses a microstructure crystalline grains with randomly orientated crystallographic axes, and therefore possess negligible net magnetocrystalline anisotropy.

If the size of a magnetic material is reduced in one or more dimensions it can eventually become comparable in scale to characteristic lengths of the material, for example the domain wall thickness $\delta = \pi\sqrt{A/K}$, and the critical single domain radius (both dependant on the exchange/anisotropy balance). Such circumstances can easily be created via thin film deposition methods such as electron beam vacuum evaporation (section 3.2), and sub-micron resolution lithographic techniques such as electron beam lithography (EBL) (section 3.1). For a continuous Py thin film of $\sim$ 10 nm thickness it is favourable for magnetisation to lie in the plane of the film and for lateral domain patterns to form (with little variation of $\mathbf{M}$ with depth). Crystalline grain sizes of $\sim$ 10 nm are typically found, while latteral domain size can be much larger, $\sim$ 10 μm. With decreasing lateral size, the Py film will be able to sustain a decreasing number of domains [34]. If made small enough the magnetic element will no longer find it energetically favourable to form domain structures and will become single domain, typically at lateral sizes of 100's - 10's nm, figure 1.2. Here the cost of sustaining a demagnetising field is sufficiently less than the cost of a domain wall, and the single domain nanoparticle will form effectively a magnetic dipole, with a north (N) and a south (S) pole like a small permanent bar magnet.

To minimise the demagnetising energy, it is favourable for the magnetisation of a single domain nanoelement to lie parallel to its long axis, given an elongated shape. This effect is termed shape anisotropy, and in the case of a single domain element it enforces a bistable magnetisation potential. To a reasonable approximation, this behaviour can be describe as 'Ising-like", an element possessing two opposite relaxed remanent orientations. Generally, a single domain nanoparticle

will have an energy, $E_{\mathrm{K}} = KV$, associated with an anisotropy, e.g. a magnetocrystalline or shape anisotropy as discussed, quantified by energy density K. If a particle is made small enough this energy can become comparable to its thermal energy, $E_{\mathrm{T}} = k_B T$ at a given temperature T where k_B is the Boltzmann constant. If the condition $E_{\mathrm{T}} \gtrsim E_{\mathrm{K}}$ is met, the particle will be superparamagnetic, as thermal fluctuations overcome the anisotropy and the particle will behave as if it were a large paramagnetic moment.

A single domain magnetic element will be accompanied by a dipolar field $\mathbf{H}_{\mathrm{d}}$, dependant on shape, size and material. Neglecting non-uniformities in $\mathbf{M}$ and finite size effects (increasingly valid with increasing distance $\mathbf{r}$ from such a nanomagnet), the dipolar field can be approximated by that of a point dipole of size $\boldsymbol{\mu} = VM_{\mathrm{s}}\hat{\boldsymbol{e}}_{\mu}$ located at the nanomagnet's centre of mass, where V is the volume of the single domain nanoparticle and $\hat{\boldsymbol{e}}_{\mu}$ is a unit vector, with a dipolar field given by

$$\mathbf{H}_{\mathrm{d}} = \frac{1}{4\pi}\left(\frac{3\mathbf{r}(\boldsymbol{\mu}\cdot\mathbf{r})}{r^5} - \frac{\boldsymbol{\mu}}{r^3}\right). \tag{1.1}$$

The interaction between a point dipole moment and a magnetic field $\mathbf{H}$ is described by the Zeeman energy $E_{\mathrm{Z}} = -\mu_0\boldsymbol{\mu}\cdot\mathbf{H}$, acting to align the moment with the field. If the field is non-uniform, a field gradient force is also experienced by the moment, $\mathbf{F}_{\mathrm{G}} = \mu_0(\boldsymbol{\mu}\cdot\nabla)\mathbf{H}$ [35].

The hysteretic properties of a nanoelement can be significantly different to that of bulk material, due to, for example, the different magnetic reversal mechanisms that occur. Bulk material will largely reverse via domain wall propagation, as domains which are favourably aligned with an applied field grow at the expense of those that are unfavourable. A strictly single domain element, however, will reverse via a coherent rotation of magnetisation, and this can be heavily influenced by shape anisotropy. Real elements may posses varying amounts of non-uniformity in $\mathbf{M}$, however, the smaller an element is made, the more this behaviour becomes enforced.

Interesting behaviour also occurs when nanomagnets are made to interact with each other and much research involves the fabrication of periodic arrays of magnetic nanostructures [13; 36]. The single element behaviour will be altered

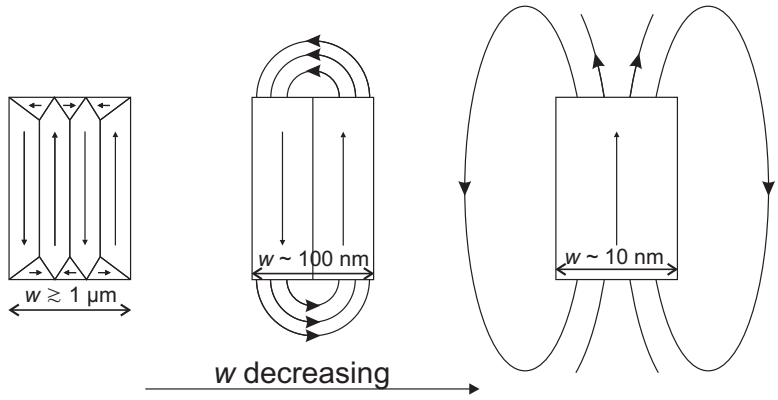

Figure 1.2: Magnetic domain behaviour as a function of the size of a magnetic particle. As the size of a particle, represented by scale w, is reduced it will sustain fewer and fewer magnetic domains. Given the particle is made small enough it will become single domain as it is no longer energetically favourable to form domains.

relative to an isolated element due to the net dipolar field from its neighbours, and an expression for the coupling can be derived from equation 1.1 and the expression for E_{Z}, where moment $\boldsymbol{\mu}_1$ experiences the field $\boldsymbol{H}_{\mathrm{d}}$ of $\boldsymbol{\mu}_2$. A given pair of elements consequently favour a North-to-South alignment. The cumulative behaviour of a large scale array of nanomagnets will be different to that of bulk or sheet material of the same expanse, due to these same effects. Such arrays can be routinely engineered and the influence of these interactions explored by varying elemetal size and shape as well as the number, orientation and spacing of neighbouring elements.

1.3 Statistical Mechanics of Distinguishable Particles

In this section some key results of statistical mechanics will be revised [37; 38].

For a system of $\mathcal{N}$ distinguishable non-interacting particles, each being able to take one of i distinct q_i-fold degenerate energy levels E_i, the number of possible

ways to arrange the system is given by

$$\Omega = \mathcal{N}! \prod_i \frac{q_i^{N_i}}{N_i!} \tag{1.2}$$

where N_i are the number of particles taking the states i. Ω is the number of microstates, the exact configurations, that belong to a given macrostate defined by N_i.

This is a powerful expression, when combined with the equation, postulated by Boltzmann, describing the entropy of a system as

$$S = k_\mathrm{B} \ln \Omega = k_\mathrm{B}(\mathcal{N} \ln \mathcal{N} - \Sigma_i N_i \ln(N_i/q_i)) \tag{1.3}$$

where k_B is the Boltzmann constant. Maximising S with respect to N_i allows for the determination of the most likely configuration of the system, i.e. the macrostate possessing the most microstates.

Often, the maximisation of S needs to be made under a suitable energy constraint, e.g. when the total energy of the system $E = \Sigma_i N_i E_i$ is constant. This corresponds to satisfying the requirements of the second law of thermodynamics: the system will possess a state of maximum accessible entropy when in thermal equilibrium. The constraints of constant energy E and particle number $\mathcal{N}$ correpsonds to writing $dE = \Sigma_i E_i dN_i = 0$ and $d\mathcal{N} = \Sigma_i dN_i = 0$ respectively. Maximising S under these constraints gives $d(\ln \Omega) = -\Sigma_i(\ln(N_i/q_i) + \alpha + \beta E_i)dN_i = 0$, where are α and β are arbitrary constants, as per Lagrange's method of undetermined multipliers. This equation can only generally be satisfied if the term within the sum is taken as equal to 0 for all i, hence,

$$N_i = \frac{q_i \exp(-\beta E_i)}{Z}. \tag{1.4}$$

This equation is known as Boltzmann's law, deszcribing the canonical distributions of populations within energy levels E_i. The term Z emerges naturally as a normalisation factor and is called the single particle partition function, $Z = \Sigma q_i \exp(-\beta E_i)$, the sum over all states. As this is a calculation for $\mathcal{N}$ particles in equilibrium, β can be shown to correspond to the reciprocal thermal energy $\beta = 1/k_\mathrm{B}T$, a factor constant for equilibriated bodies. Equation 1.4 can

be interpreted as the number of particles in the system of $\mathcal{N}$ particles that will take energy level E_i at a given temperature T. Alternatively, it represents the probability that a single particle will be found in energy level E_i. The equation is appropriate for such a system in equilibrium with a "heat bath" of constant temperature T.

1.4 Geometrical Frustration

A few words should be said explicitly addressing geometrical frustration. This effect is most commonly illustrated by means of a simple model [31]: a system of antiferromagnetically coupled Ising spins on a triangular lattice with parallel anisotropy axes, as shown figure 1.3.

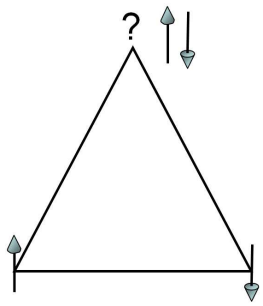

Figure 1.3: Geometrical frustration of Ising spins on a triangular plaquette. Antiferromagnetically coupled parallel Ising spins located on the corners of the triangle are unable to simultaneously satisfy all pairwise interactions.

A single spin placed on to the triangle at e.g. the lower left site, can take one of two Ising states, up or down. A second spin placed at the lower right site will favour antialignment with the first, as shown. A problem arises when a third spin ice placed on the plaquette, as it is unable to satisfy simultaneously its antiferromagnetic coupling with both existing spins. Any other way of attempting to populate the triangle suffers the same issue of incompatibility, and the system is therefore frustrated. Propagating this problem up to a system of many interlinked triangles only further complicates the allocation of a minimum energy state. Further, this is a geometric effect, due to the incompatibility of

the anisotropic triangular lattice with the antiferromagnetic coupling of spins. No long range ordered state would be expected to form spontaneously in this system, and if interactions are taken strictly as nearest neighbour, the system possesses a degeneracy of ground state configuration which scales with the size of the system.

As will be discussed, it is via a similar incompatibility of anisotropic spins on an ordered lattice that bulk crystalline spin ice materials are strongly geometrically frustrated.

Chapter 2

Literature Review

2.1 Spin Ice

"Spin ice" is a low temperature spin state found in the rare earth oxide materials $Ho_2Ti_2O_7$ [4; 39], $Dy_2Ti_2O_7$ [40], and $Ho_2Sn_2O_7$ [41; 42]. This class of materials is found to exhibit exotic low temperature behaviour, strong geometrical magnetic frustration and long range magnetic disorder down to lowest temperatures, despite/as a result of long range structural order.

Spin ice materials belong to family of oxides, $A_2B_2O_7$, where B is a non-magnetic transition metal, in which the positions of the magnetic rare earth A ions are described by a pyrochlore sublattice, figure 2.1 (a) - a face centred cubic structure, with a tetragonal basis, figure 2.1 (b) [43]. This forms a system of corner linked tetrahedra (triangular pyramids). Despite being chemically ordered, strong geometrical frustration emerges in the spin ices at low temperatures as crystal field interactions [44] strongly confine spins to local $\langle 111 \rangle$-type axes joining the body-centres of two linked tetrahedra. Spins are effectively Ising in nature, the centre of a tetrahedron therefore forming a 3D vertex at which four Ising axes meet with $2^4 = 16$ possible spin configurations. Spin ice can therefore be considered as a vertex system on the diamond lattice. Spin ice is crucially defined by ferromagnetic interactions, favouring "head-tail" configurations between two spins of a vertex. Close inspection reveals that no arrangement of spins can simultaneously satisfy all six pairwise interactions present. Antiferromagnetic

interactions result in a dynamic "spin liquid" state, however, ferromagnetic interactions result in a static spin ice system, which "freezes" in to the system at a temperature of $\sim$ 1 K [4; 41]. The first models for spin ice involved nearest neighbour ferromagnetic exchange interaction between Heisenberg spins.

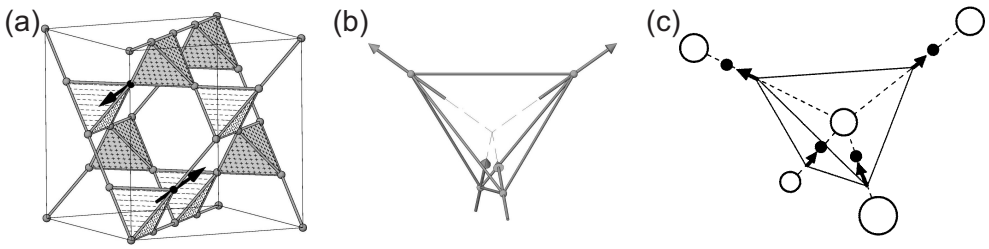

Figure 2.1: Spin ice and water ice. (a) The pyrochlore lattice. (b) tetragonal basis of spins confined along ⟨111⟩-type directions. (c) Hydrogen arrangement in water ice as determined by the ice rule. The large circles represent oxide ions, the small filled circles represent H ions. (a) and (b) after Fennell et al. [43]. (c) After Bramwell et al. [39].

For a spin ice, the ground state of a single tetrahedron is a two-in/two-out arrangement, a lowest energy compromise, shown in figure 2.1 (b). As this configuration is 6-fold degenerate, the propagation of this condition from a single tetrahedron up to a full scale crystal structure results in a system with macroscopic degeneracy of the ground state which possesses no long range order. It is from this behaviour that spin ice gets its name [4], in direct analogy with water ice in which oxide ions reside on the sites of a diamond lattice, and the midpoint between nearest neighbours forms the pyrochlore structure. Each H^+ ion sits on a connecting line between two oxide ions, displaced from this regular structure, forming a short covalent bond with one oxide, and a longer Hydrogen bond with the other [45], figure 2.1 (c). The spins of spin ice therefore map directly on to the displacement vectors of H^+ ions in water ice from the pyrochlore structure [39]. The ground state of both materials is then completely defined by the two-in/two-out condition, dubbed the "ice rules". In water ice, this corresponds to a H_2O molecule for every diamond site.

Literature often directs the reader to the work of Pauling [45] who calculated the degeneracy of the water ice ground state to be $(\frac{3}{2})^{\mathcal{N}/2}$ where $\mathcal{N}$ is the number of molecules H_2O in the system [36]. This gives a ground state entropy of $(\frac{R}{2}) \ln 3/2$ = 1.68 J mol^{-1} K^{-1} per H molecule, the system apparently remaining disordered down to 0 K, without undergoing a phase transition to an ordered state (R = molar constant). Ramirez et al. [40] showed experimentally that the spin ice material $Dy_2Ti_2O_7$ displays very closely this same finite entropy down to 0.2 K. Spin ice presented the possibility of exploring the physics of the ice system in new ways. For example, heating the system and leaving the ice regime is not possible in water ice as it implies melting the crystalline structure. In spin ice, the spin system can be "melted" and "frozen" with temperature, without destroying the chemical order of the pyrochlore structure.

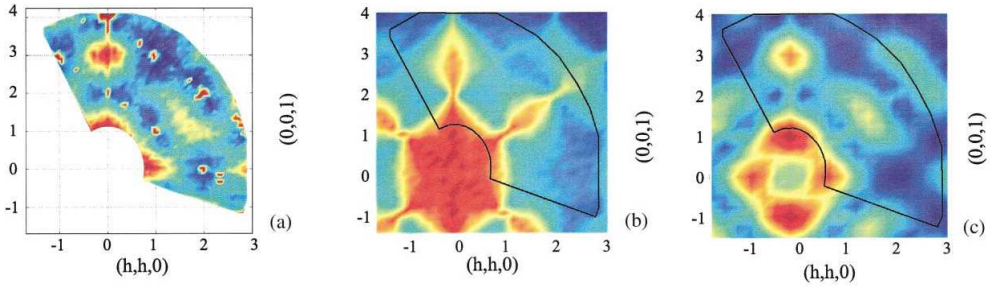

Figure 2.2: Experimental and theoretical neutron scattering maps from a spin ice material. (a) Experimentally observed scan of reciprocal structure of spin ice $Ho_2Ti_2O_7$. Also shown are results of Monte-Carlo simulations of the nearest-neighbour Heisenberg spin ice reciprocal structure (b), and the dipolar spin ice model (c). The features observed in experiment are better described by the dipolar model. After Bramwell et al. [46]

While a 1st nearest neighbour ferromagnetic Ising model was found to capture the essential behaviour of spin ice to a good degree of accuracy, the large rare earth moments are inherently dipolar in nature, hence significant interactions between spins over long ranges would also be expected [47]. This was confirmed by comparison of experimental neutron diffraction data with Monte Carlo simulations [43; 46], figure 2.2, showing that spin ices are better described by a "dipolar

spin-ice" model incorporating long range dipole interactions, as well as weaker *antiferromagnetic* nearest neighbour exchange interactions. Remarkably, this long range interaction does not strongly break the degenerate properties of the system [48], and the ground state configurations for both models are approximately equivalent as $T \to 0$. While spin ice does have a predicted ordered GS [49], for such reasons, as well as the slow relaxation times of the system due to the large energetic barriers between Ising states as well as excited non-Ising states (~ 100 K), this state has been far from accessed experimentally.

2.1.1 Magnetic Monopoles in Spin Ice

No story about spin ice would be complete without a discussion of magnetic monopole excitations. Recently, Castelnovo et al. [19] showed by direct calculation that ice rule-violating defects in spin ice, i.e. vertices possessing 3-in(out)/1-out(in) configurations, figure 2.3 (b), can take the form of magnetic monopole quasi-particles, emergent from the dipole lattice by virtue of fractionalisation. Magnetic monopoles are traditionally identified as exotic objects possessing a single sign of magnetic charge which have never been observed experimentally and are not generally considered to exist. Magnetic charges are always confined to dipoles as equal and opposite north and south poles, even as the limit of their separation $\to 0$. To date, deconfined free-space magnetic monopoles exist only in the theoretical constructs of Dirac, in which their inclusion justifies the experimentally observed quantisation of electric charge, via the quantised "Dirac string", an infinitesimally thin flux tube which connects two opposite magnetic charges [50]. However, until the discovery of free space monopoles, Maxwell's equations [32] will continue to state that $\nabla \cdot \mathbf{B} = 0$: there are no sources or sinks of magnetic flux i.e. magnetic monopoles.

Magnetic monopoles in spin ice do not violate the accepted form of Maxwell's equations. Rather, they can be regarded as a result of them. It is the above rule, implying $\nabla \cdot \mathbf{M} = -\nabla \cdot \mathbf{H}$, which gives rise to monopoles of the magnetic field $\mathbf{H}$ on the spin ice vertex lattice. For an ice-rule obeying background configuration supporting a chain of flipped dipoles, the ice rules are only broken at the ends of this chain. The chain vertices themselves obey the ice rules and present an

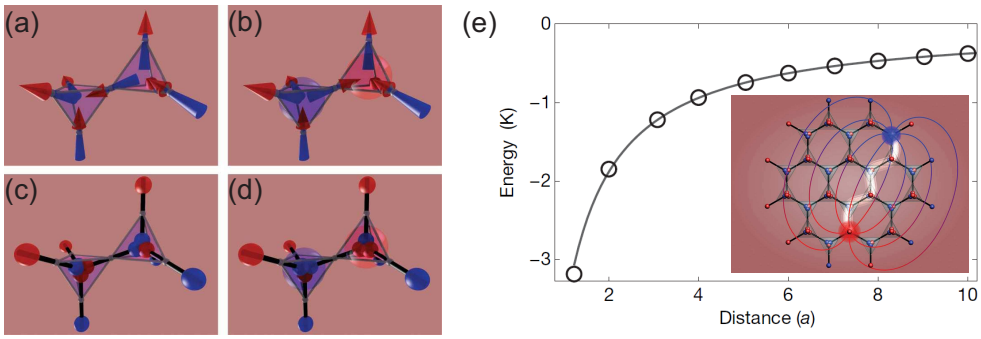

Figure 2.3: Emergent magnetic monopoles in spin ice. (a) A ground state configuration of two linked spin ice vertices, both obeying the 2-in/2-out ice rules. (b) Flipping the interlinking spin violates the ice rules at the two vertex sites, creating a 3-out/1-in and a 1-out/3-in defect configuration. (c) and (d) show the charge-dumbbell reinterpretation of the spin configurations shown in (a) and (b) respectively. The defected configurations possess an excess of North and South charge, presenting a "monopole-antimonopole" pair. (e) Flipping a subsequent chain of spins on the spin ice lattice (inset) restores the ice rules at the "chain" vertices, propagating the charges throughout the system. To a high degree of accuracy, the energy of a flipped chain configuration for increasing length r is identical for the dipolar spin ice model (circles) to that of the vertex magnetic charge model (solid line) which emerges from the dumbbell interpretation, and takes the form of a $1/r$ interaction i.e. a Coulombic attraction dependent on the charge separation. After Castelnovo et al. [19].

analogue of the flux-channeling Dirac string, running between two fractionally charged sites of excess north and south respectively. The dipolar spin ice model can be well approximated energetically by the interaction of charge dumbbells extending the length of a diamond lattice bond a, figure 2.3 (c,d), manifesting as an attractive Coulombic interaction $(1/r)$ between the two oppositely charged ice-rule defects at either end of this chain. The equivalence of the two models is illustrated in figure (e), as the monopole-antimonopole pair are incrementally separated via moment flip chain extension between discrete vertex sites. This $1/r$ relationship implies that the monopole objects are deconfined: as $r \to \infty$, the energy associated with their separation converges to zero, as for free charges in free space. A wide array of experimental evidence has since been presented validating this description [19; 51; 52; 53; 54; 55]. Again drawing on the robust nature of the mapping of spin ice onto water ice proton disorder, recently, an elegant interpretation has been shown to be viable representing monopole defects under the same framework as ionic defects on the diamond lattice [55], as appropriate for water ice. In this sense, spin ice is a "magnetolyte" possessing magnetic charge capacitance [56].

The large proportion of research into spin ice materials in currently focussed on the behaviour of magnetic monopoles. This work has had further influence inspiring the search for analogous physics in artificial spin ice systems [20; 22; 23; 24; 25; 26; 29].

2.2 Artificial Spin Ice

Artificial spin ices are lithographically patterned arrays of single domain nanomagnets [3]. The elongated shape of elements on a number of interpenetrating sublattices forms a 2D system of interlinked vertices at which coupled Ising-like dipole moments meet with incompatible interactions. Figure 2.4 and figure 2.5 show respectively the square [3] and kagome [9] lattices, the patterns currently most extensively studied. They are designed as analogues to 3D bulk spin ice materials [39; 40], in which rare-earth magnetic moments map robustly on to the proton ordering of water ice [5]. Artificial spin ices have recently become a source of intensive interest, as they allow for inter-elemental interactions to be uniquely

controlled and for direct imaging of states via magnetic microscopy. Systems formed from both isolated magnetic islands [3] and continuous interconnected wire networks [9] have been studied, over a wide proportion of possible areal scale: quasi-infinite systems [3; 9; 24], finite patterns of a few $\sim$ 100s of vertices [21], down to isolated building blocks [57; 58]. Such systems can be routinely fabricated via modern nanolithographic methods, sections 3.1 and 3.2.

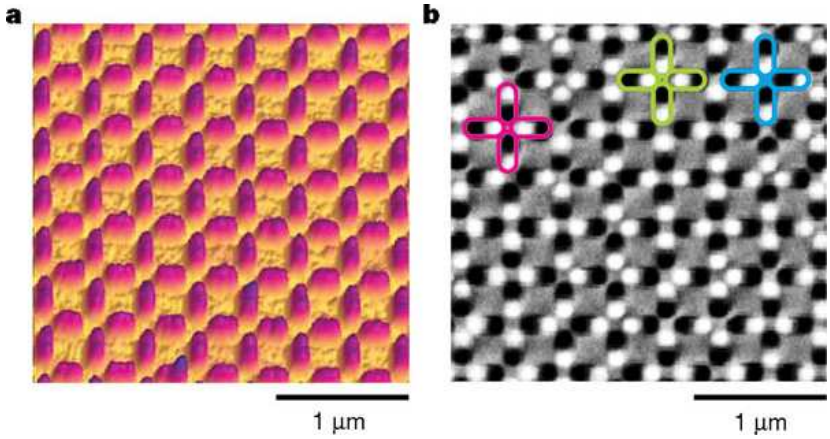

Figure 2.4: Artificial square ice. (a) Atomic force microscopy (AFM) and (b) magnetic force microscopy (MFM) of an artificial square spin ice, formed from isolated single domain ferromagnetic nanobar magnets. AFM shows the topographic arrangement of elongated elements, while MFM identifies the long axis alignment of Ising-like elemental magnetisation by dark/light contrast representative of the North/South elemental magnetic poles. Aiding interpretation of such images in terms of a vertex model, in (b), specific groups of islands are highlighted, indicating type 1 (red), type 2 (blue) and type 3 (green) magnetic vertex configurations, where four dipolar elements converge in a cross. After Wang et al. [3].

During the early/mid 2000s, Tanaka and co-workers (Keio University, Yokohama, Japan) studied magnetisation processes, domain wall configurations and magnetic ice ordering in such kagome nano-networks, recognising their close analogy with bulk water ice and spin ice [8; 59; 60; 61; 62; 63]. It was not until independent work by Wang et. al in 2006 [3] on artificial magnetic square ice

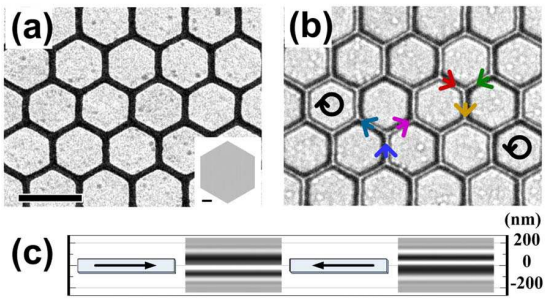

Figure 2.5: Artificial kagome spin ice. (a) Transmission electron microscopy (TEM) and (b) Lorenz-TEM (L-TEM) images of an artificial kagome spin ice nanowire network. TEM reveals the pattern's structure of three-fold rotationally symmetric vertices at which three wires converge, while L-TEM allows for identification of elemental Ising-like magnetisation alignment via the key shown in (c). MFM would not be able to identify the unique arrangement of such an interconnected network, imaging only stray flux from the centre of a vertex. After Qi et al. [9].

that the term "artificial spin ice" was coined and the growing excitement about such systems was instigated.

In nearly all experimental incarnations reported in literature, artificial spin ices are athermal when studied. For the $\sim$ 100 nm size elements typically fabricated from a standard ferromagnetic material such as NiFe, the thermal energy scales required for elemental magnetisation reversal is of the order of 10^5 K. Applied magnetic fields are therefore required to induce dynamics. Room-temperature stability allows exact microstates to be conveniently imaged using techniques such as magnetic force microscopy (MFM), figure 2.4, in which the North/South dumbbell nature of the elongated element is interpreted via light/dark contrast, section 3.4.1. Interest has largely focused on the access of well-defined statistical states [3; 8; 9; 16; 18; 30], energy minimisation [12; 16; 57; 64] and adherence to local 'ice rules' [3; 8; 9; 16; 60; 61]. As for the naturally occurring systems [19; 51; 52; 53; 54; 55; 56], an emergent "monopole excitation" description has also been invoked [18; 20; 22; 23; 24; 25; 26; 27; 65]. Being nanomagnetic systems, their implementation in magnetic device applications and

information processing is also being considered and explored [26; 28; 66]. The main experimental manipulation methods so far employed can be grouped into rotating field and dc field protocols, both of which will be addressed in this thesis.

Further illustrating the "designer-material" appeal of such patterned nanomagnet systems, many other similar lattices have been realised, such as kagome basket- [67], triangular- [68; 69] and brickwork-patterns [17]. Artificial ices can in principle be formed from arrays of any interacting Ising-like components and form part of a wider class of artificial frustrated Ising materials: 2D Ising lattices have been fabricated from superconducting flux vortex arrays [6; 7; 70; 71], close-packed colloidal spheres [72; 73], and out-of-plane anisotropic magnetic elements [74], while theoretical attention has been given to the construction of artificial ices from lattices of bistable spatial potentials containing single charged colloids [75; 76; 77] or superconducting vortices [78]. All experimental realisations of artificial ices have been nanomagnetic.

The study of these systems and methods of their manipulation have lent well to their theoretical study via Monte Carlo simulations [16; 20; 22; 27; 79; 80; 81; 82], numerical models [21; 75; 76; 77; 78], mean field calculations [21], statistical mechanics [64; 83], and finite element micromagnetics [26; 84; 85; 86].

Only recently have the effects of true thermodynamics been studied, identified via microscopy "frozen-in" to athermal square ice patterns [25], as will be discussed in chapter 6, and infered indirectly in "live" square ice patterns of low Curie temperature material using bulk-averaged magnetometry [87].

2.2.1 Square and Kagome Ice

Two complementary descriptions of artifical spin ice are often used: that of a dipole lattice and that of a vertex model [88; 89]. Figure 2.6 (a) and figure 2.7 show the $2^4 = 16$ and $2^3 = 8$ vertex configurations of the square and kagome systems respectively. As for real spin ice, no configuration of the moments converging at a vertex can simultaneously satisfy all pairwise interactions. The best that can be achieved is a lowest energy compromise. These configurations are defined by "ice rules", in analogy with bulk spin ice (and water ice), in which

2-in/2-out configurations satisfy 4 out of the 6 interactions on a tetrahedron, leading to a macroscopic ground state degeneracy.

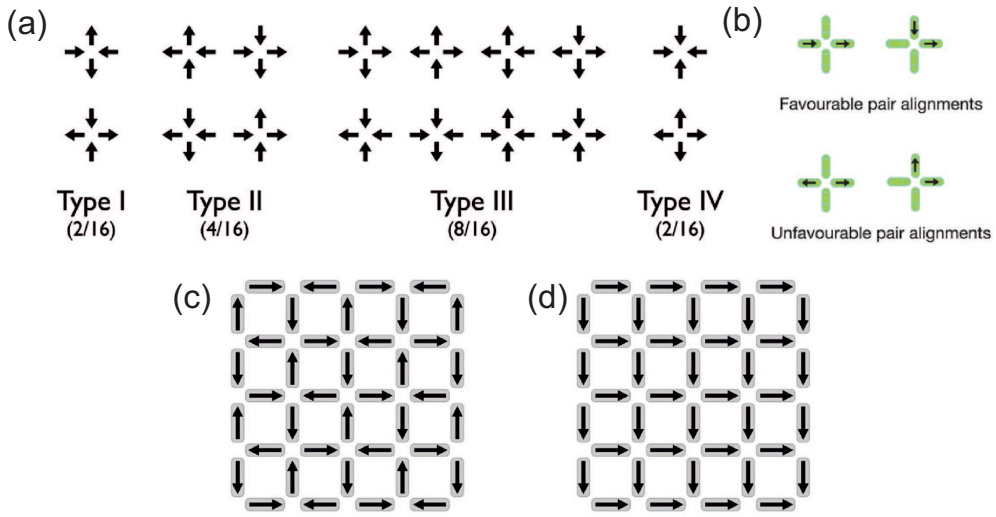

Figure 2.6: Configurations of Ising moments on the vertices of a square ice. (a) The sixteen square ice vertex configurations, grouped by vertex energy in to four types T_{1-4}, where arrows represent elemental magnetisations. The multiplicity of each type is also shown in brackets. $T_{1,2}$ obey the 2-in/2-out ice rules, but are energetically split, as square ice vertices possess a mixture of 1^{st} and 2^{nd} nearest neighbour pairs of elements. (b) At a vertex, a pair of Ising-like moments can form either a favourable or unfavourable configuration, due to their pair-wise interaction. In the case of isolated elements, this interaction is dipolar. (c) The square ice ground state (GS) comprising a pure tiling of alternating T_1 vertices, forming a chess-board pattern. Here, the ice rules are obeyed, and all 1^{st} nearest neighbour interactions are satisfied. (d) The diagonally polarised state (DPS), possessing a 100% tiling of a single T_2 vertex. The DPS also obeys the ice rules. (a,c,d) after Nisoli et al. [83]. (b) after Wang et al. [3].

The 16 square ice vertices can be grouped into four types, T_{1-4}, figure 2.6 (a), in terms of increasing vertex energy E_{1-4}, the sum of the six pairwise energy contributions on an isolated vertex. It has been shown that in various situations that a (perhaps naive) vertex energy model provides a good (mean field) approximation of the system energetics [16; 25]. $T_{1,2}$ both obey the 2-in/2-out rule, but

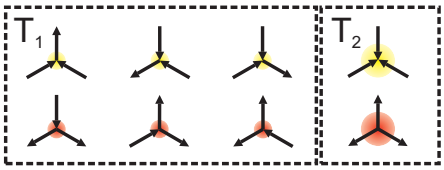

Figure 2.7: Configurations of Ising moments on the vertices of a kagome ice. Eight vertex configurations exist, which can be grouped in to two types. Lower energy T_1 vertices obey the 2-in(out)/1-out(in) kagome ice rules, with a minimised normalised vertex charge of $\pm$ 1, represented by yellow and red circles respectively. Higher energy T_2 vertices posses 3-in(out) configuration, with a normalised chage of $\pm$ 3, represented by large yellow and red circles respectively.

are however energetically split due square ice vertices comprising both 1st and 2nd nearest neighbour pairs. On a T_1 vertex, all 1st nearest neighbours are satisfied, whereas both 2nd nearest neighbour pairs are frustrated, figure 2.6 (b). On a T_2 vertex, the 2nd nearest neighbour pairs are satisfied at the expense of two 1st nearest neighbour pairs. This inequivalence is a crucial feature of square ice, in that it defines a 2-fold degenerate ground state (GS), figure 2.6 (c), a chess-board tiling of purely T_1 vertices. This is in stark contrast with the highly degenerate bulk spin ice where long-range interactions have to be invoked in order to define a GS [49] of low degeneracy. $T_{3,4}$ vertices present increasingly energetic and unfavourable configurations with an increasing number of unsatisfied pairwise interactions, having 3-in(out)/1-out(in) and 4-in(out) arrangements respectively.

Kagome vertices posses $2^3 = 8$ configurations, split in to two groups $T_{1,2}$ of low and high energy respectively where all interactions across a vertex are equivalent in strength. As a result, the system shares many properties with bulk spin ice - while theoretically having a well defined ordered GS [49; 90] (charge-ordered in the case of kagome ice), experimental access has been far from aquired. To first-order, both their ground states can be considered macroscopically degenerate. Further, long range interactions do not act to strongly lift the degeneracy of a general pure ice rule state, particularly for a zero net moment state in which long range interactions will largely cancel out. Distinctly different behaviour is therefore expected and observed between square and kagome ice patterns [17].

Within a model of "vertex-objects", each vertex type may be assigned properties in terms of magnetic charge and dipolar moment. Each converging element, dumbbell-like in finite sized elements, contribute a north or south pole to the vertex centre, and vertex charge may be considered as the sum of these. In square ice, $T_{1,2}$ vertices are magnetically neutral, obeying the ice-rules. $T_{3,4}$ posses an excess of north or south, having normalised monopole moment (i.e. charge) of $\pm$ 2 and $\pm$ 4 respectively. They present qualitative analogs of the fractionalised magnetic monopoles of Castelnovo [19], section 2.1.1. $T_{1,4}$ are unpolarised, whereas $T_{2,3}$ posses a dipole moment. On the kagome system, both $T_{1,2}$ vertex types posses excess charge, $\pm$ 1 and $\pm$ 3 respectively, and T_1 possesses a polarisation. Terminology regarding what constitutes a "monopole defect" has not yet been standardised, however, regardless of naming convention adopted, such configurations present a possibilty of studying fractionalisation in an artificial 2D system. Reliable manipulation of "monopole" configurations is therefore crucial.

While square ice patterns are studied exclusively in the work presented in this thesis, general results common to both square and kagome patterns, as well as any such general nanoarray system, are instructive in the process of understanding the manipulation of both single vertex configurations and global states. What has become increasingly evident is the role quenched disorder plays in the behaviour of these systems [6; 7; 16; 24; 26; 28; 77; 78], i.e. imperfection in the structure which is "frozen-in" and intrinsic to the system, imparting a distribution of properties to the elements about an average ideal. While this is not a new phenomenon, its effects can be drastic. Further, finite size effects have recently been directly addressed in the form of *non-point* dipole behaviour [12], and *non-Ising*-like behaviour [27].

2.3 Accessing the Ground State

2.3.1 ac Demagnetisation

In such artificial "designer" systems, a prevalent and important point of focus is the testing of fidelity to the prescribed ideal Hamiltonian via a controlled "anneal" process, [6; 7; 70; 71; 72; 73]. As previously employed to e.g. form GS

configurations in dipolar coupled nanomagnet chains [91; 92], ac demagnetisation has been extensively employed in the generation of low-moment, low-energy artificial spin ice states [3; 12; 14; 16; 17; 18; 57]. The majority of studies specifically addressing the protocol itself have been conducted by researchers at Pennsylvania State University (PSU) on mainly square ice patterns [3; 14; 16; 64; 83], an overview of which is warranted.

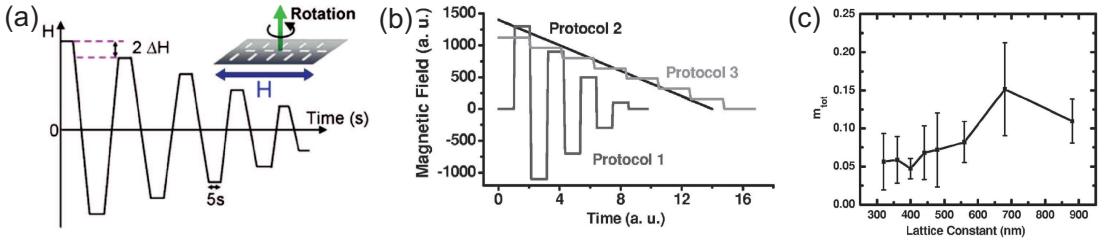

Figure 2.8: ac demagnetisation illustrations and results. (a) A cartoon depicting ac demagnetisation. The sample is in-plane rotated about an out-of-plane axis while a magnetic field is applied in-plane along a fixed axis in the laboratory frame. The field magnitude has a square function profile, with a decrease in magnitude of ΔH every half an oscillation period, $\sim$ 1 s. After Ke et al. [16]. (b) Various field protocols tested by Wang et al. [14]. Protocol 1 is as descibed in (a). Protocol 2 reduces the field in a linear fasion. Protocol 3 has a step function profile, with no change in sign of the field with time. Protocol 1 is reported to produce the most effective demagnetisation of square ice patterns. (c) The residual magnetisation of a series of square ice patterns of varying lattice constant, following protocol 1, with $\Delta H \sim 10$ Oe. (b) and (c) after Wang et al. [14].

For a general ac demagnetisation process, a sample is exposed to an oscillatory magnetic field of decreasing amplitude. Variations on this general theme can produce similar results, however, the most effective routine is reported by Wang et al. to involve an in-plane field with stepwise decreasing alternating square profile, with simultaneous in-plane sample rotation of $\sim$ 10 Hz, $\sim$ 100 ms period [14], figure 2.8 (a,b). The applied field, H_{a}, begins well above the coercive field of the arrays of $\sim$ 700 Oe, figure 2.9, with 25 nm thick NiFe islands of 80 nm by 220 nm lateral size, and lattice constants varying from $a = 320$ nm up to 880 nm.

The field is held for a number of seconds at each step. The polarity is reversed via a ramp at a rate of $\sim$ 10 kOe/s, and the magnitude is decreased by a field step of $\Delta H \sim 10$ Oe every half a period, hence fully reversing between $\pm \sim 500$ Oe in ~ 100 ms. Linear-decreasing and non-oscillating step function field profiles, also illustrated in figure 2.8 (b), were reported to be less effective, however, the reasons for this were not discussed and are undetermined.

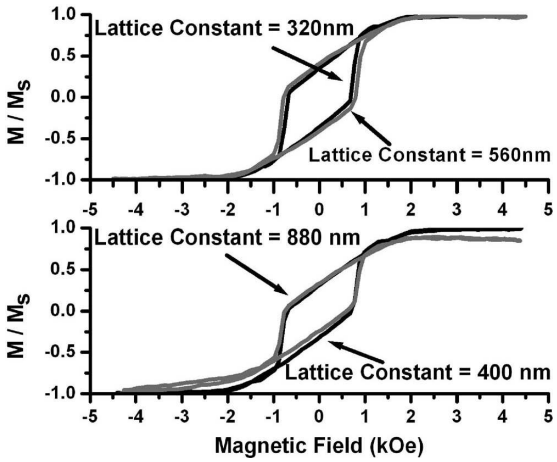

Figure 2.9: Magnetic hysteresis loops of artificial square ice patterns. Loops of principal square axis magnetisation were measured via MOKE magnetometry for patterns of lattice constant ranging from 320 nm to 880 nm, with 25 nm thick NiFe islands of 80 nm by 220 nm lateral dimenions. After Wang et al. [14].

While the exact details of the processes involved remained unclear, a number of important results emerged from the initial work [3; 14]. As the name implies, the protocol can repeatably access demagnetised states of net moment $M_{\text{tot}} \sim 0$, as shown in figure 2.8 (c) for a sequence of square ice patterns with varying lattice constant a, where M_{tot} is defined as the net digital moment magnitude, normalised to a diagonally polarised state (DPS) of Ising moments ($M_{\text{tot}} = 1$), figure 2.6 (d). Further, tuning the sample interaction strength via the lattice constant allows for repeatable control of the average ordering achieved, shorter a enhancing ice-rule vertex populations and pairwise energy-minimising short range magnetic correlations, figure 2.10 (a) and (b) respectively. As shown for a lattice of $a = 400$ nm in figure 2.4, the states achieved look distinctly disordered to the

eye, in contrast to the periodic GS, figure 2.6 (c). At $a = 880$ nm, the state achieved is statistically random, having vertex type populations as given by their multiplicity and negligible dipolar correlation. These results illustrate the large degeneracy of zero net moment states possible. This work demonstrated such patterns as an artificial spin ice, possessing bias towards ice-like configurations as a result of inter-elemental coupling and only short range magnetic correlations. Further, the fact that states can be repeatably achieved and controlled provides a powerful basis for further experiments.

Ke et al. [16] showed that the process exploits a finite field window $[H_{\text{min}}, H_{\text{max}}]$ distributed about the array square axis direction coercive field, $H_{\text{c}} \sim 700$ Oe for all a, figure 2.9. For an $H_{\text{a}} > H_{\text{max}}$ elemental moments will track the applied field, whereas an $H_{\text{a}} < H_{\text{min}}$ cannot induce any reordering. Only for $H_{\text{min}} < H_{\text{a}} < H_{\text{max}}$ do non-trivial reordering processes occur, allowing the system to explore part of its magnetic phase space under the influence of configuration dependent dipolar coupling and intrinsic island properties. Presumably, the ramping rate, fast relative to the sample rotation frequency, avoids demagnetising effects during the transient reversal parts of the field profile, such as those that would occur for a slowly linearly ramped protocol, as shown in figure 2.8 (b), passing through a $\sim$ 100 Oe window in 10 ms.

Further, the size of ΔH is crucial. Too large a ΔH results in H_{a} stepping from above to below the window in a single step, not allowing for reordering, leaving a non-zero net normalised magnetisation M_{tot}, figure 2.11. As ΔH is reduced, demagnetisation is enhanced, as H_{a} can spend more time within the range $[H_{\text{min}}, H_{\text{max}}]$, reaching a value below which $M_{\text{tot}} = 0$ states are reliably accessed. Interestingly, further reduction of ΔH produces states with increasingly strong short range GS correlations, figure 2.12, (and presumably higher populations of low energy vertices), and further reduction of net energy, figure 2.13. GS convergence was however found to be unobtainable via this method [16], figure 2.13, with energy monotonically approaching a finite value above that of the GS as $\Delta H \to 0$.

Reduction of step size makes differences between each step smaller. As the system can only make downward transitions in energy, larger steps will act to arrest and jam higher energy configurations in to the system which cannot be

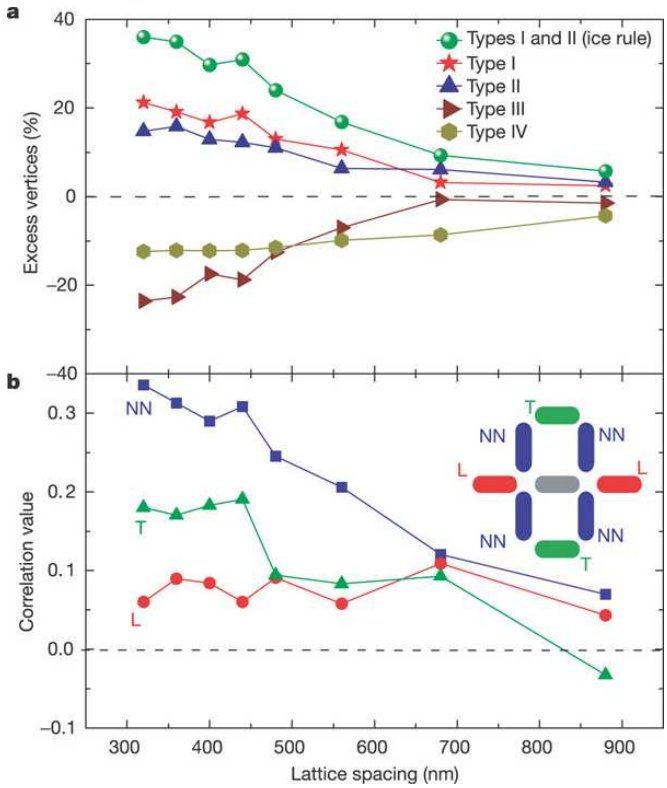

Figure 2.10: Experimental outcome of ac demagnetisation of an artificial square ice array, as determined by MFM. By tuning dipolar interaction strength between magnetic elements of the array by lattice constant a across a series of samples with nominally identical islands, the magnetic state accessed can be reliably controlled. Increasing interactions takes the state from random-like state at $a = 900$ nm to a short-range correlated icy state as a approaches 300 nm, as reflected by (a) the increasing ice-rule obeying vertex populations, and (b) pairwise energy minimising dipolar correlation, between neighbours of type as illustrated inset. After Wang et al. [3].

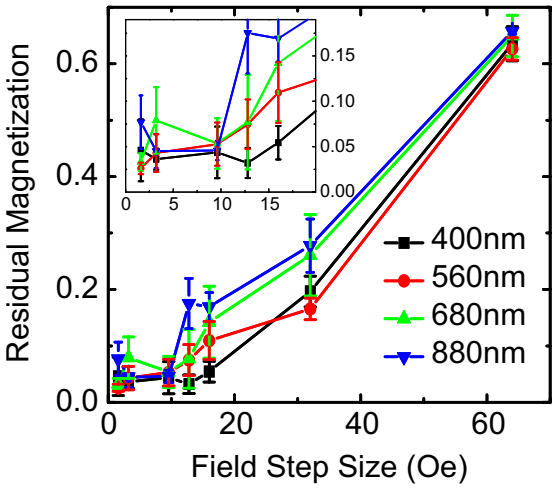

Figure 2.11: Residual net normalised digital magnetic moment of four selected square ice patterns of varying lattice consant as a function of ac demagentisation field step ΔH. All trends appear very similar and states of effectively zero magnetisation can be accessed for all patterns for ΔH below $\sim$ 15 Oe. The low ΔH range has been magnified inset. After Ke et al. [16].

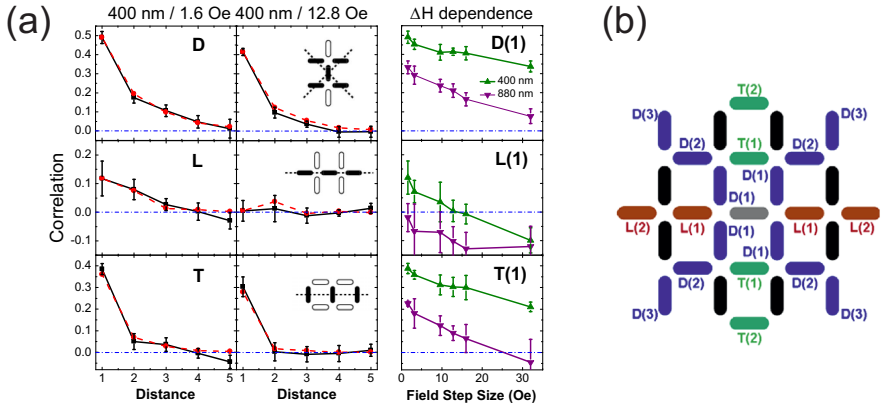

Figure 2.12: Control of magnetic order of ac demagnetised states via field step and lattice constant. (a) Ground state correlation for three directional neighbour types L, T and D, as defined in (b), for a 400 nm square ice lattice following ac demagnetisation with $\Delta H = 12.8$ Oe and $\Delta H = 1.6$ Oe. Correlations are found to be stronger as ΔH decreases. Also shown is the dependence of L(1), T(1) and D(1) on ΔH for the 400 nm and 880 nm lattices. After Ke et al. [16].

removed. Due to the square ice geometry, it is not possible to make a direct transition from a T_2 to a T_1 vertex configuration, requiring two moment reversals via a T_3 configuration. While kagome ice can make direct transitions between high and low energy vertex configurations, a similar result is found [17; 57], reflecting an underlying property of either the system or the protocol acting to suppress GS order. Further, the process is not found to create exactly identical order each time, only order that is on average reproducible.

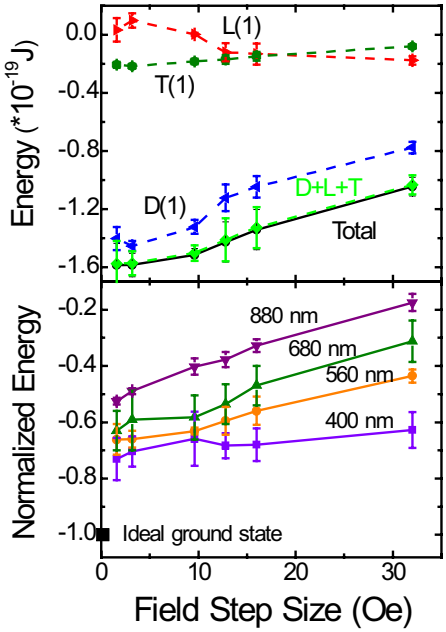

Figure 2.13: The net energy of square ice patterns following ac demagnetisation, determined by correlation values and micromagnetics. After Ke et al. [16].

These experiments focussed on bulk areas of quasi-infinite patterns. A recent report has shown evidence of finite area effects during demagnetisation [27], however, its interpretation was not discussed. Recent theoretical work has explicitly addressed such effects [21], and will be discussed in section 2.3.4.

2.3.2 Effective Thermodynamics

Growing evidence exists that the ac demagnetisation process discussed in section 2.3.1 behaves in some ways analogously with a *thermal* anneal process. Clearly,

it forms states distinctly disordered under the influence of internal interactions. Following the intial results of Wang et al. [3], an equilibrium statistical mechanical formalism was introduced by Nisoli et al. [64; 83] well describing data from ac demagnetisation experiments in terms of "effective thermodynamics". While such treatment of athermal systems is not a new thing, for example the application of statistical mechanics to powder mixtures [93] and vibration fluidisation of granular matter [94], ac demagnetisation appears qualitatively to be more like stirring a box of sand than shaking it. It is not immediately evident that it is a thermal-like process when compared with "artificial Brownian motion".

Initially, results were reported to show that ac demagnetised states for short lattice constants possesed a net average vertex energy, or specific vertex energy, $\tilde{E} = \sum_i n_i E_i = E_2$, where n_i are the fractional population of vertices for $i = 1$ to 4, and E_i are the (isolated) vertex energies respectively, perhaps appealing to the idea of a thermodynamical equilibrium ensemble, maximising its entropy under the above energy constraint - clearly, ac demagnetised states are highly disordered, however, "feel" the influence of dipolar coupling. Further, this motivated a qualitative desciption of the process as first preparing a background diagonally polarized state (DPS) of a single T_2 vertex tiling, figure 2.6 (d), by virtue of the large initial applied field, which subsequently carves out defect vertices onto this background as the field decreases in magnitude by switching elemental Ising states which eventually become arrested.

The first port-of-call for tackling this problem would no doubt be a mean field approximation, treating the system as a non-interacting vertex lattice, in which vertex sites can take one of the four energy states E_i, with degeneracy $q_i = 2$, 4, 8 and 2 respectively. As per section 1.3, the number of ways, Ω, to arrange $\mathcal{N}$ vertices with N_i configurations of vertices $i = 1$ to 4 is then given by equation 1.2. Here, dipolar correlations beyond a vertex are neglected.

The equilibrium fractional vertex populations, n_i, can then be calculated by maximising the entropy S with respect to N_i, or alternatively, maximising $S/\mathcal{N}k_B = (1/\mathcal{N}) \ln \Omega = -\sum_i n_i \ln n_i/q_i$ with respect to n_i. Nisoli et al. [83] found that this model failed to correctly describe the observed vertex population in MFM. This is not too surprising as the field treatment is distinctly non-thermal.

It was found, however, that a much better agreement could be aquired by adopting a model in which the DPS background vertex population and defected vertex population were taken explcitly into account.

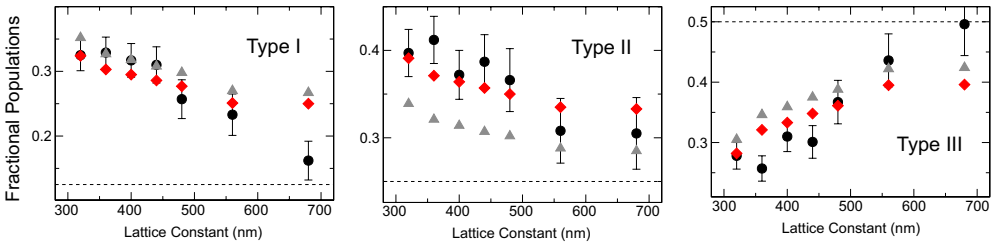

Figure 2.14: Square ice vertex populations following experimental ac demagnetisation compared with those given by statistical mechanical calculations. Variation in vertex populations as function of lattice constant for (left) T_1, (centre) T_2 and (right) T_3 vertices, for (black circles) experimental ac demagnetised data, (grey triangles) a standard canonical distributed calculation, and (red diamonds) the extended model. After Nisoli et al. [83].

Now, the number of ways to place $\mathcal{D}$ defects onto the lattice is given by

$$\Omega = \frac{\mathcal{N}!}{(\mathcal{N}-\mathcal{D})!}\prod_i \frac{q_i^{N_i}}{N_i!}. \tag{2.1}$$

where N_i are explicitly the defected vertex populations. Further, entropy can be normalised and written as $S/\mathcal{N}k_\mathrm{B} = -[\rho\ln\rho + (1-\rho)\ln 1-\rho] + \rho\sigma$, where $\sigma = -\sum_i \nu_i \ln(\nu_i/q_i)$, ρ is the fractional defect density, and ν_i are the fractional populations of vertex types within the defect population. $\rho\nu_i$ gives the absolute populations of "defect" vertices in the whole system, such that n_i and ν_i are related by the expressions

$$\begin{aligned} n_i &= \rho\nu_i \quad \text{for} \quad i = 1,3,4 \\ n_2 &= (1-\rho) + \rho\nu_2 \end{aligned} \tag{2.2}$$

where $(1-\rho)$ is the fractional population of background T_2 vertices. Expressions for the "equilibrium" values of ν_i and ρ can be calculated by maximising σ with respect to ν_i under the energy constaint $\sum_i \nu_i E_i = E_2$, and maximising $S/\mathcal{N}k_\mathrm{B}$

with respect to ρ unconstrained (as background vertices contribute E_2 to the system per site). This yields an equilibrium distribution of vertices within the defect population

$$\nu_i^* = \frac{q_i \exp(-\beta E_i)}{Z} \tag{2.3}$$

and an equilibrium defect density

$$\rho^* = \frac{1}{\exp(-\sigma^*) + 1} \tag{2.4}$$

where $\sigma^* = -\Sigma_i \nu_i^* \ln(\nu_i^*/q_i)$ and Z is the partition function over ν_i^*.

The "equilibrium" values of n_i can then be calculated from equations 2.2. At lower lattice constant, when interactions are of greater significance during demagnetisation, this formalism was found to yield good agreement with the experimental data trends, as shown by red diamonds in figure 2.14. Note: the Lagrange multiplier, an effective reciprocal temperature, must be taken as $1.3(E_2 - E_1) \equiv 1.32 \times 10^5$K, which is the only identifiable fitting parameter used. The equivalent corresponding standard calculations are also shown as grey triangles. This is an interesting and curious result, suggesting that ac demagnetisation behaves as if to maximise the entropy of a population of defect vertices in internal equilibrium, in turn itself in equilibrium with the background.

The subsequent results of Ke et al. [16], however, appear to be at odds with this picture of scrambling the system under a constant net vertex energy constraint, showing that the energy and GS correlation (and presumably the relative populations of vertex types) of the demagnetisated states aquired were dependent on field step ΔH, figure 2.13, hence $\tilde{E} \neq E_2$ in general.

Further work on this model [64] showed how taking a ratio of canonical defect vertex populations, equation 2.3, gives

$$\beta(E_j - E_i) = \ln\left(\frac{q_j \nu_i}{q_i \nu_j}\right). \tag{2.5}$$

As $\nu_i/\nu_j = n_i/n_j$, given $i, j \neq 2$, equation 2.2, this allows for the effective temperature $T_{\text{eff}} = 1/k_B\beta$ of a state to be inferred directly from a magnetic microscopy image by simply counting the vertex populations, rather than by

fitting. Further, the variation in n_i with β can be calculated, as q_i and E_i are known. For convenience, an energy scale setting $E_1 = 0$ and $E_3 = 1$ was used. It was found that using a vertex-charge energy model, in which E_i are calculated as the net Coulombic interaction between the four North/South magnetic poles at a vertex, excellent agreement between theory and the experimentally observed populations was found, figure 2.15 (a). This provides the correct ratio of energies $E_i = 0,\ 0.452,\ 1$ and 3.094, for $i = 1,\ 2,\ 3$ and 4 respectively, which are not dissimilar to that obtained via micromagnetics for short lattice spacing [15]. In normalised energy units, all experimental data sets, incorporating a range of lattice constants and values of ΔH, collapse on to the same set of four curves, reflecting an underlying property of the ac demagnetisation process. Further, β can be increased by decreasing the lattice constant, making the effects of dipolar coupling stronger, and by decreasing ΔH. In fact, as shown in figure 2.15 (b), a linear relationship between β and ΔH is found. This is an intuitive result which captures the trend in state found by Ke et al. with ΔH [16].

The continuation of this model is however strange. As mentioned, generally it is not clear whether $\tilde{E} = E_2$. If not true, ρ is required to be explicitly energetically constained for the maximisation of entropy, meaning that equation 2.4 no longer stands. (It should also be noted that $\tilde{E}$ does not include dipole-dipole interaction which extend beyond a vertex.) Further, to justify both the introduction of a background vertex population and the energy model, Nisoli et al. present the graph shown in figure 2.16, plotting $\ln(5n_1/2n_2)$ against $\ln(8n_1/2n_3)$, and finding an apparently proportional relationship with a gradient close to E_2. It is stated that in the low β limit, that n_i are in fact approximated by a set of canonical distributions with $q_2 = 5$, an "anomalous degeneracy" apparaently accounting for the four T_2 defects possible and the one T_2 of the background. These calculations are however not shown. This raises the question of why the extended model is taken as correct whereas the description given by the conventional calculation is not. These points will be returned to later in section 6.4.1.

It is not necessarily apparent why such a desciption should work in a clearly non-equilibrium situation. ac demagnetisation, as noted by Nisoli et al., is not thermal equilibration. The dynamics are not stochastically driven, and are in fact periodically biased. It has become apparent that ac demagnetisation has become

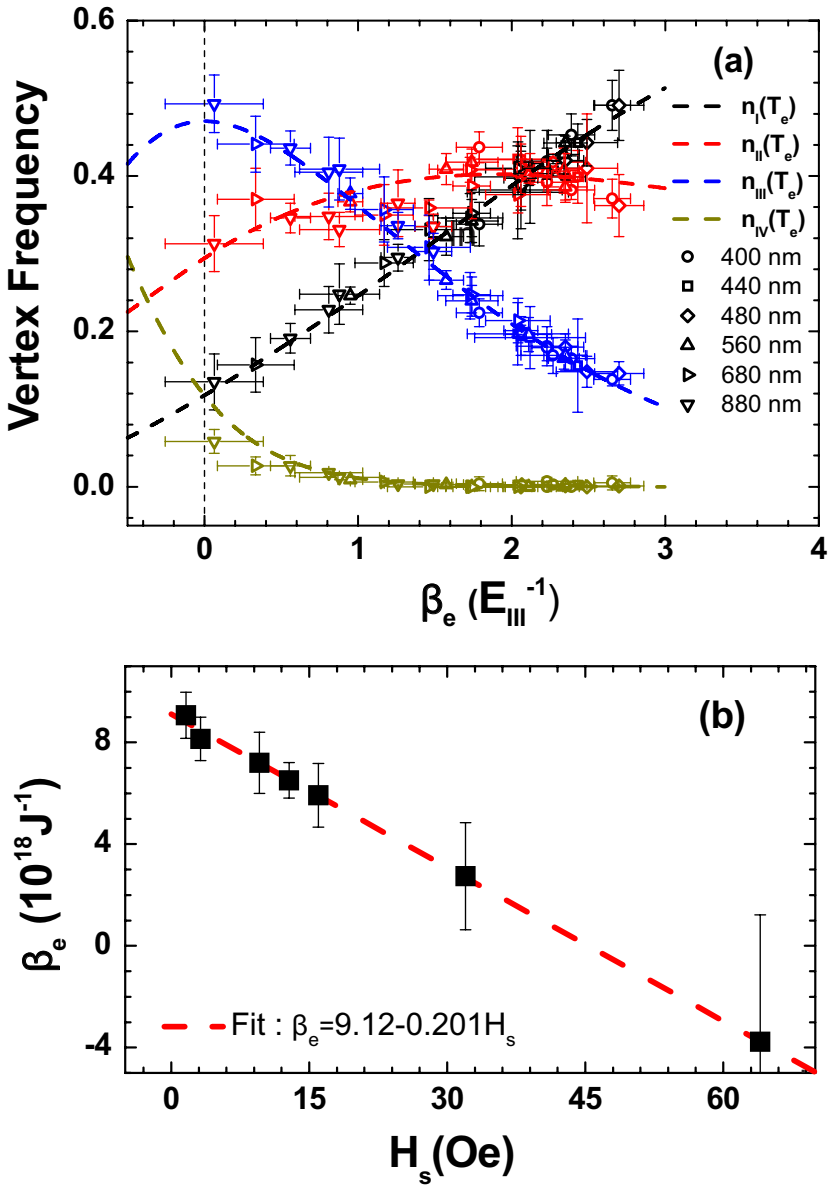

Figure 2.15: Comparison of experimental data from ac demagnetisation experiments with the calculations of the extended statistical mechanical model. (a) Experimental vertex populations as a function of β, the reciprocal of the effective temperature of demagnetisation, for a series of square ice patterns of varying lattice constant, ac demagnetised with protocols of a range of field step ΔH. (b) The linear variation of β with ΔH. After Nisoli et al. [64].

increasingly assumed to be an equilibrating process equivalent to true thermodynamics, to the extent that experimental ac demagnetised states have been directly compared with thermally annealed states of Monte Carlo simulations [12].

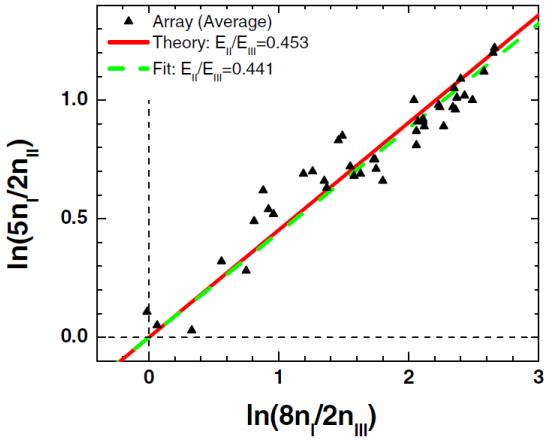

Figure 2.16: The square ice vertex energy ratio E_2/E_3, as calculated from data of ac demagnetised states. As appropriate for canonically distributed vertices with an anomalous degeneracy of $q_2 = 5$, a proportioanl relationship exists between two logarithms of vertex population ratios, as shown. After Nisoli et al. [64].

In chapter 6 of this thesis, these concepts will be returned to, and similar ideas will be extended to truly thermally equilibriated systems - the concept of T_{eff} still being meaningful in a system equilibriated at a finite "real" temperature.

2.3.3 "Demagnetisation" of Superconducting Square Ice and the Role of Disorder

Libál et al. [78] presented a theoretical model of an artificial square ice system formed from superconducting vortices in a thin film superconductor. Such objects are vortices of persistent supercurrent, along the centre of which a magnetic flux tube passes [95]. Arrays of vortices can form spontaneously under the correct low temperature conditions. A detailed understanding of superconductivity is not required to understand the model of Libál et al., and a qualitative discussion will be given to illustrate the important outcomes.

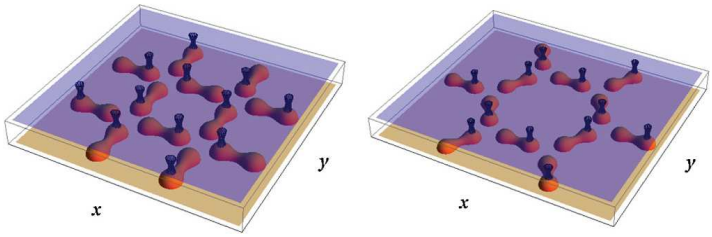

Figure 2.17: An illustration of an artificial spin ice formed by superconducting vortices pinned by an array of bi-stable traps. Vortices experience a mutual repulsive interaction, and find potential minima where the superconducting thin film thickness is lower, hence, double-hump non-superconducting islands buried in the film define a lattice on which ice-like physics may be studied. Shown on the left is a square ice, and the right a kagome ice. After Libál et al. [78].

The important aspects of the model are that (1) vortices experience a repulsive interaction between each other, decreasing with increasing separation, (2) vortex pinning potential minima are located at lateral positions where the superconducting film is thinner, and (3) vortices can be driven laterally by an applied current. Hence, pinning traps could be artificially created experimetally by depositing the superconducting thin film on top of a pattern of non-superconducting nanostructures. An elongated element with a "double hump" profile can further allow for a bistable potential well to be formed, creating an interacting Ising-like entity defined by the displacement of the vortex into one of the two minima. Minima are spaced by $l = 5/3\lambda$, where λ is the London penetration depth which defines an interaction length scale. In the model, a square ice array of such elements is defined, illustrated in figure 2.17, with one vortex per element. Again, a 16 vertex model can be considered, however with an altered isolated single vertex degeneracy compared with that of magnetic square ice, for example, 4-out is now the lowest energy configuration on a vertex, and 4-in is the highest energy.

A dynamical anneal process, analogous to ac demagnetisation of a nanomagnet array, is realised by the application of a rotating-direction in-plane current, with step-wise decreasing alternating amplitude. The outcome of such a protocol is investigated for varying strengths of quenched "frozen-in" disorder, the pinning potential barrier heights being allocated from a normal distribution of width σ

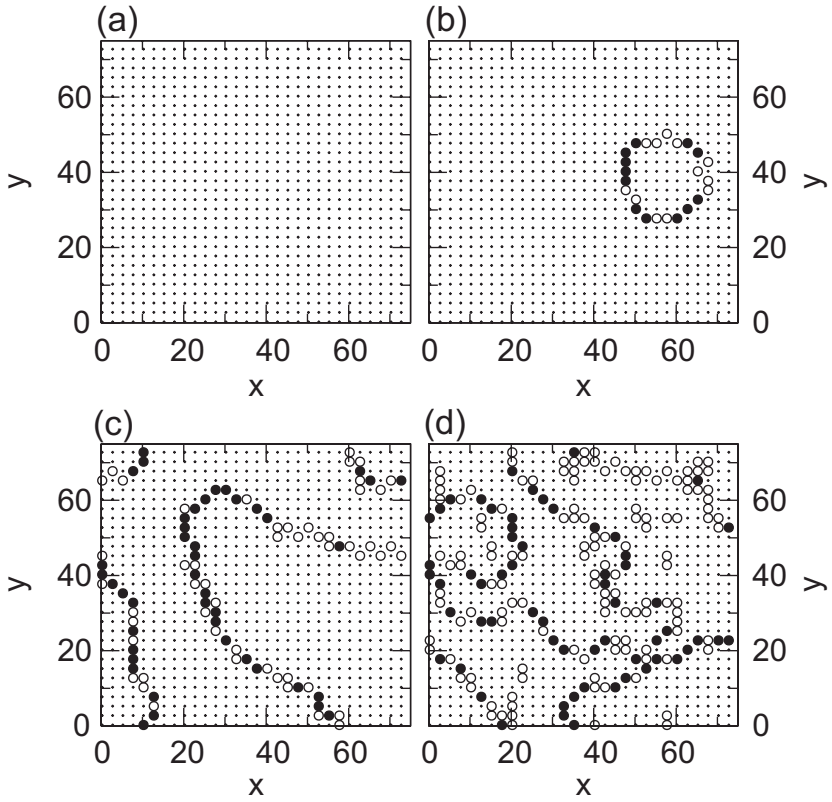

Figure 2.18: Final superconducting square ice states following a dynamic anneal process mediated by applied current, analogous to ac demagnetisation of a nanomagnet array. Dots represent a lowest energy GS ice-rule vertices, which map directly onto the magnetic square ice T_1 vertices. Filled circles represent non-GS ice rule vertices, which map on the T_2 magnetic square ice vertices. Open circles represent non ice-rule defects. (a-d) show results for increasing potential barrier height disorder, with values taken from a normal distribution of width $\sigma = 0$, 0.1, 0.5 and 1 respectively. Increasing barrier height disorder suppresses GS vortex ordering (which maps on the the nanomagetic square ice GS) and leaves an increasing density of defect structures in the form of grain boundaries and isolated defects for the results presented of highest disorder. After Libál et al. [78].

about a constant average, and for varying lattice parameters a. Periodic boundary conditions were used for a 80 × 80 vertex system.

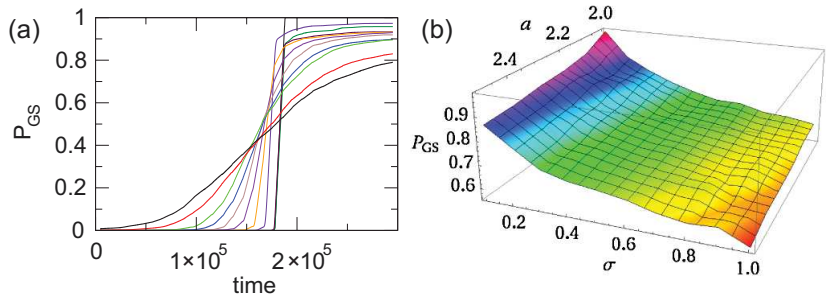

Figure 2.19: Variation of ground state ice-rule obeying population density P_{GS} for simulated "demagnetisation". (a) P_{GS} as a function of simulation time, for barrier height disorder varying from 0 (steepest curve) to 1 (least steep curve) for $a = 2.7\lambda$. (b) Final P_{GS} as a function of disorder strength σ and lattice spacing a. After Libál et al. [78].

Figure 2.18 shows final state configurations following "demagnetisation" for increasing σ at constant $a = 2.5\lambda$. Dots represent GS vertices (which map on to T_1 vertices as defined in figure 2.6), closed circles represent non-GS ice-rule vertices (which map on to T_2 vertices), and open circles represent non ice-rule defects. For $\sigma = 0$, a pure GS configuration is formed. The familiar square ice GS is realised, mapping onto that of magnetic square ice, despite not being formed from the lowest energy isolated vertices. This state is in stark contrast to the long-range disordered ac demagnetised state in experimental nanomagnet arrays. As disorder increases, $0.1 < \sigma < 0.7$, increasing numbers of non-GS vertices are found, forming grain-boundary structures of increasing length. For the highest disorder shown, $\sigma = 1$, some isolated defects are also observed. This can be understood by elements of larger-than-average barrier height acting as pinning sites of order at higher current, acting as nucleation sites for GS order or possibly as pinning sites for grain boundaries as the current magnitude is reduced. The suppression of the GS is illustrated temporally in figure 2.19 (a), showing the fractional GS vertex population P_{GS} as a function of the simulation time. The curve for $\sigma = 0$ corresponds to that with the sharpest jump, from $P_{\mathrm{GS}} = 0$ to

$P_{GS} = 1$ at a time of 1.75×10^5. The sharp transition indicates a small "critical field window" $[I_{min}, I_{max}]$ in which dynamics are allowed. $\sigma = 1$ corresponds to the least steep curve, illustrating that the onset of GS-ordered vertices begins much sooner but is however strongly suppressed, attributable to the wider critical window.

Figure 2.19 (b) shows a 3D plot of P_{GS} as a function both σ and a, agreeing with the initial results of Wang et al. [3]: increased interaction strength (reduced a) acts to enhance square ice GS ordering, against the effects of quenched disorder. Disorder in the anisotropic barrier heights between the Ising states of nanomagnets in an artificial ice array is most certainly present. These simulations suggest that the structural disorder present in nano patterned magnetic arrays is appreciably large, states of such strong GS order having never been achieved by field. Further, the suppression of GS order as found by Wang et al. is not a result of the frustrated lattice geometry, but largely an effect of quenched disorder. The critical field window, while influenced by configuration dependent dipolar coupling, is most strongly influenced by the intrinsic distribution of island properties.

It is perhaps due to such a barrier height distribution that ac demagnetisation can be described by using the statistical mechanical formalisms of Nisoli et al. [64] - true thermalisation acts to disorder a system via random "kicks" or moment flips of randomly "chosen" elements against the influence of dipolar coupling. While the field protocol is periodically directionally biased, disorder imparts a randomising effect on the correlated field-flipping of moments. For example, the moments that first arrest during the routine are those of higher barrier height, which are allocated effectively at random. This process will continue with every field magnitude step, arresting further elements under the same competition between correlation and randomisation.

2.3.4 Constant H Protocol

Limited information is currently available as to the exact dynamical processes which occur during such rotating field protocols as described in the previous sections. Recently, work by Budrikis et al. [21] has provided valuable insight into

this area. Numerical simulations of finite scale arrays of point Ising dipoles were used to address field mediated dynamics of square ice under a rotating magnetic field of constant magnitude. Two finite pattern types were used, open- and closed-edged, as defined in figure 2.20 (a) and (b) respectively, with 400 and 420 elements respectively, $\sim 20 \times 20$ vertices. Within the model framework, normalised units were used, with the nearest neighbour dipolar interactions $= \pm 3/2$. Spins reverse their magnetisation under the condition that $-(\mathbf{h} + \mathbf{h}_i^{\mathrm{d}}) \cdot \mathbf{s}_i > h_c$, where $\mathbf{h}$ is the applied field, $\mathbf{h}_i^{\mathrm{d}}$ is the total dipolar field acting on spin i with unit vertor $\mathbf{s}_i$, and h_{c} is the critical switching field magnitude given to all spins. h_{c} is set $= 10$, which is larger than the net dipolar field acting on any spin in the system i.e. a spin can only reverse under the application of an applied field when the projection of the total field along the spin Ising axis excedes a critical value. While this is an ideal approximation of island behaviour, strong deviations from Ising behaviour is only expected to occur for very large total fields.

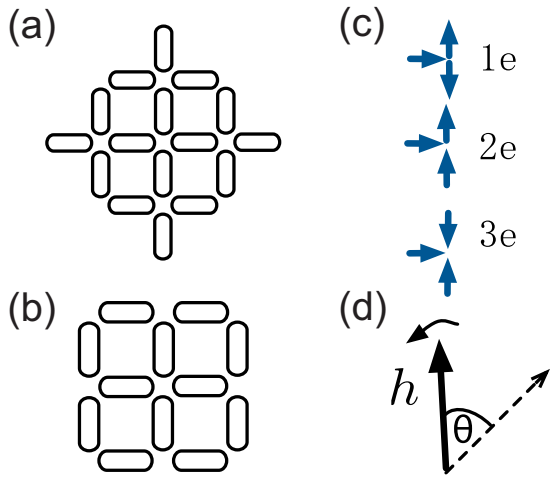

Figure 2.20: Finite area square ice patterns. (a) Open and (b) closed edge square ice patterns. Open arrays are fully defined by the 16 vertex model, however, closed arrays required definition of three edge vertices, as shown in (c). (d) The initial applied field direction (dashed line) and subsequent field rotation direction. Modified from the work of Budrikis et al. [21].

Both field and net array moment begin parallel to a square lattice diagonal, an initial DPS with 100% T_2, figure 2.6 (d). $\mathbf{h}$ then rotates anticlockwise, figure 2.20

(d), in angular increments of $d\theta = 0.01$. At each increment, spins are selected at random and flipped if the switching criterion is met until no more flips can occur. This is continued until a steady-state solution is found. Here, θ is equivalent to a unit of time.

The behaviour of the systems and the final state achieved were found to be crucially dependent on the array edge type and the value of $h = |\mathbf{h}|$. In both open and closed arrays, all non-trivial behaviour begins by edge-nucleation events, due to the local coordination and net $\mathbf{h}_i^{\mathrm{d}}$ favouring this, with bulk nucleation disallowed. For open edges and a correctly tuned h final states of greater than 90% T_1 vertex populations are achieved i.e. strong GS ordering.

Figure 2.21 (a) and (b) show respectively the T_1 and T_3 populations for the open edge systems as a function of θ for three select values of h, while inset in (a) is the final T_1 populations against h, illustrating the presence of four field regimes. Two trivial regimes exist: for $h < 9$, no switching can occur, and for $h > 11$ spins indefinately track $\mathbf{h}$. In the two non-trivial regimes, spin reversal nucleates at the edges, forming T_3 "monopole" configurations of opposite charge at opposite edges, which incrementally propagate into the bulk via sequential spin flip chains. In the low field regime, energetic constraints only allow propagation via chains of T_1 vertices incremented every field cycle. As h increases a gradual transition is made into the high field regime where propagation is increasingly allowed via T_2 chains, dependent on local $\mathbf{h}_i^d$, ultimately suppressing the final T_1 populations obtained.

Closed arrays have distinctly different behaviour, figure 2.22, due to the behaviour edge vertices 1e, 2e, and 3e, figure 2.20 (c). T_3 nucleation is only possible from a 2e edge vertex, whereas configuration 1e suppresses nucleation. Further, the critical field for nucleating a T_3 vertex is larger than the field required to propagate a T_3 vertex via T_2 chains, hence, no low field regime exists, and large T_1 populations are not possible.

This is a distinctly non thermal process, relying on the system's bias towards low energy configurations on local scales and exploiting only downward transitions in energy. It is also the first work to explicitly address an intrinsic source of a critical switching window, section 2.3.1, not related to quenched disorder which is in fact absent from the model, ideal elements closer to the edge of a DPS tiled

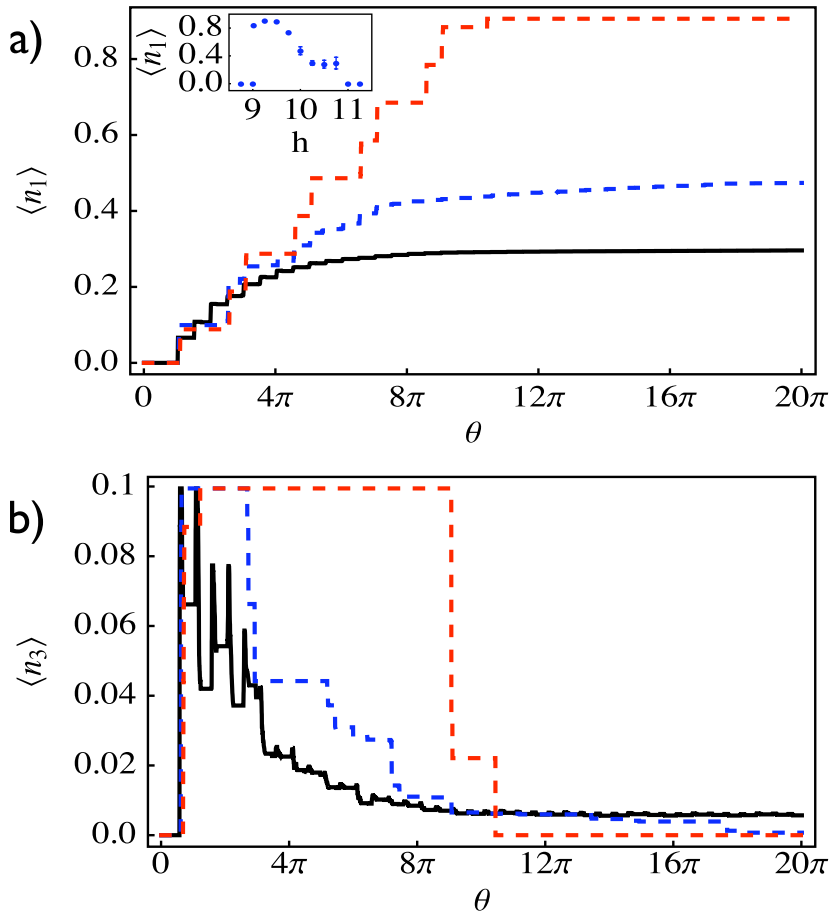

Figure 2.21: Results of simulated constant magnitude rotating field treatments of open edge square ice patterns. (a) Variation of the fractional population of T_1 vertices $\langle n_1 \rangle$, averaged over 100 simulation runs, as a function of time for a constant field protocol for three values of field magnitude $h = 10.75$ (solid black line), 10 (blue dashed line) and 9.25 (red dotted line), representing the high field regime, a cross-over region and the low field regime respectively. Populations converge to a final steady state value after $\sim 10\pi$ rotations. Shown inset is the final steady state value of $\langle n_1 \rangle$ as a function of h. (b) The corresponding $\langle n_3 \rangle$ populations as a function of time. After Budrikis et al. [21].

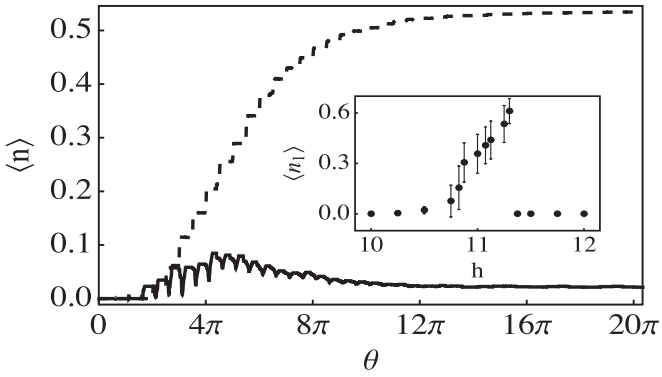

Figure 2.22: Results of simulated constant magnitude rotating field treatments of closed edge square ice patterns. Temporal variation of T_1 (dashed lines) and T_3 vertices (solid line) at an optimal field, as indicated inset where the converged steady state T_1 population is shown as a function of field magnitude. After Budrikis et al. [21].

array having a lower effective switching condition that those in the bulk. Further to this, it suggests that large T_1 populations and GS order can be achieved by a field protocol much simpler than ac demagnetisation, making clear direct observations and predictions regarding field mediated dynamics. This model does however neglect the effects of quenched disorder, a point which will be returned to in chapter 5.

2.4 dc Field Treatment and Magnetic Reversal

A significant volume of work exists on the response of artificial spin ice systems to simple protocols involving applied dc fields. Attention has focussed on local-scale magnetic microscopy measurements [18; 23; 24; 26; 28] as well as bulk global properties using magnetometry [67; 86] and magnetoresistance measurements [8]. Micromagnetics has played a useful role in complementing both, as well as bridging the gap between them.

dc fields can be used to easily and reproducibly prepare well defined states, such as the square ice DPS [30], figure 2.6 (d), and the low energy charge ordered kagome ice state [18; 23; 24], figure 2.23 (a,d). Such states, while not being

GS configurations, obey their respective system's ice rules, which allows them to behave as background states for the creation and manipulation of "monopole" charge defects.

A number of reports have recently addressed experimental dc-field magnetic reversal processes, subsequent to forming such background states [8; 18; 23; 24; 26; 28]. An important aspect of interest is how the moments of the system are correlated during reversal due to interactions and frustration. A variety of different phenomena have been observed, owing to key differences between the patterns studied and the overlap between the finite critical windows of switching field $[H_{\min}(\theta), H_{\max}(\theta)]$ of each sublattice for a given applied field direction θ, again due to configuration dependent inter-elemental interactions and an intrinsic switching properties. When this overlap is small, a high energy charged ordered state can form during the midstages of kagome reversal [18], figure 2.23 (b,e). When this overlap is significant, kagome ice reversal mediates via moment flip cascades which nucleate and propagate apart monopole-like configurations throughout the pattern on the charge-ordered ice-rule (but not GS [65; 90]) background, incrementally pinning at sites of higher local switching field $H_{\rm s}(\theta)$ [23; 24], figure 2.23 (c,f). The connecting chain of reversed moments can be considered as a Dirac string analog. Similar behaviour is found in simulations of the reversal of an optically trapped colloidal kagome ice system [76] (a very similar model to the trapped superconducting vortex ice discussed previously), showing that quenched disorder is indeed crucial in such processes. Weakly disordered systems typically reverse via system-scale correlated avalanching, while strong disorder suppresses interactions, reversal mediating via single uncorrleated spin flips. Intermediate disorder allows for incremental pinning of avalanches of varying length.

A domain wall Coulomb charge interaction model has been proposed to describe transient states involved in cascading and propagation in nanowire networks [96] and it has been given credence via experimental observations [26; 28], however, no evidence has been identified for the fractionalised monopole-monopole vertex object interactions as envisaged by Castelnovo et al. [19].

The work of Phatak et al. [27] also addressed Monte Carlo simulations of a magnetic reversal process of square ice, with field applied along a diagonal symmetry axis, begining from the DPS and mediating strong GS order via similar

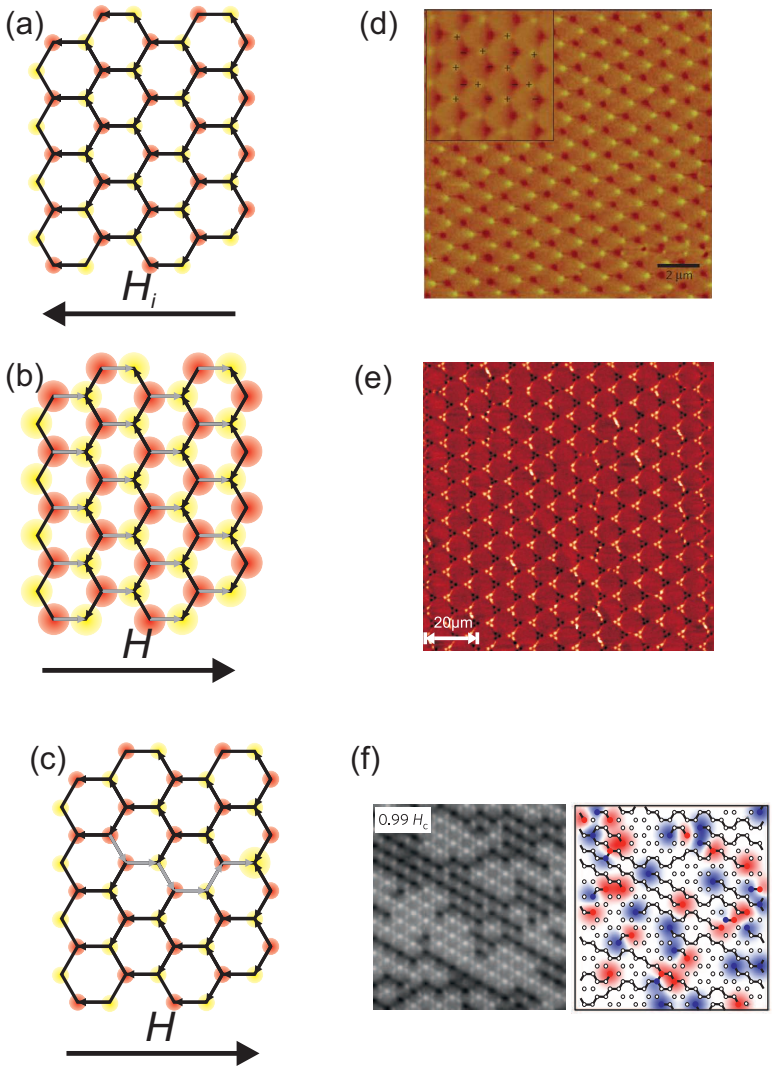

Figure 2.23: Ordering on a kagome lattice. (a,d) Schematic of the low energy charge ordered Kagome ice state and MFM of its realisation in a Kagome network respectively. Alternating vertical columns of vertices have charges ±1, represented by yellow and red circles respectively. After Ladak et al. [23]. (b,e) Schematic of the high energy charge ordered Kagome ice state and MFM of its realisation in a nanoelement array respectively. All horizontal moments are reversed from the low energy state (grey), alternating vertical columns of vertices possessing charges ±3, represented by large yellow and red circles repectively. After Schumann et al. [18]. (c,f) A correlated flipped moment cascade (grey) on the low energy background and the observation of such objects in x-ray photoemission microscopy data respectively. The coloured diagram indicates interpretation of the observeed configuration as monopoles with assosiated Dirac strings. After Mengotti et al. [24].

T_1 chain propagation, as previously discussed in the context of constant magnitude rotating field protocols, section 2.3.4. An experimental reversal of artificial square ice will be addressed in chapter 4 of this thesis, for fields applied along an off-symmetry direction.

2.5 Square Ice Monopole Defects

To date, little work exists addressing the understanding of interactions between vertices and charge defects as composite objects. The work of Mól et al. [20; 22] has shed light on this area via direct calculation of the energetics of dipolar chain defects on the square ice GS, and how this can be interpreted in terms of magnetic charge and string interactions.

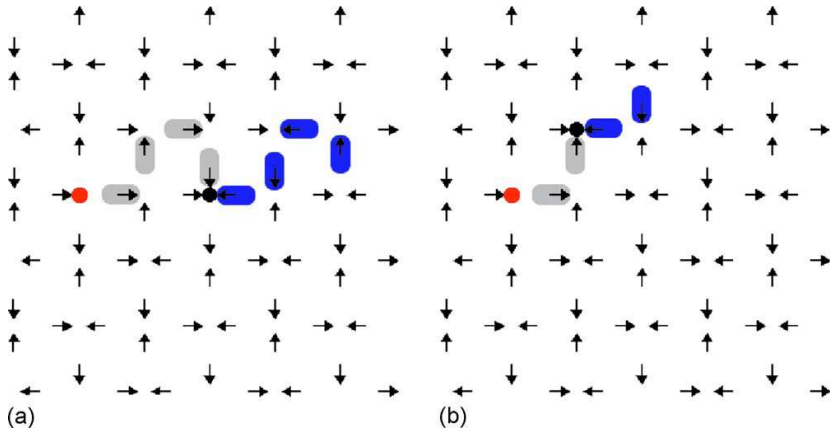

Figure 2.24: Square ice monopole defects on the ground state. (a) Horizontal and (b) diagonal square ice ground state chain excitations, formed from repeated flip chain sections, as shown by the reversed arrows shown in grey and blue. After Mól et al. [20].

Initially, Monte Carlo simulations were used to thermally anneal square ice arrays of point dipoles, confirming the chessboard square ice GS, figure 2.6 (c). With this established, Mól et al. went in search of the energetic behaviour of defect configurations, where a "monopole-antimonopole" pair of T_3 vertices are

formed and separated on the lattice by extending a flipped moment string, forming a chain of T_2 vertices. For simplicity, only straight-line chain extensions were considered, formed by repeated sequences of set moment flips, as shown in figure 2.24 (a) and (b), separating charged sites horizontally or diagonally respectively. It should be noted that both open and periodic boundary conditions were used, for lattices of varying size, however, quantitatively close results were found for all realisations. As in the work of Castelnovo et al. [19], it is desirable to calculate the net dipolar energy of a configuration, and to construct a re-interpretation of it in terms of fractionalised object interactions.

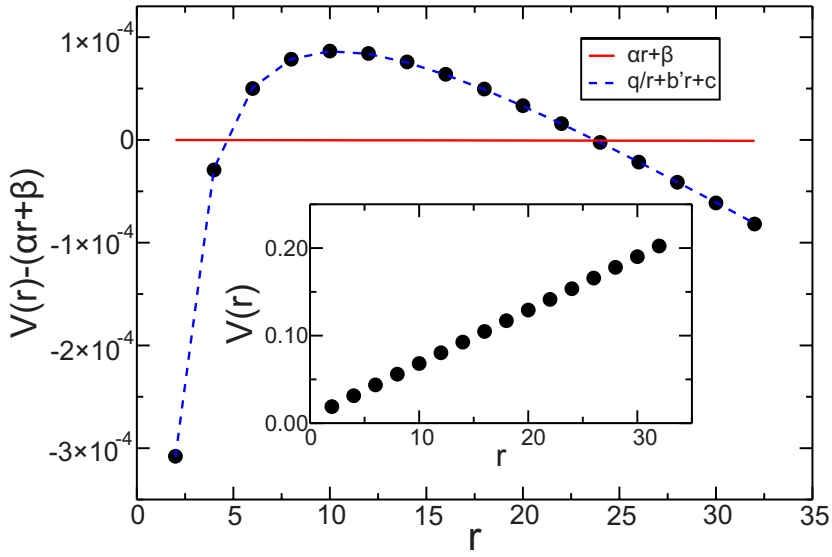

Figure 2.25: The energetics of chain defects on the square ice ground state. As discussed in the main text. After Mól et al. [20].

Figure 2.25 shows inset the net dipolar energy $V(r)$ of a defect chain configuration of the type shown in figure 2.24 (a), as a function of r, the charge separation distance. $V(r)$ is in units of $\mu_0\mu^2/4\pi a^3$, and r is normalised to the lattice constant. The trend appears to be quite linear. In the main panel of figure 2.25, the difference between $V(r)$ and a linear best fit of $V(r)$ is plotted (black dots), illustrating a clearly non-linear behaviour. The linear fit baseline is shown in red, emphasising this point. It was found, however, that a fit to the trend $V(r) = q/r + bX(r) + c$, provided excellent fitting, shown as a blue dashed line.

The three terms of this equation can be interpreted as follows. The first term is a Coulombic term, for magnetic charges q separated by distance r. The second term is the product of a "string tension" b and a string configuration term $X(r)$. The third term is a charge-pair creation constant. For string paths as shown in figure 2.24 (b), very similar values are found.

While this is an elegant interpretation of the charge/string defects on the square ice lattice, it shows explicitly that square ice monopoles are not deconfined as in the crystalline pyrochlore spin ice lattice. In chapter 6 of this thesis, the first experimental observation of such square ice defects as excitations out of the GS will be discussed, as recently reported in reference [25], as well as the energetics of more general configurations.

2.6 Summary

Artificial spin ices are realisations of 2D geometrically frustrated systems and 2D Ising models [3; 9]. Experimental methods for their manipulation have, until very recently, been exclusively field-based due to their typically athermal nature. In all studies, their behaviour is strongly influenced by the inter-elemental interactions as desired, however, quenched disorder in the patterning acts against this in a randomising fashion [24; 78]. Access to ice-rule obeying states is currently being extensively investigated [16; 21; 30], providing backgrounds for the propagation of charge defects [23; 24; 25] - objects of interest both fundamentally and for potential device applications [26; 66]. While athermal systems are convenient for the purposes of microscopy, a great wealth of underlying physics is no doubt inaccessible, and the exploration of thermal ordering effects has only just begun [25; 87].

Chapter 3

Methods

In this chapter, the main techniques and methods used for the preparation and experimental study of artificial square ice patterns will be overviewed.

3.1 Electron Beam Lithography

Electron beam lithography (EBL) is a technique initially developed in the late 1970's [97; 98; 99], and is a natural choice for the patterning of sub-micron structures [13; 100; 101]. EBL utilises a focused electron beam incident onto a substrate coated in a thin film of electron sensitive polymer resist to form a lateral nanoscale template through which material can be deposited to grow a desired structure from the substrate up. Original systems used the beam of an SEM (scanning electron microscope - section 3.3) to perform patterning. More recently, dedicated EBL tools have been developed.

A typical EBL process is shown in figure 3.1. Initially the resist, dissolved in solvent, is spin-coated at several thousand RPM onto the surface of a substrate. The solvent is then allowed to evaporate, or the substrate is heated to promote solvent evaporation, leaving behind a resist layer of $\sim$ 100 nm thickness. Under vacuum conditions, the resist is then exposed to the focused electron beam, which penetrates into the resist. The position of the beam spot is controlled via a computer with patterning software and a specified design is mapped out at a given resolution or line spacing. It is a matter of choosing the correct current and exposure time to achieve the appropriate level of electron dosage.

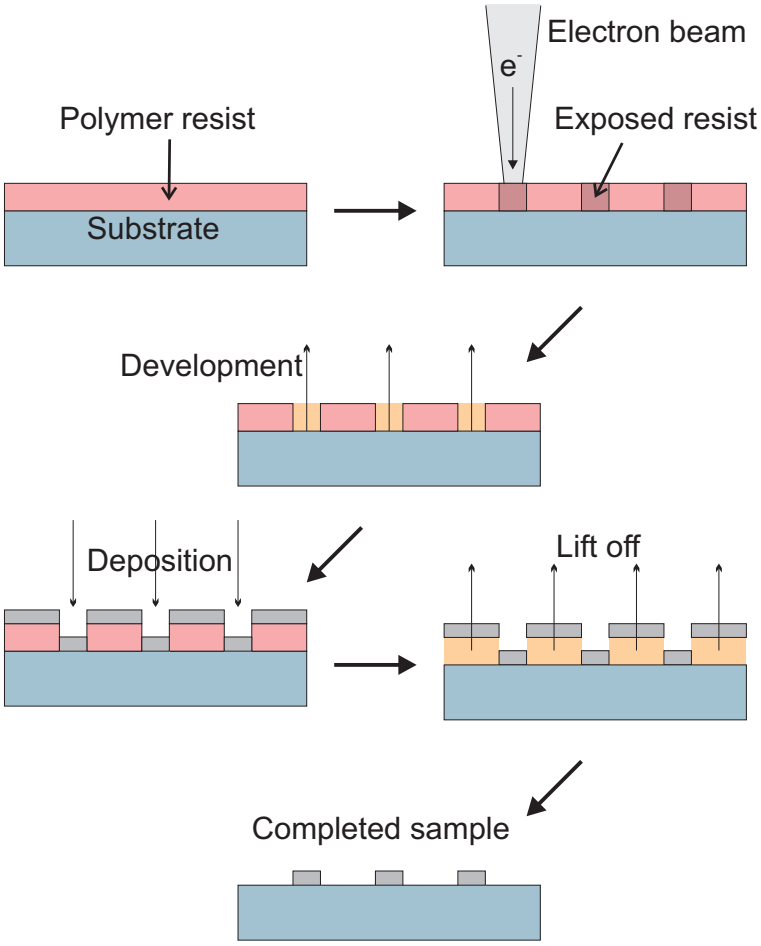

Figure 3.1: Schematic of the employed electron beam lithography fabrication process. A substrate is spin-coated with an electron sensitive resist and dried. It is subsequently exposed to a focussed electron beam controlled by a computer with patterning software. The sample is then developed in a solvent leaving a patterned resist structure. Material is then deposited through the gaps in the resist and finally the remaining resist is removed in a solvent lift-off process, leaving behind the desired patterned structure.

Two processes can occur upon electron beam exposure of the resist; (i) the random breaking of polymer chains resulting in a reduced average polymer molecular weight, and (ii) cross-linkage of polymer chains resulting in an increased average molecular weight. A positive/negative resist is one in which the former/latter dominates. A positive degrading resist is developed using a mixture of chemicals, one of which is a solvent of the resist polymer, one of which is not. This results in a solvent that will more readily dissolve resist polymer below a certain molecular weight, and this is effective given that the molecular weight distribution of the degraded polymer fractions lies sufficiently below that of the original unexposed resist polymers. Using the correct combination of initial polymer content, electron beam exposure parameters, and development time, the desired template can be patterned. Material can then be deposited through this pattern using common thin film growth techniques, such as electrochemical deposition, sputter deposition or vacuum evaporation [102] (section 3.2). Following deposition the remaining resist and the unwanted material deposited on top of the resist can be removed by a final solvent bath, a process called "lift-off", leaving behind the desired patterned structure. Optimal parameters are typically obtained via a trial and error process.

An alternative fabrication route is to use a subtractive etching method, in which a thin film is first deposited on an unpatterned substrate, on top of which a patterned template is formed, either by a resist layer itself or a hard mask of subsequently deposited material. A method such as Ar ion milling is then used to remove material, in which a beam of ions is accelerated and incident on to the patterned sample surface, the thin film lying beneath the template being protected. Such a process was not used for the samples studied in this thesis.

All samples discussed in this thesis were fabricated at the Center for Functional Nanomaterial (CFN), Brookhaven National Laboratory (BNL). The fabrication procedure employed, as illustrated in figure 3.1, used commercially bought Si substrate with a single layer of ZEP520A:acetol (1:1) resist solution (Nippon Zeon Company), spun at 5000 RPM about an out-of-plane axis for 30 seconds, and hot-plate baked at 180°C for 3 minutes. Substrates were often cleaned using an oxygen plasma prior to processing, as well as being solvent-cleaned with

acetone (typically three 30s sonicated baths in acetone to remove surface contaminants, followed by three 30s sonicated baths in isopropanol to remove residual acetone, and dried using a compressed nitrogen gun.) The patterned resist was developed in xylenes for 90 seconds, and a bath of Posistrip® EKC™ solvent was used for liftoff, assisted by a rinse in DI water. ZEP resist has a resolution less than $\sim$ 10nm. Material deposition will be discussed in section 3.2. Two EBL systems were used. Initially a Helios Nanolab™ (FEI Company) was employed, with a 30keV beam. More recently, a JEOL JBX-6300FS system was available, with a 25 - 100 keV electron beam, providing significantly larger write field areas $\sim$ 1 mm, sub 20 μm stitching, faster write time and the automated ability to calibrate beam configuration and monitor it during the patterning process. This allowed for $\sim$ 10 arrays of several 1 mm ^{2} area each to be patterned on a single 6" Si wafer over the time frame of $\sim$ 1 to 10 hours.

A variety of different sized patterns were made; small area square ice arrays of $\sim$ 400 elements with different edge types (JEOL), up to patterns of several mm^2, either made from many closely spaced small area patterns (Helios) to those continuous over 0.5 mm by 0.5 mm areas (JEOL).

3.2 Electron Beam Vacuum Evaporation

The thin film structures of all samples discussed in this thesis were fabricated via the vacuum evaporation of material [102; 103], heated using an electron beam, in a Lesker PVD chamber at the CFN.

The chamber is shown schematically in figure 3.2. A crucible of target material (initially in pellet form) is positioned in the base of the chamber, at a vacuum pressure of $\sim 10^{-6}$ Torr. A $\sim$ 5 kV potential is applied between the crucible and a filament positioned under the base of the system. Electrons are produced by thermionic emission from the filament. Under the field of a permanent magnet, the electrons are deflected through a $\sim$ 10 cm radius arc of $\sim 270°$, and are incident onto the target material, with currents of $\sim$ 10A. The incident electron beam heats the target material, causing it to melt and evaporate, (or sublime). Evaporated material particles leave the surface from a point source with a cosine distribution relative to the surface normal, and, under vacuum conditions,

have a long mean free path. This process, therefore, produces a highly unidirectional deposition source, making it ideal for deposited growth into pattern resist structures of high aspect ratio.

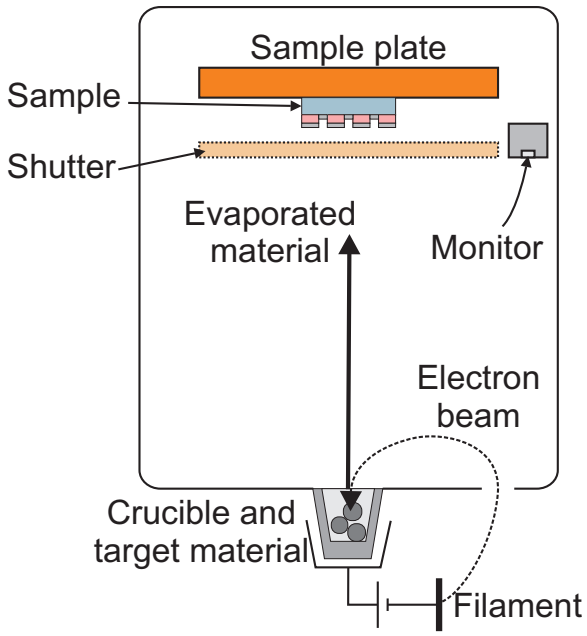

Figure 3.2: Diagram of the Lesker PVD electron beam evaporation chamber. Electrons emitted from a filament are accelerated by a potential of $\sim$ 5-10 kV in a 270 $^{\circ}$ arc into a crucible of target material in the base of the chamber. Through heating, target material is made to evaporate. The emitted material flux is then incident onto a sample surface held above on the sample plate. The thickness of deposited material is monitored by a quartz oscillator monitor. A shutter is positioned in front of the sample plate to allow for control of deposition time. Three crucibles of target material are held on a rotating stage in the chamber base, one of which is permitted to be exposed to the electron beam at time.

A sample surface is held on a plate above the material source, the incident evaporated material becoming deposited on the surface. The amount of material deposited is monitored by an oscillating quartz detector. A shutter is positioned between the source and sample allowing for the incident material beam to be

blocked - this allows for the source to reach a steady evaporation/deposition state rate before deposition is begun. Rates of typically ~ 0.05 nm/s are aquired. Three target crucibles could be loaded simultaneously, being held on a rotating stage in the chamber base, only one of which could be exposed to the incident electron beam at a time. The beam is circulated over the target material to promote uniform heating, and beam configuration was not exactly reproducible between deposition runs.

The artificial spin ice samples were fabricated on commercially bought Si substrate with a layer of electron beam patterned ZEP resist (section 3.1) and an evaporated ~ 25 nm thick layer of polycrystalline $Ni_{80}Fe_{20}$ (Permalloy - Py). Typically, a ~ 3 nm thick buffer layer of e.g. Cr or Ta was first deposited, as well a ~ 3 nm capping layer of Al to reduce oxidation. The source-sample distance and sample plate diameter were large enough to deposit a film of uniform thickness over a large area, allowing for multiple samples to be deposited on simultaneously.

3.3 Scanning Electron Microscopy

A scanning electron microscope (SEM) is a tool commonly used for imaging surfaces and structures of material down to the nanometer scale [101; 104]. Under vacuum, a focused electron beam is raster scanned across the surface of a sample, resulting in the emission of both electrons and electromagnetic radiation from the exposed volume, which can then be collected as a function of beam position to build a 2D image.

Primary electrons are produced and accelerated to ~ 0.1-30 keV by an electron gun, directed down a column towards the sample chamber, where the sample of interest is held on a translatable stage. Along the column a number of electron lenses and apertures are located, to produce a focussed spot of $\sim 1-100$ nm size at the sample surface, as well as a set of scanning coils for beam deflection. The incident electrons enter the sample surface and typically disperse throughout a pear-shaped region named the excitation volume, figure 3.3 (a), where a number of interactions, both elastic and inelastic, take place at different depths, producing a number of useful signals for different modes of microscope operation.

The most commonly employed operation mode exploits the emission of secondary electrons, (SE), which are produced as a result of the ionisation of sample atoms and excitation of loosely bound electrons, defined as having energy < 50 eV. As a result of their low energy, only those within an escape depth of $\sim$ a few nm of the surface interface are able to leave the surface without being recaptured by ionised atoms. Subsequently, they are then easily deflected by a potential to an Everhart-Thornley detector [105] positioned on the side of the sample chamber. Due to their generation at close proximity to the sample surface, SEs generate a surface sensitive signal. Variations in surface topography result in variations in the escape volume (the region of excitation volume within the escape depth), resulting in variations in emitted and detected signal, figure 3.3 (b), hence the edges of topographic features often appear brighter. Topography can also affect the amount of signal reaching the detector by shadowing. All SEM data presented in this thesis were generated in SE mode, using field emission gun sources, typically providing a resolution of $\sim$ 10 nm. To enhance surface sensitivity, lower incident electron energies are required, resulting in reduced surface penetration and a more strongly surface-confined excitation volume, particularly with samples of lighter elements.

Other commonly used signals are backscattered electrons (BSEs) and characteristic x-rays. BSEs are incident electrons which are elastically scattered by sample atomic nuclei and outer shell electrons through an angle $> 90°$, reemerging from the sample surface, typically defined as having energies > 50 eV. Due to their large energy, such electrons are not readily absorbed by the sample material, penetrating deeper into the surface resulting in a larger excitation volume and, therefore, lower resolution relative to that of SEs. BSEs provide atomic number contrast.

3.4 Atomic Force Micrscopy

Atomic force microscopy (AFM) is a scanning probe microscopy (SPM) technique invented in the mid 1980s [106], which has since become a standard tool for studying material surfaces. A small $\sim$ 10 nm radius tip protruding from the underside of a cantilever arm is brought close to a sample surface where it experiences a

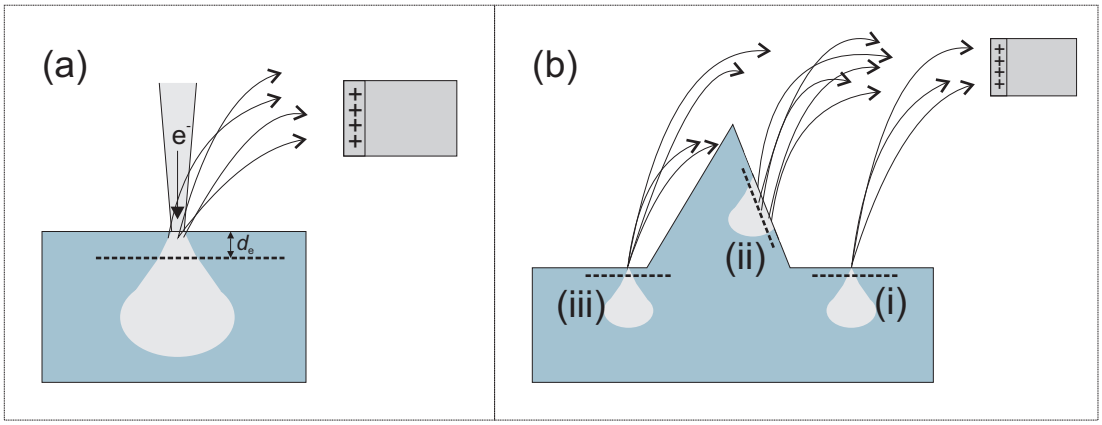

Figure 3.3: SEM secondary electron imaging and image constrast. (a) An electron beam (grey) incident on a surface disperses into the material through a pear-shaped excitation volume. Secondary electrons produced within the electron escape depth, d_e, will be able to escape the surface an be collected by a biased detector. (b) The emitted electron intensity is sensitive to topography, region (ii) having a greater volume lying within the escape depth than region (i) will produce a larger signal - consequently, edges and steps often appear brighter in an SEM image. Region (iii) will produce the same emitted intensity as region (i), however, the total electron count reaching the detector is reduced by topographic shadowing, resulting in a lower detected electron count, appearing darker in an SEM image.

combination of possible forces. Via one of various operating modes, properties of the cantilever are then monitored and recorded as the tip is raster scanned over a given area of sample surface, allowing a 3D image to be built. Tip-sample interactions are formed from many components e.g. [107; 108], attractive van der Waals-type forces, repulsive Pauli forces, as well as longer range forces such as electromagnetic forces.

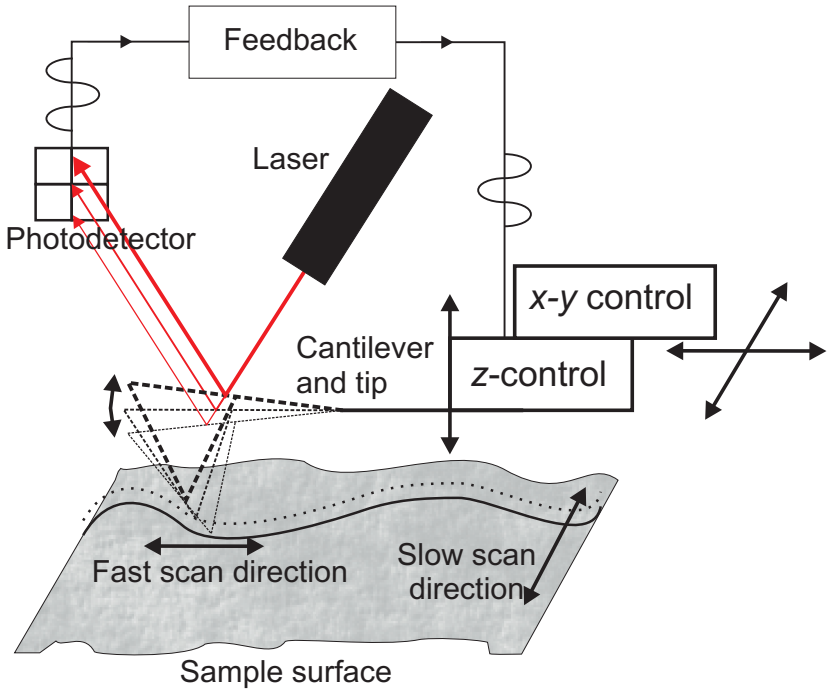

Figure 3.4: Diagramatic representation of the tapping-mode operation of an atomic force microscope. Described in the main text.

The AFM images contained in this thesis were exclusively generated using Veeco Multimode and Veeco Nanoman systems (available at Leeds, ISIS and the CFN) operating under "tapping mode", using Veeco MESP catilevers, table 3.1. A basic diagramatic representation of operation is shown in figure 3.4. A laser beam is reflected from the top-side of a cantilever onto the centre of a four-quadrant photodetector, allowing cantilever deflection to be monitored. The cantilever is driven to oscillate by a driving force of set amplitude F_0 and frequency ω_{d} close the cantilever natural resonant frequency $\omega_{\mathrm{R}} = \sqrt{k/m_{\mathrm{eff}}}$, where k and m_{eff}

are the cantilever natural spring constant and effective mass respectively. A given cantilever can be well described by the equation of motion of a damped, forced harmonic oscillator [108; 109], with sinusoidal steady-state solution of amplitude $D_0 = (F_0/m_{\text{eff}})/\sqrt{(\omega_{\text{R}}^2 - \omega_{\text{d}}^2)^2 + (A\omega_{\text{R}}^2\omega_{\text{d}}^2)}$, where A is a constant.

Table 3.1: MESP - Magnetic Etched Silicon Probe - Specifications

Parameter	Quoted Value (for LM-MESP low moment tips)*
Thickness	2.5 - 3.5 μm
Length	200 - 250 μm
Width	23 - 33 μm
Resonant frequency f_0	60 - 100 kHz
k	1 - 5 N/m
Co/Cr layer thickness	10 - 250 nm
Coercivity H_{c}	400 Oe ($<$ 400 Oe)*
μ	1×10^{-13} emu (0.3×10^{-13} emu)*

For small amplitude oscillation [110], typically 10-100 nm [111], under the influence of a force gradient F', such as that due to the sample surface, the spring constant becomes effectively $k_{\text{eff}} = k - F'$, resulting in a shift in ω_{R} and, therefore, D_0 [106; 112].

To initiate operation, the oscillating tip is moved towards the sample surface, modifying ω_{R}, until an amplitude set point in D_0 is achieved. During operation, as the oscillating tip is then raster scanned across the sample surface, variation in topography resulting in variation in ω_{R} and D_0. A closed feedback loop acts to maintain a constant D_0 by adjusting the tip-sample rest separation distance (the separation given no oscillation or interactions), which is recorded line-by-line to generate 3D topographic information. Adjustable proportional and integral gain parameters, as well as a variable scan rate, allow for surface tracking to be optimised. The intricacies of the behaviour of a cantilever during tapping-mode operation, under the influence of both its driving potential and a typical Lennard-Jones type potential, is still an ongoing research area [113; 114]. Following data collection, various image processing steps can be employed to e.g.

subtract plane linear and parabolic backgrounds, made using either the Veeco Nanoscope software or the WSxM package [115].

Tapping-mode offers benefits over constant contact operating modes, reducing the force applied to the surface and therefore damage as well as reducing the effects of adhesive surface forces. Active feedback reduces the risk of tip crashing as experienced in constant height modes, allowing relatively tall structures to be imaged.

An example portion of an AFM image of an $a = 500$ nm lattice spacing spin ice array is shown in figure 3.4 (a). While atomic resolution can effectively be achieved, resolution on the order of ~ 10 nm is typically found under reasonably tuned ambient conditions. The image can be considered a convolution of the surface with the shape of the given tip used, which can limit resolution. Tips can also become blunted under use which acts to exaggerate features such as edge crowning [107].

The Multimode V system has a maximum field of view of 13 μm $\times$ 13 μm, whereas the Nanoman system has a maximum field of view many times greater in size. For larger area images, resolution becomes limited by a finite pixel sample density, and the largest scan size used was 40 μm $\times$ 40 μm. Compared to other microscopy methods, image aquisition time can be relatively slow ($\sim 1 - 10$ minutes), however, minimal sample preparation time is required.

3.4.1 Magnetic Force Microscopy

Not long after the invention of AFM, the potential of studying magnetic tip-sample interactions was realised [116; 117], the techniques used quickly developing into what is now termed "magnetic force microscopy" (MFM). Such measurements can be performed under an operating mode of the Veeco AFM systems discussed in section 3.4. For the measurements presented in this thesis, MESP cantilevers with a thin coating of Cr/Co were used (table 3.1), which were first magnetised normal to the sample plane using a small permanent magnet (external to the microscope and sample environment). A tip forms, therefore, a magnetic dipole-like object (section 1.2), sensitive to the normal component of the gradient of stray fields originating from the sample surface. The microscope

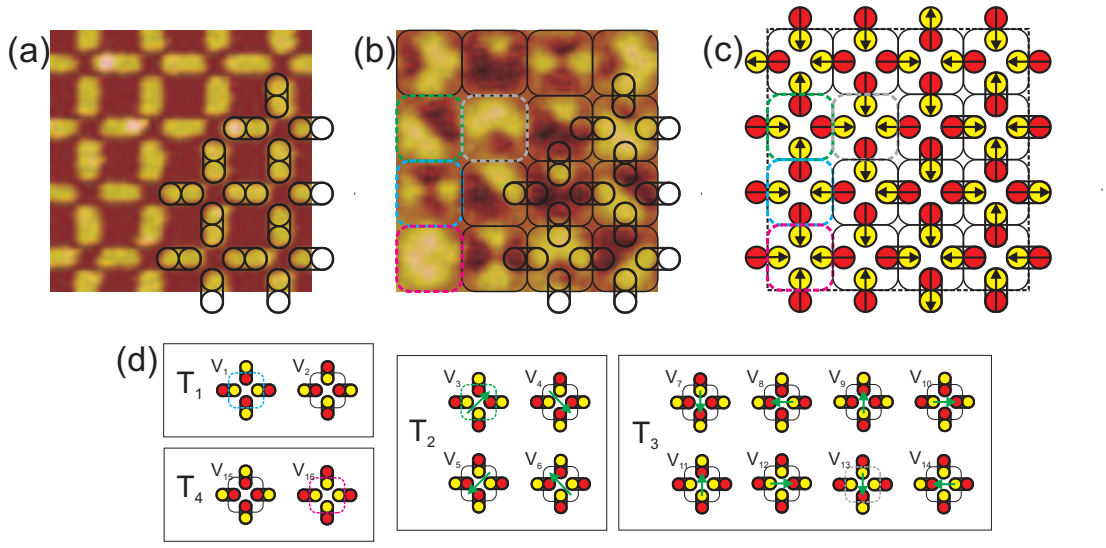

Figure 3.5: Interpretation of magnetic force microscopy data. Example (a) AFM, and (b) MFM images of an artifical square ice pattern. These images are overlayed with schematics of the location of the magnetic islands and the location of the north and south poles. Also boxed are the vertex sites, which can be interpreted by the four poles converging at their centres. (c) shows a mapping of the magnetic configuration shown in (b) into a system of Ising moments (arrows). (d) shows the sixteen vertex configurations V_{1-16} as North-South dumbbells, also with the four charges at their centres boxed, grouped by type $T_{1,2,3,4}$. Examples of $T_{1,2,3,4}$ vertices have been emphasised in (b-d) by cyan, green, grey and pink boxes respectively. This scheme presents a convenient way to understand an MFM image by eye.

is then operated in "lift mode". An initial line scan of standard tapping mode AFM operation is conducted and the topographic profile recorded. A second scan across the same lateral line is then made at a constant user-defined height offset above this topological profile, typically $\sim 10 - 100$nm, acting to eliminate non-magnetic variations in the tip-sample interaction. The normal component of the force gradient due to stray fields from variations in surface magnetisation can thus be mapped from the phase or amplitude of the cantilever oscillation, creating an image representative of the surface magnetic charge distribution, with excess magnetic north and south pole yielding light and dark contrast. Figure 3.4 (b) shows a MFM image corresponding to the AFM image in (a). The exact nature of these interactions, the modelling of which can be extremely lengthy [111], are highly dependent on the specific properties of a given tip and cantilever, with significant variations from tip to tip, (table 3.1). We therefore use MFM as a qualitative probe, allowing for the magnetic microstate of a sample to be inferred and interpreted within an Ising dipole picture, as set out by previous authors [3]. Various statistical parameters can be used to define a given microstate, as will be discussed in section 3.5.

As this is an intrusive technique, it is therefore possible to locally reconfigure sample surface magnetisation distributions, particularly for soft magnetic materials [118; 119]. For the studies presented in this thesis, islands, which are also aided by shape anisotropy, are found to be adequately stable under imaging. Initial characterisation studies were always performed on samples prior to undertaking experimental procedures to test for stability, moments that are unstable due to tip interactions being identifiable in a given image by features such as sharp discontinuities in magnetic contrast.

As well as intrusive tip-sample interactions, a brief consideration should be given to the methods which samples were held under the microscope, specifically for the Multimode systems, with which samples are adhered to a ~ 1 cm diameter magnetic disk, which is then held to the top of the variable-height microscope column under the cantilever. This immediately raises concern as unwanted stray fields are therefore incident on the sample. Measurements using a standard Gauss probe gives maximum fields ≈ 100 Oe immediately above a mounted magnetic disk, both in-plane and out-of-plane. These fields are sufficiently small as not to

disturb the magnetic configuration of islands of the dimensions used of a given mounted sample, at least in terms of an Ising dipole interpretation. While it is possible that the internal magnetisation of elements is adjusted, this is beyond the scope of the work contained in this thesis. Negligible fields are found above an unmounted magnetic disk, as well as the Nanoman sample plate.

3.5 Interpretation of Microscopy Data

Figure 3.5 (a,b) show a portion of AFM and corresponding MFM data taken from an $a = 500$ nm lattice constant square ice array, both images overlayed with a schematic showing the locations of a selection of elements. In the MFM image, the north and south poles of each element are visible as circular regions of light and dark contrast. Such arrangements confirm that elements are single domain and magnetised along their long axes by their shape anisotropy. Figure 3.5 (c) shows a full diagramatic representation of the magnetic charge arrangement in (b), yellow and red circles representing the elemental north and south poles. Also shown are arrows representing the inferred underlying dipolar configuration. From an MFM image it is thus possible to completely infer the microstate of the imaged array. A number of useful statistical parameters can then be extracted, within an Ising dipole approximation. In understanding the configurations observed, it is instructive to make comparisons with well-defined statistical reference states - shown in figure 3.6 are (a) the ground state (GS), (b) the diagonally polarised state (DPS), and (c) a random state (RS).

3.5.1 Dipolar Statistics

For later discussion, it is instructive to consider the square ice system as two identical, orthogonal, interpenetrating sublattices of dipole moments, which will be referred to as the X and Y sublattice in reference their islands' easy axis orientation with respect to cartesian x- and y-directions, as shown in 3.6 (a) as black and grey arrows respectively. A number of useful statistical parameters can be extracted from the dipolar configuration.

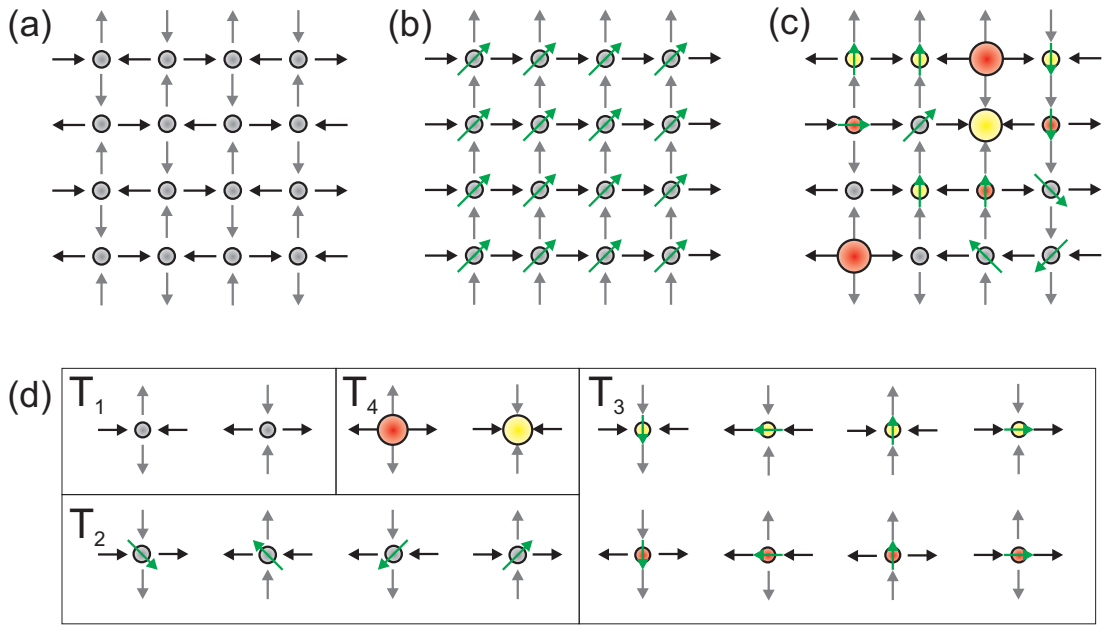

Figure 3.6: Ideal square ice states. (a) The ground state (GS). (b) The diagonally polarized state (DPS). (c) A random state (RS). (d) The sixteen square ice vertex configurations labelled by vertex properties. Grey circles represent the zero normalised vertex charge of $T_{1,2}$ vertices, and yellow and red circles represent the positively and negatively charged vertices, their size representing the size of the charge, ± 1 and ± 2 for T_3 and T_4 vertices respectively. Green arrows represent the polarisation of $T_{2,3}$ vertices.

Normalised Magnetisation

The net normalised magnetisation of a state can be calculated as $\mathbf{M} = M_{\mathrm{X}}\hat{\mathbf{x}} + M_{\mathrm{Y}}\hat{\mathbf{y}}$, where $M_{\mathrm{X,Y}} = \langle m_{\mathrm{X,Y}} \rangle / \sqrt{2}$, and $m_{\mathrm{X,Y}} = \pm 1$ for Ising moments on X and Y aligned/antialigned with the x, y-directions respectively. This is a useful parameter for examining e.g. the effectiveness of a demagnetisation procedure. Both the GS and RS, as well as many other states (e.g. the "in-between" ac demagnetised states discussed in section 2.3.1), have $|\mathbf{M}| = M_{\mathrm{X}} = M_{\mathrm{Y}} = 0$, illustrating the system's degeneracy in $\mathbf{M}$, whereas the DPS has $|\mathbf{M}| = \langle m_{\mathrm{X}} \rangle = \langle m_{\mathrm{Y}} \rangle = 1$. The factor of $\sqrt{2}$ above normalises the magnetisation to the DPS, the state of largest possible $|\mathbf{M}|$.

Correlation

In order to gain insight into the possible effects that arise due to inter-island dipolar coupling, a number of nearest neighbour correlation values can be calculated, defined in reference to two well defined states. For studies of demagnetised $\mathbf{M} = 0$ states (either field or thermally induced) the square ice GS will be used, figure 3.6 (a), using similar definitions to those used by Ke et al. [16]. For studies of magnetic reversal the DPS provides a more instructive comparison, figure 3.6 (b), and ferromagnetic-like correlations are considered. While these two definitions are similar, for clarity, they will be described separately. In general, three kinds of neighbour can be defined, L, P and D, relative to elements on both sublattices X and Y, as shown in figure 3.7. L(P)-type are those with easy axes parallel aligned along a line parallel (perpendicular) to their easy axes. D-type lie along square diagonal lines, with odd-order neighbours aligned perpendicularly to a given reference island.

Ground State Correlation

If a pair of $n_{\mathrm{d}}^{\mathrm{th}}$ neighbour elements along L, P or D, on the X or Y sublattice as shown in figure 3.7 (a) and (b) respectively, are relatively aligned/antialigned to that observed in a GS configuration, they are assigned a value $c = \pm 1$ respectively. A GS correlator is then given by $C^{\mathrm{GS}}_{\mathrm{X,Y}}(n_{\mathrm{d}}) = \langle c \rangle_{\mathrm{X,Y}}$, where $C = L, P, D$ and the average is taken over a given imaged configuration.

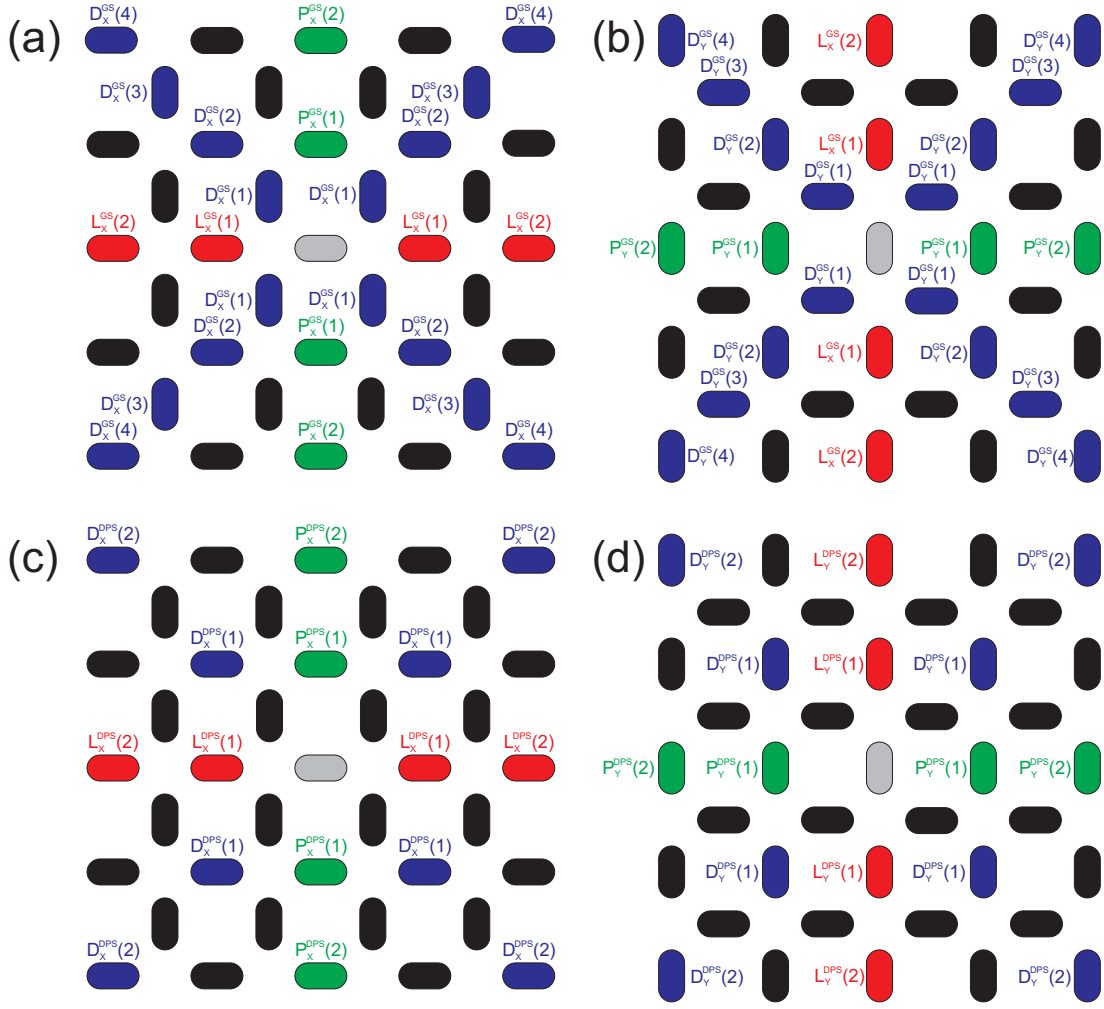

Figure 3.7: Dipolar neighbours on the square ice system. L-, P- and D-type neighbours (red, green and blue respectively) relative to the grey reference element, as defined when using (a,b) GS-type correlation functions $C^{\mathrm{GS}}_{\mathrm{X,Y}}$, or (c,d) DPS-type correlation functions $C^{\mathrm{DPS}}_{\mathrm{X,Y}}$. Correlations can be defined relative to elements on the (a,c) X and (b,d) Y sublattices independently. For $C^{\mathrm{DPS}}_{\mathrm{X,Y}}$, it is not necessary to consider correlation between sublattices X and Y (chaper 4).

The GS correlators defined previously by Ke et al. [16], $C^{\mathrm{GS}}(n_{\mathrm{d}})$, can then be obtained by taking the average of $C^{\mathrm{GS}}_{\mathrm{X}}(n_{\mathrm{d}})$ and $C^{\mathrm{GS}}_{\mathrm{Y}}(n_{\mathrm{d}})$ for a given L, P, D and n_{d}, however, this results in the loss of information arising from possible asymmetries between the behaviour of the X and Y sublattices.

Figure 3.8 (a) shows the behaviour of C^{GS} for the ideal states defined in figure 3.6. The GS yields all values of $C^{\mathrm{GS}}(n_{\mathrm{d}}) = 1$, for L, P and D for all n_{d}. The DPS results in an oscillatory behaviour, with all odd/even order values of L and $P = \mp 1$ respectively, and all odd/even order values of $D = 0$ and 1 respectively. The RS results in all $C^{\mathrm{GS}}(n_{\mathrm{d}}) = 0$.

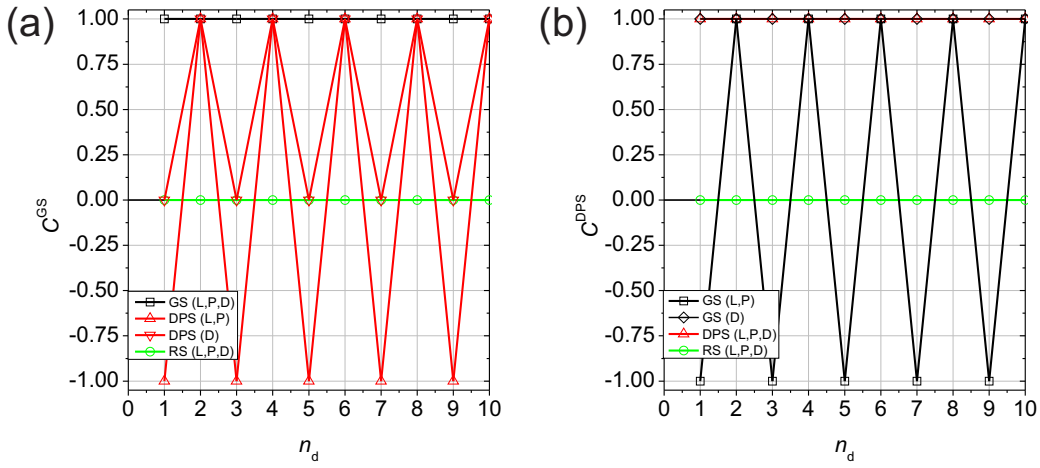

Figure 3.8: Correlation statistics of ideal states. The behaviour of the (a) C^{GS} and (b) C^{DPS} correlation values as a function of neighbour n_{d}, for the GS, DPS and RS.

DPS Correlation

For MFM studies of magnetic reversal processes, chapter 4, it is appropriate to define an alternative set of correlators, $C^{\mathrm{DPS}}(n_{\mathrm{d}}) = \langle \mathbf{m}_i \cdot \mathbf{m}_{i+n_{\mathrm{d}}} \rangle_i$ with $C = (L, P, D)_{\mathrm{X,Y}}$ for $n^{\mathrm{th}}_{\mathrm{d}}$ nearest neighbour pairs defined on X and Y independently with moments $\mathbf{m} = \mathbf{m}_{\mathrm{X,Y}} = \pm 1$ respectively, as indicated in figure 3.7 (c,d). Perfect alignment/antialignment of all $n^{\mathrm{th}}_{\mathrm{d}}$ pairs yields $C^{\mathrm{DPS}}(n_{\mathrm{d}}) = \pm 1$ respectively.

Random alignment yields $C^{\mathrm{DPS}}(n_{\mathrm{d}}) = 0$. Note, C^{DPS} does not distinguish between flipped and unflipped moments, and in the studies presented it was not necessary to consider D-type correlation between the X and Y sublattices (as for GS correlation) by considerations of symmetry. As for C^{GS}, $C^{\mathrm{DPS}} = (C^{\mathrm{DPS}}_{\mathrm{X}} + C^{\mathrm{DPS}}_{\mathrm{Y}})/2$.

For the ideal states shown in figure 3.6, the behaviour of the ferromagnetic correlators are also shown in figure 3.8 (b). $C^{\mathrm{DPS}}(n_{\mathrm{d}}) \mp C^{\mathrm{GS}}(n_{\mathrm{d}})$ for all $C = L, P$ with even/odd n_{d} respectively. Further, $D^{\mathrm{DPS}}(n_{\mathrm{d}}) = D^{\mathrm{GS}}(2n_{\mathrm{d}})$.

3.5.2 Vertex Statistics

As discussed previously, the square ice can also be interpreted as a system of interlinked cross-shaped vertices [3], with $2^4 = 16$ possible vertex configurations, V_{1-16}, commonly grouped into four types, T_{1-4}, in order of increasing energy. These are displayed in figure 3.5 (d), as cartoons of that observed in the MFM imagery, each consisting of four converging charge dumbbells. The four central poles/charges of a vertex provide an effective way of visualizing the system and interpreting the MFM data. In figure 3.5 (b,c,d), as well as the magnetic poles and moments being indicated, regions surrounding the four central poles of each vertex are also boxed, identifying vertices as one of 16 possible tiles, 3.5 (d). T_1 vertices appear as "bow-tie"-like tiles (blue), T_2 vertices roughly resemble a yin-yang symbol (green), T_3 vertices resemble the 1980s arcade game character Pac-Man (grey), and T_4 vertices appear as uniformly coloured tiles (pink), all of which can be observed in figure 3.5 (b,c).

Properties

Each vertex can be further classified according to their net vertex charge and vertex dipole moment, figure 3.6. $\mathrm{T}_{1,2}$ obey the 2-in/2-out ice rules and are charge neutral. $\mathrm{T}_{3,4}$ posses excess north or south pole, and therefore posses a normalised magnetic charge of +1 and +2 respectively. $\mathrm{T}_{2,3}$ both posses intrinsic dipoles.

Of course, due to the underlying dipole structure, certain arrangements of tiles are not allowed by topology, e.g. a V_2 vertex cannot be placed at the right-hand neighbouring site of a V_{15} vertex, their linking moment on the square ice

Ising dipole lattice being unable to simultaneously take both values of $m_X = \pm 1$. As well as vertex correlations arising from topology, there is also current interest in determining whether long range interactions in the system give rise to vertex-vertex coupling [20; 22], which would validate discussion of the system to in terms of fractionalised vertex objects, analogous to the monopole objects envisaged by Castelnovo et al. [19], rather than a vertex picture providing a convenient identification and naming convention.

Populations

For a given image, the absolute populations of each of the 16 individual vertex configurations T_{1-4} can be counted, from which a percentage population can be determined. It is often convenient to compare these values with those expected from a random state [3], given by the vertex multiplicities, $q_i/16$, for $q_i = 2$, 4, 8, 2 for $i = 1$, 2, 3, 4 respectively.

Vertex Density Functions

To explore understanding of these systems in terms of a vertex object within the vertex model, looking beyond interpretation in terms of its underlying dipoles, vertex density functions provide a useful point of interpretation. Here, the fractional density of vertex or configuration of type B at a given separation in 2D from reference vertices of configuration or type A, averaged over a state, is calculated. This may be calculated for vertex types T_{1-4} or for individual vertex configurations V_{1-16}, allowing for vertex-vertex correlations to be addressed.

3.5.3 Dipolar Energy Calculations

It is useful to calculate the net dipolar energy of configurations observed in MFM images, and the various ideal cases discussed. This can be done straightforwardly within the point dipole Ising interpretation of a state or configuration, section 1.2. For such calculations, finite regions of square ice are considered of $N \times N$ vertices, summing over all pairwise dipolar interaction energies. Further to this, a normalised dipolar energy unit $u = \mu_0 \mu^2 / 4\pi a^3$ will be used, where μ is the

dipole moment of a single nanomagnet, a is the array lattice constant, and μ_0 is the magnetic permeability constant.

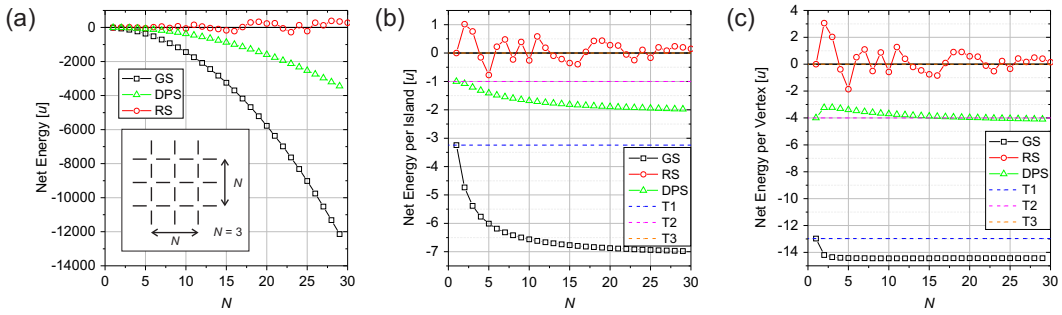

Figure 3.9: Ideal square ice state energies. (a) The net energy, (b) the net energy per moment, and (c) the net energy per vertex of an $N \times N$ square ice array of vertices of point dipoles configured as per the GS, DPS and a realisation of a RS. Shown also in (b) and (c) are the energies per island and per vertex of single vertex configurations (dashed lines).

Figure 3.9 (a) shows the total energy of an $N \times N$ sized array, tiled in the GS, DPS and RS respectively as a function of N, with finite array size defined inset. The RS configurations were generate using a pseudo-random coin-toss to assign each elemental Ising magnetisation as $m_{\mathrm{X,Y}} = \pm 1$. (b) and (c) show the net energy per island and per vertex respectively as a function of N, where the number of islands $= 2N^2 + 2N$ and number of vertices $= N^2$. Also shown in (b) and (c) are the net dipolar energies per island and per vertex of single vertices of each type T_{1-4}.

Chapter 4

Magnetic Reversal of an Artificial Square Ice

4.1 Introduction

In this chapter, magnetic reversal of an artificial square ice pattern subject to a sequence of magnetic fields applied slightly off the diagonal symmetry axis will be presented, as investigated via magnetic force microscopy of the remanent states that result. As reported in reference [29], sublattice independent reversal is observed via correlated incrementally pinned cascades of flipped elemental dipole moments along parallel chains, as evident from analysis of vertex populations and dipolar correlation functions in comparison with that expected of a randomly mediated uncoupled reversal process. Further, weak dipolar interactions between adjacent chains favour antialignment and give rise to weak charge ordering of "monopole" vertices during the reversal process.

Consideration of the energetics of chain defects via dipolar calculations indicates that such objects are not energetically well-defined on the DPS background. Diagonal chain defects are also addressed, of the type occurring in references [21; 27], which are found to fit the same energetic approximations as chain defects on the GS background [25]. These calculations show that long range interactions are not negligible between a strongly polarized background state and defects comprising vertices of non-zero dipole moment.

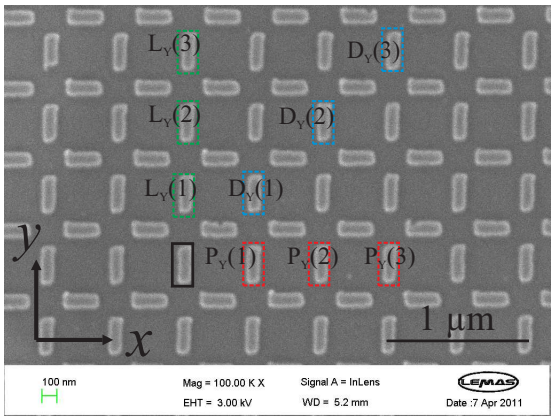

Figure 4.1: SEM of a 500 nm lattice constant magnetic square ice pattern. Relative to a reference element (black box), nearest neighbour types $(\mathrm{L,P,D})_{\mathrm{Y}}$ on the sublattice Y (defined in section 3.5 figure 4.2) are highlighted in green, red and blue boxes respectively. $(\mathrm{L,P,D})_{\mathrm{X}}$ are the rotationally symmetric nearest neighbours on the orthogonal sublattice X.

4.2 Experimental Protocol

A square ice sample was prepared by electron beam lithography, using a Helios Nanolab SEM system, of ZEP520A:acetol (1:1) resist spin-coated on a Si substrate, vacuum evaporation, and liftoff, as described in chapter 3. Elements of 100 nm $\times$ 250 nm were formed on a lattice of 500 nm lattice constant over multiple 20×20 μm^2 subarrays tiled at a spacing of ~ 1 μm on a square grid. A total area of ~ 1 mm^2 was formed. A thin film structure of Ta(2 nm)/$\mathrm{Ni_{80}Fe_{20}}$(25 nm)/Al(2 nm) was deposited. This formed islands with magnetic moments of $\sim 5 \times 10^7$ μ_{B}, giving rise to dipolar fields of ~ 10 Oe imparted on one island by each of its closest neighbours. An SEM image of the region of sample of interest is shown in figure 4.1 (a).

The system was then subjected to a field protocol similar to that utilised in the artificial kagome ice pattern magnetic reversal experiments discussed in section 2.4 [18; 23; 24; 26], under which qualitatively similar results would be expected. In-plane hold-fields of ~ 1 s duration were applied along a direction $\theta \approx 10^\circ$ offset from the diagonal to the x and y axes, as shown in figure 4.2 (b), such

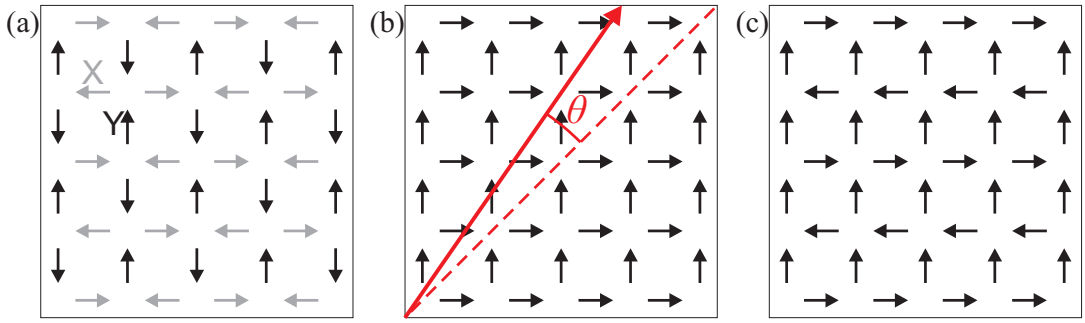

Figure 4.2: Well-defined square ice states. (a) The square ice ground state (GS) for single domain Ising-like dipole elements. The sublattices X and Y are shown as grey and black arrows respectively, defined by their easy axis orientation. Moments on each sublattice form a chessboard pattern of alternating alignment, while energy is minimised by the relative arrangement between sublattices. All $(L,P)_{X,Y}$-type lines of moments posses an antiferromagnet-like arrangement, and all $D_{X,Y}$-type moments are aligned with a ferromagnet-like arrangement. (b) The diagonally polarised state (DPS) defined by hard polarisation of both X and Y. The experimentally applied field direction is shown as a red arrow. (c) The Y-polarised state (YPS) on which Y is hard polarised and X minimises energy under this constraint.

that $H_y \approx 1.4H_x$. The average remanent magnetic configuration was followed by magnetic force microscopy (MFM) using a Veeco Multimode V system, imaging $\sim 13 \times 13$ μm^2 areas at the centres of ~ 5 closely positioned subarrays after each applied field. The single domain Ising nature of the nanobars was confirmed via the appearance of each element as a dumbbell of light and dark contrast, figures 4.3 and 4.4. It should be noted that fields were applied to sample external to the microscope, requiring transferal of the sample between an electromagnet and the microscope for each field step. As a result, exactly the same areas were not reimaged at each field step due to the limitations of positioning the microscope field-of-view, however, varying amounts of overlap do occur between images at successive field steps. While edge effects are potentially important in finite arrays, acting as nucleation sites for reversal [21; 27], strong evidence exists that significant quenched disorder can result in dominant bulk processes [23; 24; 26; 28].

Initially, a magnetic field of $H = +1.5$ kOe was applied, sufficiently large to form the DPS at remanence, figure 4.2 (b), with 100 % population of T_2 V_3 vertices (see figures 3.5 (d) and 4.4 for a vertex key). Increasingly negative hold-fields were then applied from -313 Oe up to -688 Oe, taking the system through a full reversal to the oppositely magnetized DPS, a full tiling of T_2 V_5 vertices. While applied fields will disturb the Ising-nature of the nanobars, we find, as previous authors report, that we can interpret the remanent states in terms of an ideal Ising dipole picture. No evidence has been presented in literature suggesting that such a "pulse-probe" experimental treatment yields behaviour modified with respect to that which might occur under the application of a monotonically increasing applied field, apparently due to the Ising-like hysteresis of the elemental moments.

4.3 Results

4.3.1 MFM of reversal

Example MFM images from the reversal sequence are shown in figures 4.3 and 4.4, with key configurations boxed and mapped schematically (insets) in terms of elemental Ising dipoles (arrows) and magnetically charged T_3 vertices (red and

yellow circles). Note: the sequence does not strictly show the same region of square ice elements in each image. Also shown in figure 4.4 for reference is a key indicating the four elemental magnetic poles which converge at the centre of each of the sixteen vertex configurations, similar to that shown previsouly in figure 3.5. In figure 4.5 (a) the normalised net digital magnetisation (section 3.5.1) $\mathbf{M} = M_{\mathrm{X}}\widehat{\mathbf{x}} + M_{\mathrm{Y}}\widehat{\mathbf{y}}$ is tracked. The average populations of the 16 individual vertices are followed for each step and those of specific interest are shown as solid lines in figure 4.5 (b-d). A small number of counting errors occur due to structural defects and tip-sample interactions, figure 4.3, however these occur on $\sim 0.3\%$ of islands imaged and do not have a significant effect on the system or statistics. In the vast majority of cases, there are no obvious structural features or defects correlated with the magnetic configurations that form during the reversal.

For $-375 \lesssim H < 0$ Oe, the initial DPS is observed with $\langle m_{\mathrm{X}} \rangle = \langle m_{\mathrm{Y}} \rangle = 1$, giving a 100 % V_3 T_2 tiling. Full reversal then takes place via two largely independent, but qualitatively similar, stages: initially, reversal of Y occurs between -438 Oe and -563 Oe, followed by reversal of X between -563 Oe and -688 Oe, figure 4.5 (a). For a given applied field angle, θ, a given element on X or Y will have an intrinsic switching field (i.e. the total field required to reverse its Ising state observed at remanence) $H_{\mathrm{s}}^{\mathrm{X,Y}}(\theta)$. At $\theta = 0$, it would be expected that $\langle H_{\mathrm{s}}^{\mathrm{X}}(0) \rangle = \langle H_{\mathrm{s}}^{\mathrm{Y}}(0) \rangle$, were X and Y identical under a 90° rotation of the system. While an intrinsic anisotropy may be possible from patterning, SEM reveals no obvious structural stigmation, however, very small asymmetric artifacts are present on one corner of each element, figure 4.1. Slight quantitative differences were observed in behaviour at different locations across the sample, e.g. variation in $\langle H_{\mathrm{s}}^{\mathrm{X}}(\theta) \rangle)$, which appears to vary in the subarray-patterning slow scan direction, presumably the result of a gradual drift in eletron beam exposure conditions with time during patterning. Such variation is small in comparison with the separation in field of the two independent sublattice reversal events. This effect is therefore attributed predominantly to the applied field angular offset, $\theta = 10°$, meaning that $H_y > H_x$ and $\langle H_{\mathrm{s}}^{\mathrm{Y}}(\theta) \rangle < \langle H_{\mathrm{s}}^{\mathrm{X}}(\theta) \rangle$. As previously described, attention will focus here on one self-contained local region, other regions behaving in a qualitatively identical way. (As an aside, the study of anisotropic systems is a

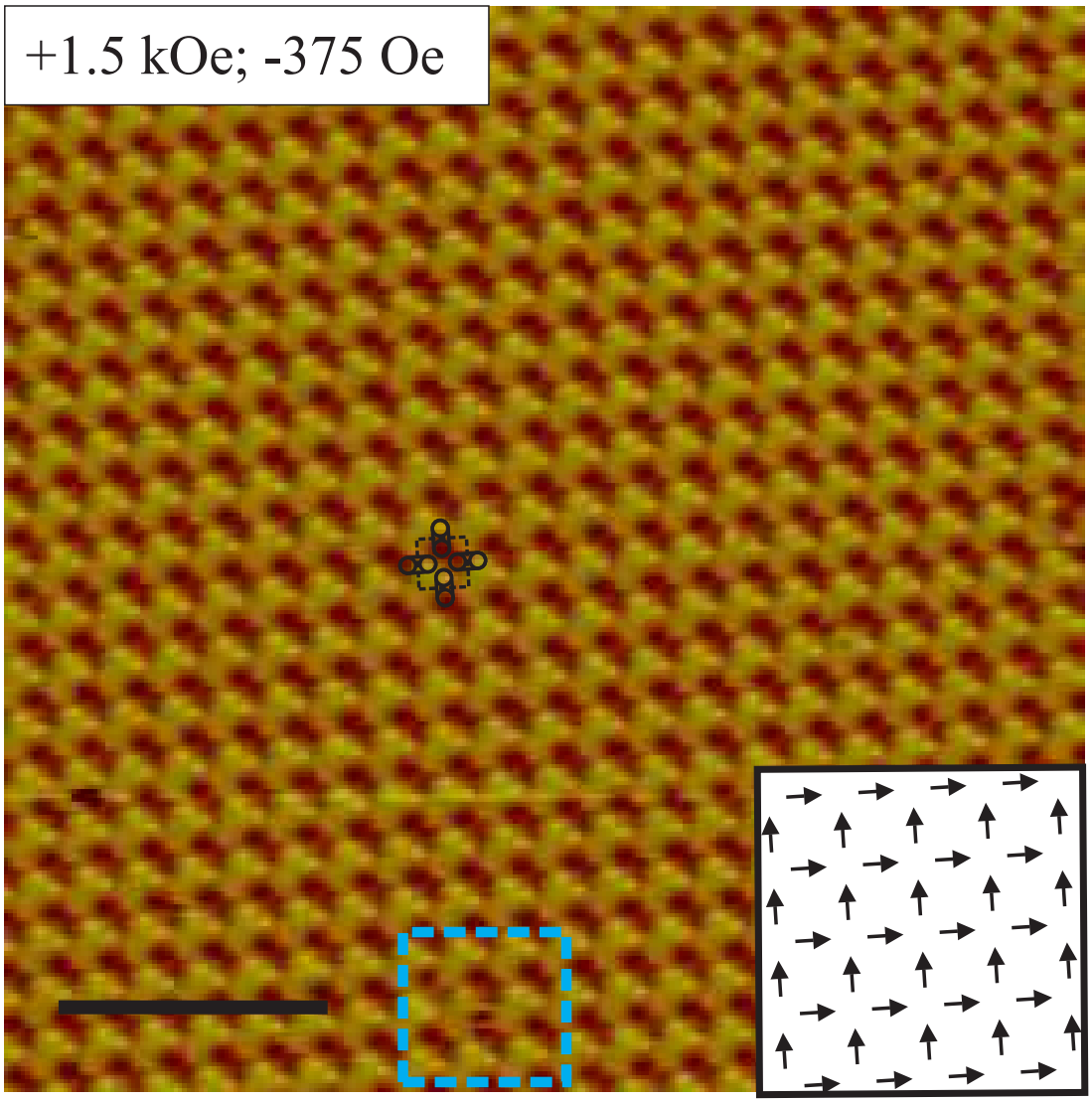

Figure 4.3: MFM image of the remanent state of a square ice pattern following an off-diagonal applied hold-field of +1.5 kOe, and subsequent hold-fields of − 313 and − 375 Oe, returning to remanence between each step. The scale bar is 3 μm. The initial field irreversibly aligns the moments of the system producing the DPS at remanence as seen in the periodic magnetic image, illustrated schematically inset, while the second and third applied hold fields of opposite direction is not large enough to produce further reordering. The state is a pure tiling of T_2 V_3 vertices, one of which is explcitly highlighed. Also, boxed in blue is an imaging error.

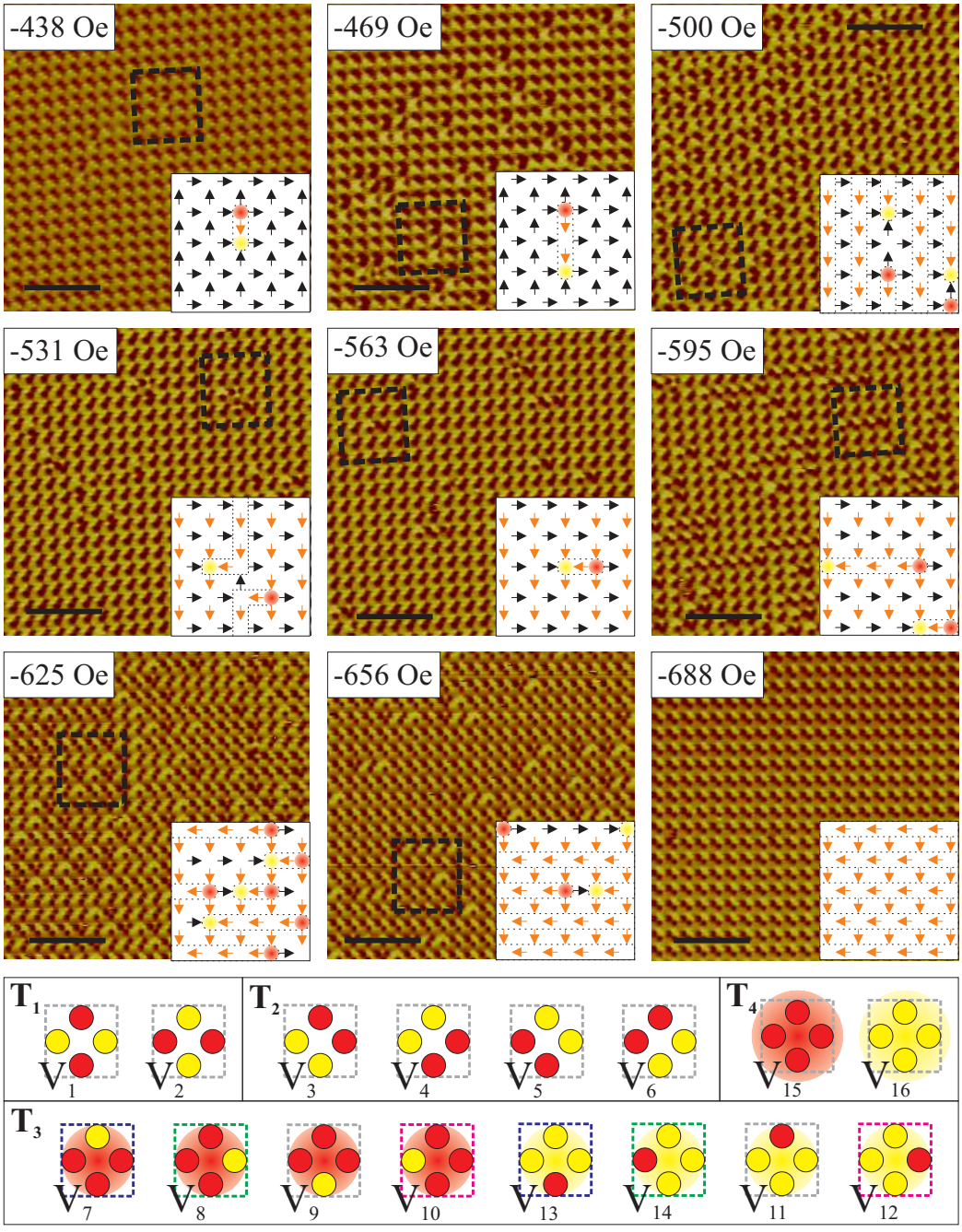

Figure 4.4: Example MFM images from the off-diagonal magnetic field square ice reversal sequence. Scale bars are 3 μm. The reversal process is described in the text. Key structures are mapped schematically (insets) in terms of unflipped and flipped Ising moments (black and orange arrows respectively), charged T_3 vertices and their propagation paths (dashed boxes). A vertex key is shown with oppositely charged T_3 pairs colour coded.

potentially interesting avenue of research yet to be extensively explored. Patterning induced anisotropy has been identified as imparting a weak breaking of the threefold symmetry of ac demagnetised kagome ice states [12] and simulations have shown modification of square ice behaviour during thermal annealing by consideration of more general rectangular lattices [81; 82].)

At −438 Oe a low density of isolated flipped-moment events is observed on Y, attributed to elements with lowest $H_s^Y(\theta)$. These correspond to nucleation events of oppositely charged T_3 pairs, $V_{10,12}$, at the expense of two V_3 T_2 vertices, leading to a reduction in M_Y. At −469 Oe a higher density of single flipped moments and associated T_3 pairs is observed, as well as longer sequentially flipped chains further separating oppositely charged T_3 pairs in the y-direction connected by V_4 T_2 vertex chains with polarisation rotated 90° to the initial V_3 DPS. While the DPS is not the GS, we can draw analogy here with charge separation in real and artificial kagome spin ice [19; 24], where background and chain are of the same ice-rule-obeying vertex type, with oppositely charged poles propagating in opposite directions.

At −500 Oe, over 50% of Y moments have reversed. $M_Y = 0$ is estimated to be at ~ -490 Oe, indicated in figure 4.5 (b-d) by dashed orange lines at the intersection points of the $V_{3,4}$ populations. Qualitatively, the state is very similar to that at −469 Oe, with a substantial population of T_3 vertices and $\sim 50\%$ V_4 T_2. The state appears more like a background of V_4 on which chains of unflipped moments now stand out, figure 4.4 (inset). Due to the coarseness of the field step, the exact reordering processes of specific groups of moments reimaged at successive steps could not tracked, therefore, it is not possible to say whether a chain of ≥ 3 moment flips is formed by sequential flipping, or by the oppositely charged ends of two separate chains on the same line of elements meeting and annihilating. At −531 Oe the flip-chains on Y have almost completely propagated out, reversing Y to $\langle m_Y \rangle \approx -1$. A small number of unflipped moments remain and the state appears qualitatively like that at −438 Oe, reflected about the x-axis. A symmetry should be emphasised, resultant of the degeneracy of the DPS. T_3 pair nucleation and annihilation processes appear qualitatively as the inverse of each other. The same is true comparing the extension of a flipped moment chain with the shrinking of an unflipped moment chain. Hence, given no

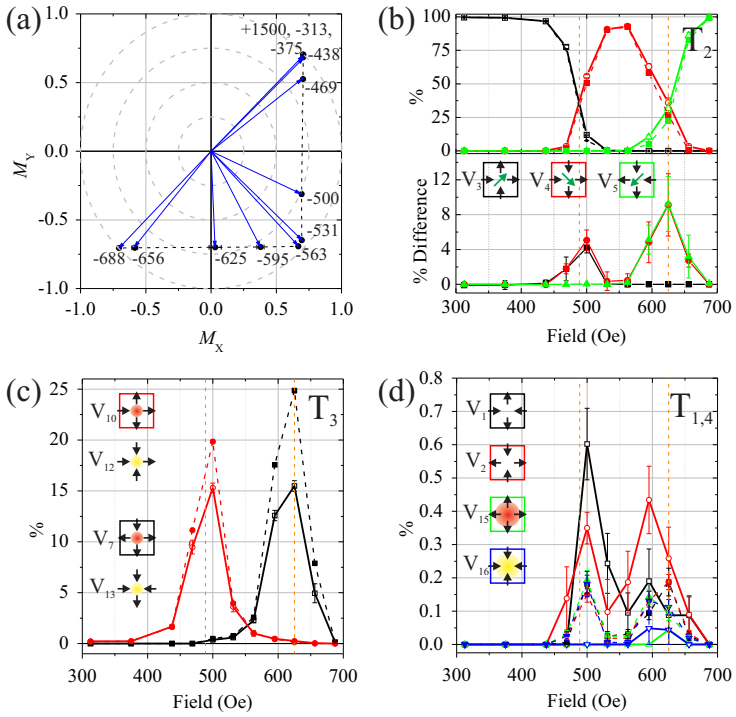

Figure 4.5: Magnetisation and vertex population statistics during a magnetic square ice reversal sequence. (a) Normalised net digital magnetisation vector during the reversal, labelled with corresponding field pulse maximum values (in Oe). Reversals of sublattices Y and X occur independently due to the applied field offset angle. (b-d) Experimental and random reversal vertex populations vs field step (solid and dashed lines respectively). The specific vertices are shown and referenced by colour. Both reversals occur via a peak in complementary positive/negative T_3 pairs, $V_{10,12}$ and $V_{7,13}$, which must nucleate to mediate reversal. Note, for clarity, the lower panel of (b) shows the difference between the experimental and random reversal T_2 populations. Further, only the populations of V_{10} and V_7 are plotted in (c), within error possessing equivalent populations to their oppositely charged partners, V_{12} and V_{13} respectively. Sequential moment chain reversal acts to transfer vertices within the T_2 group V_3 to V_4, and V_4 to V_5. Experimental $T_{2,3}$ vertex populations fall significantly far/short of random during reversal, indicating correlated cascade propagation. Initial and final stages of both reversals appears random-like. Weak enhancement(suppression) is observed of $T_{1(4)}$. Strong suppression of all other vertices is also found. The values of field where $M_{X,Y} = 0$ are marked by vertical orange lines, estimated as where the growing/falling T_2 populations cross.

knowledge of field history, the initial DPS background and propagation direction are not revealed from an MFM image. Overall conservation of charge is always maintained, for example, $V_{10,12}$ are always observed in equal numbers within error, small discrepancies only occurring over a MFM image due to single poles of such pairs having propagated across the image edge boundary.

Subsequently, for increasing fields, the sublattice X then reverses via the symmetrically equivalent processes — nucleation of $V_{7,13}$ T_3 pairs, propagation and annihilation, with V_5 increasing at the expense of V_4. Full reversal is achieved by -688 Oe. At -625 Oe, a state of $M_X = 0$ has been achieved, which by symmetry should posses a maximum in $V_{7,13}$ T_3. This is also indicated in figure 4.5 (b-d) with dashed orange lines. Only a small amount of overlap between the reversal of Y and X occurs, inhibiting the creation of $T_{1,4}$ vertices at all fields, as indicated by their small fractional populations. As an example, T_1 vertices can only form if a chain of sequentially reversed moments crosses sublattices, in a manner shown inset in figure 4.4 at -531 Oe, where the propagation of charged sites from their straight line paths along the y-direction has been diverted in to the x-direction, allowed to occur by the conversion of a $V_{10,12}$ pair into a $V_{7,13}$ pair. Such infrequent events are negligible in the reversal regime accessed. While the two sublattices do interact via dipolar coupling, by symmetry there is no net effect of the frozen polarised X(Y) sublattice on Y(X) (except for weak long range interactions), therefore, the same one-dimensional lines of charge carrying propagating N-N and S-S configurations would be expected if X(Y) were removed. It is likely, however, that the frozen sublattice imparts additional disorder on the reversing sublattice via local variations in dipolar fields.

It is conceivable that the reversal-mediating processes identified could occur in a non-interacting system, the reversal occurring by random flipping events determined by the local values of $H_s^{X,Y}(\theta)$, presumably randomly allocated across the pattern and distributed about $\langle H_s^{X,Y}(\theta)\rangle$. To test this, ideal maps of moments were generated with set fractions reversed at random from the initial DPS (the coordinates chosen by a pseudo-random number generator), corresponding to the experimental **M** states. (Here, the results presented are averaged over ten 40×40 element vertex maps for each field step, although the results are

not sensitive to the absolute size). The resultant random reversal vertex populations are plotted with dashed lines in figure 4.5 (b-d). It is clear that during both reversals, the T_2 populations exceed what would be expected for random arrangements of moments, as emphasised by the excess of percentage populations plotted in the lower panel of (b), whilst the T_3 populations similarly fall short of what would be expected. This indicates that sequential chain flipping is significantly correlated - dipolar interactions bias the system towards reversal via incrementally pinned correlated dipolar cascades, consequently enhancing above random the population of T_2 vertices which must occur on these chains. It also appears that the initial and final stages of both experimental reversals follow a random-like trend, implying that the nucleation and annihilation events are random-like processes. This is consistent with the expected distribution of elemental properties imparted by quenched disorder, e.g. chain defects appearing on X(Y) at sites of lower-than-average $H_s^{X,(Y)}(\theta)$, giving rise to random-like statistics when an averaged-state picture is adopted. Y and X reversal appear to be quantitatively different, the latter appearing to have greater suppression of T_3 vertices. Interestingly, the small populations of $T_{1,4}$ that occur are slightly enhanced/suppressed with respect to random respectively, reflecting their favorable/unfavorable moment configurations.

Making a visual comparison with a recent report of chain propagation on a kagome ice array [24], while our stronger isolation of sublattice switching strongly suppresses instances of potential "monopole-trapping" configurations (e.g. figure 4.4, −531 Oe inset) where charged T_3 vertex sites become trapped on the chains of an adjacent defects, much weaker cascade correlation is apparent. This can be seen, for example, by comparing our $M_X = 0$ state in which a maximum flipped chain length of ~ 8 dipoles is found, figure 4.4 −625 Oe, with the state following application of 99 % the coercive field of the kagome pattern, figure 2.23 (f) section 2.4, in which notably longer coherent chain lengths are found of $\sim$ 20 dipoles can be identified. This is attributable to a higher ratio of disorder strength to inter-elemental interaction strength giving rise to a higher density of random-like nucleation and pinning events in the square ice pattern discussed here.

4.3.2 Dipolar correlations

To further explore these spatial correlations, six correlation functions $C^{\mathrm{DPS}}(n_{\mathrm{d}}) = \langle \mathbf{m}_i \cdot \mathbf{m}_{i\pm n_{\mathrm{d}}} \rangle_i$ can be calculated, with $C = (L, P, D)_{\mathrm{X,Y}}$ for $n_{\mathrm{d}}^{\mathrm{th}}$ nearest neighbour dipole pairs, for L, P, or D type neighbours on sublattice X or Y, as defined in figure 4.1 and in section 3.5. Perfect alignment/antialignment of all $n_{\mathrm{d}}^{\mathrm{th}}$ pairs of a given neighbour type yields $C(n_{\mathrm{d}}) = \pm 1$ respectively. Random alignment yields $C(n_{\mathrm{d}}) = 0$. Note, C does not distinguish between flipped and unflipped moments, and no correlations between X and Y are considered as their reversals are almost totally unmixed.

The observed correlations $C^{\mathrm{DPS}}(n_{\mathrm{d}})$ are plotted for Y and X in figure 4.6 (a,b) (solid lines with symbols), as well as those calculated for the random moment reversal sequence (dashed lines). To aid discussion, it should first be noted that all random $C^{\mathrm{DPS}}_{\mathrm{X(Y)}}$ behave identically with state and have no dependence on n_{d}, and hence the average random reversal correlation $R_{\mathrm{X(Y)}} = \langle L^{\mathrm{DPS}}_{\mathrm{X(Y)}}(n_{\mathrm{d}}) \rangle_{n_{\mathrm{d}}}$ is plotted for clarity. For this double reversal process, the collective trend is for R_{Y} to initially decrease from a value of $+1$ in the initial DPS towards 0 at $M_{\mathrm{Y}} = 0$, then to rise again towards $+1$ as Y reversal is complete. Subsequently, R_{X} follows the same pattern.

Experimentally, all $C^{\mathrm{DPS}}_{\mathrm{X,Y}}(n_{\mathrm{d}})$ are indistinguishable from random, with the exception of certain short range correlations during the mid-stages of both reversals. During reversal of sublattice Y, at -469 Oe and -500 Oe, enhanced $L^{\mathrm{DPS}}_{\mathrm{Y}}(1)$ correlation is observed above random, a greater enhancement for the smaller $|M_{\mathrm{Y}}|$ state, indicating the propagation of correlated sequential sublattice Y moment flips along the y-direction. Interestingly, weak suppression of $P^{\mathrm{DPS}}_{\mathrm{Y}}(1)$ is observed at -500 Oe. This can be interpreted as $P^{\mathrm{DPS}}(1)$ neighbours favouring antialignment, a consequence of solely their direct dipolar interaction (unlike GS correlated configurations). This implies that flip chains on adjacent rows on sublattice Y weakly resist nucleating or propagating along side each other, and bias towards a state as shown in figure 4.2 (c) is present, where sublattice Y minimises its energy under the constraint of the hard polarised uninfluential X sublattice. (As an aside, this state may be expected in a square ice lattice of coupled superparamagnetic moments under an x-(y-)directed applied field.)

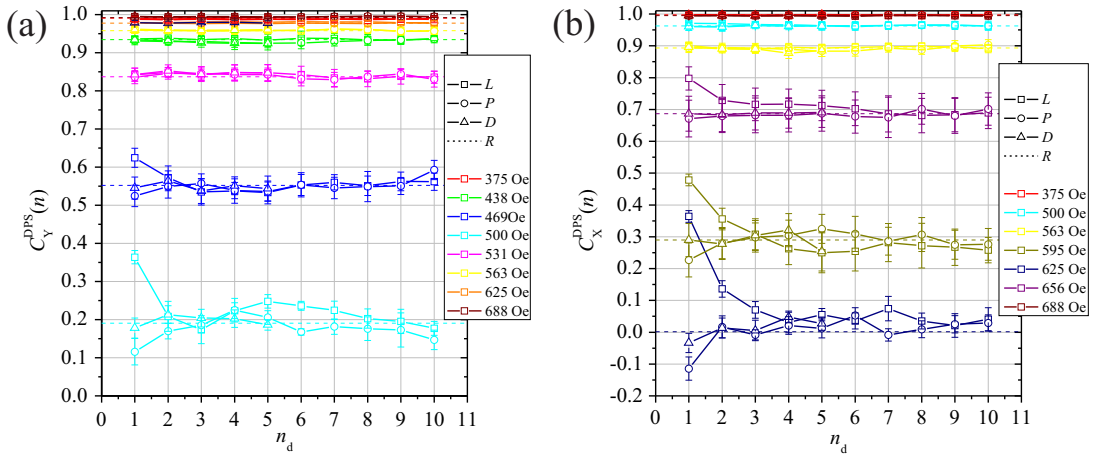

Figure 4.6: Dipolar correlations during a magnetic square ice reversal sequence. Experimental $L_j^{\mathrm{DPS}}(n_\mathrm{d})$ (open squares), $P_j^{\mathrm{DPS}}(n_\mathrm{d})$ (open circles) and $D_j^{\mathrm{DPS}}(n_\mathrm{d})$ (open triangles) dipolar correlations for the (a) $j = \mathrm{Y}$ and (b) $j = \mathrm{X}$ sublattices, as a function of the $n_\mathrm{d}^{\mathrm{th}}$ nearest neighbouring element (solid lines). Dashed lines show the expected random correlations R_j, equivalent for all $(\mathrm{L,P,D})_j^{\mathrm{DPS}}$ at all n_d. Random-like correlation is observed experimentally for all $(L, P, D)^{\mathrm{DPS}}(n_\mathrm{d})$ at all fields, with the exception of short-range L_j^{DPS} and P_j^{DPS} correlations which are enhanced and suppressed respectively during the mid-stages of both Y and X sublattice reversal. This confirms that correlated cascades propagate in the reversal direction, and shows that two cascades propagating on adjacent rows weakly resist passing each other. These effects are most pronounced at $H = -625$ Oe where a $M_\mathrm{X} = 0$ state has formed.

Again, reversal of the X sublattice is observed to behave qualitatively like reversal of the Y sublattice, however, with an apparently stronger enhancement of short range $L_{\mathrm{X}}^{\mathrm{DPS}}$ compared to $L_{\mathrm{Y}}^{\mathrm{DPS}}$ during reversal mid-stages, either due to the applied field θ-offset or an intrinsic patterning bias. This is observed distinctly at -625 Oe with enhanced correlation up to $n_{\mathrm{d}} = 3$. As this is a demagnetised $M_{\mathrm{X}} = 0$ state, it is expected by symmetry that the effects of dipolar coupling on correlation will be strongest here. Again, suppression of $P^{\mathrm{DPS}}(1)$ is observed, now with a true anticorrelation, the random correlations R_{X} lying at 0. No significant correlation can be seen in $D_{\mathrm{X}}^{\mathrm{DPS}}$ at any n_{d} indicating that chain-chain interactions are weak and local. Agreement of experimental and random correlation during early and late stage of each reversal confirm that nucleation and annihilation of oppositely charged T_3 pairs are random-like processes.

4.3.3 Charge density functions

Qualitative evidence for the effects of the $\mathrm{P}^{\mathrm{DPS}}(1)$ neighbour interactions can be seen in the formation of configurations such as that shown inset in figure 4.4 for -625 Oe. A number of oppositely/like charged pairs of T_3 $\mathrm{V}_{7,13}$ vertices, propagating via flip chains on adjacent lines on sublattice X, appear to be pinned/antipinned at adjacent sites, attributable to the weak resistance of the chains to propagate along side each other. This is an exciting idea as it works towards validating understanding of the system in terms of coupled vertex objects, rather than its underlying dipoles. To this end, we focus on the $M_{\mathrm{X}} = 0$ state achieved at -625 Oe, and calculate the average fractional vertex type density $\rho_{-\pm}(n_{\mathrm{V}})$ of positively or negatively charged T_3 vertices relative to all other negative T_3 vertices at a separation of n_{V} vertex sites in the y-direction (perpendicular to propagation), and compare these to ideal random values $\rho^{\mathrm{R}}{}_{-\pm}(n_{\mathrm{V}})$ (inferred by symmetry), shown in figure 4.7. As a hard-polarised Y sublattice is demanded in this state, only 4/16 of the vertices are compatible with this condition and, therefore, allowed to occur, $\mathrm{V}_{4,5,7,13}$. For a random allocation, producing a state with $M_{\mathrm{X}} = 0$, it would be expected that at any given distance relative to a negatively charged T_3 vertex (or indeed any other reference vertex) both positively and negatively charged T_3 vertices will have an average density of $\rho^{\mathrm{R}}{}_{-\pm}(n_{\mathrm{V}}) =$

0.25, except at $n_V = 0$, where $\rho(n_V)$ must always be 0 or 1 respectively. The randomly reversed maps agree closely with these ideal values. Experimentally, the general suppression of both positive and negative T_3 vertices relative to the random reversal state by virtue of correlated chain propagation is reflected in the average density of $\rho_{-\pm} \sim 0.17$, at all $|n_V| > 1$, agreeing closely with that observed in figure 4.5 (c). For $n_V = \pm 1$, however, it is observed that the suppression of ρ_{-+} is notably weaker, maintaining a value close to ~ 0.23, while ρ_{--} is much more strongly suppressed with a value ~ 0.09. (Calculations for $\rho_{+\pm}$ yield a similar result for like/opposite charges.) From this we can directly infer that during the reversal process, oppositely/like charged monopole-like T_3 vertices do indeed couple, at least over short ranges. While such vertices also posses a N-S dipole moment, figures 3.5 (d) and 4.4, this component is identical for both the oppositely charged T_3 $V_{7,13}$ vertices allowed during the reversal of sublattice X and is part of the uninfluential sublattice Y. Therefore, this weak T_3 vertex coupling, which produces weak charge ordering, can be attributed purely to the ± 2 magnetic charge carried by their N-N/S-S components.

4.4 Defect Energetics

It is interesting to consider the excitation energy of these field-mediated chain defects, in a similar manner to how excitations above the GS have been treated [20; 22; 25], sections 2.5 and 6.2.3. It is clear that in the midstage reversal states discussed in the previous sections high densities of chain objects are present, hence it might be expected that they cannot be treated as isolated individual entities, however, these calculations present a similar study to that of Mól et al. in reference [20]. As in charge separation in a bulk crystalline spin ice [19], and unlike square ice chain defects on the GS, the dipolar chains connecting an oppositely charged pairs of vertices on the square lattice DPS as discussed form the same 2-in/2-out type of vertices as composing the ice-rule obeying background. While the DPS is not a GS background, it raises the question of whether a "monopole-antimonopole" pair are deconfined when their connecting chain is confined to a 1D line, as a simple isolated vertex energy model approximation is often found to well-describe these system.

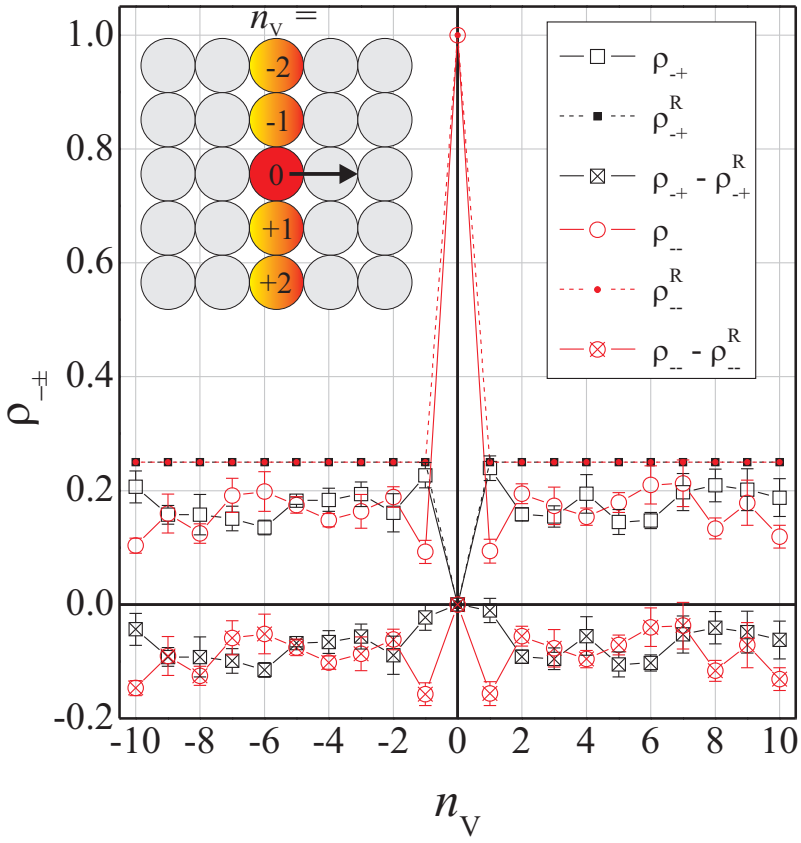

Figure 4.7: Charge density functions at a $M_X = 0$ state during magnetic reversal of square ice sublattice X. Fractional density $\rho_{-\pm}(n_V)$ of positive or negative T_3 vertices relative to negatively charged T_3 vertices in the $M_X = 0$ state compared to ideal random values for nearest vertex neighbour distance n_V. The schematic shows the propagation direction of a negatively charged T_3 vertex, and its n_V^{th} Y-direction neighbours. The general suppression of average T_3 density from 0.25 to ~ 0.17 for $n_V > 1$ is understood by the enhanced cascade propagation processes. At $n_V = 1$, however, a higher/lower density of unlike/like poles is observed, indicating weak charge ordering by attractive/repulsive pinning/antipinning.

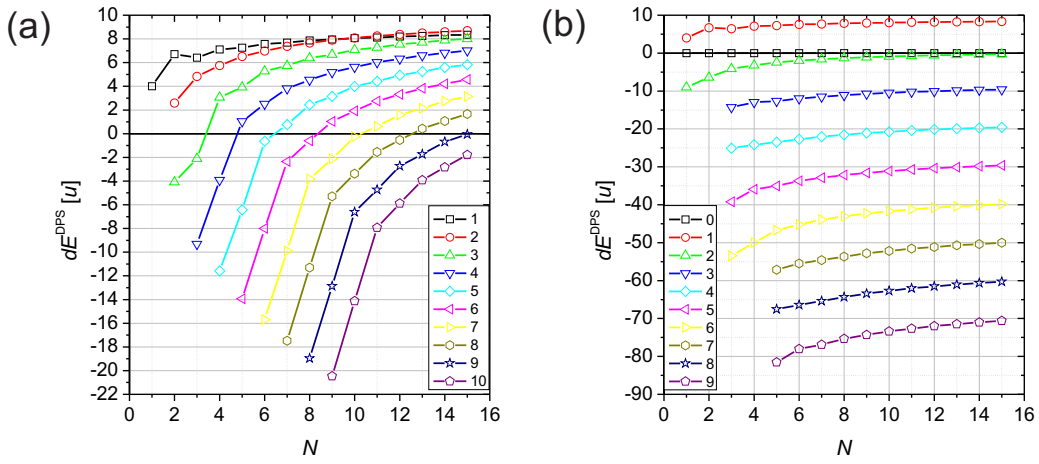

Figure 4.8: Energetics of flipped moment chain defects on the diagonally polarised state. (a) The dipolar energy of excitation, dE^{DPS} above the DPS of a centrally positioned flip chain defect (of length l shown inset) as a function of the array size N. (b) The dipolar energy of excitation, dE^{DPS} above the DPS of a centrally positioned diagonal flip chain defect (of length l shown inset) as a function of the array size N.

Calculations are performed by summing the dipolar interactions over an $N \times N$ array of vertices of ideal point dipoles. Note, effects of quenched disorder are not included in the calculations, a possible effect being a distribution of moment size. A background DPS is taken, and a flip chain object of the type discussed in this chaper of increasing length is placed with its midpoint at the array centre. The energy difference between the defected configuration and the pure DPS, denoted dE^{DPS}, is plotted in figure 4.8 (a) as a function of N.

It is apparent that dE do not converge quickly with $N \times N$ size to a bulk limit, for any value of chain length l. This implies that net long range interactions, (that are strongly screened and approximately cancel out as for the GS, as will be discussed in chapter 6), do not die off to a negligible amount and even the shortest chains are sensitive to the system edges for $N = 10$. Adopting a vertex model interpretation, here, both background and excitation are formed

from vertices possessing intrinsic dipoles, $T_{2,3}$, in contrast to defects on the intrinsically unpolarized antiferromagnet-like GS. Further, an approach of simply counting the number of vertices composing the chain defect does not appear to yield an energy approximation as for GS excitations [25] (chapter 6).

For the range of N considered, oppositely charged sites at the ends of a chain appear to be repelled from each other, reducing energy by extension of the chain. This is locally attributable to the P(1) interactions favoring antialignment i.e. it is most favorable, as one sublattice is held fixed and polarised, for a chain to fully propagate from edge to edge, possessing an energetic bias to a state as shown in figure 4.2 (c). This requires a small initial energy to flip a single moment, forming two unfavorable antialigned L(1) moment pairs, forming the N-N/S-S charge configurations of an oppositely charged T_3 vertex pair. Once formed, the number of unfavorable L(1) pairs remains constant as a chain extends until the charges reach the system edges and are expelled. There will also be an interaction between the array "surface charge" of the DPS configuration and the bulk charged vertex sites.

Above $N = 10$ it appears that extension of a chain from $l = 1$ to $l = 2$ no longer reduces the energy, revealing a weak attraction. By $N = 15$ a chain of $l = 1$ is of similar energy to a chain of $l = 3$, and it is anticipated that with increased N such interactions will also become attractive. Improved less-intensive calculations are required to go beyond $N = 15$. Further, for chains of $l \sim N$ the "repulsion" between poles becomes stronger, decreasing the energy by larger steps, and is perhaps more adequately described therefore as an attraction of the poles to the charged edges. It should be noted that such a growth process, nucleating at the array centre and extending isotropically in both directions is rather ideal, and distinctly different quantitative behaviour might be expected depending on where the nucleation site is placed.

This result of the influence of longer range interactions will be generally true for any polarized nanomagnet array - being an "artificial magnetic material", the system naturally favours energetically a demagnetised state. The chain defects observed on low energy charge ordered kagome backgrounds [23; 24] will also be subject to similar energetics, with defects comprising polarised vertices on a

polarised background. A given selected defect vertex or chain configuration is not energetically well-defined, despite having a well defined topological configuration.

Further, similar flip chains of a diagonal type have been observed on the DPS in experiments and in simulations [21; 27], separating T_3 pairs via chains of T_1 vertices. In figure 4.8 (b), the same calculations are shown for such chain defects, again with the defect midpoint positioned at the array centre. No longer is one sublattice fixed in a hard polarised configuration. While convergence to a bulk limit again appears slow, energetically, chains obey the same rules as excitations on the GS (reference [25] and section 6). Nucleating a chain defect, increasing from $l = 0$ to $l = 1$, creates two T_3 vertices from two T_2 vertices. The $l = 1$ defect in both (a) and (b) are the same, and their energy appears to tend to $dE \sim 8u$. Each subsequent flip removes a T_2 vertex from the system and adds a T_1, reducing the energy by $\approx 10u$ per flip. This holds reasonably well even for lower N (the far-from-converged limit). The over all nicer behaviour of these diagonal chains and reduced interaction with the system edge can be attributed to the fact that the "defected" vertices are mainly unpolarised T_1 vertices, which have negligible net interactions with the background at long ranges or with the "surface charge". Again, the oppositely charged ends of the string experience a "repulsive interaction", propagates them respectively towards edges of opposite charge - while interaction between T_3 vertices may possibly be treated as Coulombic [20], the net effect of their connecting chain is to propagate them until the charges are expelled from the system edges.

It should be remembered that these calculations reflect ideal systems of finite size, and are intended to reflect a general underlying property of the system. In a real system, effects of quenched disorder may alter the influence of longer range interactions.

4.5 Summary

In the propagation regime accessed by our protocol, X and Y square ice sublattices reverse independently via L-type neighbour flips chains. The ends of these chains are the N-N/S-S soliton-type objects [120] possessed by T_3 vertices, which carry the vertex charge component along adjacent 1D channels. While

we do not address their interactions quantitatively, we show that the underlying coupling of the dipole lattice manifests as vertex charge ordering, adjacent like/unlike charges being weakly repelled/attracted. While the observed charge coupling is only evident at $n_{\mathrm{V}} = \pm 1$, long range interactions also can play an important role in such systems [12; 21], which may manifest as long range vertex interactions, and accessing a strong coupling/low disorder regime is desirable to aid their observation. Pairs of moments posses an interaction which weakens with their separation, however, the distribution widths of properties imparted by quenched disorder (e.g. the $H_{\mathrm{s}}^{\mathrm{X,Y}}(\theta)$ distributions) are constants of the system. Interactions between dipolar neighbours of increasing separation therefore become quickly swamped by quenched disorder. Longer range dipolar correlations, and therefore vertex correlations, resultant of direct interactions consequently do not sum coherently. A full quantitative understanding could require a model incorporating charge and dipolar vertex components.

It should be noted that modification of ideal Ising dipole behaviour, e.g. due to internal or external fields, is not explicitly revealed in this study, however, non-uniform island magnetisation is possible in elements of similar dimensions [27] and symmetry-breaking field history dependent remanent vertex configurations have been reported in kagome networks of significantly longer NiFe nanowires [26], formed by pinned transverse domain wall charge distributions with width comparable to the wire-width. Such quasiparticles have also been shown to couple on continuous adjacent wires [121] when sufficiently close together. It is possible that the elements studied in this chapter, by virtue of their size, reverse via a more coherent rotation of magnetization, as opposed to domain wall propagation, which could impart different transient magnetic dynamics. This would certainly be the case for elements of lesser volume, of dimensions comparable with a domain wall width, which is well within the capabilities of modern nanofabrication. Due to the non-ideal nature of the elemental moments, the relaxation of the system under remanent conditions between each applied hold-field could act to modify the observed chain propagation relative to that induced by a monotonically increasing field. For example, modification of the internal magnetisation distributions of the magnetic elements could in turn affect elemental reversal. Likewise, the imaging of elements with a magnetic probe tip at each step could also redistribute

elemental internal magnetisation and perturb the incrementation of chain defects. Such "pulse-probe" effects however are not expected to have critically altered the observed phenomena.

It is worth noting that the low [18; 23; 24] and high energy [18] charge ordered states previously reported in kagome ice patterns are both results of field-condensation, section 2.4. While the latter is resultant of independent sublattice reversal, neither occur by virtue of charge or dipolar interactions and would be observed in an uncoupled system.

Furthermore, alternative reversal regimes may be accessed by altering θ. Specifically, decreasing θ to more closely align the field with the lattice diagonal would allow for increased overlap between the distributions of $H_{\mathrm{s}}^{\mathrm{X}}(\theta)$ and $H_{\mathrm{s}}^{\mathrm{Y}}(\theta)$, potentially enhancing T_1 GS tile formation [27]. Understanding the myriad of methods by which to mediate order could allow for realisation of frustrated patterns as magnetic information processing devices [66; 122].

Chapter 5

Constant Magnitude Rotating Field Protocol

5.1 Introduction

As previously discussed, experimental access of artificial spin ice ground states (GSs), e.g. figure 2.6 (c), has proven to be a non-trivial task. While thermal annealing can allow access to long range GS ordering in artificial square ice [25], producing large "chess-board" tiled T_1 vertex domains of two possible sense (chapter 6), following fabrication the magnetic elements are typically athermal and field-driven annealing must be employed via ac demagnetization to drive systems towards low energy states [3; 9; 12; 16; 17; 18; 57].

In large area patterns, the most effective routine is reported to involve a stepwise decreasing in-plane square function field profile, with simultaneous in-plane sample rotation [14], section 2.3.1. A critical field window exists, $[H_{\text{min}}, H_{\text{max}}]$, defined by the intrinsic distribution of elemental properties due to quenched disorder and configuration dependent net dipolar interactions, in which the applied field can mediate non-trivial reconfiguration of the elemental Ising states allowing the system to explore its magnetic phase space.

Recent theoretical work of Budrikis et al. has suggested that an alternative simplified protocol might enable extensive GS ordering [21], section 2.3.4. In simulation, finite sized square ice systems of point Ising dipoles, beginning in a diagonally polarized state (DPS) of pure T_2 vertex tiling, figure 2.6 (d), were

subject to a rotating in-plane hold-field $\mathbf{H}_{\mathrm{h}}$ of constant magnitude H_{h}. The final steady-states were found to have significant dependence on the open or closed array edge-types studied, figure 2.20, and the value of H_{h}. All non-trivial behaviour is found to occur within a critical field window (a result not dissimilar to that reported for ac demagnetisation [16; 78], sections 2.3.1 and 2.3.3), with the modified edge coordination providing chain-nucleation sites by virtue of modified net dipolar interaction. For open arrays, two non-trivial field regimes were found, and strong GS vertex populations and GS ordering can be achieved.

In the low field regime, T_3 sites are incrementally propagated into the bulk with each field rotation where the only allowed reversals are via chains of T_1 vertices. Opposite charges meeting in the middle annihilate leaving behind near perfect GS tiling. In the high field regime, propagation is also allowed via chains of T_2 vertices, which consequently results in charge trapping and jamming, with reduced ability to access GS configurations. In closed-edge patterns, no low field regime exists as T_3 vertices are not allowed to nucleate until H_{h} is above the threshold for T_2 chain propagation.

In this chapter, an experimental realization of such a constant magnitude rotating field protocol will be presented. Square ice patterns of equivalent shape and size to those of reference [21] were studied with MFM, figures 5.1 and 5.2 respectively, in search of the strong GS ordering and edge effects predicted. Neither of these predicted effects are found. For both open and closed patterns an identical variation of vertex populations with hold field, H_{h}, is observed, with optimal GS order and demagnetization occurring at $\sim$ 520 Oe, however, this is significantly suppressed relative to predictions. This is attributed to the absence of the effects of quenched disorder in the theoretical studies discussed.

5.2 Experimental Protocol

Five nominally identical arrays of both open and closed edge were patterned on a single Si chip with electron beam lithography, using a JEOL 6300 system, and vacuum evaporation, as per sections 3.1 and 3.2. Islands were $\sim$ 85 nm $\times$ 280 nm in lateral size on a lattice of $a = 400$ nm constant, with a thin film structure of Cr(2nm)/NiFe(30nm)/Al(2nm), forming moments of $\sim 10^6 \mu_B$, with nearest

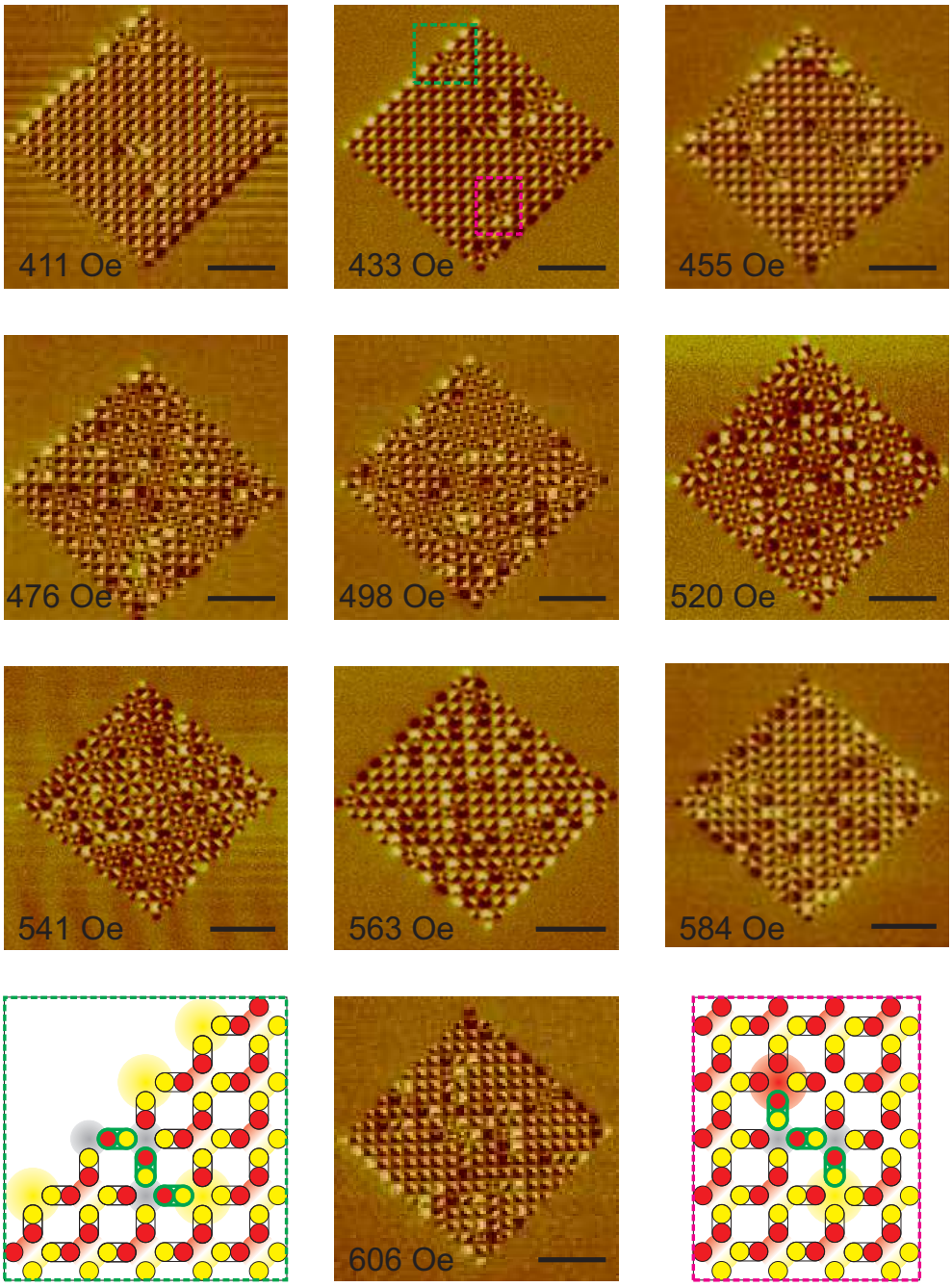

Figure 5.1: MFM series for open edge patterns following the rotating field protocol at hold field H_{h}. The moment configurations boxed in green and pink at 433 Oe are mapped schematically with dipolar dumbbells in the lower left and right panels respectively. Both schematics show moment chains reversed against the DPS (green outlined dumbbells), one connected to the open edge (lower left panel) and one isolated in the bulk (lower right panel). Both dipolar chains propagate T_3 vertices via chains of T_1 vertices. Scale bars are 2μm.

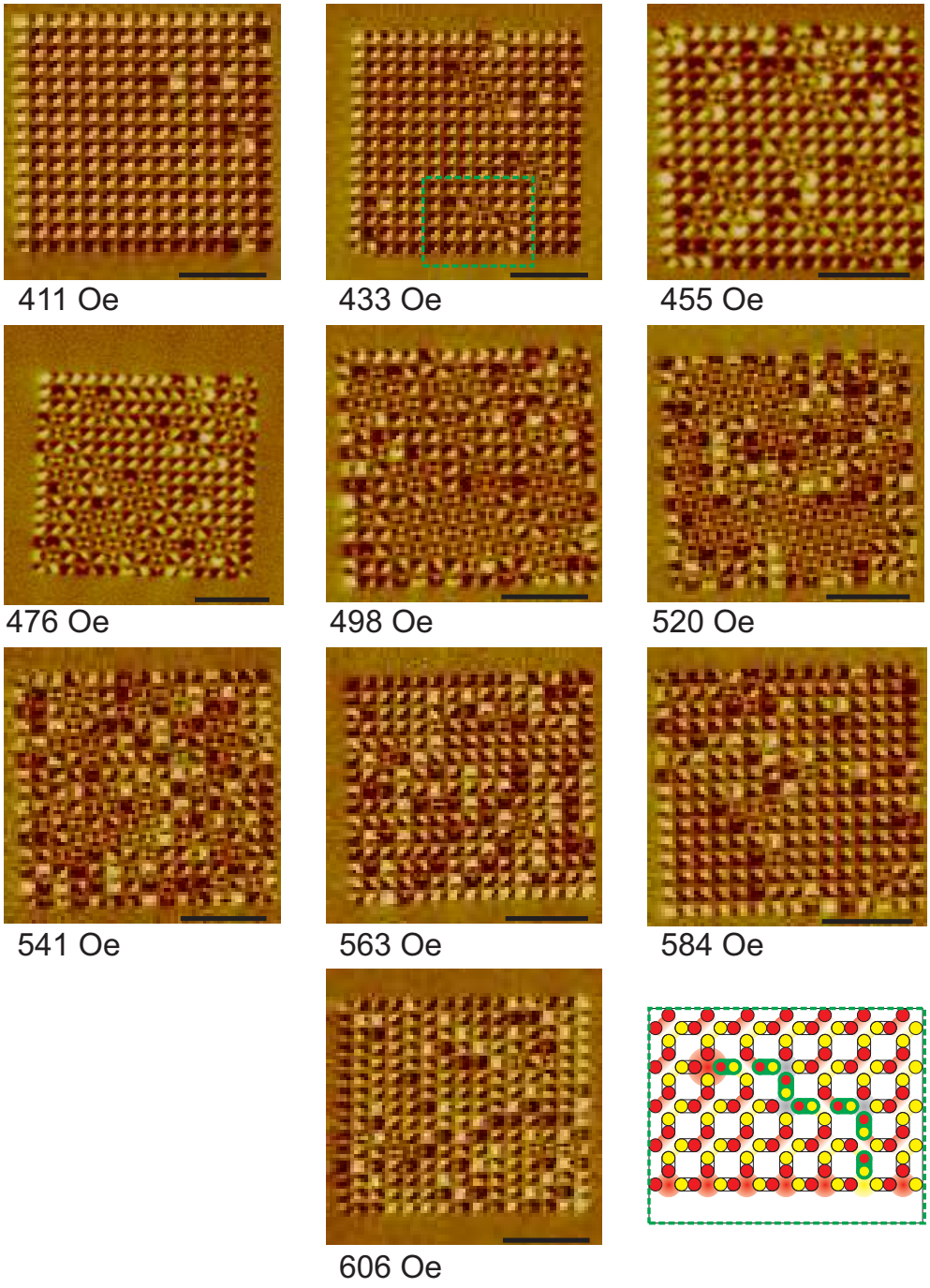

Figure 5.2: MFM series for closed edge patterns following the rotating field protocol at hold field H_{h}. The moment configuration boxed in green at 433 Oe is mapped schematically in the lower right panel as dipolar dumbbells, showing the propagation of charge from the closed edge into the bulk via a chain of moments reversed against the DPS (outlined in green), forming a T_3 vertex at the end of a chain of both T_1 and T_2 vertices. Scale bars are 2μm.

neighbour coupling of $\sim$ 10 Oe. A large in-plane field $H = 1.8$ kOe was applied along a diagonal symmetry axis to first prepare a 100% T_2 DPS, [30]. The field was then reduced to a hold value H_h. In-plane rotation of the sample with a period of 29.4 ms was then begun. After $\sim 20s$, $\sim$ 680 full rotations, sufficiently more than required to reach a predicted steady-state [21], the field was ramped to zero at a rate of $\sim$ 10,000 Oe/s. It should be noted that the finite ramp-down time is not expected to drastically effect the outcome of the experiment - estimating $H_{max} - H_{min} \approx 100$ Oe (as will be subsequently confirmed), the ramping field will cross this range within a single sample rotation. As a function of H_h, the remanent state of each array was then imaged by MFM (also confirming the single domain dumbbell behaviour of each moment), at 22 Oe increments between 411 Oe and 606 Oe. Uncertainties in all values quoted are calculated as the standard error over the five arrays imaged.

5.3 Experimental Results

Figures 5.1 and 5.2 show example MFM images from the H_h sequence for open and closed edge arrays respectively. Note, the same array is not strictly imaged in each micrograph. Note, as per chapter 4, an averaged-state interpretation will be adopted. Key configurations of interest are boxed are mapped schematically (insets) in terms of dipole moments, and vertex type. The normalised digital magnetization vector, $\mathbf{M}$, as previously defined (section 3.5.1), and percentage vertex type populations are tracked in figures 5.3 respectively. A number of important points should first be noted. Firstly, no significant difference is found between the statistics for open and closed arrays for all H_h. Secondly, an optimum T_1 populations is found at $H_h = 520$ Oe coincident with $\mathbf{M} \sim 0$, however, this maximum is significantly suppressed to that predicted from the ideal point Ising dipole model simulations [21]. Both these observations can be understood by the fact that real systems are inherently imperfect due to quenched disorder.

Below $H_h \sim 433$ Oe, $H_h < H_{min}$ for all islands. The initial DPS state is therefore retained at remanence. For $H_h = 433$ Oe to 455 Oe the lower region of the critical window is accessed, with an increasing number of correlated moment reversal events occurring, figures 5.1 and 5.2, forming sequential chains of $T_{1,2}$

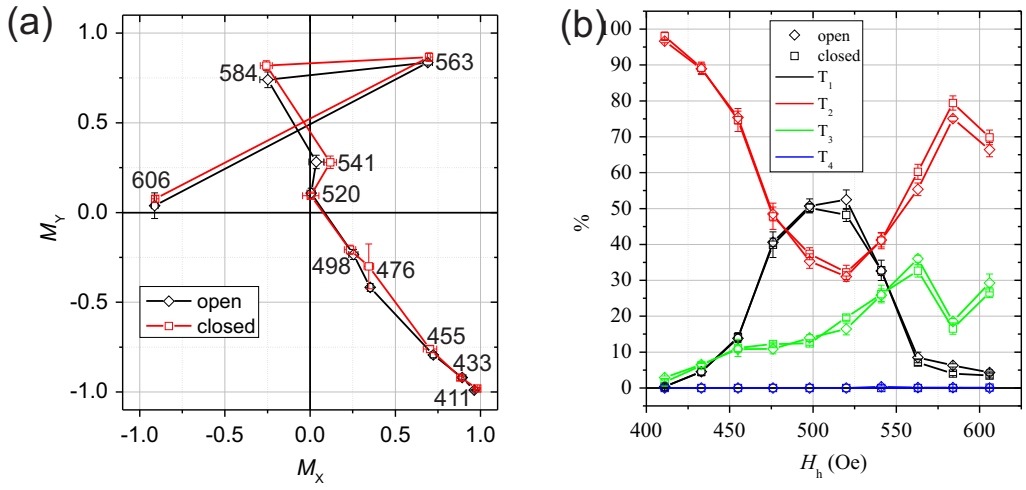

Figure 5.3: Statistics of open and closed edge square ice states following constant magnitude rotating field treatment. (a) Normalised digital magnetisation for open and closed edge square ice patterns, following a constant magnitude rotating field protocol, with magnitude H_{h} as labelled. (b) Vertex populations as a function of H_{h}.

vertices with T_3 at their ends, accompanied by a linear decrease in **M** with $M_X = M_Y$. Such chain objects are similar to those reported previously in uniaxial dc field experiments which occur by virtue of random-like nucleation, dipolar coupling, correlated cascading and random-like pinning [23; 24; 27; 29], as discussed in section 2.4 and chapter 4. A significantly DPS-like background is still maintained. While some chains are edge-connected, it is clear from the MFM that bulk chain nucleation must be predominant.

As H_h is increased to 476 Oe, figures 5.2 and 5.1, small patches of GS-like tiling begin to form, and mixed DPS/GS phases are found, as H_h can reverse increasing numbers of moments from the initial DPS but is not large enough to subsequently destroy GS the order formed. As 520 Oe is approached, **M** approaches 0 and T_1 populations approach a maximum of $\sim$ 50 % where significant GS ordering is established. Populations of all four T_2 (V_{3-6}) vertices reach a similar value here (not shown). The state adopting such an averaged four-fold rotational symmetry implies that memory of the initial DPS has been lost. Narrow domain wall structures similar to that following thermal ordering [25], chapter 6, are also observed.

Increasing H_h beyond 520 Oe results in the rapid suppression of GS order. The upper limit of the critical window is accessed, and only those moments which are most strongly pinned are not periodically dragged by the field. This is evident in the increasingly polarized states observed, figure 5.3, the magnitude of **M** increasing but with an apparently random direction, which becomes increasingly dependent on the field direction at the time ramp-down occurred. From 5.3 (b), $H_{max} - H_{min} \approx 100$ Oe, which will be crossed by the applied field in $\sim$ 10 ms, within a single rotation of the sample, avoiding demagnetization effects which would occur for a slowly ramped protocol, such as the linear decreasing ramp discussed in section 2.3.1 (figure 2.8 (b), protocol 2 [14]).

5.4 Discussion

It is clear that the edge effects predicted by Budrikis et al. [21] are not found. This is not however a failiure of the model used, rather it is due to strong enhancement of chain nucleation across the whole array span giving rise to bulk effects which

are blocked by energetic constraints in an ideal system. Whether the non-Ising or non-point dipole nature of the elements are contributing factors is unclear. Non-Ising dipoles are likely to be a strong contributor to quenched disorder, whereas non-point dipoles would most likely not qualitatively alter the observed behaviour.

Further insight can be gained into the role of both disorder and finite ramping rates by incorporating these effects into simulation, which is currently being explored with collaborators [123], the authors of reference [21]. By incorporation of a finite Gaussian distribution of switching fields h_c into the same simulations discussed in section 2.3.4, the experimental results presented in this chapter can be qualitatively and semi-quantitatively reproduced, figure 5.4, capturing the same suppression of edge-effects and GS ordering by the enhancement of bulk nucleation and pinning, as well as similar vertex populations, for correctly tuned disorder strength [123].

The growth and evolution of chain structures and order have not been tracked temporaly in the study presented in this chapter. A more elaborate experimental set-up would be required to perform such an investigation. Further, it could prove interesting to correlate the orientation of dipoles and the positions of vertices for the same pattern following repeat field treatment or following treatment at different H_h, as the averaged interpretation given here does not reveal such information. Such experiments could reveal the effects of parameters such as quenched disorder strength on the repeatable access of states [77], pinning and nucleation.

5.5 Summary

In this experiment, the theoretical predictions for the behaviour of initially polarised finite sized square ice patterns under a constant magnitude rotating applied field [21] have been tested. The distinct suppression of edge effects which are predicted to lead to strong GS order can be understood by the influence of quenched disorder on the switching properties of the systems' elemental components. These effects are currently under further theoretical investigation.

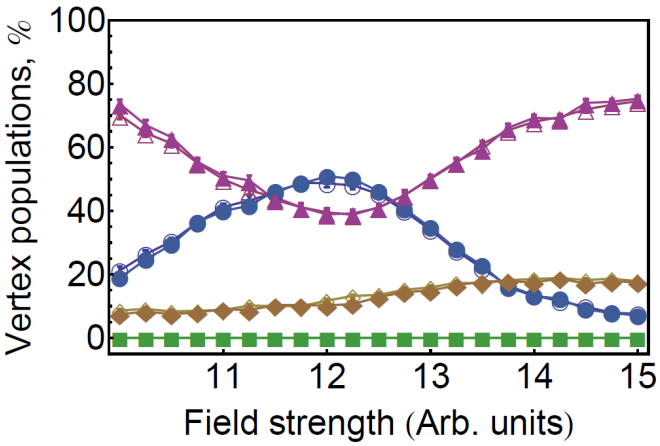

Figure 5.4: Simulated variation of final vertex populations for open and closed edge square ice patterns with the inclusion of quenched disorder. Populations of vertex types T_{1-4} are shown in blue, purple, yellow and green respectively, with open and closed symbols representing open and closed edge patterns respectively. By incorporating the correct amount of disorder via a Gaussian distribution of randomly allocated switching fields, h_c, as well as a finite field ramp-down time, very good agreement can be achieved between simulations and the experimental results of figure 5.3. Figure courtesy of Z. Budrikis and R. Stamps [123].

Chapter 6

Thermal Ordering in as-fabricated Systems

6.1 Introduction

In this chapter, the as-fabricated states of artificial square ice patterns will be addressed, imaged using MFM, section 3.4. It has been found that fabrication via a standard process of electron beam patterning of polymer resist (section 3.1) and vacuum evaporation of material (3.2), allows for a magnetic self-ordering process to occur during early stages of metallisation, when the elemental magnetic moments, coupled via dipolar interactions, are in a thermalised phase [25]. A specific case-study will be largely focussed on, as recently reported [25], where evidence for thermal ordering is found qualitatively in the microscopy, in which large GS domains spanning ~ 10 μm are observed, separated by domain walls of higher energy vertices. Further, quantitative evidence is found in the Boltzmann factor-weighted monopole/string magnetic defects [20; 22] observed on the GS background. This work presents the first experimental acquisition of any true spin ice ground state over any significant long range length scale, and contains the experimental first observation of isolated square ice "magnetic" monopole defects above this GS. More generally, it is the first example of long range thermal ordering of any such patterned nanomagnet system, resolved by microscopy.

Further, it will be shown that long range ordering can be controlled by tuning both the interaction strength between elements, and the sample underlayer/buffer

roughness. While the exact quantitative reproducibility of this anneal process has not yet been realised, due to currently unisolated fabrication-stage parameters, a high level of GS ordering can be achieved over a wide parameter range. Using a straight-forward statistical mechanical formalism, it will also be shown that the states observed are truly equilibrated. This allows for a direct comparison to be made with the effective thermodynamical description of ac demagnetisation put forward by Nisoli et al. [64], section 2.3.2, providing insight and inference into mechanisms common to both processes, as well as crucial differences.

6.1.1 Evidence for as-fabricated Order

As part of routine sample characterisation, prior to conducting any extensive experimental procedures, samples were imaged using MFM to test for single domain Ising moment behaviour and magnetic stability of elements when subjected to the magnetic probe tip. Figures 6.1 and 6.2 show example SEM images for an a = 700 nm and 500 nm lattice constant sample, respectively. The 700 nm sample was patterned using the Helios system as an array of 25 μm by 25 μm writefields, as seen in figure 6.1 (a), spaced by $\sim$ 1 μm, over a total area of $\sim$ 2 mm by 1.6 mm, with a thin film structure of Ta(3 nm)/NiFe(25 nm)/Al(3 nm) and lateral island dimensions of 280 nm by 85 nm, figure 6.1 (b,c). The 500 nm sample was patterned using the JEOL 6300 system using 0.5 mm $\times$ 0.5 mm writefields, stitched together with an accuracy of 20 nm, over a total area of 1 cm $\times$ 1 cm, with a thin film structure of Ti(3 nm)/NiFe(30 nm)/Al(2.5 nm) and island dimensions of 90 nm $\times$ 250 nm.

Samples were imaged in their as-fabricated states via AFM and MFM at several different locations over $\sim$ 12 μm $\times$ 12 μm areas distributed across the extent of the patterns. Figures 6.3 and 6.4 show representative (a) AFM and (b) MFM images of these respective samples. It should be noted that no global magnetic fields were intentionally applied to the samples discussed in this chapter prior to imaging their "as-fabricated" states. By visual inspection, the states appear demagnetised and disordered. Analysis of the MFM images as per section 3.5 gives the as-fabricated net normalised magnetisation of the a = 700 nm spaced pattern (figure 6.3) and the a = 500 nm spaced pattern (figure 6.4) to be (M_{X}

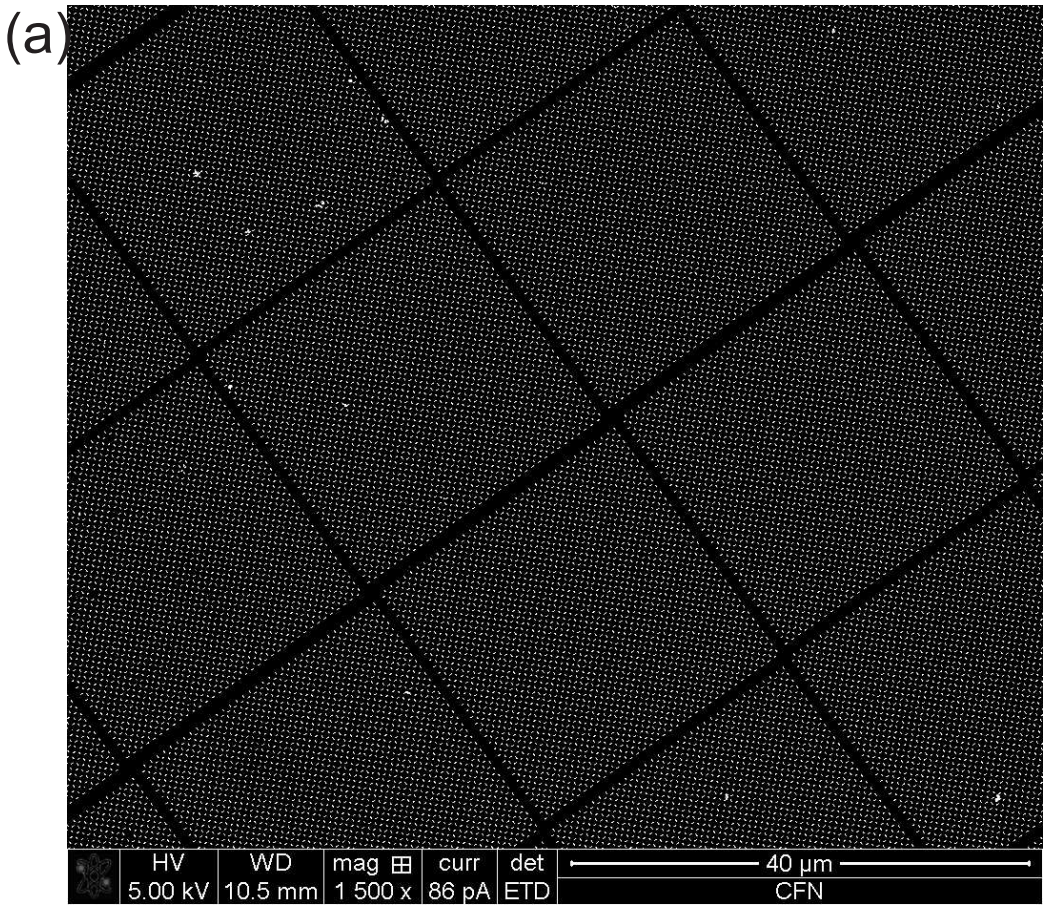

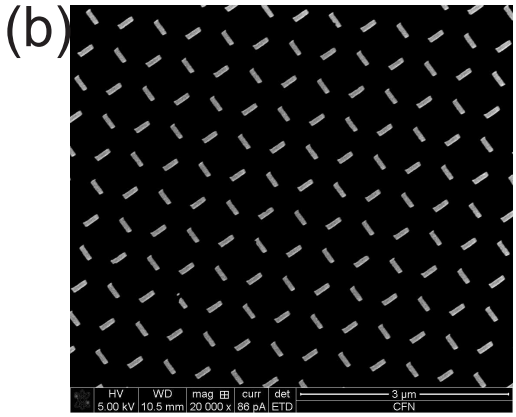

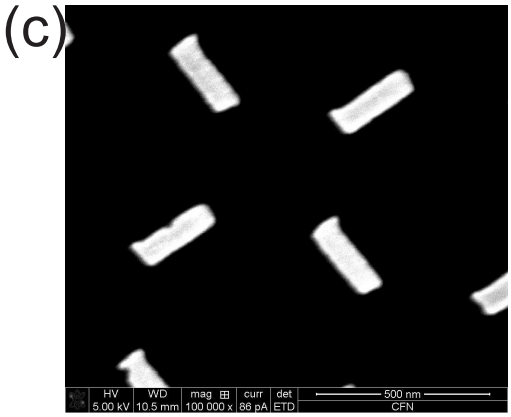

Figure 6.1: SEM of an $a = 700$ nm spaced artificial square ice patterned using the Helios system. Sample details are discussed in the main text. Images are taken at relative magnifications of (a) ×1,500, (b) ×20,000, and (c) ×100,000. (a) shows the ~ 20 μm sized square ice patterns, each spaced edge-to-edge by ~ 1 μm. (b) and (c) show the elements in higher detail, revealing presence of a recurring patterning artefact, with "boot-shaped" elements.

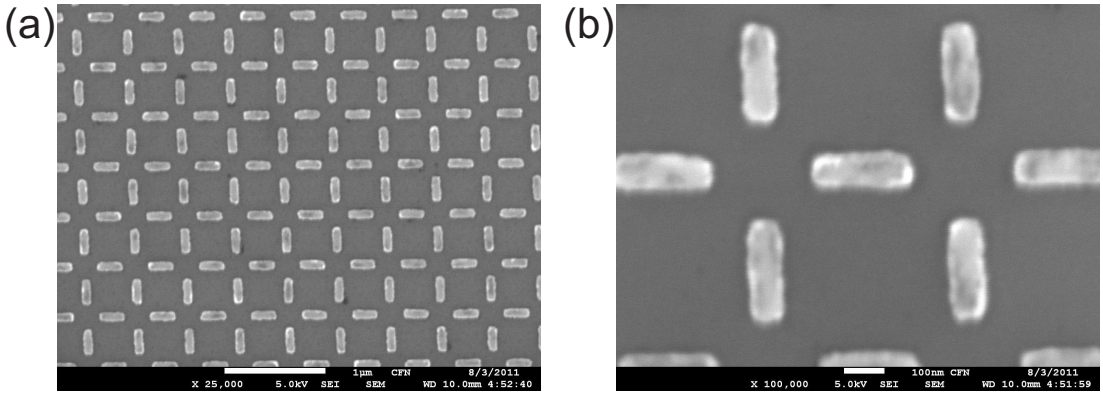

Figure 6.2: SEM of $a = 500$ nm spaced artificial square ice, patterned using the JEOL system. Sample details are discussed in the main text. Images are taken at relative magnifications of (a) ×25,000, and (b) ×100,000 are shown. Elements appear more symmetric that for the pattern shown in figure 6.1, resolving the "roughness" of the elemental edge structure.

= -0.06 ± 0.03, $M_{\mathrm{Y}} = 0.07 \pm 0.02$) and ($M_{\mathrm{X}} = 0.04 \pm 0.03$, $M_{\mathrm{Y}} = 0.01 \pm 0.06$) respectively, confirming the former point. This is not too surprising as negligible magnetic fields are expected at the sample plate during material deposition (section 3.2) and no fields are purposely applied post-deposition. While it would not be unreasonable to assume the random allocation of the Ising orientation of each element, evidence contrary to this is found in the vertex populations (in excess of the RS) and GS dipolar correlation statistics, shown in (c) and (d) respectively for both figures 6.3 and 6.4. Firstly, a surplus/deficiency of lower/higher energy $\mathrm{T}_{1,2}/\mathrm{T}_{3,4}$ vertices is seen, compared to that expected of a random state, which would lie at 0% excess in (c) for all T_{1-4}. Secondly, the as-fabricated sample states possess weak short range magnetic correlation (d), not dissimilar from that obtained by ac demagnetisation, see section 2.3.1. Over long range ($\geq$ 2 nearest neighbours) random correlation is observed with all $C^{\mathrm{GS}}(n_{\mathrm{d}}) = 0$ over all $n_{\mathrm{d}}^{\mathrm{th}}$ neighbours of type $C = L, P, D$. For both arrays, weak GS correlation is observed for $P(1)$ and $D(1)$. Interestingly, weak anticorrelation for $L(1)$ is found, implying short range alignment of moments along L-type chains of neighbours, perhaps indicative of a polarizing field effect. However, as the states are found

to have negligible net moment, this suggests that such polarised chains lie with an equal distribution of orientations along the $\pm\, x, y$-directions.

While this apparent self-ordering is weak, it is clear that the states imaged are well-defined across the span of the patterns. It was initially hypothesised that the observed ordering was a result of thermal ordering, under the influence of elemental dipolar coupling. Evidence is present that the ordering is sensitive to the lattice constant a, i.e. the island-island interaction strength, the 500 nm lattice constant sample possessing a stronger surplus/deficiency of low/high energy vertices and short range correlation. It will be shown that this is indeed the case. The two samples have, however, a number of distinct differences. They were separately patterned on different substrate with a different coating of resist using two different EBL tools with different beam parameters, and were separately metallised at different times, as well as having islands of slightly different size. It is possible that a number of these factors contribute to the intrinsic structural disorder of the patterns, affecting the elemental edge and thin film interfacial roughnesses, in turn affecting the distribution of magnetic island properties.

As a further example, figure 6.5 (a,b) show two $\sim$ 10 μm $\times$ 10 μm MFM images of two different nominally identical samples of 400 nm lattice spacing, fabricated within a few days of each other using the JEOL 6300 EBL system (section 3.1) and vacuum deposition systems. It is clear that two distinctly different states have formed. This drastic lack of quantitative reproducibility has been observed across a large number of samples, and is suggestive that there are subtle but significant difference between the patterning and/or growth processes between samples. Evidence is also present that patterning using the JEOL system produces stronger effects than the Helios (features such as the "boot-shape" of the elements of the $a = 700$ nm sample, figure 6.1, can play an influential role in the behaviour of a nanoelement [92]). Exploration of these hypotheses would require involved controlled experiments addressing the fabrication parameters. For such reasons, close attention has been maintained on as-fabricated states. Conclusive evidence for thermal ordering has been found, as recently reported [25]. The observation of a face-like configuration in figure 6.5 (b) is believed to be coincidental, however, what is striking about this image is the high uniformity of the magnetic state achieved.

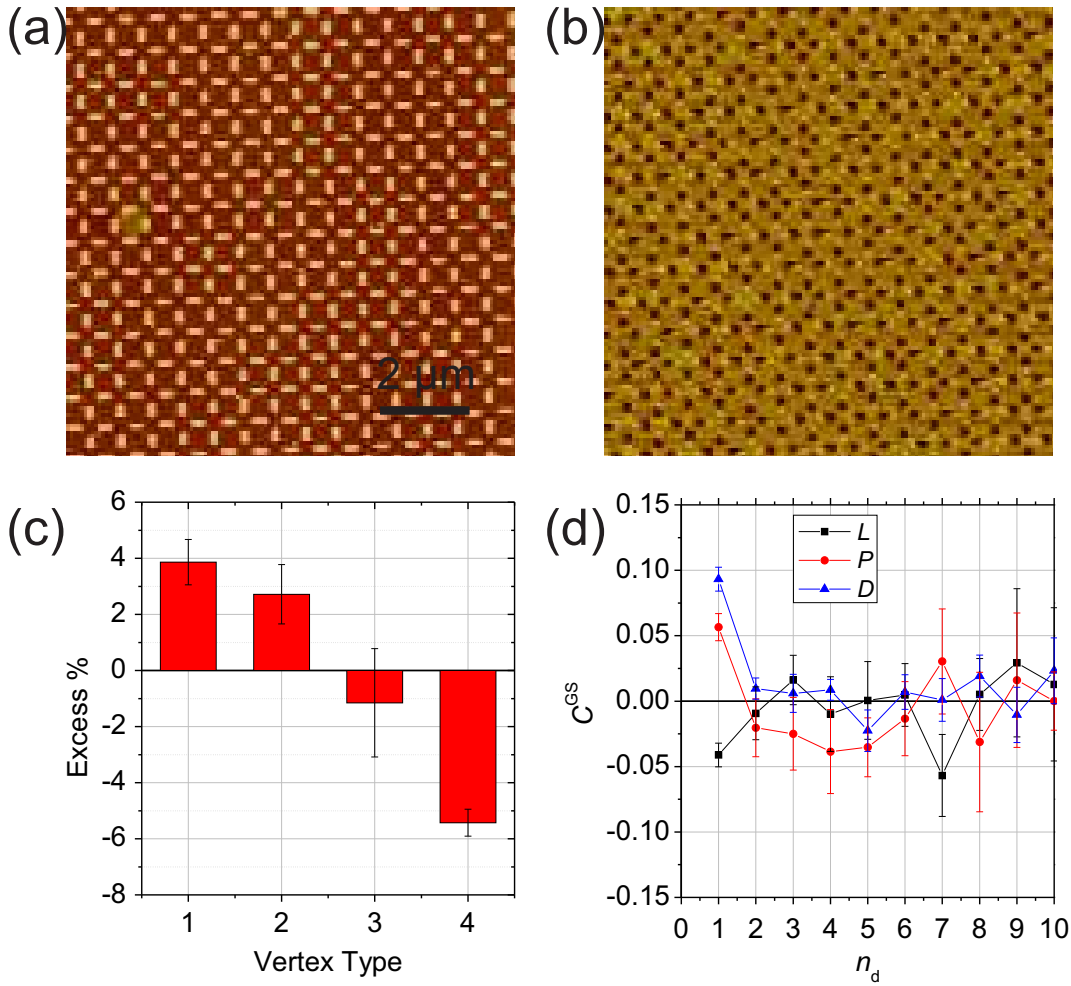

Figure 6.3: Microscopy of the as-fabricated state of an $a = 700$ nm lattice constant square ice array. (a) Atomic and (b) magnetic force miscrographs of a ~ 12 μm $\times$ 12 μm region of the as-fabricated state, as discussed in the main text. Evidence for self-ordering is found in (c) the surplus/deficit of lower/higher energy vertex populations, and (d) short range magnetic correlation for $n_{\mathrm{d}} = 1$.

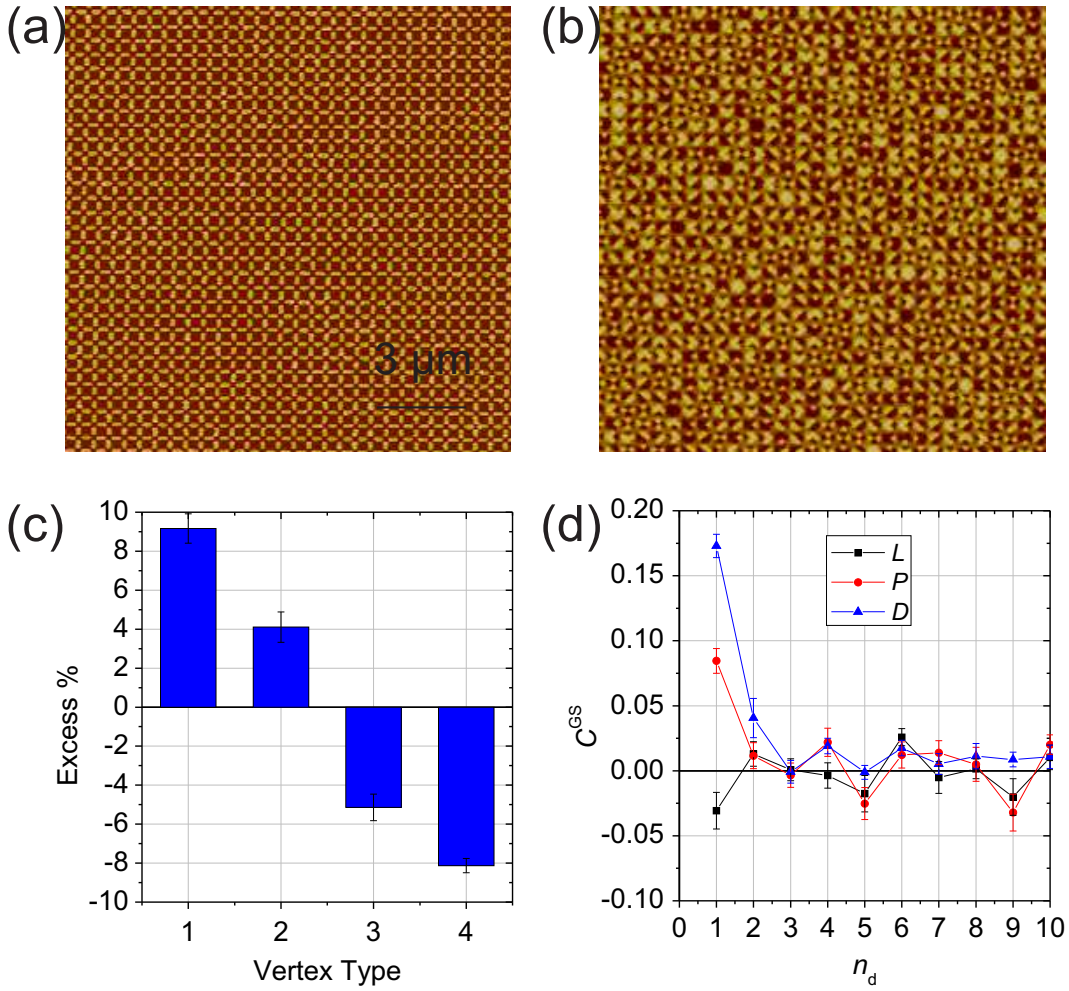

Figure 6.4: Microscopy of the as-fabricated state of an $a = 500$ nm lattice constant square ice array. (a) Atomic and (b) magnetic force miscrographs of a ~ 12 μm $\times$ 12 μm region of the as-fabricated state, as discussed in the main text. It appears that the effect of self-ordering is stronger in this pattern, in comparison with that in figure 6.3, with (c) stronger surplus/deficit of lower/higher energy vertex populations, and (d) stronger short range magnetic correlation, extending to $D(2)$.

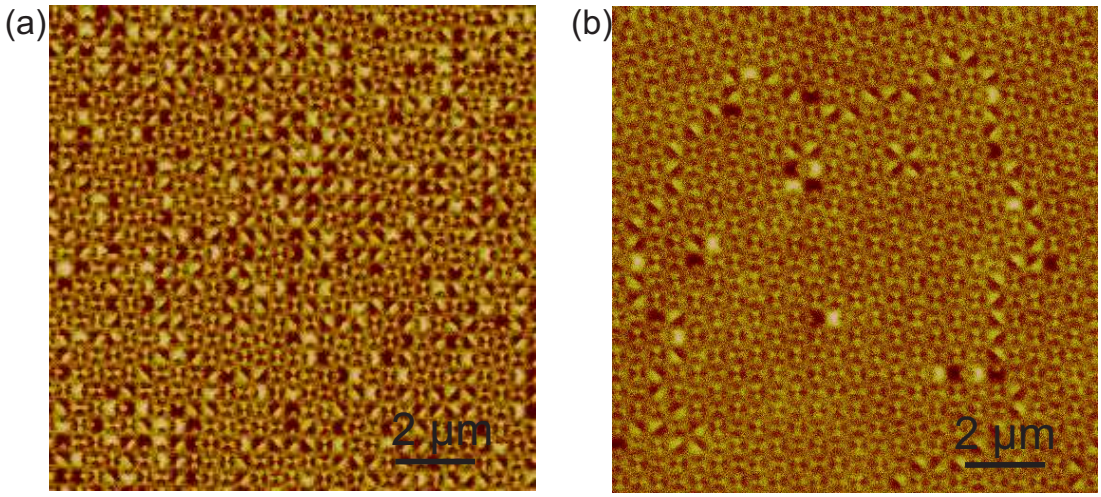

Figure 6.5: MFM images of the as-fabricated states of two nominally identical square ice patterns of $a = 400$ nm. Distinctly different as-fabricated magnetic states have been accessed, that in (a) appearing distinctly more disordered that shown in (b).

6.2 Ground State Ordering

In this section attention will focus on a case study of a single sample, specifically that imaged in figure 6.5 (b). While the lack of exact control of ordering is non-ideal, it will be assumed that the conditions and parameters during fabrication are homogeneous across single samples, the observed states being well-defined across the patterns. The statistics presented in figures 6.3 and 6.4 support this assumption. A fabrication run is in this sense "self-contained".

The pattern consisted of islands of lateral area $A = 280$ nm $\times$ 85 nm, on a lattice of pitch $a = 400$ nm, with a thin film structure of Ti(3 nm)/NiFe(26 nm)/Al(2.5 nm), shown under SEM in figure 6.6. A minimum edge-to-edge spacing of ≈ 50 nm is found. A total patterned area of 2.5 mm^2 was formed from multiple 0.5 mm^2 writefields, with a stitching error of approximately 20 nm. Nine $\sim 40 \times 40$ μm^2 areas were imaged with MFM, at locations distributed ~ 1 mm appart and far from the edges, surveying approximately $13,700$ μm^2 and approximately 165,000 magnetic elements in total. The complete data series is given in appendix A.

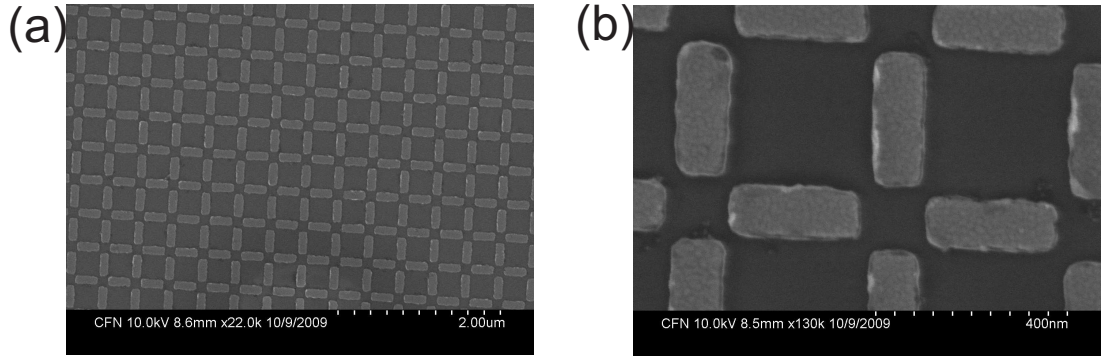

Figure 6.6: SEM images of the $a = 400$ nm lattice constant square ice pattern, as shown by MFM in figure 6.5. Images are taken at magnifications of (a) $\times$22,000, and (b) $\times$130,000. The elemental shape and edge structure is very well resolved in (b).

6.2.1 MFM Identification of Ground State Ordering

An example image from the MFM survey is shown in figure 6.7 (a), of 40 μm $\times$ 40 μm. It is clear, as for figure 6.5 (b), that a state of uniform background order has formed with distinct chain-like defects distributed across (as also shown later in figures 6.17 and 6.18). A 10 μm $\times$ 10 μm area is shown magnified inset, along with a vertex key, with key features of interest boxed and labelled, each further magnified in (b) with configurations mapped out in terms of magnetic moments and vertex types.

The first area of interest is that labelled **GS** - when mapped out, it is revealed that the state's uniform background is perfectly GS-tiled over length scales of $\sim 20a$, the chess-board of bowtie-like T_1 tiles being clearly identifiable. This is emphasised in figure 6.8, where a schematic representation of the GS in terms of dipoles and their corresponding north and south poles is partially overlayed on a similar section of MFM image, highlighting the arrangement. All 1^{st} nearest neighbours, as indicated in figure 6.8, are arranged north-to-south, all 2^{nd} and 3^{rd} nearest neighbours consequently being antialigned. The second areas of interest are **DW1** and **DW2**. Here, two regions of GS order are separated by chains of $T_{2,3}$ vertices, as indicated in figure 6.7 (b) by green arrows and blue/red circles respectively. Close inspection reveals that the two regions are of opposite sense of the two-fold degenerate GS, indicated by black and grey arrows - these two senses are inherently incompatible, hence the meeting of two regions of opposite sense must form such higher energy vertex chains. Hence, we are observing a state consisting of large incompatible T_1 GS domains of ~ 10 μm size, separated by domain walls (DWs) of higher energy $T_{2,3}$ vertices, analogous to those in an antiferromagnet, which can be seen by considering a single X or Y sublattice of the system. The image in figure 6.7 is representative of all images collected (appendix A). Interestingly, no T_4 vertices are observed across the entire survey, a point which will be returned to subsequently.

As well as DWs, the system possesses a number of smaller isolated defect objects distributed across, as contained in region **1**. When mapped out, region **1** is shown to be of GS order with a single moment flipped against it, forming two oppositely charged T_3 vertices at the expense of two T_1 vertices, analogous to

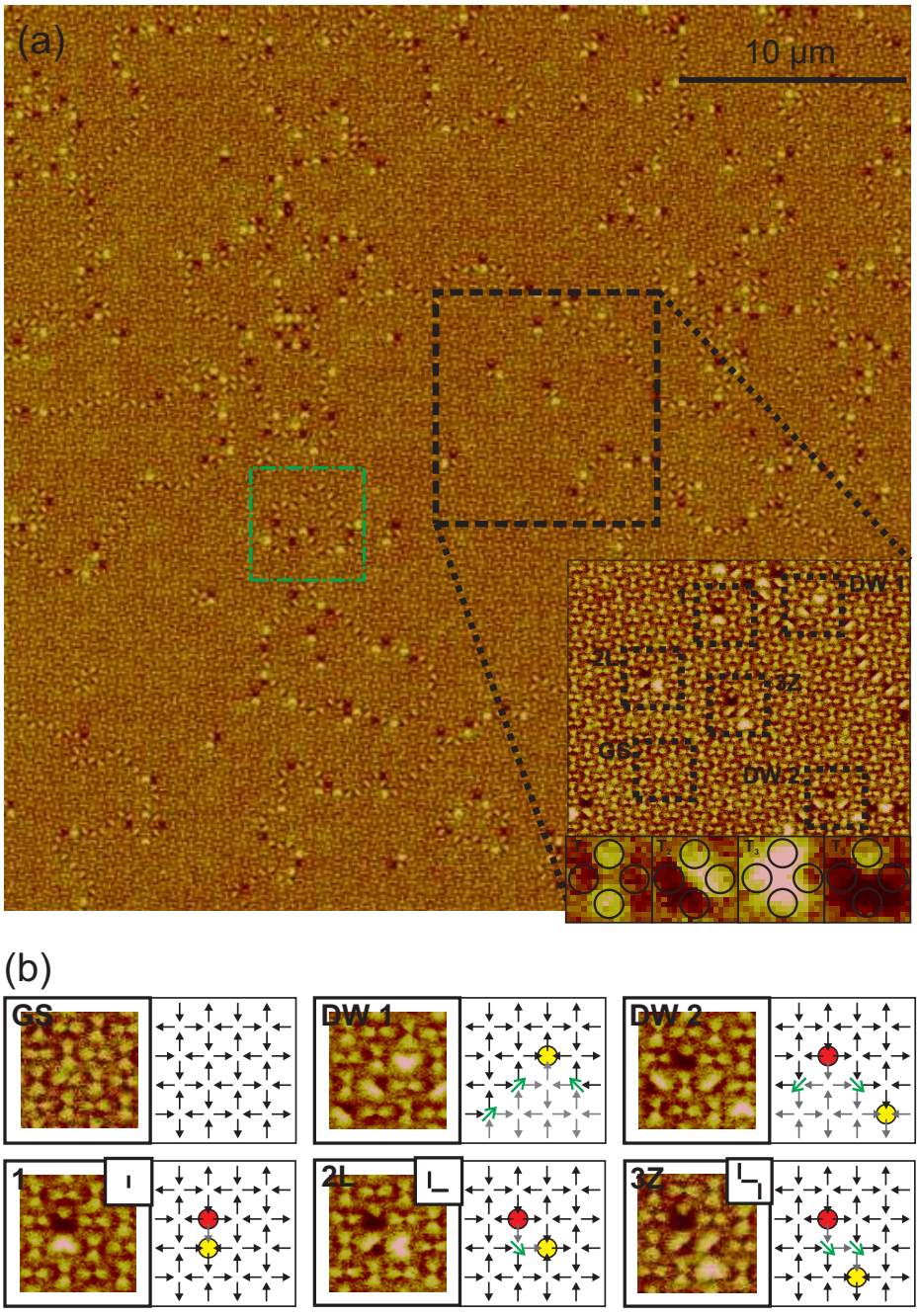

Figure 6.7: Long range square ice ground state ordering, as observed by MFM. (a) A 40 μm $\times$ 40 μm area MFM image, taken from the as-fabricated survey of the $a = 400$ nm lattice constant square ice. A state of distinctly uniform background order is observed, with distinct chain-like objects distributed ~ 10 μm apart, as well as smaller localised object. A 10 μm $\times$ 10 μm area is magnetified inset, as well as a vertex key. Mapping out the dipolar moment configuration of the selected boxed regions, (b), reveal that a state of strong GS ordering of T_1 vertices has formed, with chain structures formed from higher energy $T_{2,3}$ vertices.

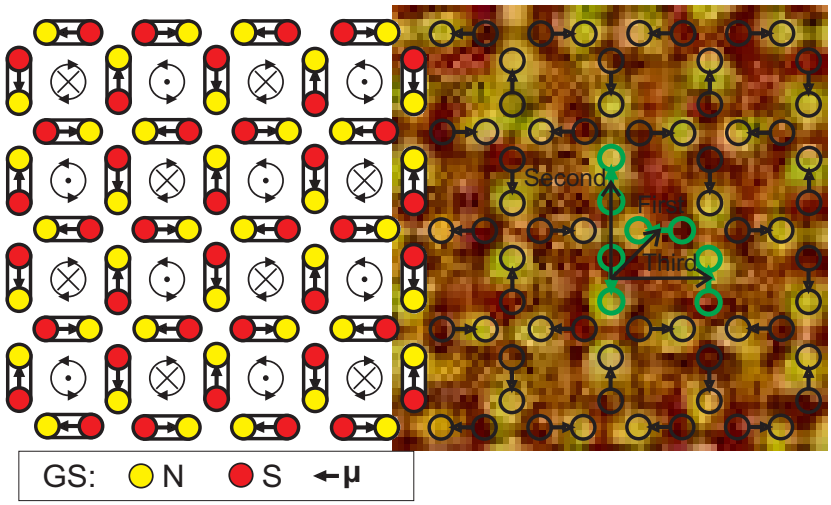

Figure 6.8: MFM of the square ice ground state. A schematic representation of the GS overlayed on a section of an MFM image, highlighting the magnetic ordering of elemental magnetic dipoles. 1st, 2nd and 3rd nearest neighbour element pairs are indicated in green.

the magnetic monopole defects in real spin ice [19]. Regions **2L** and **3Z** contain similar objects, where sequential chains of moments are flipped against the GS background, and the sequence **1**, **2L**, **3Z** represents a monopole/antimonopole pair separation process along a connecting chain of T_2 vertices. Such defect objects will be further discussed in section 6.2.3.

6.2.2 Thermal Ordering Model

This is the first reported experimental observation of long range GS ordering in a spin ice system, of both artificial square and kagome geometry, as well as in real spin ice where a true GS of periodic nature has been predicted [49]. It is also the first experimental observation of isolated square ice monopole objects on the GS background, as discussed theoretically [20; 22]. The immediate question that is however raised is - how did this highly ordered state form? It is extremely unlikely that an applied field induced this state: dc fields greater than the islands' switching fields result in long range ferromagnetic polarisation [30] (see chapter

4), while ac demagnetisation has been shown to access short range correlated states. As previously stated, thermal ordering is a promising candidate, however, the systems are athermal at ambient temperature with exceedingly large barriers to activation and are stable under imaging.

The possibility still remains for such ordering to occur via thermalisation, taking place during the early stages of material deposition. An island will form a continuous magnetic layer within $0 < d \lesssim 1$ nm of NiFe growth (for a detailed discussion of thin film nucleation and growth, see the textbook of Ohring [103]). At temperature T, its moment $\mu(d,T) = AdM(T)$, where magnetisation $M(T) \propto 1 - cT^{3/2}$ for constant c [31]. Nanoelement dynamics will occur according to a Néel-Arrhenius rate $\propto \exp(-\beta E_\mathrm{b})$ [31], where the reversal barrier energy $E_\mathrm{b} = KAd$ for shape anisotropy $K(d,T) = \mu_0 DM^2(T)/2$ (the demagnetising factor D will depend on d as it affects the element aspect ratio [124]), and $\beta = 1/k_\mathrm{B}T$, with k_B the Boltzmann constant. Dipolar interactions are then $\propto \mu(d)^2/r^3$ where r is the centre-centre separation of two islands. This slightly lowers/raises E_b for moments in energetically unfavourable/favourable configurations, biasing transitions towards lower energy states, allowing interactions to locally resolve before the moments block (freeze) at $d \sim$ a few nm. Correct tuning of interactions/barriers allows for strong GS ordering in ideal optically-trapped colloidal square ice [75], and likewise, we are aided here by short inter-island distances. As seen in simulations of superconducting vortex ice [78], section 2.3.3, finite levels of weak disorder lead to multiple GS-order nucleation centres. Compatible regions coalesce, while incompatible regions must form DWs, which become frozen-in as dynamics slow down. Slowly raising d, therefore, has an equivalent effect to a decreasing-T anneal. A finite d-dependent probability also exists for localised defects to occur within the GS domains, which have also been preserved. Combined AFM and MFM show no obvious underlying structural defects on those particular elements that support these magnetic defects, so they are presumably subtle, as illustrated in figure 6.9. (Note, it is often not possible to clearly resolve the finite gap between the 1$^\mathrm{st}$ nearest neighbour elements of a closely packed pattern, hence a number elements in these images appearing connected. SEM shows that this is not the case, figure 6.6.) Compelling evidence

that such a thermal ordering process is the correct explanation for the observed order will shortly be presented.

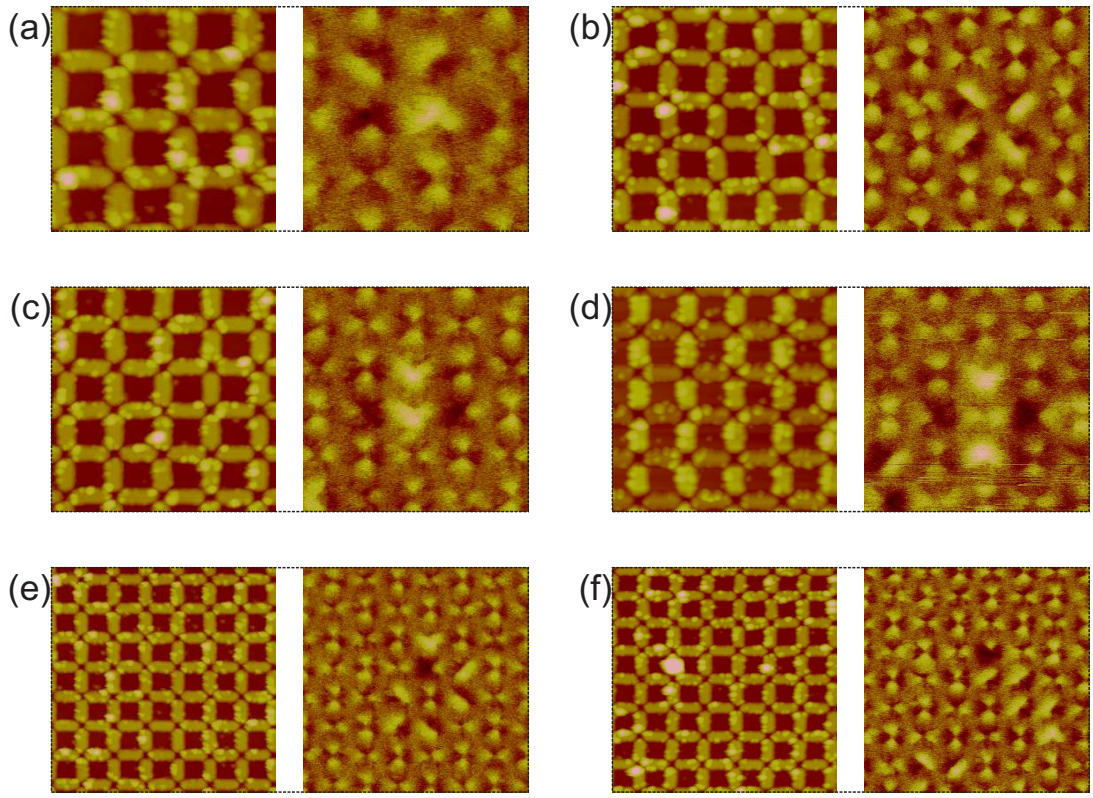

Figure 6.9: Comparison of AFM and MFM images at the locations of magnetic defects. Close-up AFM (left) and MFM (right) images of regions containg magnetic defect configurations. The MFM shows defect (a) **3U**, (b) **4O**, (c) **3T**, (d) **4+**, and (f) **5Z** (in reference to figure 6.10). Islands supporting magnetic defects possess no obvious underlying structural defects. Note the apparent height difference between the two sublattices in some images is not real and is an artefact of image processing.

Thermally ordered ground states have previously been sought in other artificial model systems. Artificial 2D Ising antiferromagnets have been previously studied, using superconducting flux vortex arrays [6; 7; 70; 71] and close-packed colloidal spheres [72; 73]. In the former, thermal annealing could not access long-range ordered states, even where an unique GS was defined, partly attributed to

patterning disorder. In the latter, "annealing" produced a compressible "glassy" phase, rather than the triangular GS. As-fabricated square ices have been studied in previous works following milling of sputter deposited films [30], not allowing thermalisation.

It would perhaps be misleading to omit a reminder of one specific feature of the fabrication process, not mentioned above. While the magnetic elements are being deposited from the base up on the substrate during evaporation, so is a magnetic thin film being deposited on the surface of the $\sim$ 100 nm thick patterned resist template, which is subsequently removed via the liftoff stage of fabrication. The behaviour of the film during growth, taking the form of an "anti artificial square ice", is currently unknown, as are its interactions with the square ice system. In the following analysis, no evidence is found that this unwanted film has any influence on the system, suggesting that it is either too far away to have an effect, or that it forms a magnetisation distribution which minimises stray field. NiFe is a soft magnetic material, naturally forming large magnetic domains, hence minimising the presence of domain walls and associated stray fields which often emerge from thin film material surfaces. Under a point dipole approximation, at a point 100 nm away along a direction perpendicular to its vector moment, a Permalloy element of $\sim$ 1 nm thickness and magnetisation $M = 860 \times 10^3$ Am^{-1} [125] will generate a dipolar field of magnitude $H_\mathrm{d} \approx 1600$ Am^{-1} $\cong$ 20 Oe, in a direction antiparallel to the vector moment (equation 1.1).

6.2.3 Magnetic Defects and Excitations

Imaging an athermal system of islands with large d provides no information about the dynamics of ordering or defect formation, allowing only for the end results to be observed. Despite this, examination of the frozen configurations provides strong evidence for the occurrence of thermally mediated ordering at low d, supporting the thermal ordering hypothesis outlined previously, as well as insight into likely growth and propagation pathways of defects.

Qualitative classification of localised defects provides a useful starting point. As introduced in figure 6.7 (b), localised defects may be represented by reversed moment maps (insets) indicating the sequence of moments that must be flipped

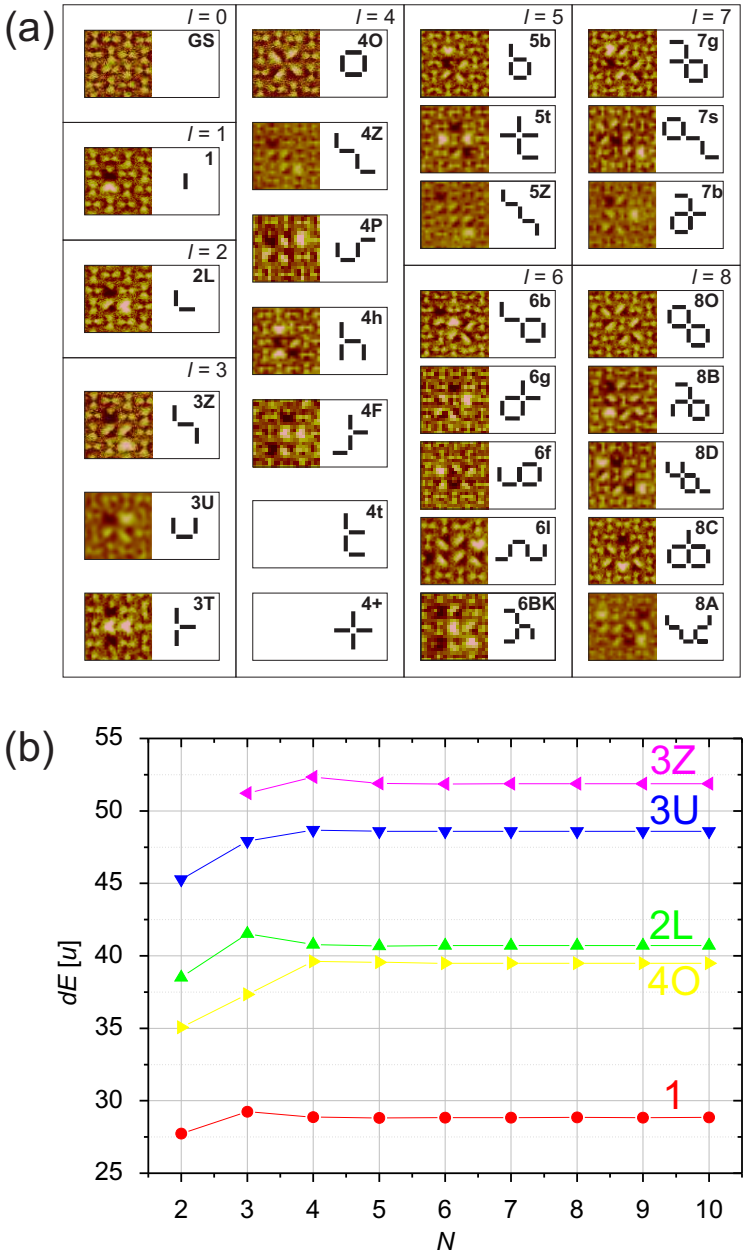

Figure 6.10: Magnetic defects observed on the square ice ground state. (a) Examples of magnetic defect structures, shown as regions of MFM and moment flip maps. l defines the number of moments flipped against the background in a defect, which is used to label an excitation, along with a letter representative of shape. (b) The excitation energy, $dE(N)$, of an array of $N \times N$ vertices, with various defect confiurations positioned at the centre. $dE(N)$ converge close to a "bulk" limit by $N \sim 4$, given defects well-defined excitations energies. Note: energy is calculated in normalised energy units u, as defined in the text.

against the GS to form a given defect configuration; translation, rotation, reflection or inversion of a map produces an energetically equivalent defect on the GS by symmetry. Localised defects may be assigned a number, l, equal to their number of moments reversed against the GS, and a mnemonic character in reference to their shape. A representative selection of defects with corresponding flip maps is shown in figure 6.10. Many of these configurations are observed multiple times in the MFM survey, particularly those with low l. Visual inspection suggests that all defects may be considered as formed from sequentially flipped chains of 1$^{\text{st}}$ nearest neighbour moments. No defects possess sequential 2$^{\text{nd}}$ nearest neighbour flips, unless they share a common flipped 1$^{\text{st}}$ nearest neighbour. This is equivalent to the observation that no T_4 vertices occur, as illustrated in figure 6.11 - sequential reversal of a 2$^{\text{nd}}$ nearest neighbour pair transforms three T_1 vertices into two T_3 vertices and a single T_4 vertex. Typically, these isolated defects are spaced by at least several vertices. A small fraction of configurations are observed where sequential $\sim$ 3$^{\text{rd}}$ nearest neighbour reversals occur, unconnected by 1$^{\text{st}}$ nearest neighbour reversals, figure 6.12. Qualitatively, they appear as two separate chains of sequential 1$^{\text{st}}$ nearest neighbour flips, as shown in their respective flip-maps.

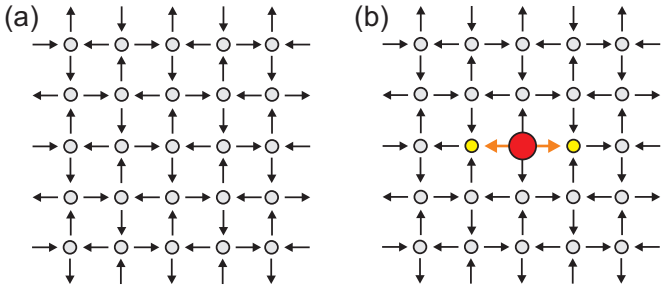

Figure 6.11: The simplest configuration that could form a T_4 vertex on the square ice ground state. Two sequentially flipped 2$^{\text{nd}}$ nearest neighbour moments removes three T_1 vertices from the ground state (a), and forms (b) two like-charged T_3 vertices and one central oppositely charged T_4 vertex. T_4 configurations are strictly not observed in the MFM survey.

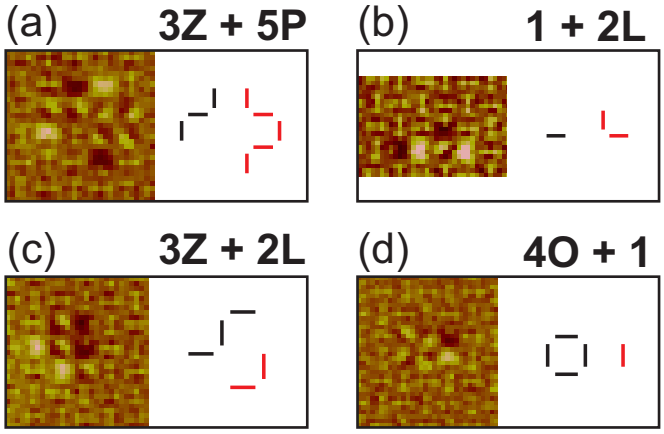

Figure 6.12: MFM of composite excitations. Magnetic configurations found in the MFM survey which can be interpreted as two closely positioned, weakly interacting, excitations, e.g. (c) defecct (**3Z + 2L**) being comprised of a **3Z** and a **2L**, which are two chain defects, represented with black and red flip maps respectively, unjoined by a 1st nearest neighbour link.

Defect Energetics

It is desirable to treat moment configurations and magnetic defects energetically, in order to gain better understanding of their nature, and from the point of view of their reliable manipulation. As presented, isolated defects can, at least qualitatively, be treated as topologically well-defined entities, formed from only 1st nearest neighbour flip chains. Any flipped moments separated by more than a 1st nearest neighbour can be considered as part of two separate defect objects. Simple dipolar energy calculations, section 3.5.3, provide powerful further instruction. Summing the interaction energies over an $N \times N$ array of vertices of point dipoles [20; 22; 57; 74], the excitation energy dE above a GS background for a given configuration may be calculated in units of $u = \mu_0\mu^2/4\pi a^3$, as outlined in section 3.5.3. Positioning individual defect configurations at the centre of a GS-ordered array, $dE(N)$ converges acceptably closely to the large array limit by $N \gtrsim 4$, figure 6.10 (b). This indicates that defects need to be at least ~ 2 vertices away from an edge to no longer "see" it. All shapes therefore have well-defined bulk dE (given for all excitations in figure 6.10 (a) in appendix A), i.e. they are

elementary excitations of the square ice system. Further, dE tends to increase with l, however, the necessity to consider defects as chains of at minimum 1st nearest neighbours is illustrated, dE not being simply proportional to l. Calculations show that excitations must be only 2-3 vertices away from other defects (excitations, DWs, edges) to be non-interacting. Table 6.1 shows the values of dE for the configurations shown in figure 6.12, as well as those for the two individual subshapes they comprise and the linear sum of these two values. Two excitations separated by a third nearest neighbours distance, figure 6.12 (a) (**3Z + 5P**) and (d) (**4O + 1**), couple to lower their combined energy by $\sim 1\%$. Such configurations could be considered as a composite excitation, however, the frequency of such occurrences and excitation density are sufficiently low to neglect this in further analysis. Most excitations observed are therefore largely unaffected by lying within a finite domain, coupling producing only a small perturbation to this approximation.

Table 6.1: Dipolar excitation energy of composite excitations shown in figure 6.12. Shown are the composite excitation names (**A + B**), the bulk values for the two component excitations' energies, $dE(\mathbf{A})$ and $dE(\mathbf{B})$ respectively, their linear sum $dE(\mathbf{A}) + dE(\mathbf{B})$, the composite excitation energy $dE(\mathbf{A} + \mathbf{B})$, and the % energy shift caused by their interaction.

A + B	$dE(\mathbf{A})$	$dE(\mathbf{B})$	$dE(\mathbf{A}) + dE(\mathbf{B})$	$dE(\mathbf{A} + \mathbf{B})$	% shift
(a) **3Z + 5P**	51.88	71.74	123.63	119.20	-3.71
(b) **1 + 2L**	28.84	40.72	69.56	69.47	-0.13
(c) **3Z + 2L**	40.71	51.88	92.60	94.42	1.93
(d) **4O + 1**	39.49	28.84	68.34	66.66	-2.52

Figure 6.13 (a) shows calculated values of dE for a 15 $\times$ 15 vertex array of point dipoles on which a type-**1** excitation is centred at position $x = 8$ as shown in (b,c). A second type-**1** is then incrementally propagated across the centre of the array. The dotted line shows the energy $2dE(\mathbf{1})$. Two orientations of the excitations are considered, as shown. In both cases, the combined energy of the two excitations is only modified from the linear combination when the moving defect is positions at the edge-most site, $x = 1$, or within 2 vertices of

$x = 8$ where the stationary excitation is held (the value of $dE = 0$ at $x = 8$ is a result of positioning two identical excitations at the same location i.e. flipping an island which is already flipped against the GS). This further illustrates that these excited configurations interact only weakly and at short range with other defects, excitations and edge structures.

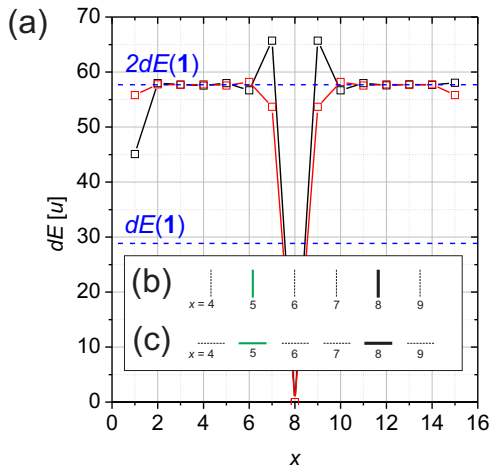

Figure 6.13: Excitation energy proximity test calculations. (a) The dipolar excitation energy of a $N = 15$ square ice on which a defect **1** is held at the centre, while a second **1**-defect is incrementally moved across the same central row of moments, at position x, calculated for two orientations of defects, as illustrated in (b) and (c). The red series in (a) corresponds to the process illustrated in (b), whereas the black series corresponds to that shown in (c). Also shown in (a) is the bulk-limit value of $dE(\mathbf{1})$ and $2dE(\mathbf{1})$ (blue dashed lines). Deviation from a simple linear sum only occurs when the propagating defect is positioned close to the stationary defect, or close to the system edges.

Over the MFM survey, the relative abundances of the different excitations have been counted, ~ 500 in total. As shown in figure 6.14(a), the observed frequencies decrease exponentially with dE, as would be expected for thermal excitations. This distribution may hence be described as being given by Boltzmann factors $\sim \exp(-\beta dE)$. The line of best fit (red dashed line) returns a value of $k_{\mathrm{B}}T =$

$1/\beta = 10.0 \pm 0.5$ in units of u. It can therefore be written that $k_{\mathrm{B}}T = 10\frac{\mu_0}{4\pi}\frac{(MAd)^2}{a^3}$. Estimating sample temperature to be $T \approx 350$ K during growth, and $M \approx 860 \times 10^3$ Am^{-1} for Permalloy, this gives a value of $d \approx 0.9$ nm, an estimate for the island thickness at which the thermal ordering occured, comparable with the thickness at which the magnetic layer will become continuous. (Note, the inverse argument could have been made by initially estimating $d \sim 1$ nm to be the thickness at which ordering occured which returns a realistic value of T.) This is compelling evidence that these excitations are thermally activated, and that thermal ordering can take place during the early-growth stages of sample fabrication.

Internal Structure and Growth of Excitations

Whilst the overall trend is for dE to increase with l, exceptions may be found, e.g. **2L** and **4O** both have $dE \approx 40u$, figure 6.10 (b) and 6.14 (a). It is instructive, therefore, to further classify a given excitation in terms of s and p, the number of T_2 vertices and number of oppositely charged T_3 vertex pairs respectively. Grouping excitations by p, dE is found to be quite linear in s, figure 6.14 (b), with each group having $F = d(dE)/ds \approx 10u$ per element, and separated by $\Delta E \approx 30u$. Hence it can be written that $dE \approx sF + p\Delta E$ for any given excitation. F is a "force" acting to unflip a chain of moments, and ΔE is a pole-pair creation cost. Close agreement is found with the calculations of Mól et al. for straight-line monopole separation processes [22], for which a value of $dE \approx 29u$ is found for an excitation configuration equivalent to excitation **1** which possesses two oppositely charged T_3 vertices only (see figure 6.10 and table A.1). Small deviations from this approximation are attributable to topological differences between excitations with the same s and p values e.g. **3U** and **3Z**. As interactions are negligible beyond $\sim 3a$, these perturbations can be attributed to an excitation self-interaction, which may include in part a magnetic Coulomb interaction. As $\Delta E \approx 3F$, excitations form a well-defined band structure, figure 6.14, due to numerous combinations of s and p producing approximately the same dE, at spacings of $\sim 10u$. Possible excitations that were not observed in the nine MFM survey images have not been included in figure 6.14, e.g. **4+** and **4t**, despite also fitting into this band picture.

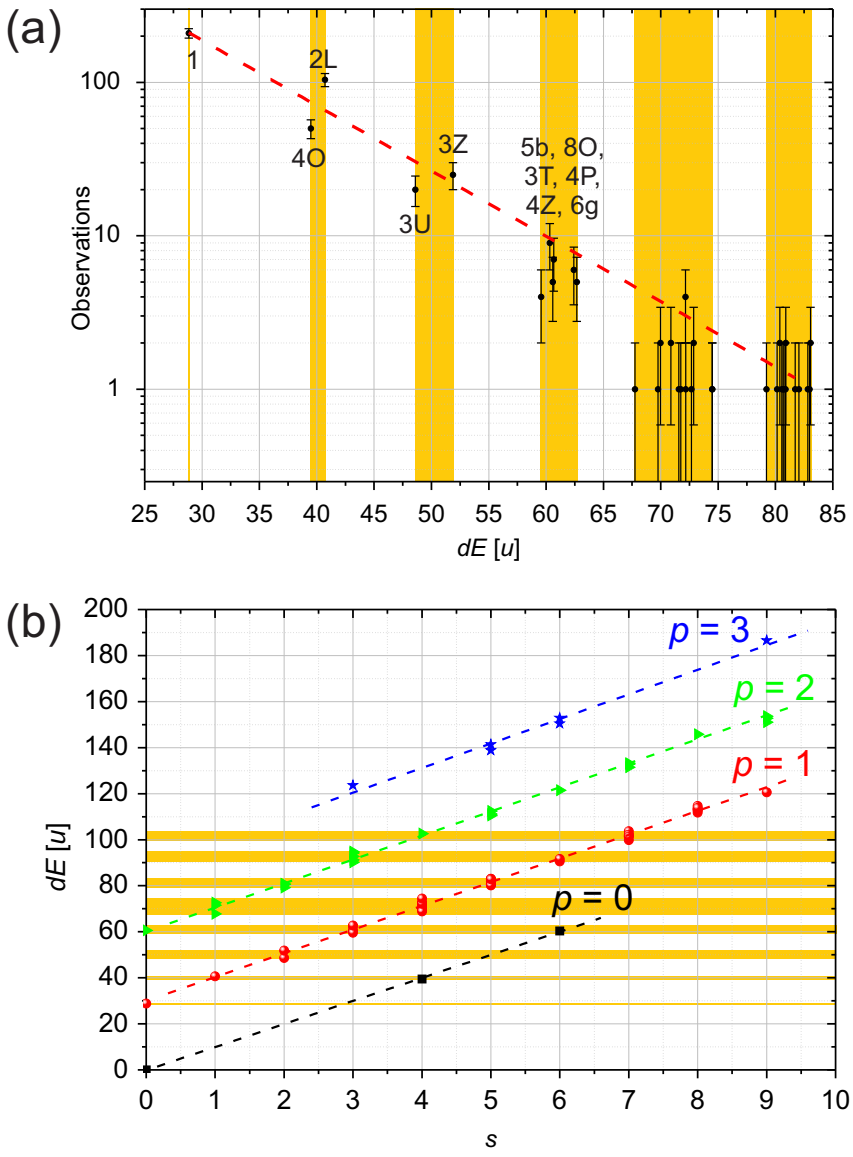

Figure 6.14: Statistics and dipolar energy band structure of square ice ground state excitations. (a) The number of observation of excitations of energy $dE < 80u$ as a function dE. Excitations fall into distinct energy bands, as indicated by the yellow stripes, and those of the lowest four bands are labelled in increasing energetic order. The trend with dE takes the form of an exponential decay $\sim \exp(-\beta dE)$, as expected for thermal excitations. (b) dE against the number of T_2 vertices s for all observed excitations of $dE < 200u$. Grouping the excitations by their number of T_3 poles pairs, p, as indicated by colour, shows that dE cluster closely to $\sim$ equally-spaced linear trends in s, all of similar gradient, as indicated by the dashed best fit lines.

Note, **4+** has once been observed in this sample during subsequent independent microscopy studies, figure 6.9.

As a function of l, excitations can explore the band structure by various processes, assuming 1^{st} nearest neighbour flips only. Starting from a GS background ($s, p = 0$), an initial flip nucleates a pair of oppositely charged T_3 vertices ($\Delta p = +1$), excitation **1**, costing ΔE. T_2-string extension ($\Delta l, \Delta s = +1$, $\Delta p = 0$), e.g. GS $\rightarrow$ **1** $\rightarrow$ **2L** $\rightarrow$ **3Z** (figure 6.7(b)), adds links to the end of a flip-chain at a T_3 site, costing $dE \approx 10u$ per link. T_2-branching adds a flip to the middle of a chain at a T_2 site, e.g. **2L** $\rightarrow$ **3T**. Here, $\Delta p = +1$ and $\Delta s = -1$, allowing an excitation to jump up a group, with net cost $\approx 20u$. For T_3-branching, for instance **3T** $\rightarrow$ **4+**, $\Delta s, \Delta p = 0$. Generally, monopoles form wherever the ice rules are broken. Annihilation occurs where two existing, oppositely charged T_3 poles meet, (e.g. **3U** $\rightarrow$ **4O**). Here $\Delta l = +1$, $\Delta s = +2$ and $\Delta p = -1$, saving $\approx 10u$. The number of possible shapes rapidly becomes very large for increasing l.

Interestingly, despite individual excitation statistics becoming poor beyond $l = 4$, a preference to form closed configurations, rather than long open strings, is observed. This is clear evidence of attractive monopole-antimonopole interactions acting to minimise excess charge during thermally driven island-flip dynamics. **4O** is an isolated string loop with no T_3 sites (reminiscent of a "loop move" in pyrochlore systems [49]), and is observed as a sub-shape of larger excitations, e.g. **5b**, **6g**, **7g**. Excitation **8O** ($p = 0$, $s = 6$) is formed from two corner-linked **4O** shapes, sharing a single central T_1 vertex, the smallest possible antiferromagnetic domain. Much larger excitations are also observed, with multiple central T_1 vertices equivalent to the background, e.g. that boxed in green in figure 6.7 (a), fitting the criteria of being isolated defect objects on the GS background. Their energies also follow the above approximation, and dE is localised at their walls. Excitations spanning $\gtrsim 3a$ are no longer self-interacting across their whole span, hence only local energetics govern propagation, locally indistinguishable from large-scale DWs. DWs will be given further attention subsequently.

Curiously, specific excitations (e.g. **4+** ($p = 2$, $s = 1$), and $p = 3$ shapes with $s < 4$) are absent, despite a significant probability of occurrence, based purely on dE, e.g. the T_4 configuration shown in figure 6.11 has $dE = 65.7$ (3 sig. fig.).

Note this corresponds to the configuration formed at $x = 7$ or 9 in figure 6.13. As these unobserved excitations are typically small in extent, this may be explained by the short-range attractive "monopole-antimonopole" interactions, acting to annihilated opposite charges and "close-off" excitations. Two like poles occupying the same site (a T_4 vertex) is either strictly avoided, or else such vertices exist only very briefly, quickly propagating to more favourable configurations. It is possible for such a configuration to not form a local potential minimum, depending on the potential barrier height of the elements in the dipolar field of their neighbours. The combination of attractive annihilation and repulsive separation appears to act to maintain an average monopole density along excitation and domain walls of $p/(s+p) \approx 0.3$.

Domain Walls

While the observed profiles of domain walls are generally "rough", possessing a rich variety of structures, specific types of domain wall configurations can be seen, examples of which are shown in figure 6.15 via MFM, accompanied by dipole/vertex maps.

Three domain wall types have been shown, $W_{1,2,3}$. W_1 separates two opposite-sense GS domains via a chain of a single T_2 vertices, in this case V_3, diagonally orientated with respect to the principal square axes of the system. W_2 is also comprised of T_2 vertices, however, follows a horizontal or vertical path, comprising alternating $V_{3,6}$ tiles. The large scale domain structures that are observed in e.g. figure 6.7 are made up of distinct sections of $W_{1,2}$ type configurations, which can link together continuously, or link via T_3 vertices, allowing for the T_2 orientations of the $W_{1,2}$ sections to change. A simple domain wall comprising only T_3 vertices, W_3, is also considered, comprising alternating $V_{10,12}$ vertices along a principal square lattice direction. Performing similar calculations to those presented for isolated excitations, positioning each $W_{1,2,3}$ across the centres of finite $N \times N$ square ice patterns creating two opposite-sense GS domains, the net dipolar energy can be studied as a function of N, as shown in figure 6.16. Here, the number of vertices in the domain wall defect is N. (a) presents dE, the energy of the state above the pure GS. All dE appear to grow linearly with N for $N \gtrsim 2$

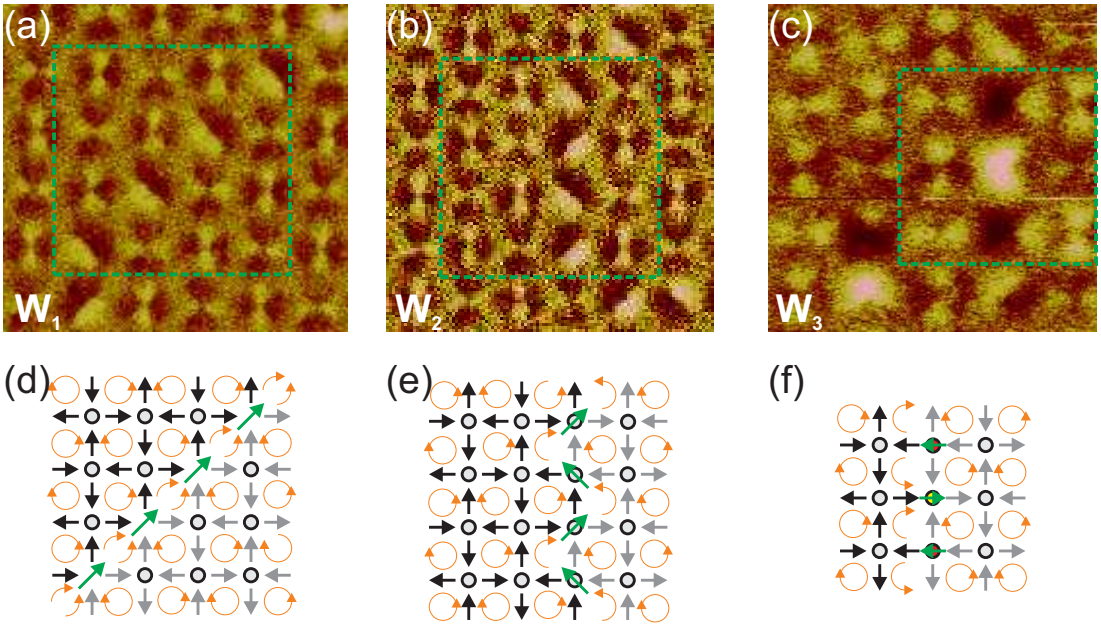

Figure 6.15: MFM of domain walls configurations. (a-c) show respectively MFM image of three GS domain wall types, $W_{1,2,3}$. (d-f) show corresponding schematics, with elemental dipoles represented by black and grey arrows, indicating those compatible with the two GS senses respectively. $T_{1,2,3}$ vertices are represented by grey circles, grey circles with green arrows and red/yellow circles with green arrows respectively. Orange circular arrows indicate the chirality of the dipolar closure loops of the GS, with broken loops indicated by broken arrows.

indicating that a bulk-like state is quickly achieved. $W_{1,2}$ also posses very similar trends to each other. This motivates the calculation of dE/N, the energy per domain wall vertex, shown in (b). For both $W_{1,2}$, there is a bulk energy cost of $\sim 10u$ per T_2 vertex, whereas for W_3 there is a cost of $\sim 14u$ per T_3. Here we see that the domain wall energies follow the same rules as isolated excitations, where their total energy may be estimated by simply counting the number of $T_{2,3}$ vertices. dE is again shown to be locally confined to the DWs. The slightly lower energy of W_2 when compared to W_1 can be understood as it breaks less GS flux closure loops, or, alternatively, it has a lower net moment and lower net self-interaction.

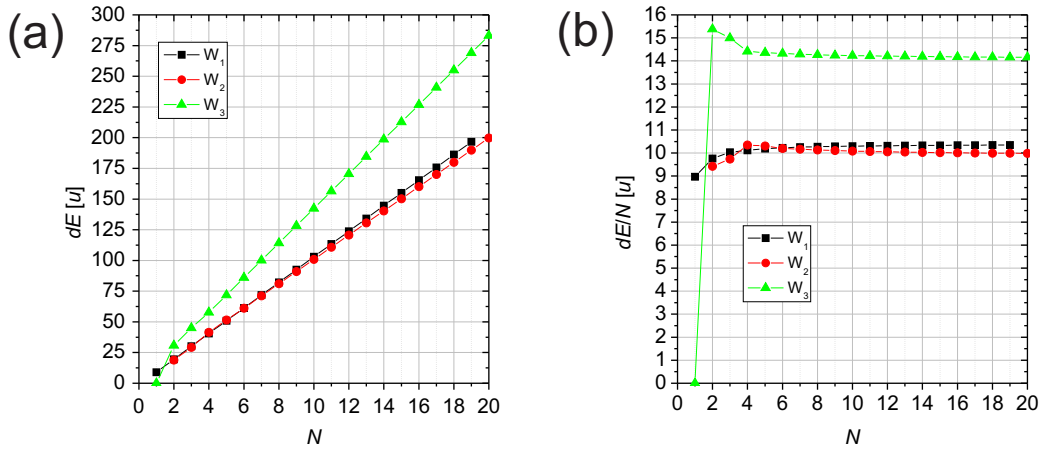

Figure 6.16: Domain wall energetics. (a) The dipolar excitation energy $dE(N)$ and (b) $dE(N)/N$ of a $N \times N$ vertex square ice pattern, with domain wall types $W_{1,2,3}$ positioned across the centre.

Edges

As a final consideration of defects, figure 6.17 shows AFM (left) and MFM (right) images of two edge regions of the square ice pattern discussed, (a) and (b). No obvious evidence is observed for any distinct edge effects. The lowest energy configurations at the edge type shown are completely compatible and identical

to the bulk GS. As per the calculations presented, the edges will have little effect on the bulk of the sytem, only local interactions being important in such a demagnetised and GS-ordered state.

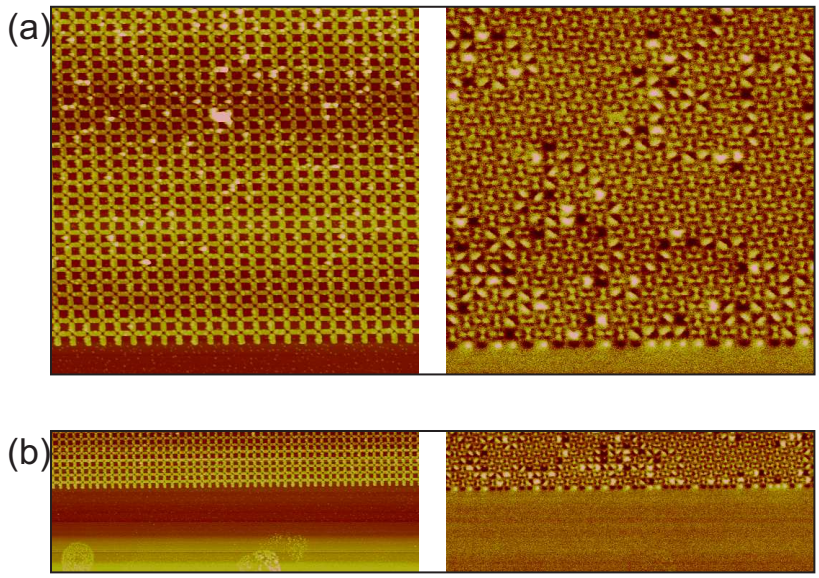

Figure 6.17: Microscopy of edge regions of the surveyed as-fabricated square ice pattern. (a) and (b) both show AFM (left) and MFM (right) images. Magnetic ordering is not obviously modified relative to the bulk.

6.2.4 Square Ice Statistics

Some analysis of the MFM survey data series has been made in terms of vertex population and dipolar correlation statistics, section 3.5. Due to the large scans required to capture a sufficient area of sample, and the subsequent low resolution of data, this was an extremely time consuming processes and it was not deemed a priority to explore this extensively for the time being. For completeness, a representative example will be briefly discussed.

Figure 6.18 shows a 30 μm $\times$ 30 μm MFM image from the survey, again showing large GS domains, domain walls and a variety isolated defects. (b) shows the corresponding absolute percentage populations of vertices, with that expected in the RS shown as dotted lines. An extremely large T_1 population of $\sim$ 85% is

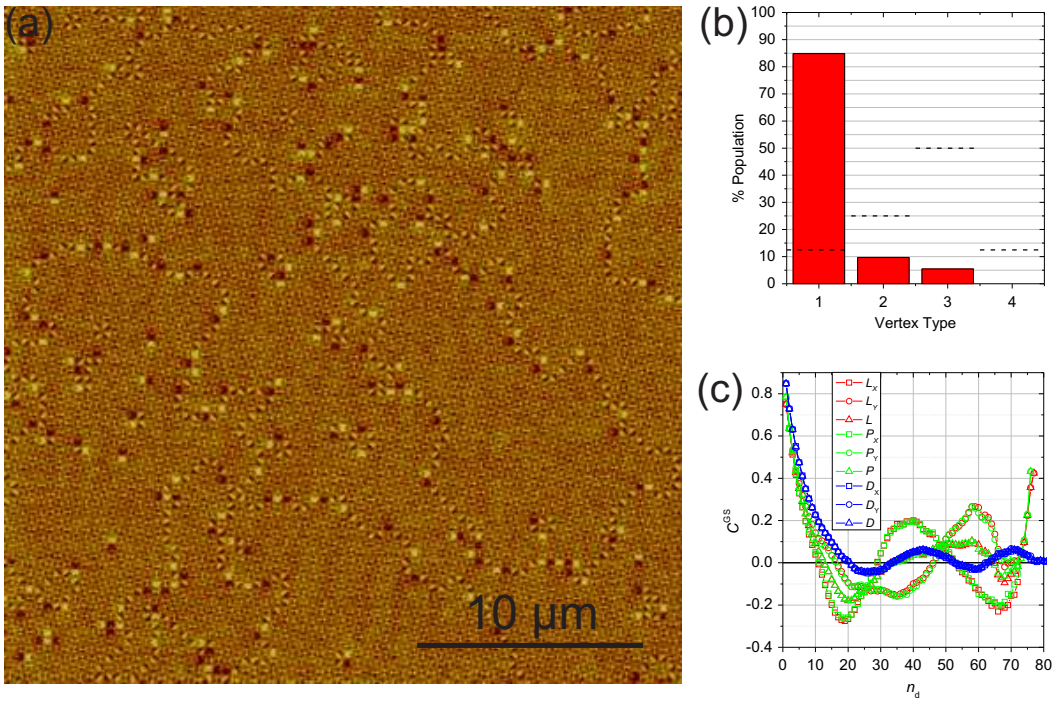

Figure 6.18: An example of statistical analysis of a large area MFM image from the as-fabricated sample survey. (a) A 30 μm $\times$ 30 μm area MFM image of a region of the strongly GS-ordered square ice pattern, with corresponding (b) vertex populations and (c) $C^{\mathrm{GS}}_{\mathrm{X,Y}}$ correlation statistics, as discussed in the main text.

found, accompanied by a low $T_{2,3}$ populations of 10% and 5% respectively, and 0 populations of T_4 vertices. In (c) the $C^{GS}_{X,Y}$ GS correlation values are shown as a function of n^{th}_d dipolar neighbour. The strong long range GS correlation is clear, with all $C^{GS}_{X,Y}(1) \sim 0.8$, and decreasing towards 0 over a length scale of $n_d \sim 10$. The domain structures are reflected in the subsequent oscillatory behaviour of $C^{GS}_{X,Y}$ about 0 for increasing n_d, which appear to slowly die off. As the images collected are roughly four domains across, and the states are highly correlated, long range values become increasingly sensitive to artefacts of the finite image size. Further, the "limited" area sampled is possibly responsible for the X and Y sublattice statistics not matching, as opposed to an anisotropy in the system. L and P are nearly identical with n_d, which is imposed by GS ordering.

This gives a rough estimate of ≈ 25 vertices as the average distance required to travel from a given position in one domain to reach a domain of opposite GS sense i.e. the average domain size. Very approximately, the correlation values behave as damped sinusoidal functions, and therefore will possibly give an estimate of domain size and a domain "roughness" from the oscillation period and damping coefficient respectively. To minimise the effects of finite-size artefacts, average statistics over a number of images would need to be calculated, before reliable fitting of such parameters could be conducted.

6.3 Control of Ground State Ordering

The current inability to quantitatively reproduce the ordering of the aquired as-fabricated states poses a limitation on systematically exploring this process. For example, studying the states as a function of lattice constant a and interaction strength, as previously explored in ac demagnetisation experiments [3; 14; 15; 16; 17], is problematic if each fabrication run possesses different unisolated parameters. Extensive characterisation of the patterning and deposition processes would be needed to ascertain the exact source of the problem. Variation in the strength of pattern quenched disorder is a possible contributor to this problem.

With this in mind, to explore the physical thermalisation process of interest, a means to bypass this constraint was devised, based on the assumption that

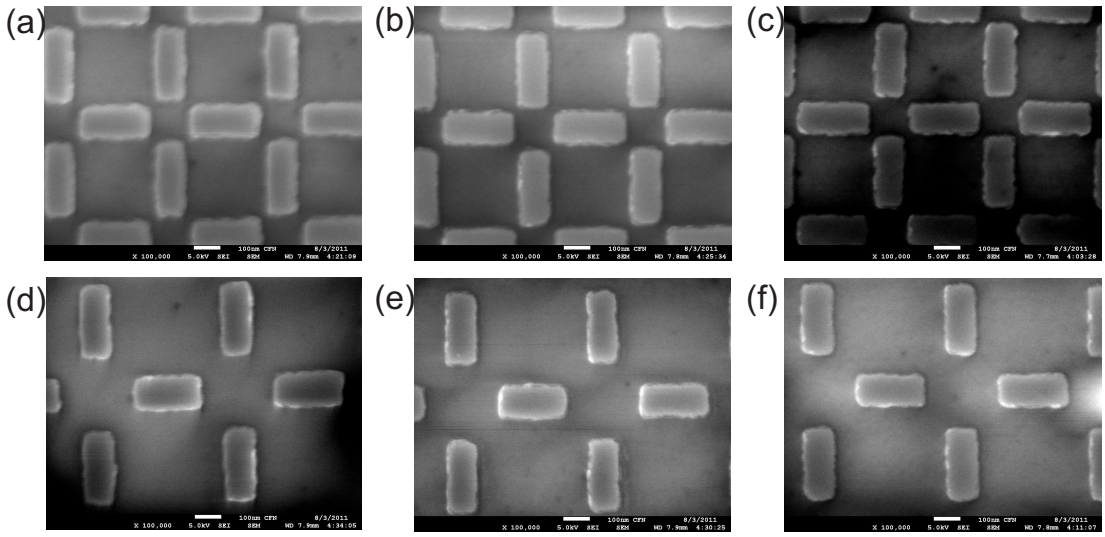

Figure 6.19: SEM images of square ice patterns from the batch-fabricated series. (a-c) and (d-f) show SEM images of the 433 nm and 550 nm lattice constant square ice patterns for underlayers of blank Si substrate, Ti (3 nm) and Cr (3 nm) respectively.

the patterning and deposition processes were consistent and homogeneous across elements patterned and grown within single fabrication runs (as already observed across single samples of appreciable total area). Three series of 0.5 mm $\times$ 0.5 mm area patterns were fabricated, sequentially patterned in a single EBL run (JEOL 6300) on a single 3" diameter Si substrate, spaced by $\sim$ 1 cm in the same resist coating, and simultaneously developed. Each series contained six patterns, with lattice constants of a = 400 nm, 433 nm, 466 nm, 500 nm, 550 nm and 600 nm. Sequential patterning should make islands across the series as identical as possible. As the JEOL system possesses the ability to check and correct patterning parameters at user-defined intervals, the risk of drift in conditions over such an exposure is minimised. Further to this, to explore the idea that pattern disorder influences magnetic order, each series was prepared with a different underlayer on to which the magnetic NiFe layer was deposited. One series was given a buffer of Ti (3 nm), one given a buffer of Cr (3 nm), and the remaining series left unbuffered providing a blank Si underlayer. A layer

of NiFe (25 nm) was then deposited on all patterns simultaneously (no capping layer was deposited due to a subsequent timely evaporator malfunction) and all patterns were placed in lift-off together. Figure 6.19 shows SEM images taken at the centres of the (a-c) 433 nm and (d-f) 550 nm spaced arrays for each underlayer layer, Si, Ti and Cr, respectively. By eye, there is no detectable difference between each pattern of a given a, with islands of lateral dimensions of 270 nm $\times$ 115 nm. While the same nominal island size was defined for all patters in the e-beam patterning process, those patterns with $a = 550$ nm appear to possess slightly smaller islands, due to proximity effects which occur due to the close-packing of islands. While one element is being exposed in the electron sensitive resist, electrons can"spill-over" to the surrounding area by scattering, over-exposing the resist in which nearby features are written. As a result this over-exposed resist dissolves and develops at an increased rate relative to unexposed resist. Such effects are common in the fabrication of such patterned systems. While in some of the SEM images shown in figure 6.19, e.g. (a), islands on sublattice Y appear more elongated relative to those on sublattice X, perhaps indicating a beam stigmation issue during patterning, such features can often be an artefact of the SEM imaging process, resultant of slow-scan direction drift. If this is a real feature, it does not appear to be large, however, further investigation is required to make any definitive conclusions. Such properties will present a form of intrinsic anisotropy in a pattern, which has been shown to be a significant detectable effect [9; 12], however, no extensive studies of pattern anisotropy have yet been presented. Differences between islands on patterns of different a appear to be small and are therefore not expected to have a drastic influence on results.

6.3.1 Microscopy and Vertex Populations

Commercial Si has a surface roughness of $\sim$ 0.1 nm [126]. The buffer layers deposited on top are expected to therefore have a roughness greater than this. This should reduce the uniformity of the magnetic islands' thin film structure, particularly during the early deposition stages when thickness d is small ($\sim$ 1 nm), therefore imparting a wider distribution of magnetic properties to the islands within a pattern. As the NiFe layer of all samples is simultaneously deposited,

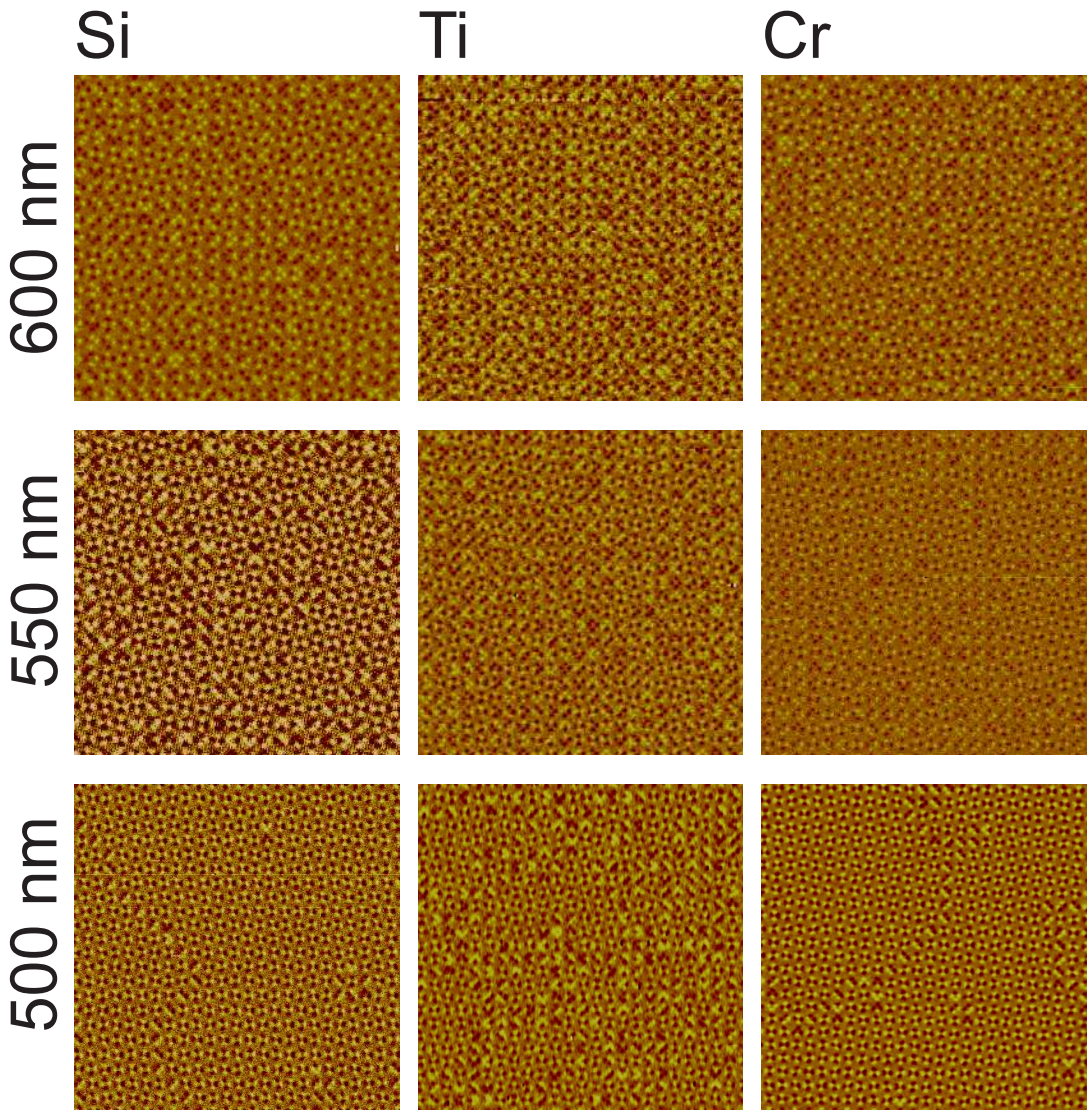

Figure 6.20: Example 13 μm $\times$ 13 μm area MFM images of square ice arrays of each value of a (rows) and each underlayer (columns) from the batch-fabricated samples series. (Continued in figure 6.21.

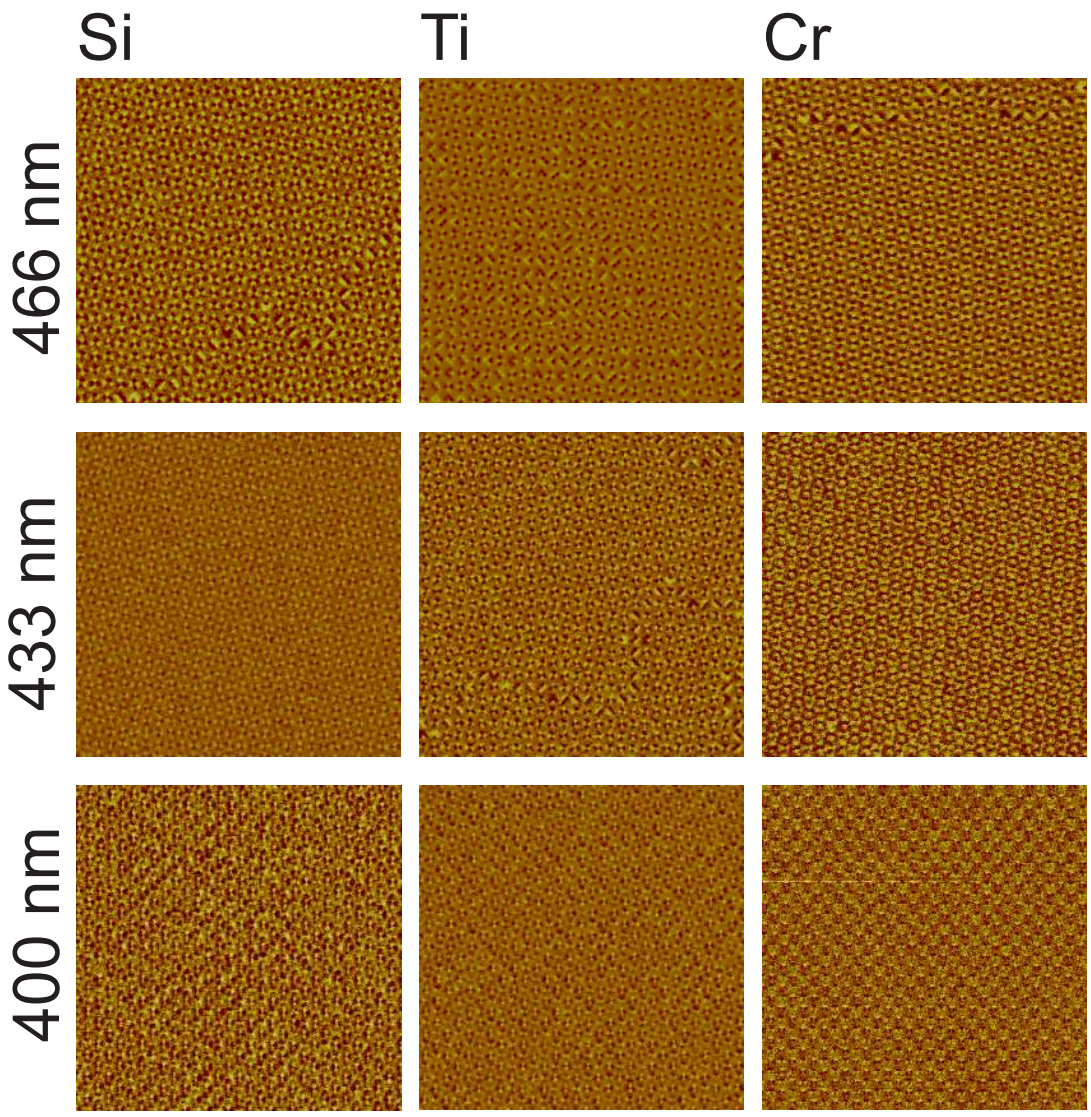

Figure 6.21: Continued from figure 6.20.

the average island of a given pattern should posses the same moment size and properties as that of all other patterns of equal a and different buffer.

Each pattern was imaged via MFM using a Veeco Multimode V with low moment probe tips over five evenly spaced 13 μm $\times$ 13 μm areas positioned across its span, an example image for each value of a and each underlayer shown in figure 6.20. All error bars presented on subsequent data for these samples are calculated as the standard error over the five images for each a and underlayer. At 600 nm, all magnetic states appear (by eye) to be quite disordered. It is apparent that as a function of decreasing lattice constant a, domains of T_1 GS order begin to "condense". What is quite notable, is that long range GS ordering has been obtained over a wide range of parameters and at values of a much larger than previously obtained (again illustrating the variability of the ordering process). For all series, the domain size quickly becomes larger than the (maximum possible) field-of-view of the microscope. It is also apparent by eye that for the Ti buffer series, the onset of strong GS order is suppressed, both the $a = 500$ nm and 466 nm states appearing significantly more magnetically disordered than the equivalent Si and Cr buffer series. This is encouraging, fitting the hypothesis of the influence of a buffer layer. No difference however can be seen by eye between the states of the blank Si and Cr buffer underlayered series.

Figure 6.22 (a) shows the fractional vertex type populations for each series. The general enhancement of GS T_1 vertex configurations with increased interaction strength is clear for each series. The suppression of GS order for a given a with buffer is also apparent. Compared to the blank Si series, the Ti series possesses lower counts of T_1 vertices over all $a > 400$ nm, while a subtle suppression is observed for the Cr series for $a < 466$ nm. The T_1 supression is made up for by enhanced numbers of $T_{2,3}$ vertices, while negligible difference is observed in T_4 populations between each series. As mentioned, many low-a images posses 100% populations of T_1 vertices, however, this does not necessarily mean that the entire patterns are perfectly GS-ordered, the study being limited here by the finite microscope field-of-view, therefore subtle differences at low-a may have been missed. The data presented are however consistent with the assumption that fabrication parameters are constant and homogeneous across all patterns fabricated within

a single run, as well as the hypothesis that interfacial roughness between the underlayer and NiFe layer imparts quenched disorder, in turn suppressing magentic order. Further investigation is required to correlate interfacial roughness with the magnetic order achieved, to fully confirm/disconfirm these ideas. The formation of strong GS order over a wide range of parameter space presents the possibilty of preparing samples for systematic studies of the square ice GS e.g. the evolution of the GS under an applied field, as well as the response of existing isolated excitations and DWs.

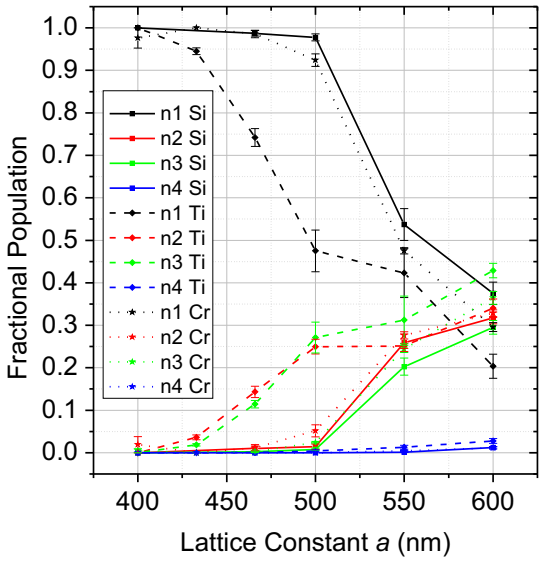

Figure 6.22: The variation in vertex populations for as-fabricated sample states as a function of lattice constant a, for three different underlayers: Si substrate with no buffer, a 3 nm thick Ti buffer and a 3 nm thick Cr buffer.

6.4 Effective Temperatures

Having established that GS order can be controlled by variation in lattice spacing a, as well as finding encouraging evidence that increased structural disorder

supresses magnetic order, a clear analogy is presented to the work of Wang et al. on ac demagnetised square ice state, allowing for demagnetised states to be accessed with similar influence of a over order [3; 14; 16]. Further to this, the work of Nisoli et al. [64; 83] suggests an interesting avenue of exploration. As compelling evidence is found that the states accessed and discussed in the preceding sections are a result of true thermal activation and thermal equilibration, a similar statistical mechanical treatment of the states observed in MFM should be possible, as such states allow the concept of temperature to be defined.

Employing a mean field approximation, each non-interacting vertex in the system taking possible energy states E_i for vertex types T_i for $i = 1$ to 4, the canonical distributions of fractional vertex populations are given by

$$n_i = \frac{q_i \exp(-\beta_{\mathrm{eff}} E_i)}{Z}, \tag{6.1}$$

as per sections 1.3 and 2.3.2. Again, the Lagrange multiplier β_{eff} is a reciprocal effective temperature, which can be calculated by taking ratios of n_i, directly measurable from an MFM image, yielding

$$\beta(E_j - E_i) = \ln\left(\frac{q_j n_i}{q_i n_j}\right). \tag{6.2}$$

Calculating E_i from a point dipole model, each vertex comprising four point dipoles, normalising energy units such that $E_1 = 0$, $E_2 = 0.69$, $E_3 = 1$ and $E_4 = 2.1$ gives $\beta_{\mathrm{eff}} = \ln(8n_1/2n_3)$. Excellent agreement is found between calculations and the experimentally determined populations, shown in figure 6.23 as solid lines and symbols respectively. In normalised units, all data sets collapse onto the same set of curves for n_i, states of weaker GS order possessing a lower value of β. All n_i approach their random multiplicities as $\beta \to 0$ (infinite temperature), and n_1 tending to 1 as β increases. Significantly higher values of $\beta \approx 7$ (i.e. lower temperatures) have been accessed than those previously reported following ac demagnetisation, for which $0 < \beta < 3$. Those data points posessing $n_1 = 1$ and $n_3 = 0$ posses a value of $\beta_{\mathrm{eff}} = \infty$ and therefore do not appear in figure 6.23.

Within an underlayer series, shorter a produces stronger interactions and acts to increase β, allowing closer approach to the GS, the same intuitive results as obtained by Nisoli et al. [64]. Further, for a given value of a, increased

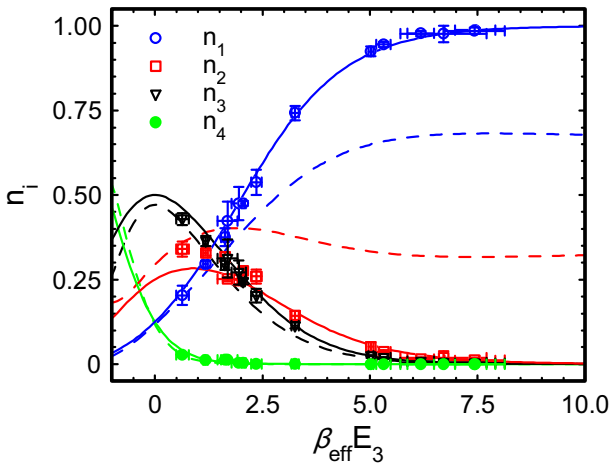

Figure 6.23: Variation of vertex populations n_i as a function of effective temperature β_{eff} for (symbols) an as-fabricated experimental sample set, (solid lines) the standard meanfield distribution model calculation using point dipole vertex energies, and (dashed lines) the extended model with four-charge model vertex energies.

underlayer roughness decreases β, showing a clear illustration of the interplay between interaction strength and quenched disorder.

The mean field approximation appears to describe the system very well, indicating that moments have negligible interaction beyond a vertex and that the vertices are therefore approximately non-interacting. This can be understood as in a generally demagnetised state (e.g. the RS, the GS, or and ac demagnetised state) long range interactions on average sum to zero. It should be noted that at low β there are slight experimental deviations from the calculated curves, small deficiencies of $n_{1,3,4}$ at $\beta \approx 1$ creating a surplus of n_2. This is currently under investigation, and is possibly a result of an anisotropy which breaks the degeneracy of the T_2 vertices, as would be found if the states were formed under a weak external magnetic field, an effect which would be most prominent for longer a where inter-elemental interactions play a weaker role in ordering. Further, as β increases, the experimental observation of a given vertex in a given state becomes increasingly correlated with the state of its neighbouring vertices, true for both T_1 vertices of a GS ordered domain, and the $T_{2,3}$ vertices of a domain wall struc-

ture or isolated excitation. Such correlations are not accounted for in the mean field approximation used.

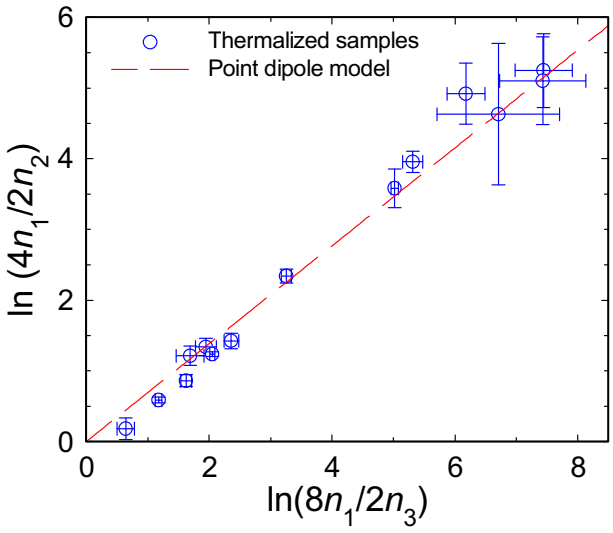

Figure 6.24: Determination of the energetic ratio E_2/E_3 from the as-fabricated series. Symbols show $E_2 = \ln(4n_1/2n_2)$ vs $E_3 = \ln(8n_1/2n_3)$ for the experimental data, with a proportional line of best fit shown as a red dashed line.

To further test the model, a plot of $\ln(q_2 n_1/q_1 n_2) = E_2\beta$ against $\ln(q_3 n_1/q_1 n_3) = \beta$ is shown as blue circles in figure 6.24. A proportional fit yields a value of $E_2/E_3 = 0.64 \pm 0.02$, (red dashed line) close to the value of $E_2 = 0.69$, implying that the point dipole model is a good approximation. It is curious that the approximation holds well across all a, as it might be expected that the appropriate model should change as a function of a, closely spaced dipolar islands being much less "point-like" with interactions better described by a micromagnetic calculation [84] or a multipolar model [127]. (It should be noted that modifying the value of E_2 used in the above calculations of n_i to 0.64 does not correct for the slight disagreement at low β discussed.) Interestingly, such a statistical formalism has been previously applied to as-fabricated states of small area arrays of 190 nm diameter NiFe pillars [128], each pillar taking one of several possible well-defined internal magnetic domain configurations. Little insight was however given as to the meaning of calculated energetic ratios, although the complication of interpretation due to

pattern imperfections was noted.

It is worthwhile to consider the physical meaning of an "effective temperature" in a system that has been thermally annealed at a finite "real temperature". Rather than arresting over a narrow window resulting from local variation in magnetostatic coupling as might be expected in a near-perfect system, moments begin to "freeze" by virtue of locally higher thermal reversal barriers imparted by structural disorder. The randomising thermalisation within the system is combined with the randomisation of quenched disorder. If both distributions are assumed to be Gaussian-distributed, their widths will simply add in quadrature. Quenched disorder, hence, effectively raises the temperature of the final state observed state, when the effects are averaged over the system. Within the model, the system is a perfect point Ising dipole lattice, disorder representing an intrinsic "effective thermal energy" within the system, which should persist in the system down to a real temperature of absolute zero.

6.4.1 Real vs Effective Thermodynamics

It is interesting to consider a comparison of the standard statistical mechanical formalism implemented above for thermalised states with the extended model of Nisoli et al. [64] appropriate for describing the model of effective thermodynamics of ac demagnetisation, section 2.3.2. Further, this provides an appropriate opportunity to discuss some peculiarities of the extended model, as previously mentioned.

The extended model divides the system into background vertices of one possible T_2 configuration and sixteen defect vertices, T_{1-4}, figure 2.6 (a). ρ is the fractional defect density, ν_i are the fractional population of defected vertices within the defect population, and n_i are the absolute fractional populations of vertices. Equations 2.2, 2.3 and 2.4 describe the "equilibrium" distribution of of these parameters for a given value of effective temperature β, equation 2.5. A four-charge vertex energy model is used to correctly fit the data, which may seem unusual at first, however the consequent relative vertex energies are similar to that given by micromagnetics for short a, so this is not of immediate concern. The four-charge model is however justified using a plot and proportional fit of $\ln(5n_1/2n_2)$ against

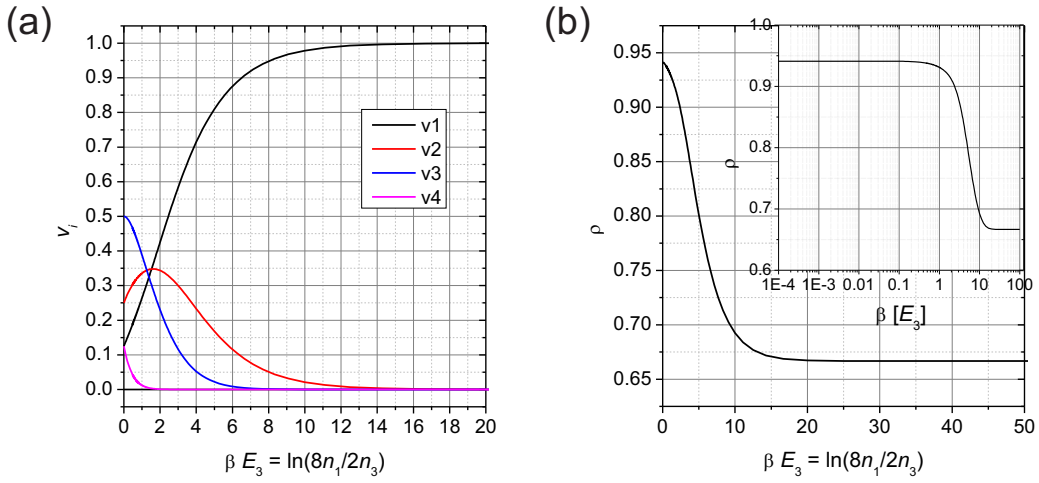

Figure 6.25: Calculated variations of (a) $\nu_i(\beta)$ and (b) $\rho(\beta)$ as defined by the extended model appropriate for describing ac demagnetised data.

$\ln(8n_1/2n_3)$, figure 2.16. This would only be valid if n_i were themselves canonical distributions, which they are explicitly not in the extended model. However, as stated in reference [64], at low β, the extended model and standard canonical distributions (equation 1.2) with an anomalous $q_2 = 5$ are approximately the same. Further, the extended model was initially introduced in a case where ρ did not require energetic constraining during the maximisation of entropy [83], the resultant states all possessing a specific vertex energy (energy per vertex) $\tilde{E} = E_2$. It is not clear whether the results of Ke et al. [16] are at odds with this equality or whether the continuation of the model is valid [64].

Figure 6.25 shows (a) $\nu_i(\beta)$ and (b) $\rho(\beta)$ as calculated using the equations 2.3 and 2.4 respectively. Shown in inset in (b) is the same calculated trend on a logarithmic temperature scale. At $\beta = 0$ all ν_i tend to the random values as given by their multiplicities $q_i = 2$, 4, 8 and 2 for $i = 1$, 2, 3 and 4 respectively. As β increases, the most energetically favorable vertex, T_1, tends to a fractional population of $\nu_1 = 1$. It should be emphasised that ν_i are the fractional populations within the defect population. The fractional defect population $\rho(0) = 16/17$ exactly, the random result (as there are 16 defect vertices and one background).

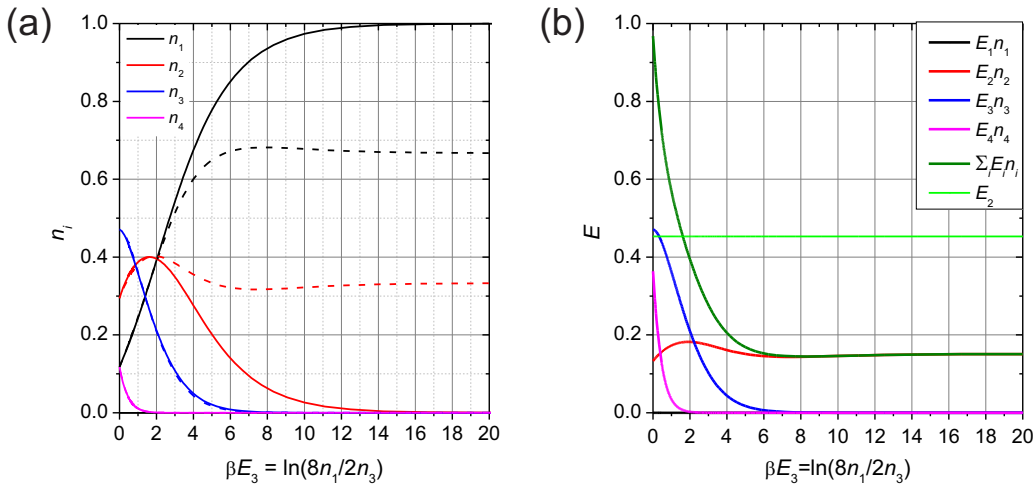

Figure 6.26: Further calculations of the extended model. (a) Calculated variation of fractional vertex population $n(\beta)$ for the extended model introduced to describe ac demagnetised data (dashed lines) and a standard canonical distribution calculation using an "anomalous" degeneracy $q_2 = 5$ (solid lines). The models are very close for the range $0 < \beta < 3$ considered in reference [64], however, the extended model does not predict ground state convergence as β increases. (b) The calculated variation of the ac demagnetised systems' energetic components, $E_i n_i$, with β, calculated using the curves of (a) which very closely match experimental data in the discussed low β range. The calculated specific energy $\tilde{E} = \Sigma_i E_i n_i \neq E_2$, contradicting the requirements of the extended model.

As β increases ρ tends to exactly 2/3, hence, as temperature decreases, the background population increases and tends to 1/3. The subsequently calculated values of n_i are plotted as dashed lines in figure 6.23. As shown, all $n_i(0) = q_i/17$, the random infinite temperature result, however, due to the behaviour of ρ, the extended model predicts that the system does not approach the GS at any value of β, with n_1 and n_2 converging to 2/3 and 1/3 as β increases. This, however, does not correspond to experimental findings that GS convergence has not been obtained via ac demagnetisation [16], as these experimental results are contained within a low $\beta < 3$ region [64], far below the converged limit. Further, the predictions of the extended model do not agree with the simulations of Libál et al. [78], in which values of n_1 close to 1 are obtainable in a low quenched disorder (high β) limit. While the superconducting vortex trap system considered by Libál et al. is clearly different to a dipole lattice, other reports suggest strong GS order and GS vertex populations should be achievable by field [21].

In figure 6.26 (a), the extended model is again plotted, along with n_i given by the standard canonical distribution calculation 1.2. What is striking is that in the range considered in reference [64], both of these calculations yield almost identical results, as mentioned in reference [64]. Further, looking at the range of $\beta > 3$, the simple standard model predicts GS convergence.

It should be restated that the form of ρ derived initially in reference [83] was introduced on the basis of the specific energy $\tilde{E}$ of ac demagnetised state at lower a being equal to E_2 (for an appropriate model), allowing it to be unconstrained in the maximisation of entropy as background vertices all inherently possess a vertex energy of E_2. The continuation of the model [64] is therefore dependent on this equality holding, otherwise, ρ would require explicit constraining. In figure 6.26 (b) $\tilde{E}(\beta)$ is plotted as predicted by the extended model, using the four-charge vertex energy model, which fits well the reported experimental ac demagnetised data at low β [64] (hence, over this range, it can be considered an appropriate substitute for the real data). Over this range, $\tilde{E}$ is not found to generally equal E_2, only approximately equal, hence the unconstraint of ρ is not valid for these data. Hence, equation 2.4 and the extended model do not stand.

As the data presented in reference [64] only cover a low range $0 < \beta < 3$, where both extended and simple models are equally "valid" (fitting the data),

why opt for the more complicated extended model? While the extended model was introduced as an attempt to account for an anomalous value of $q_2 = 5$ via an explicit background vertex population, which is perhaps justifiable given the initial polarised state of the system, inital states have no meaning at thermal equilibrium. Further, the lack of an energetic constraint on ρ is not correct, and the model has peculiar behaviour for large β. A more interesting question is why, in the standard model, a degeneracy of $q_2 = 5$ is needed to reproduce the experimental trends. Further, the extended model is not required to treat the system in terms of effective thermodynamics or to appeal to the concept of an "effective temperature", which would emerge in any model where an appropriate Lagrange multiplier was used.

6.4.2 Energetic Models

Figures 6.27 and 6.28 present results from ac demagnetisation tests of square ice patterns, showing (a) AFM, (b) MFM, (c) vertex populations in excess of the RS, and (d) GS correlation values C^{GS} (error bars are estimated as the standard error over multiple MFM images collected across the samples). Figure 6.27 is of the same $a = 700$ nm spaced pattern disussed at the beginning of this chapter (for its as-fabricated state). Figure 6.28 (e-h) presents the results of a repeat ac demagnetisation performed on the $a = 500$ nm spaced pattern, with similar structure to the 700 nm sample. Samples were rotated at ~ 10 Hz, an initial in-plane field of ~ 1 kOe was applied, and the oscillating square function field profile stepped down in magnitude by ~ 10 Oe every half a field period. All final states posses similar statistics, with net normalised magnetisations of ($M_{\mathrm{X}} = 0.06 \pm 0.02, M_{\mathrm{Y}} = 0.11 \pm 0.03$), ($M_{\mathrm{X}} = 0.01 \pm 0.01, M_{\mathrm{Y}} = 0.01 \pm 0.01$) and ($M_{\mathrm{X}} = 0.02 \pm 0.02, M_{\mathrm{Y}} = -0.01 \pm 0.01$) respectively, as well as a similar surplus/deficit of lower/higher energy vertex configurations. It should be noted that these results form part of an early ac demagnetisation trial, conducted before the importance of various parameters were realised, hence the approximate quoted values. This may explain the little difference between the results for the 700 nm and 500 nm lattice constant patterns. In general these results suggest that the results of Wang et al. [3] are qualitatively reproducible. Further, the statistical states

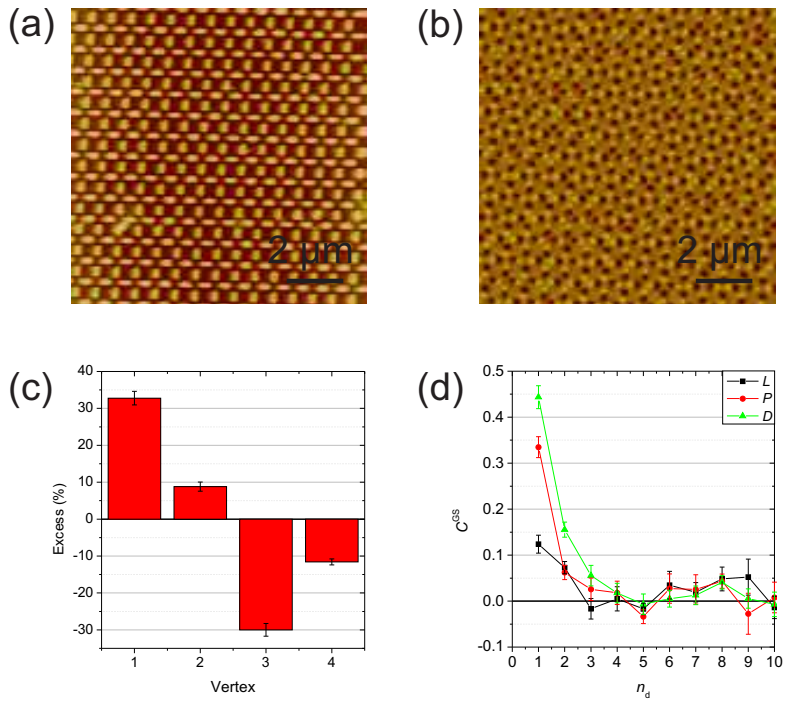

Figure 6.27: Statistics of an ac demagnetised state of an $a = 700$ nm lattice constant square ice pattern. (a) and (b) show example AFM and MFM images respectively. (c) shows the excess vertex populations above the RS and (d) shows the GS correlation functions C^{GS}. The sample was previously imaged in an as-fabricated state, figure 6.3.

appear well-defined across the imaged areas, and the similar statistics following repeat demagnetisation of the 500 nm spaced sample indicates that the results are repeatable, although this was not explored extensively.

Next, attention will be turned to the effective temperatures of these states. Do these results fit the constructs outlined in reference [64] and section 2.3.2 for ac demagnetised states? Nisoli et al. suggest that the ratio of $\ln(5n_1/2n_2)$ to $\ln(8n_1/2n_3)$ should yield a value close to E_2 in units normalised to E_3, working with the 4-charge vertex dumbbell energy model. The above states yield values of 0.55 ± 0.03, 0.62 ± 0.02 and 0.59 ± 0.04 respectively, all lying roughly half way between that given by the four-charge model and the point dipole model. It is not clear whether this is a result of differences in the ac demagnetisation protocol employed, or due to the samples themselves. The four-charge model agrees closely with values given by micromagnetics for short lattice constants [15], and the point dipole model is expected to be more appropriate for systems with large values of a. It is not unreasonable to consider that the elements and interactions of one patterned array are more point dipole-like than another, and a value lying between the two is therefore not unreasonable. It is however surprising that a four-charge energy model should work for arrays of large lattice constant a, Nisoli et al. studying up to $a = 880$ nm for islands for 80 nm $\times$ 280 nm, and likewise, that the point dipole model should work so well down to short lattice spacing in the studies presented here.

As previously discussed, the sample of 700 nm lattice constant was also studied in an as-grown state, figure 6.3. Taking the ratio of $\ln(4n_1/2n_2)$ to $\ln(8n_1/2n_3)$ as appropiate for the standard canonical ensemble desciption, shown previously to be appropriate for as-grown patterns, a value of 0.6 ± 0.3 is returned. While this value agrees closely with that determined for the corresponding ac demagnetised state, there is a very large uncertainty, resultant of the propagation of errors involving logarithms. These results are suggestive that the appropriate energy model for either the field or thermal demagnetisation process is sample dependent.

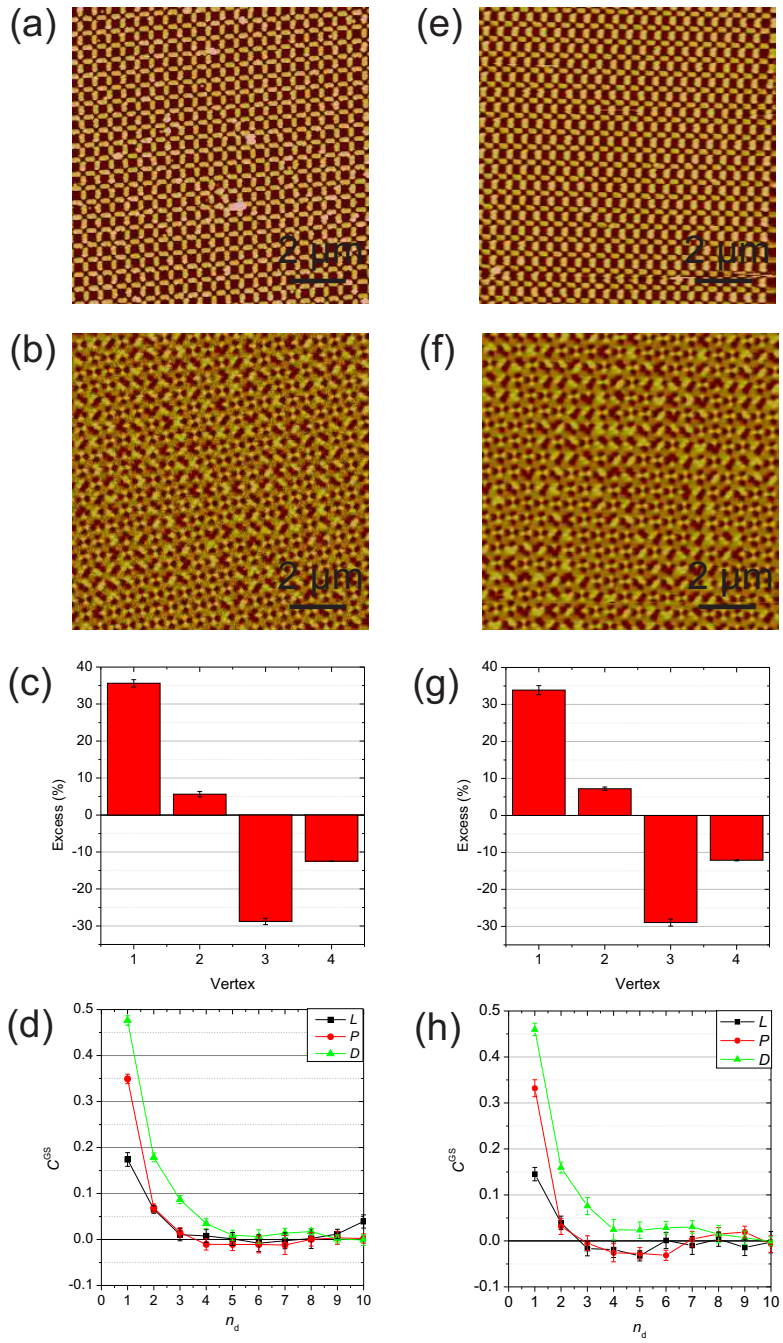

Figure 6.28: Statistics of an ac demagnetised state of an $a = 700$ nm lattice constant square ice pattern. (a) and (b) show example AFM and MFM images respectively. (c) shows the excess vertex populations above the RS and (d) shows the GS correlation functions C^{GS}. (e-h) show the same data types from a repeat demagnetisation run.

6.4.3 The Role of Disorder in ac Demagnetisation

Energetic model aside, a more pressing question is evident: why does an equilibrium statistical mechanical model describe the ac demagnetised data at all? While the agreement with experimental data is beautiful, there is no clear reason why this unusual model should work so well, or even at all.

Consideration should be given to the difference between the processes involved in ac demagnetisation, and true thermalisation. While both explore the magnetic phase space under the influence of inter-island dipolar coupling, the former is periodically directionally biased with all moments experiencing the same applied field, whereas the latter is (ideally) resultant of local normally distributed random thermal "kicks". A description in which the defect populations form what look like standard canonical distributions suggests that there must be a randomising influence in the system playing the role of thermalisation, even though field-mediated dynamics are directionally biased and not obviously stochastic. Considering the ideal point Ising dipole model of Budrikis et al. [21], a perfect system presents highly correlated field-mediated dynamics and domino-effect chain cascade behaviour. The similar chain objects found in dc-field reversal experiments are clearly bulk nucleated and pinnned by the effects of quenched disorder [23; 24], chapter 4. It is not unreasonable therefore to attribute the randomisation of magnetic state which occurs duing ac demagnetisation to the same structural quenched disorder, randomising the average magnetic states achieved when interpreted as topological configurations of Ising moments. The tuning of β with ΔH is likely a result of the interplay of the field with the switching property distribution. In a situation where quenched disorder is extemely low, such as the simulations of superconducting vortex ice of Libál et al. [78], near perfect GS order can be obtained via ac demagnetisation, which will most likely be mediated via perfectly correlated dynamics, as observed by Budrikis for similar protocols et al. [21]. (It should be rememebered though that the system of Libál et al. will not be described by a simple meanfield canonical ensemble approximation model, which would most likely predict a ground state of 100 % 4-out configurations, which is not the true square ice GS and, more importantly, unphysical.)

As well as the reordering processes being different, there are also distinct differences between the samples during the processes. The samples studied via ac demagnetisation are fully formed elements of $\sim$ 25 nm thickness, whereas the thermalisation occur when elements are approximately 1 nm thick. This clearly imparts different nearest neighbour interaction strength, as well as the shape of the anisotropic barriers to magnetisation reversal of Ising state [31]. Island reversal under an applied field is highly dependent on the instantaneously angle of the applied field, and will occur via the nucleation of a domain wall at the end of an island.

6.5 Summary

It has been shown that true thermal ordering has occured during the early-growth stages of fabrication of the artificial square ice patterns studied in this thesis. Initial evidence was presented by weak GS-like statistics of as-fabricated state, as inferred from MFM. Strong conclusive evidence was presented in a case study of a pattern possessing a strongly GS-ordered as-fabricated states, with isolated defects which present themselves as well-defined dipolar excitations of the square ice system. The relative abundances of these excitations are Boltzmann factor-weighted and fit realistic values of temperature and elemental dimensions. Similar to the description of Mól et al. [20], excitations can be described energetically approximately by the number of non-GS vertex configurations possessed, yielding a dipolar energy band structure. Inference has been allowed in to the likely growth and propagation mechanisms of such excitations through the band structure, and indirect evidence is present for charged vertex interactions playing a role in thermal ordering.

Subsequent results show that the GS ordering strength can be controlled, (although not exactly reproducibly between sample batches), via interaction strength, with compelling evidence that reduction in elemental uniformity, controlled by the use of different underlayers, decreases the ordering strength by increasing quenched disorder. The square ice GS is potentially accessible over a large range of parameter space, presenting interesting future experimental directions. This technique is of course universal, therefore, it would be exciting to

investigate the as-grown states of alternative patterns, an obvious choice being the kagome ice lattice, particularly as it possesses a ground state of distinctly higher degeneracy than the square ice.

Further, a simple meanfield canonical ensemble model is shown to describe the variations of vertex populations very well as a function of an effective temperature, suggesting that the states achieved are truly equilibrated (as opposed to thermally quenched). Much lower effective temperatures (stronger GS ordering) have been achieved than those reported in ac demagnetisation experiments [64].

By comparison, the extended model for ac demagnetisation is shown to be distinctly "non-thermal", despite being described at higher effective temperatures by a similar formalism, failing to predict a convergence to the GS at low effective tempertures. While the experimental work of Ke et al. [16] revealed a distinct lack of GS convergence in ac demagnetised systems, this is attributable to quenched disorder keeping states in the low β range reported by Nisoli et al. [64].

This work provides instructive insights into thermalised magnetic patterns. Future studies of artificial spin ices are aimed towards systems in which thermal activation is controllably accessible at convenient temperature scales, by the use of low Curie temperature materials [87] or superparamagnetic elements [36]. This will allow the systems to better approximate the behaviour of real bulk crystalline spin ice material.

Chapter 7

Summary

7.1 Summary and Conclusions

This thesis has experimentally addressed the behaviour of athermal artificial square spin ices [3], and the preparation of various "icy" states on which charge defects can be created. Magnetic force microscopy (MFM) allows for the local configurations of microstates to be inferred, from which various statistical parameters can be extracted. The work has allowed for the consideration of varying facets of correlated behaviour due to dipolar interactions as well as the uncorrelated behaviour imparted by intrinsic quenched disorder inherent to any such patterned system [6; 28; 129].

This thesis has addressed field reversal on the diagonally polarised state (DPS) [30] under an off-diagonal axis applied field, recently reported in reference [29]. Similarly to reversal observed on artificial kagome ices [23; 24], reversal is found to mediate via correlated flipping of dipolar chains, which act to propagate the charged vertex sites which exist at their ends along the field direction. Due to the field offset, this propagation occurs independently on the square ice system's two orthogonal sublattices. Chains are nucleated in the bulk at random-like locations and are incrementally pinned by the effects of quenched disorder, imparting a distribution of switching characteristics to the islands. Further to this, the qualitative effects of charge-charge interactions have been identified during the midstages of reversal, the system forming a state of weak-charge order due to pinning/antipinning of charges propagating along adjacent parallel channels as they

pass each other. Further, the correlated dipolar and charged vertex behaviour is found to be considerably weak, displaying the drastic decorrelating effects of quenched disorder.

Access of the square ice GS has been addressed via two methods: constant magnitude rotating field annealing, and fabrication-stage thermal annealing.

Field annealing was conducted on small area patterns of $\sim$ 400 elements, in search of edge effects and strong GS ordering predicted by recent theoretical modelling [21]. The systems, beginning from the DPS, are predicted to nucleate charged vertex sites at their edges which incrementally propagate into the bulk, meeting and annihilating at the middle. While an optimium GS vertex population is found as a function of field magnitude, it is considerably suppressed relative to predictions. Further, no edge dependence is found and the predominance of bulk nucleation effects are found in the magnetic force microscopy images at lower fields. Again, quenched disorder in elemental properties acts to randomise the behaviour of the system, allowing for bulk processes to occur which would otherwise be blocked in an ideal system. Such ideas are currently being explored using this data and an extended theoretical model with the authors of reference [21]. The order obtained appears comparable to that achieved via the more elaborate ac demagnetisation process often employed [3; 14; 16].

From early on in the project, interesting results were found in data from as-fabricated samples states, indicating varying amounts of GS-like correlation and vertex populations. Strong conclusive evidence was found that this self-ordering was infact a thermally mediated phenomenon, which is allowed to occur during the very early stages of magnetic material deposition of the thin film structure of the NiFe elements, as reported in reference [25]. When thin, elements are superparamagnetic and explore configurations thermally. This behaviour will become suppressed as the island thickness increases, eventually blocking and arresting the system. A specific sample of short lattice spacing was found to possess large continuous GS-tiled domains separated by domain walls between domains of opposite GS sense. Quenched disorder allows for the finite domain size to be accounted for, as islands with slightly large barriers to thermal reversal will arrest first on average, which will occur according to the random uncorrelated allocation of barrier heights. Further, the topological defects existing within the

GS domains are found to be relatively weighted by Boltzmann factors, giving a trend of abundance with energy suggesting realistic values of island thickness and sample temperature during the process. Such defects interact only over short range, and present a dipolar energy excitation band structure. Evidence exists for charged vertex interaction playing a role in thermal ordering.

While the ordering process is not currently exactly quantitatively reproducible due to the influence of variable fabrication parameters, a study of a self-contained samples batch showed that GS order can be achieved over a wide pattern parameter range, reducing lattice constant enhancing GS order. Evidence is also found that the order is also influenced by the inclusion of a buffer material layer under the NiFe thin film, relative to that achieved when deposited on blank Si substrate. This can be understood by the buffer layer acting to roughen the surface on to which the NiFe layer is deposited, which will decrease the island uniformity and increase the level of quenched disorder in the system, particularly when elements are very thin. Further study is need to correlate underlayer roughness with the degree of magnetic order.

As recently reported for ac demagnetised states [64; 83], a mean field canonical ensemble model was found to well-describe the distribution of vertex populations in these thermally annealed systems, and significantly lower effective temperatures are accessed. It is observed that decreased lattice spacing/stronger interaction strength acts to lower the effective temperature and enhance the formation of GS order, while increased quenched disorder via the buffer layer acts to increase the effective temperature and randomise the system.

Finally, discussion and comparison of the real and effective thermodynamics is given. Discussion suggests that quenched disorder manifests as an apparent increased temperature, acting against correlation due to randomisation of configurations.

All aspects of this work illustrate the importance of the competition between correlated interactions and randomising quenched disorder. The effective termperature formalisms for both ac demagnetisation and thermalisation illustrate how quenched disorder acts to make the system behave as if “hotter”, when the common averaged-state interpretation of ideal Ising moments is used.

7.2 Future Work

The work presented in this thesis provides a basis for various interesting avenues of further research. Firstly, a number of points of address are left outstanding regarding this work. While evidence for charge vertex-vertex interactions have been found in both field and thermally mediated processes, further information may be present in the data regarding their relative correlation, in all studies presented. The study of vertex interaction on a given state are perhaps limited in the arrested athermal systems studied.

During magnetic reversal, the onset and destruction of charge ordering has not been considered, although, statistics for states other than the $M_{\mathrm{X}} = 0$ state considered in section 4.3.3 are expected to be very weak. The constant magnitude rotating field protocol is currently under further investigation under collaboration with the authors of reference [21], which will potentially yield important results addressing the effect of disorder on accessing (or not) the ground state. Further, similar simulations could be used to investigate the behaviour of systems under ac demagnetisation - a number of unanswered question exist regarding effective thermodynamics which could be efficiently explored.

An obvious and simple outstanding experiment is to apply magnetic fields to the highly GS-ordered systems achieved, and to study the transition from the demagnetised state to one of strong polarisation. Further, the response of isolated defects and domain walls to applied fields may be interesting [77]. Direct correlation of buffer roughness to the degree of magnetic order achieved in as-fabricated patterns is needed to help support the apparent observed influence.

Isolating and addressing the fabrication parameters which currently prevent exact quantitative reproducibility of magnetic as-fabricated order (and possible effect the behaviour of the final athermal systems achieved) may prove useful, as fabricating self-contained samples batches is not ideal.

Two general avenues of future research are anticipated: the study of thermalised systems and the study of the effects of quenched disorder. As these studies show, thermalisation is an experimentally accessible phenomenon and that ordering is viable via the use of superparamagnetic elements [25]. A clear

goal is to access such behaviour at experimentally realistic temperatures in a repeatable manner. Thermal activation is also possible via patterns of low Curie temperature material, as recently reported [87]. The reduction of quenched pattern disorder is extremely desirable. Upon its reduction, the effects of intrinsic anisotropy in the patterned systems (due to patterning stigmation or material properties) may become increasingly apparent. Both will push the systems to be closer analogues of crystalline spin ice materials.

Appendix A

Ground State Order in as-fabricated Patterns

In this appendix, data will be presented complementing the work discussed in chapter 6.

A.1 MFM Survey

The complete MFM survey of nine images used for the statistical study of thermally ordered as-fabricated square ice systems are given in figures A.1 to A.9.

A.2 Excitation Energies

In table A.1 a summary of the values of l, s, p and dE of the GS excitations shown in figure 6.10 is given.

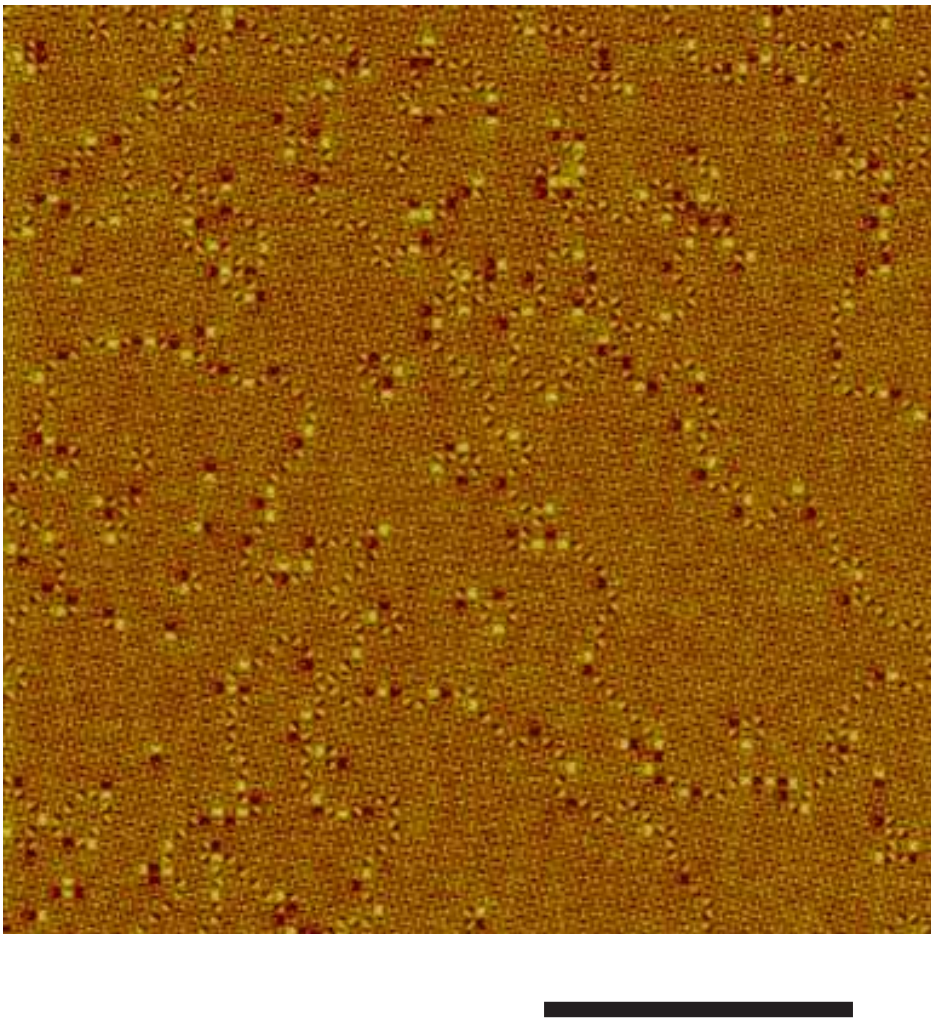

Figure A.1: MFM survey of thermally ordered as-fabricated square ice pattern. All scale bars correspond to 10 μm. All images were taken using a Veeco Nanoman system with standard MESP tips. The image series in continued in figures A.2 to A.9.

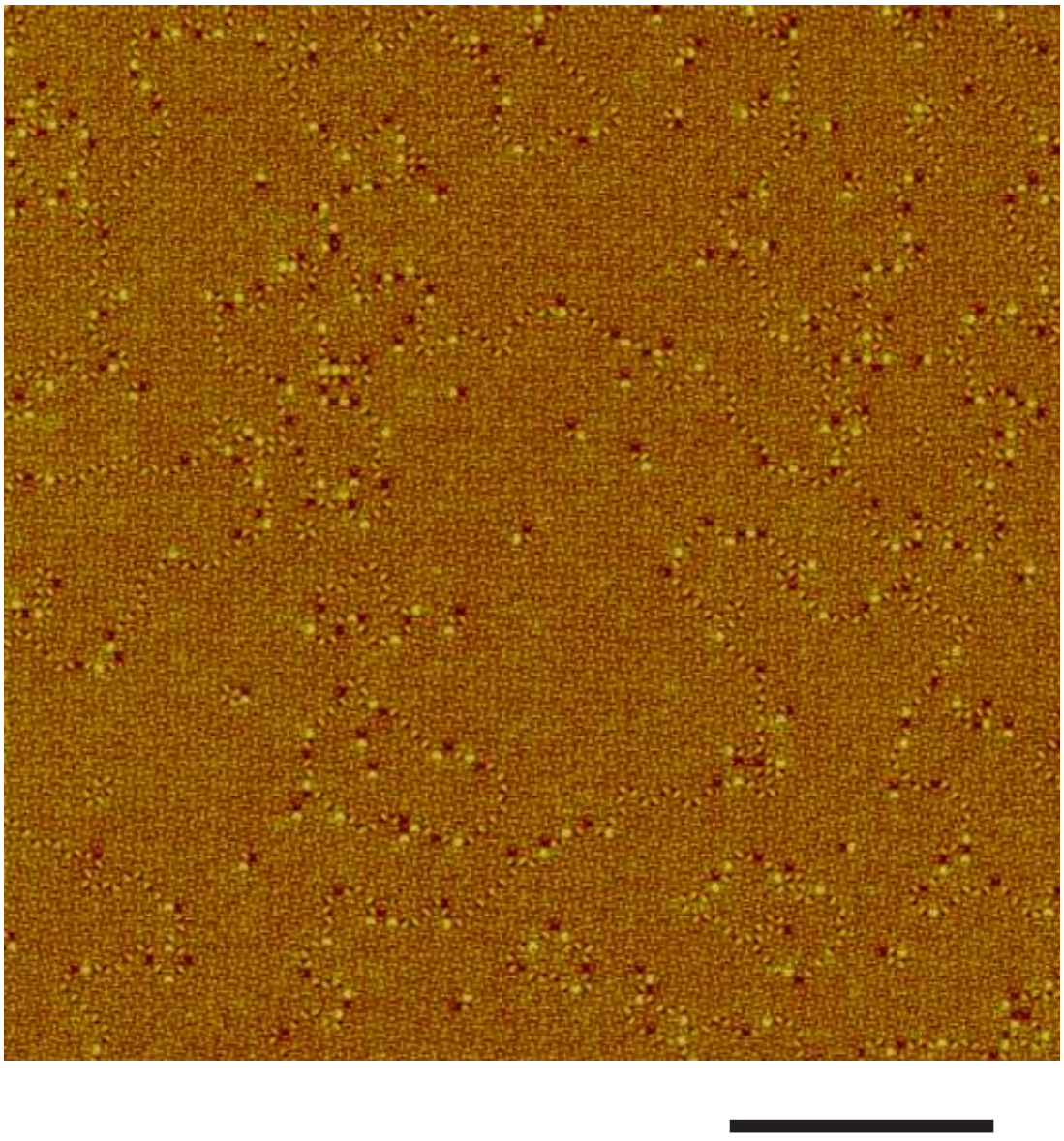

Figure A.2: MFM survey, continued from figure A.1.

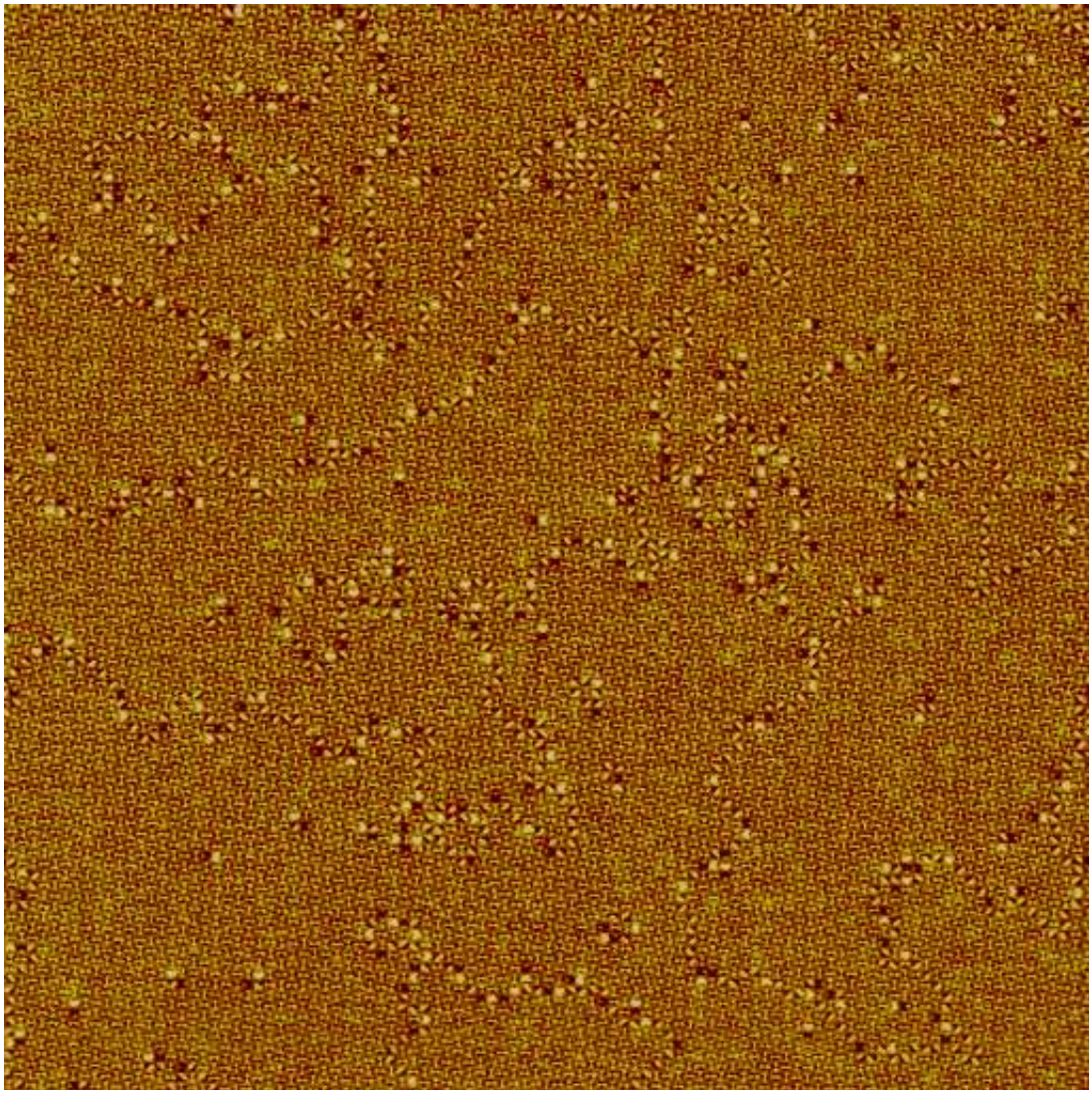

Figure A.3: MFM survey, continued from figure A.2.

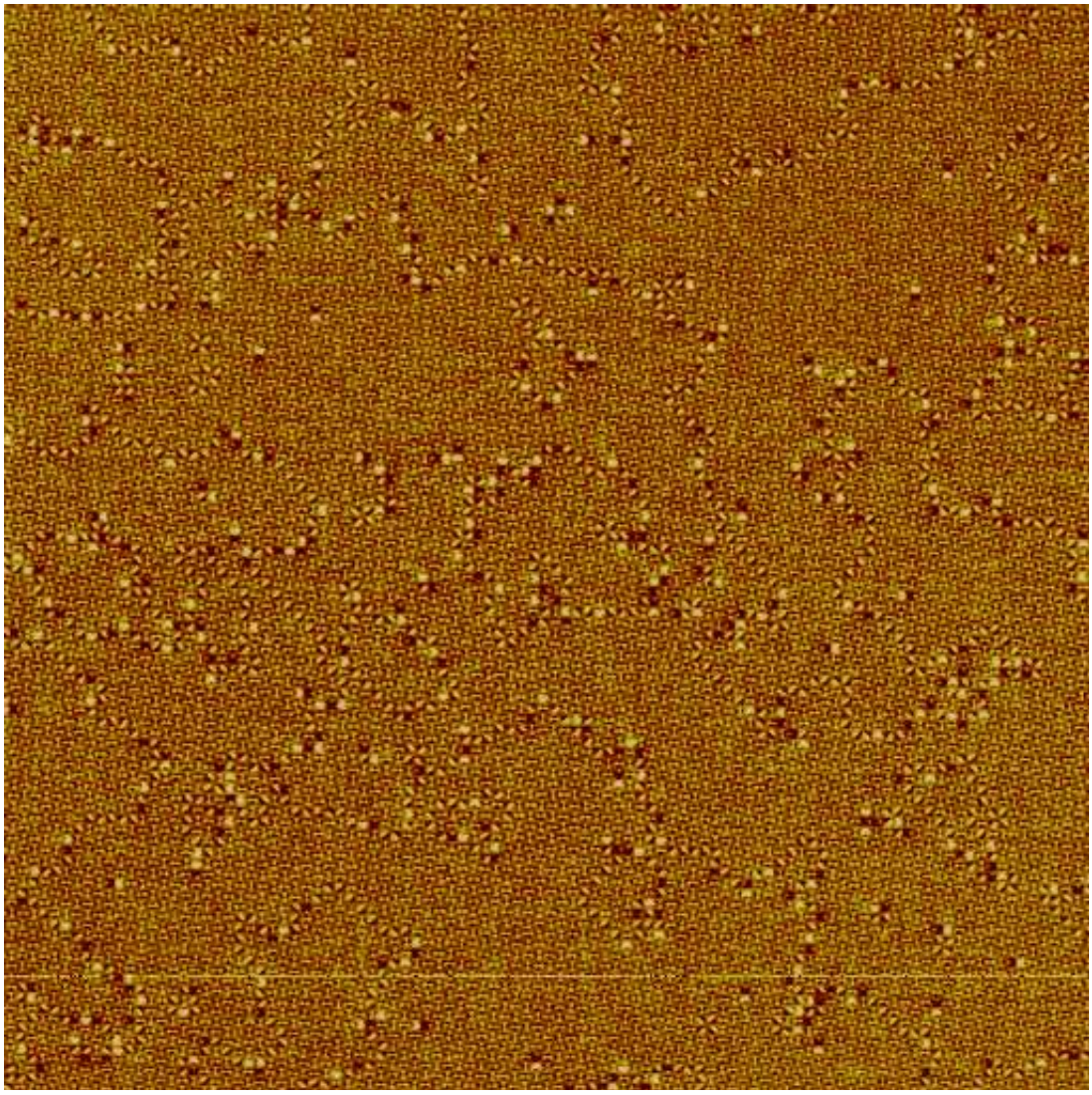

Figure A.4: MFM survey, continued from figure A.3.

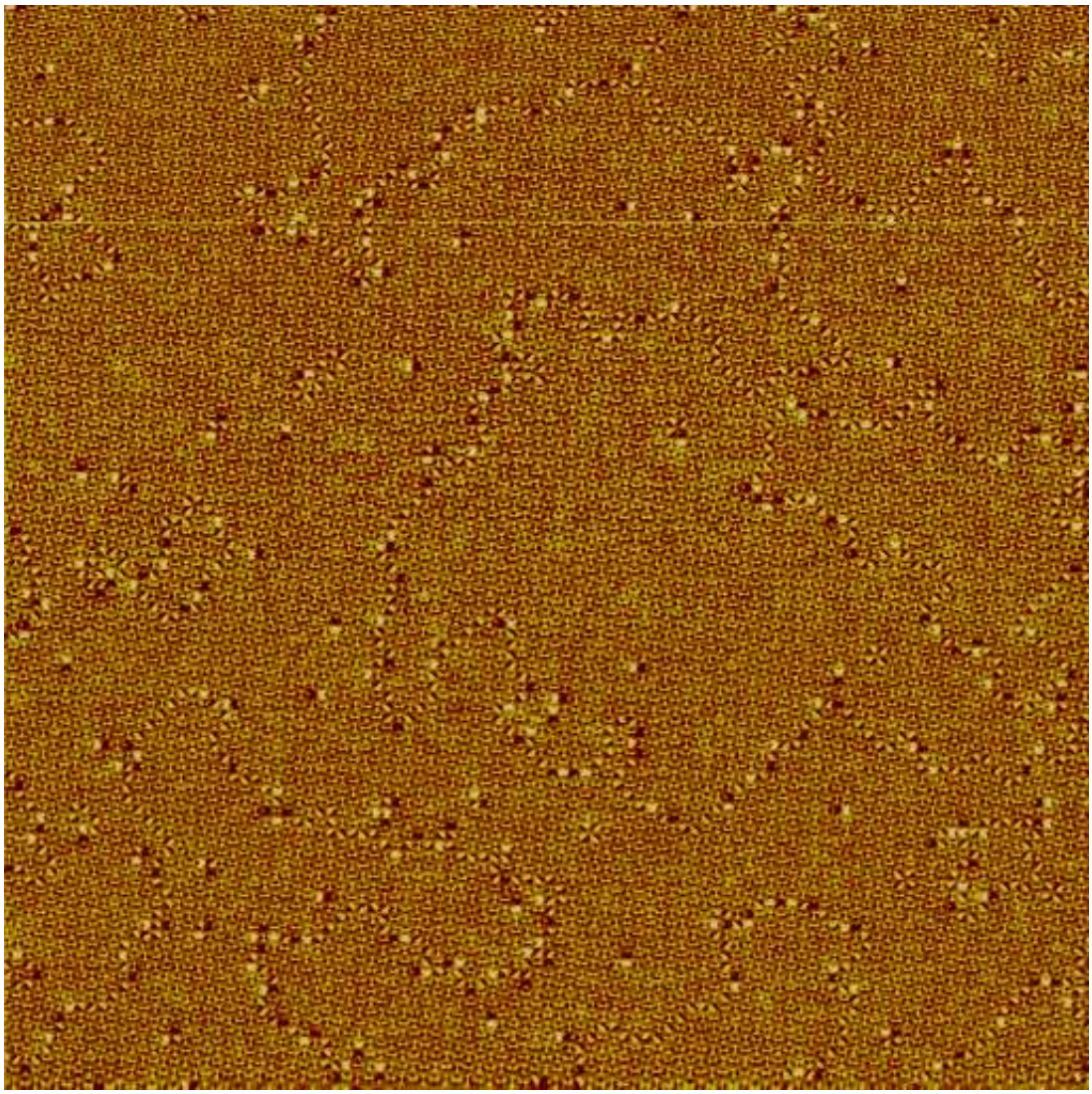

Figure A.5: MFM survey, continued from figure A.4.

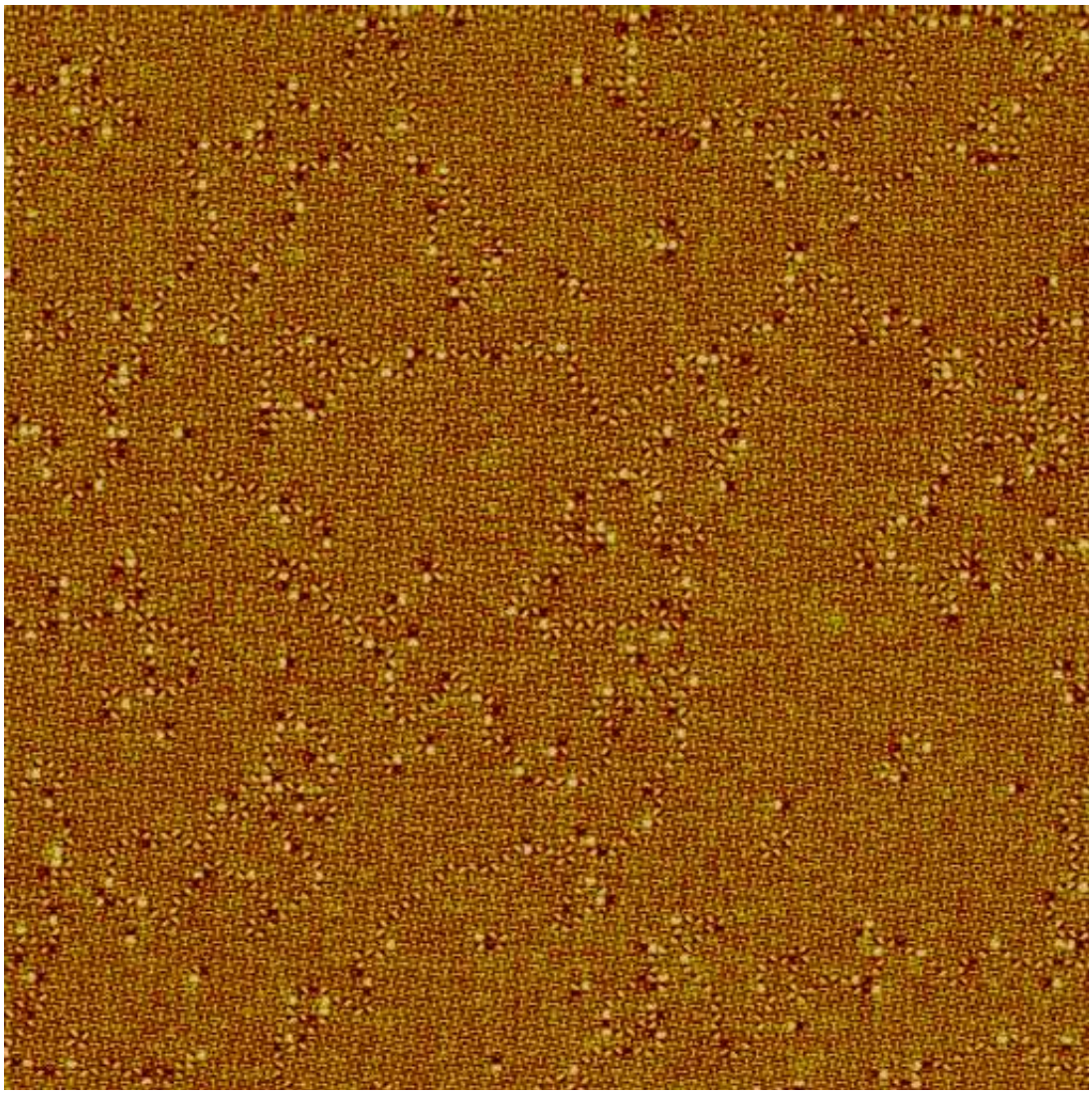

Figure A.6: MFM survey, continued from figure A.5.

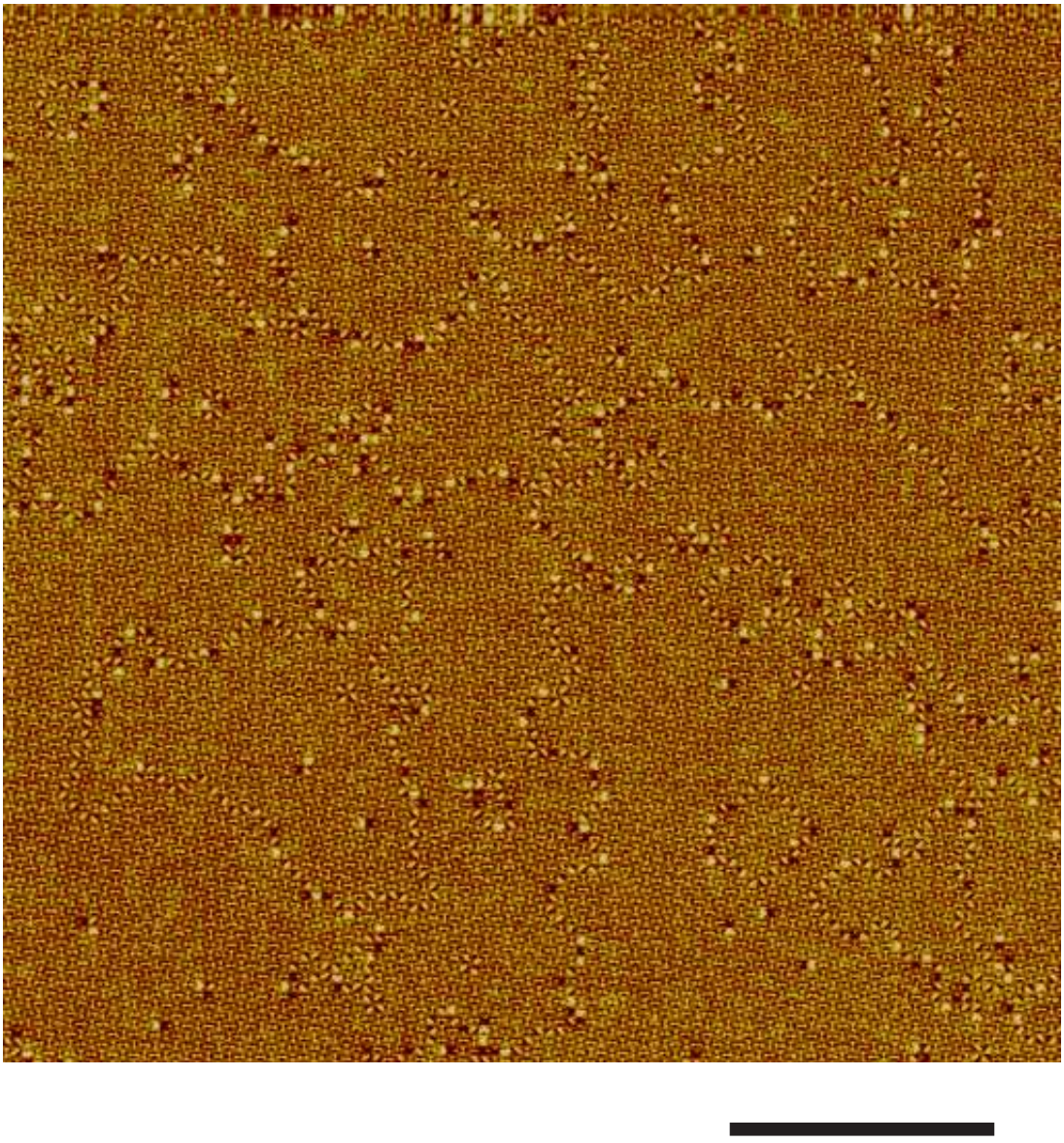

Figure A.7: MFM survey, continued from figure A.6.

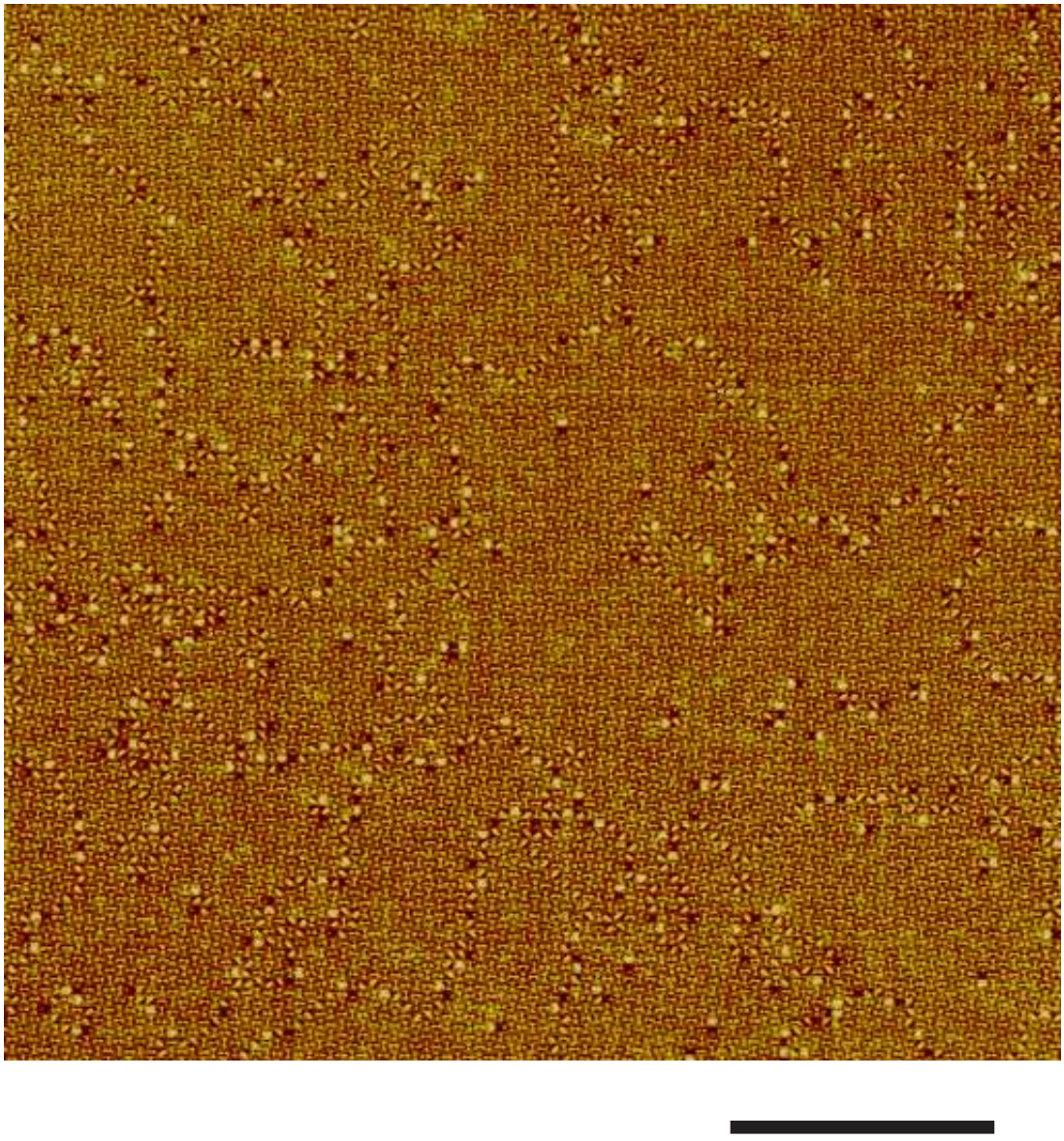

Figure A.8: MFM survey, continued from figure A.7.

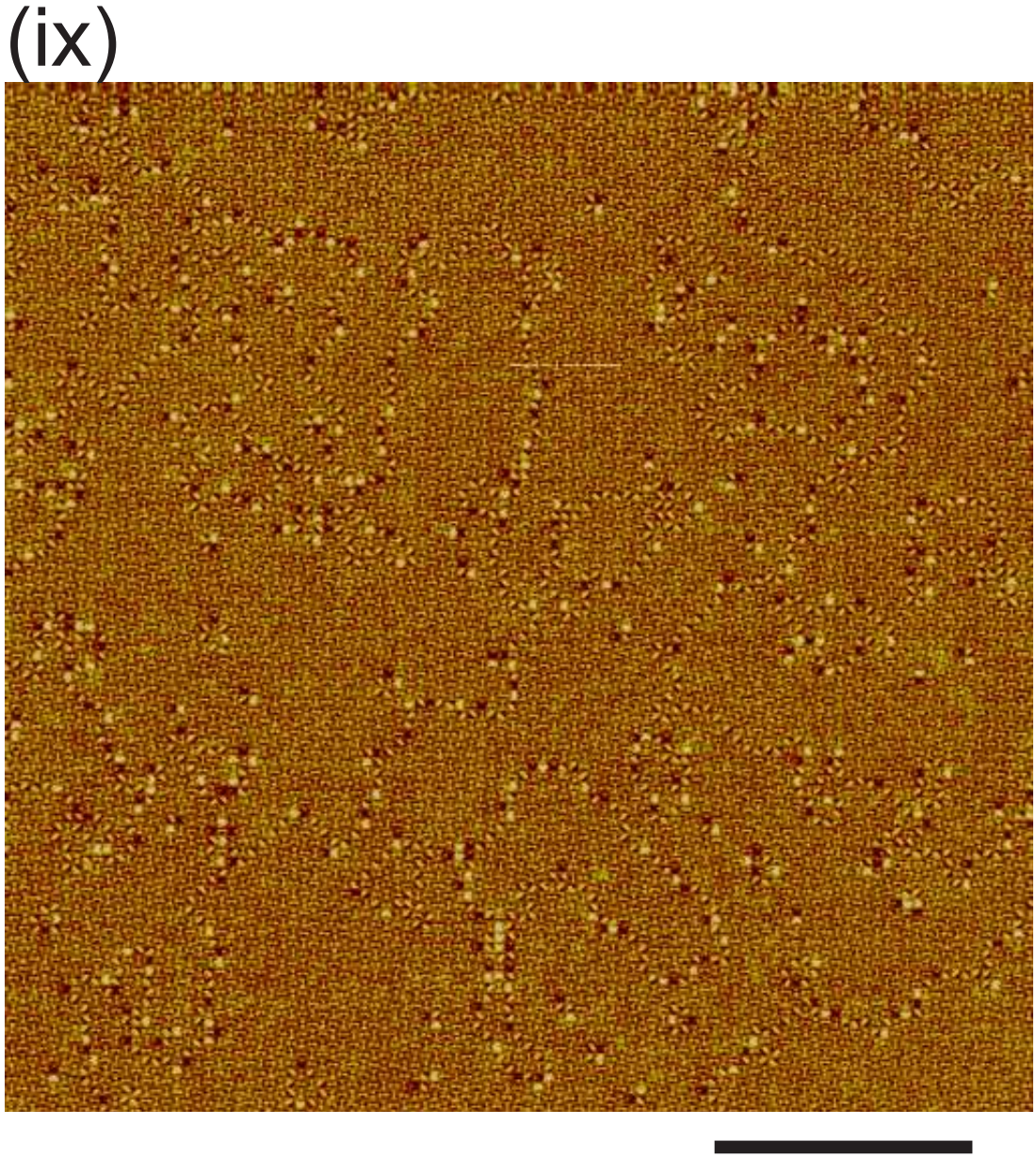

Figure A.9: MFM survey, continued from figure A.8.

Table A.1: A summary of l, s, p and dE values of ground state excitations. l represents the number of flipped moments in a given excitation, as indicated by the excitations name. s is the number of T_2 vertices, p is the number of oppositely charged T_3 pairs, and dE is the bulk-limit dipolar excitation energy of a given excitation.

Excitation	s	p	dE
GS	0	0	0
1	0	1	28.84
2L	1	1	40.72
3Z	2	1	51.88
3U	2	1	48.59
3T	0	2	60.59
4O	4	0	39.49
4Z	3	1	62.42
4P	3	1	60.67
4h	1	2	67.76
4F	1	2	72.67
4t	1	2	69.37
4+	0	2	63.49
5b	3	1	59.57
5t	1	2	71.57
5Z	4	1	72.87
6b	4	1	70.87
6g	3	1	62.67
6f	4	1	69.76
6I	5	1	80.89
6BK	3	2	92.69
7g	4	1	69.98
7s	5	1	82.04
7b	4	1	72.16
8O	6	0	60.31
8B	5	1	80.38
8D	3	2	90.14
8C	4	1	72.18
8A	5	2	110.51

References

[1] J. Mydosh, "Disordered magnetism and spin glass," *J. Magn. Magn. Mater.*, vol. 157/158, p. 606, 1996. 1

[2] R. Kamien and J. Selinger, "Order and frustration in chiral liquid crystals," *J. Phys.: Condens. Matter*, vol. 13, pp. R1–R22, 2001. 1

[3] R. F. Wang, C. Nisoli, R. S. Freitas, J. Li, W. McConville, B. J. Cooley, M. S. Lund, N. Samarth, C. Leighton, V. H. Crespi, and P. Schiffer, "Artificial 'spin ice' in a geometrically frustrated lattice of nanoscale ferromagnetic islands," *Nature*, vol. 439, pp. 303–306, 2006. 1, 2, 17, 18, 19, 21, 24, 25, 27, 30, 39, 48, 61, 67, 68, 91, 128, 135, 142, 149, 150

[4] M. J. Harris, S. T. Bramwell, D. F. McMorrow, T. Zeiske, and K. W. Godfrey, "Geometrical frustration in the ferromagnetic pyrochlore $Ho_2Ti_2O_7$," *Phys. Rev. Lett.*, vol. 79, no. 13, p. 2554, 1997. 1, 12, 13

[5] L. Pauling, "The structure and entropy of ice and of other crystals with some randomness of atomic arrangement," *J. Am. Chem. Soc.*, vol. 57, p. 2680, 1935. 1, 17

[6] D. Davidović, S. Kumar, D. Reich, J. Siegel, S. Field, R. C. Tiberio, R. Hey, and K. Ploog, "Correlations and disorder in arrays of magnetically coupled superconducting rings," *Phys. Rev. Lett.*, vol. 76 (5), pp. 815–818, 1996. 1, 20, 23, 113, 149

[7] D. Davidović, S. Kumar, D. H. Reich, J. Siegel, S. B. Field, R. C. Tiberio, R. Hey, and K. Ploog, "Magnetic correlations, geometrical frustration, and

tunable disorder in arrays of superconducting rings," *Phys. Rev. B*, vol. 55, pp. 6518–6540, Mar 1997. 1, 20, 23, 113

[8] M. Tanaka, E. Saitoh, H. Miyajima, T. Yamaoka, and Y. Iye, "Magnetic interactions in a ferromagnetic honeycomb nanoscale network," *Phys. Rev. B*, vol. 73, p. 052411, 2006. 1, 18, 19, 43, 44

[9] Y. Qi, T. Brintlinger, and J. Cumings, "Direct observation of the ice rule in an artificial kagome spin ice," *Phys. Rev. B*, vol. 77, p. 094418, 2008. 1, 2, 17, 18, 19, 48, 91, 130

[10] A. Wills, R. Ballou, and C. Lacroix, "Model of localized highly frustrated ferromagnetism: The *kagomé* spin ice," *Phys. Rev. B*, vol. 66, p. 144407, 2002. 2

[11] Y. Tabata, H. Kadowaki, K. Matsuhira, Z. Hiroi, N. Aso, E. Ressouche, and B. Fåk, "Kagomé ice state in dipolar spin ice $Dy_2Ti_2O_7$," *Phys. Rev. Lett.*, vol. 97, p. 257205, 2006. 2

[12] N. Rougemaille, F. Montaigne, B. Canals, A. Duluard, D. Lacour, M. Hehn, R. Belkhou, O. Fruchart, S. El Moussaoui, A. Bendounan, and F. Maccherozzi, "Artificial kagome arrays of nanomagnets: A frozen dipolar spin ice," *Physical Review Letters*, vol. 106, p. 057209, 2011. 2, 19, 23, 24, 35, 77, 89, 91, 130

[13] J. I. Martín, J. Nogus, K. Liu, J. L. Vicent, and I. K. Schuller, "Ordered magnetic nanostructures: fabrication and properties," *J. Magn. Magn. Mater.*, vol. 256, pp. 449–501, 2003. 2, 4, 7, 49

[14] R. F. Wang, C. Nisoli, R. S. Freitas, J. Li, W. McConville, B. J. Cooley, M. S. Lund, N. Samarth, C. Leighton, V. H. Crespi, and P. Schiffer, "Demagnetization protocols for frustrated interacting nanomagnet arrays," *J. Appl. Phys.*, vol. 101, p. 09J104, 2007. 2, 24, 25, 91, 97, 128, 135, 150

[15] R. Wang, *Geometrical magnetic frustration and demagnetization of artificial spin ice*. PhD thesis, The Pennsylvania State University, The Graduate School, Department of Physics, 2007. 2, 33, 128, 144

[16] X. Ke, J. Li, C. Nisoli, P. E. Lammert, W. McConville, R. F. Wang, V. H. Crespi, and P. Schiffer, "Energy minimization and ac demagnetization in a nanomagnet array," *Phys. Rev. Lett.*, vol. 101, p. 037205, 2008. 2, 19, 20, 21, 23, 24, 26, 28, 29, 32, 33, 48, 64, 66, 91, 92, 128, 135, 139, 141, 148, 150

[17] J. Li, X. Ke, S. Zhang, D. Garand, C. Nisoli, P. Lammert, V. H. Crespi, and P. Schiffer, "Comparing artifical frustrated magnets by tuning the symmetry of nanoscale permalloy arrays," *Phys. Rev. B*, vol. 81, p. 092406, 2010. 2, 20, 22, 24, 29, 91, 128

[18] A. Schumann, B. Sothmann, P. Szary, and H. Zabel, "Charge ordering of magnetic monopoles in triangular spin ice patterns," *Appl. Phys. Lett.*, vol. 97, p. 022509, 2010. 2, 19, 24, 43, 44, 45, 71, 90, 91

[19] C. Castelnovo, R. Moessner, and S. L. Sondhi, "Magnetic monopoles in spin ice," *Nature*, vol. 451, p. 42, 2008. 2, 15, 16, 17, 19, 23, 44, 47, 68, 77, 84, 111

[20] L. A. Mól, R. L. Silva, R. C. Silva, A. R. Pereira, W. A. Moura-Melo, and B. V. Costa, "Magnetic monopole and string excitations in two-dimensional spin ice," *J. Appl. Phys.*, vol. 106, p. 063913, 2009. 2, 17, 19, 20, 46, 47, 68, 84, 88, 100, 111, 117, 147

[21] Z. Budrikis, P. Politi, and R. L. Stamps, "Vertex dynamics in finite two-dimensional square spin ices," *Phys. Rev. Lett.*, vol. 105, p. 017201, 2010. 2, 3, 18, 20, 29, 39, 40, 42, 43, 48, 70, 73, 88, 89, 91, 92, 95, 97, 98, 141, 146, 150, 152

[22] L. A. Mól, W. A. Moura-Melo, and A. R. Pereira, "Conditions for free magnetic monopoles in synthetic square ice dipolar nanoarrays," *Phys. Rev. B*, vol. 82, p. 054434, 2010. 2, 17, 19, 20, 46, 68, 84, 100, 111, 117, 120

[23] S. Ladak, D. E. Read, G. K. Perkins, L. F. Cohen, and W. R. Branford, "Direct observation of magnetic monopole defects in an artificial spin-ice system," *Nature Physics*, vol. 6, p. 359, 2010. 2, 17, 19, 43, 44, 45, 48, 71, 73, 87, 90, 97, 146, 149

[24] E. Mengotti, L. J. Heyderman, A. Fraile Rodríguez, F. Nolting, R. V. Hügli, and H. B. Braun, "Real-space observation of emergent magnetic monopoles and associated dirac strings in artificial kagome spin ice," *Nature Physics*, vol. 7, pp. 68–74, 2011. 2, 3, 17, 18, 19, 23, 43, 44, 45, 48, 71, 73, 77, 80, 87, 90, 97, 146, 149

[25] J. P. Morgan, A. Stein, S. Langridge, and C. H. Marrows, "Thermal ground state ordering and elementary excitations in artificial magnetic square ice," *Nature Physics*, vol. 7, pp. 75–79, 2011. 2, 3, 17, 19, 20, 21, 48, 70, 84, 87, 88, 91, 97, 100, 104, 150, 152

[26] S. Ladak, D. Read, T. Tyliszczak, W. Branford, and L. Cohen, "Monopole defects and magnetic Coulomb blockade," *New Journal of Physics*, vol. 12, p. 023023, 2011. 2, 17, 19, 20, 23, 43, 44, 48, 71, 73, 89

[27] C. Phatak, A. Petford-Long, O. Heinonen, M. Tanase, and M. De Graef, "Nanoscale structure of the magnetic induction at monopole defects in artificial spin-ice lattices," *Phys. Rev. B*, vol. 83, p. 174431, 2011. 2, 19, 20, 23, 29, 44, 70, 73, 88, 89, 90, 97

[28] S. Ladak, D. Read, W. Branford, and L. Cohen, "Direct observation and control of magnetic monopole defects in an artificial spin-ice material," *New Journal of Physics*, vol. 13, p. 063032, 2011. 2, 20, 23, 43, 44, 73, 149

[29] J. P. Morgan, A. Stein, S. Langridge, and C. H. Marrows, "Magnetic reversal of an artificial square ice: dipolar correlation and charge ordering," *New Journal of Physics (at press)*, 2011. 2, 3, 17, 70, 97, 149

[30] A. Remhof, A. Schumann, A. Westphalen, H. Zabel, N. Mikuszeit, Y. Vedmedenko, T. Last, and U. Kunze, "Magnetostatic interactions on a square lattice," *Phys. Rev. B*, vol. 77, p. 134409, 2008. 3, 19, 43, 48, 95, 111, 114, 149

[31] S. Blundell, *Magnetism in Condensed Matter*. Oxford University Press, 2001. 4, 10, 112, 147

[32] I. Grant and W. Phillips, *Electromagnetism*. The Manchester Physics Series, Wiley, 2 ed., 1990. 4, 15

[33] A. Hubert and R. Schäfer, *Magnetic Domains: the analysis of magnetic microstructures*. Springer, 1998. 6

[34] A. Hirohata, H. Leung, Y. Xu, C. Yao, W. Lee, J. A. C. Bland, and S. Holmes, "Magnetic domain evolution in Permalloy mesoscopic dots," *IEEE Transactions on Magnetics*, vol. 35, no. 5, pp. 3886–3888, 1999. 6

[35] Q. A. Pankhurst, J. Connolly, S. K. Jones, and J. Dobson, "Applications of magnetic nanoparticles in biomedicine," *J. of Phys. D: Appl. Phys.*, vol. 36, pp. R167–R181, 2003. 7

[36] R. Cowburn, A. Adeyeye, and M. Welland, "Controlling magnetic ordering in coupled nanomagnet arrays," *New Journal of Physics*, vol. 1, pp. 16.1–16.9, 1999. 7, 148

[37] F. Mandl, *Statistical mechanics*. John Wiley & Sons Ltd., 1971. 8

[38] A. M. Glazer and J. S. Wark, *Statistical mechanics: A survival guide*. Oxford University Press, 2001. 8

[39] S. T. Bramwell and M. Harris, "Frustration in Ising-type spin models on the pyrochlore lattice," *J. Phys.: Cond. Matt.*, vol. 10, pp. 215–220, 1998. 12, 13, 17

[40] A. P. Ramirez, A. Hayashi, R. J. Cava, R. Siddharthan, and B. S. Shastry, "Zero-point entropy in "spin ice"," *Nature*, vol. 399, pp. 333–335, 1999. 12, 14, 17

[41] K. Matsuhira, Y. Hinatsu, K. Tenya, and T. Sakakibara, "Low temperature magnetic properties of frustrated pyrochlore ferromagnets $Ho_2Sn_2O_7$ and $Ho_2Ti_2O_7$," *Journal of Physics: Condensed Matter*, vol. 12, pp. L649–L656, 2000. 12, 13

[42] H. Kadowaki, Y. Ishii, K. Matsuhira, and Y. Hinatsu, "Neutron scattering study of dipolar spin ice $Ho_2Sn_2O_7$: Frustrated pyrochlore magnet," *Phys. Rev. B*, vol. 65, no. 14, pp. 144421 1–8, 2002. 12

[43] T. Fennell, O. A. Petrenko, B. F ˚ ak, S. T. Bramwell, M. Enjalran, T. Yavors'kii, M. J. P. Gingras, R. G. Melko, and G. Balakrishnan, "Neutron scattering investigation of the spin ice state in $Dy_2Ti_2O_7$," *Phys. Rev. B*, vol. 70, pp. 134408 1–7, 2004. 12, 13, 14

[44] S. Rosenkranz, A. Ramirez, A. Hayashi, R. J. Cava, R. Siddharthan, and B. S. Shastry, "Crystal-field interaction in the pyrochlore magnet $Ho_2Ti_2O_7$," *J. Appl. Phys.*, vol. 87, no. 9, pp. 5914–5916, 2000. 12

[45] L. Pauling, *The nature of the chemical bond*. Cornell, Ithaca., 3rd ed., 1960. 13, 14

[46] S. T. Bramwell, M. J. Harris, B. C. den Hertog, M. J. P. Gingras, J. S. Gardner, D. F. McMorrow, A. R. Wildes, A. L. Cornelius, J. D. M. Champion, R. G. Melko, and T. Fennell, "Spin correlations in $Ho_2Ti_2O_7$: A dipolar spin ice system," *Phys. Rev. Lett.*, vol. 87, no. 4, pp. 047205 1–4, 2001. 14

[47] B. den Hertog and M. J. P. Gingras, "Dipolar interactions and origin of spin ice in ising pyrochlore magnets," *Phys. Rev. Lett.*, vol. 84, no. 15, pp. 3430–3433, 2000. 14

[48] S. Isakov, R. Moessner, and S. L. Sondhi, "Why spin ice obeys the ice rules," *Phys. Rev. Lett.*, vol. 95, p. 217201, 2005. 15

[49] R. G. Melko, B. C. den Hertog, and M. P. Gingras, "Long-range order at low temperatures in dipolar spin ice," *Phys. Rev. Lett.*, vol. 87, p. 067203, 2001. 15, 22, 111, 122

[50] J. Preskill, "Magnetic monopoles," *Ann. Rev. Nucl. Part. Sci.*, vol. 34, pp. 461–530, 1984. 15

[51] L. D. C. Jaubert and P. C. W. Holdsworth, "Signatures of magnetic monopole and Dirac string dynamics in spin ice," *Nature Physics*, vol. 5, p. 258, 2009. 17, 19

[52] T. Fennell, P. P. Deen, A. R. Wildes, K. Schmalzl, D. Prabhakaran, A. T. Boothroyd, R. J. Aldus, D. F. McMorrow, and S. T. Bramwell, "Magnetic Coulomb phase in the spin ice $Ho_2Ti_2O_7$," *Science*, vol. 326, p. 415, 2009. 17, 19

[53] D. J. P. Morris, D. A. Tennant, S. A. Grigera, B. Klemke, C. Castelnovo, R. Moessner, C. Czternasty, M. Meissner, K. C. Rule, J.-U. Hoffmann, K. Kiefer, S. Gerischer, D. Slobinsky, and R. S. Perry, "Dirac strings and magnetic monopoles in the spin ice $Dy_2Ti_2O_7$," *Science*, vol. 326, p. 411, 2009. 17, 19

[54] H. Kadowaki, N. Doi, Y. Aoki, Y. Tabata, T. J. Sato, J. W. Lynn, K. Matsuhira, and Z. Hiroi, "Observation of magnetic monopoles in spin ice," *J. Phys. Soc. Jpn.*, vol. 78, p. 103706, 2009. 17, 19

[55] S. T. Bramwell, S. R. Giblin, S. Calder, R. Aldus, D. Prabhakaran, and T. Fennell, "Measurement of the charge and current of magnetic monopoles in spin ice," *Nature*, vol. 461, p. 956, 2009. 17, 19

[56] S. R. Giblin, S. T. Bramwell, P. C. W. Holdsworth, D. Prabhakaran, and I. Terry, "Creation and measurement of long-lived magnetic monopole currents in spin ice," *Nature Physics*, vol. 7, pp. 252–258, 2011. 17, 19

[57] E. Mengotti, L. Heyderman, A. Rodríguez, A. Bisig, L. Le Guyader, F. Nolting, and H. Braun, "Building blocks of an artificial kagome spin ice: Photoemission electron microscopy of arrays of ferromagnetic islands," *Phys. Rev. B*, vol. 78, p. 144402, 2008. 18, 19, 24, 29, 91, 117

[58] J. Li, S. Zhang, J. Bartell, C. Nisoli, X. Ke, P. Lammert, V. Crespi, and P. Schiffer, "Comparing frustrated and unfrustrated clusters of single-domain ferromagnetic islands," *Phys. Rev. B*, vol. 82, p. 134407, 2010. 18

[59] E. Saitoh, M. Tanaka, H. Miyajima, and T. Yamaoka, "Domain-wall trapping in a ferromagnetic nanowire network," *J. Appl. Phys.*, vol. 93, p. 7444, 2003. 18

[60] M. Tanaka, E. Saitoh, H. Miyajima, and T. Yamaoka, "Magnetization process and magnetic structure in a NiFe honeycomb nano-network," *J. Magn. Magn. Mater.*, vol. 282, pp. 22–24, 2004. 18, 19

[61] M. Tanaka, E. Saitoh, H. Miyajima, T. Yamaoka, and Y. Iye, "Domain structure and magnetic ice-order in NiFe nano-network with honeycomb structure," *J. Appl. Phys.*, vol. 97, p. 10J710, 2005. 18, 19

[62] T. Yamaoka, K. Watanabe, Y. Shirakawabe, K. Chinone, E. Saitoh, M. Tanaka, and H. Miyajima, "Applications of high-resolution MFM system with low-moment probe in a vacuum," *IEEE Transactions on Magnetics*, vol. 41, no. 10, pp. 3733–3735, 2005. 18

[63] M. Tanaka, E. Saitoh, H. Miyajima, and T. Yamaoka, "Asymmetric field variation of magnetoresistance in permally honeycomb nanonetwork," *J. Appl. Phys.*, vol. 99, p. 08G314, 2006. 18

[64] C. Nisoli, J. Li, X. Ke, D. Garand, P. Schiffer, and V. H. Crespi, "Effective temperature in an interacting vertex system: Theory and experiment on artificial spin ice," *Physical Review Letters*, vol. 105, p. 047205, 2010. 19, 20, 24, 30, 32, 34, 35, 39, 101, 135, 138, 139, 140, 141, 144, 148, 151

[65] G. Möller and R. Moessner, "Magnetic multipole analysis of kagome and artificial ice dipolar arrays," *Phys. Rev. B*, vol. 80, p. 140409(R), 2009. 19, 44

[66] P. Lammert, X. Ke, J. Li, C. Nisoli, D. Garand, V. Crespi, and P. Schiffer, "Direct entropy determination and application to artificial spin ice," *Nature Physics*, vol. 6, pp. 786–789, 2010. 20, 48, 90

[67] A. Westphalen, A. Schumann, A. Remhof, H. Zabel, M. Karolak, B. Baxevanis, E. Vedmedenko, T. Last, U. Kunze, and T. Eimüller, "Magnetization reversal of microstructured kagome lattices," *Phys. Rev. B.*, vol. 77, p. 174407, 2008. 20, 43

[68] S. Moralejo, F. Castano, C. Redondoa, R. Ji, K. Nielsch, C. Ross, and F. Castano, "Fabrication and magnetic properties of hexagonal arrays of NiFe elongated nanomagnets," *J. Magn. Magn. Mater. (2007)*, vol. 316, p. e44e47, 2007. 20

[69] X. Ke, J. Li, S. Zhang, C. Nisoli, V. Crespi, and P. Schiffer, "Tuning magnetic frustration of nanomagnets in triangular-lattice geometry," *Appl. Phys. Lett.*, vol. 93, p. 252504, 2008. 20

[70] H. Hilgenkamp, Ariando, H.-J. H. Smilde, D. H. A. Blank, G. Rijnders, H. Rogalla, J. R. Kirtley, and C. T. Tsuei, "Ordering and manipulation of the magnetic moments in large-scale superconducting π-loop arrays," *Nature*, vol. 422, pp. 50–53, 2003. 20, 23, 113

[71] J. R. Kirtley, C. C. Tsuei, Ariando, H. J. H. Smilde, and H. Hilgenkamp, "Antiferromagnetic ordering in arrays of superconducting π-rings," *Phys. Rev. B*, vol. 72, p. 214521, Dec 2005. 20, 23, 113

[72] Y. Han, Y. Shokef, A. Alsayed, P. Yunker, T. Lubensky, and A. Yodh, "Geometrical frustration in buckled colloidal monolayers," *Nature*, vol. 456, pp. 898–903, 2008. 20, 23, 113

[73] Y. Shokef and T. C. Lubensky, "Stripes, zigzags, and slow dynamics in buckled hard spheres," *Phys. Rev. Lett.*, vol. 102, p. 048303, Jan 2009. 20, 23, 113

[74] E. Mengotti, L. J. Heyderman, A. Bisig, A. Fraile Rodríguez, L. Le Guyader, F. Nolting, and H. B. Braun, "Dipolar energy states in clusters of perpendicular magnetic nanoislands," *Journal of Applied Physics*, vol. 105, p. 113113, 2009. 20, 117

[75] A. Libál, C. Reichhardt, and C. J. O. Reichhardt, "Realizing colloidal artificial ice on arrays of optical traps," *Phys. Rev. Lett.*, vol. 97, p. 228302, 2006. 20, 112

[76] C. Reichhardt, C. Reichhardt, and A. Libaĺ, "Transport, hysteresis and avalanches in artificial spin ice systems," in *Electromagnetics in Advanced Applications (ICEAA), 2010 International Conference on*, pp. 260 –263, sept. 2010. 20, 44

[77] A. Libál, C. Reichhardt, and C. J. O. Reichhardt, "Hysteresis and return point memory in artificial spin ice systems," *arXiv:1108.3584v1*. 20, 23, 98, 152

[78] A. Libál, C. J. O. Reichhardt, and C. Reichhardt, "Creating artificial ice states using vortices in nanostructured superconductors," *Phys. Rev. Lett.*, vol. 102, p. 237004, 2009. 20, 23, 35, 36, 37, 38, 48, 92, 112, 141, 146

[79] Y. Li and T. Wang, "A simulation study on the magnetic ordering in an artificial geometrically frustrated lattice," *Physics Letters A*, vol. 374, pp. 4475–4478, 2010. 20

[80] Y. Li and T. Wang, "Magnetic dipolar ordering on geometrically frustrated brick-shaped lattices," *Physica A*, vol. 390, pp. 2388–2394, 2011. 20

[81] Y. Li, T. Wang, H. Liu, X. Dai, and G. Liu, "Geometry effect on the magnetic ordering of geometrically frustrated rectangular magnets," *Physics Letters A*, vol. 375, pp. 1548–1551, 2011. 20, 77

[82] L. A. Mól, A. M. Pereira, and W. A. Moura-Melo, "Comment on "Geometry effect on the magnetic ordering of geometrically frustrated rectangular and triangular magnets"," *Physics Letters A*, vol. 375, pp. 2680–2681, 2011. 20, 77

[83] C. Nisoli, R. Wang, J. Li, W. F. McConville, P. E. Lammert, P. Schiffer, and V. H. Crespi, "Ground state lost but degeneracy found: the effective thermodynamics of 'artificial spin ice'," *Phys. Rev. Lett.*, vol. 98, p. 217103, 2007. 20, 21, 24, 30, 31, 135, 139, 141, 151

[84] M. Donahue and D. Porter, "OOMMF User's Guide, Version 1.0," Interagency Report NISTIR 6376, National Institute of Standards and Technology, Gaithersburg, MD, 1999. 20, 137

[85] H. Zabel, A. Schumann, A. Westphalen, and A. Remhof, "Order and frustration in artificial magnetic patterns," *Acta Physica Poloncia A*, vol. 115(1), pp. 59–62, 2009. 20

[86] K. Kohli, A. Balk, J. Li, S. Zhang, I. Gilbert, P. Lammert, V. Crespi, P. Schiffer, and N. Samarth, "Magneto-optical Kerr effect studies of artificial spin ice," *Phys. Rev. B*, vol. 84, p. 180412(R), 2011. 20, 43

[87] V. Kapaklis, U. B. Arnalds, A. Harman-Clarke, E. T. Papaioanou, M. Karimipour, P. Korelis, A. Taroni, P. C. W. Holdsworth, S. T. Bramwell, and B. Hjörvarsson, "Melting artificial spin ice," *arXiv:1108.1092v1*. 20, 48, 148, 153

[88] F. Wu, "Exactly soluble model of the ferroelectric phase transition in two dimensions," *Phys. Rev. Lett.*, vol. 18, no. 15, pp. 605–607, 1967. 20

[89] E. Lieb, "Exact solution of the problem of the entropy of two-dimensinoal ice," *Phys. Rev. Lett.*, vol. 18, no. 17, pp. 692–694, 1967. 20

[90] G.-W. Chern, P. Mellado, and O. Tchernyshyov, "Two-stage ordering of spins in dipolar spin ice on kagome," *Phys. Rev. Lett.*, vol. 106, p. 207202, 2011. 22, 44

[91] R. Cowburn, "Probing antiferromagnetic coupling between nanomagnets," *Phys. Rev. B*, vol. 65, p. 092409, 2002. 24

[92] A. Imre, G. Csaba, G. Bernstein, W. Porod, and V. Metlushko, "Investigation of shape-dependent switching of coupled nanomagnets," *Superlattices ad Microstructures*, vol. 34, pp. 513–518, 2003. 24, 104

[93] A. Mehta and S. Edwards, "Statistical mechanics of powder mixtures," *Physica A*, vol. 157, pp. 1091–1100, 1989. 30

[94] G. D'Anna, P. Mayor, A. Barrat, V. Loreto, and F. Nori, "Observing brownian motion in vibration-fluidized granular matter," *Nature*, vol. 424, pp. 909–912, 2003. 30

[95] J. Annett, *Superconductivity, Superfluids, and Condensated*. Oxford Master Series in Condensed Matter Physics, Oxford University Press, 2004. 35

[96] P. Mellado, O. Petrova, Y. Shen, and O. Tchernyshyov, "Dynamics of magnetic charges in artificial spin ice," *Physical Review Letters*, vol. 105, p. 187206, 2010. 44

[97] I. Haller, M. Hatzakis, and R. Srinivasan, "High-resolution positive resists for electron-beam exposure," *IBM J. Res. Dev.*, vol. 12, p. 251, 1968. 49

[98] M. Hatzakis, "Electron resists for microcircuit and mask production," *J. Electrochem Soc.:Electrochemical Technology*, vol. 116, no. 7, p. 1033, 1969. 49

[99] H. Y. Ku and L. C. Scala, "Polymeric electron beam resists," *J. Electrochem. Soc.: Solid State Science*, vol. 116, p. 980, 1969. 49

[100] C. Ross, "Patterned magnetic recording media," *Annu. Rev. Mater. Res*, vol. 31, pp. 203–235, 2001. 49

[101] W. Zhou and Z. Wang, eds., *Scanning microscopy for Nanotechnology*. Springer, 2007. 49, 54

[102] D. Mattox, *Handbook of Physical Vapor Deposition (PVD) Processing*. Noyes Publications, 1998. 51, 52

[103] M. Ohring, *Material Science of Thin Films*. Academic Press, 2 ed., 2002. 52, 112

[104] I. M. Watt, *The principles and practise of electron microscopy*. Cambridge University Press, 2nd ed., 1997. 54

[105] T. Everhart and F. Thornley, "Wide-band detector for micro-microampere low-energy electron currents," *Journal of Scientific Instruments*, vol. 37, pp. 246–248, 1960. 55

[106] G. Binnig, C. F. Quate, and C. Gerber, "Atomic force microscope," *Phys. Rev. Lett.*, vol. 56, no. 9, pp. 930–933, 1986. 55, 58

[107] D. Sarid, *Scanning Force Microscopy With Applications to Electric, Magnetic and Atomic Forces*. Oxford Series in Optical and imaging Sciences, Oxford University Press, 1991. 57, 59

[108] R. Gomez, *Magnetic imaging and its applications to materials*. Experimental Methods in the Physical Sciences, Academic Press, 2001. 57, 58

[109] A. San Paulo and R. García, "Unifying theory of tapping-mode atomic-force microscopy," *Phys. Rev. B*, vol. 66, p. 041406(R), 2002. 58

[110] Y. Martin and H. K. Wickramasinghe, "Magnetic imaging by "force microscopy" with 1000Å resolution," *Appl. Phys. Lett.*, vol. 50, no. 20, pp. 1455–1457, 1987. 58

[111] D. Rugar, H. mamin, P. Guethner, S. Lambert, J. Stern, I. McFadyen, and T. Yogi, "Magnetic force microscopy: General principles and applications to longitudinal recording media," *J. Appl. Phys.*, vol. 68, no. 3, pp. 1169–1183, 1990. 58, 61

[112] T. Albrecht, P. Grütter, D. Horne, and D. Rugar, "Frequency modulation detection using high-Q cantilevers for enhanced force microscopy sensitivity," *J. Appl. Phys.*, vol. 69, pp. 668–673, 1991. 58

[113] S. Santos, V. Barcons, J. Font, and N. Thomson, "Bi-stability of amplitude moulation afm in air: deterministic and stochastic outcomes for imaging biomolecular systems," *Nanotechnology*, vol. 21, p. 2257, 2010. 58

[114] S. Santos, V. Barcons, J. Font, and N. Thomson, "Cantilever dynamics in amplitude modulation afm: continuous and discontinuous transitions," *J. Phys. D: Appl. Phys.*, vol. 43, p. 275401, 2010. 58

[115] I. Horcas, R. Fernández, J. M. Gómez-Rodríguez, J. Colchero, J. Gómez-Herrero, and A. M. Baro, "WSxM: A software for scanning probe microscopy and a tool for nanotechnology," *Rev. Sci. Inst.*, vol. 78, p. 013705, 2007. 59

[116] J. Sáenz, N. García, P. Grütter, E. Meyer, H. Heinzelmann, R. Wiesendanger, L. Rosenthaler, H. Hidber, and H.-J. Güntherodt, "Observation of magnetic forces by the atomic force microscope," *J.Appl. Phys.*, vol. 62, no. 10, pp. 4293–4295, 1987. 59

[117] P. Grütter, E. Meyer, H. Heinzelmann, L. Rosenthaler, H.-R. Hidber, and H.-J. Güntherodt, "Application of atomic force microscopy to magnetic materials," *J. Vac. Sci. Technol. A*, vol. 6, no. 2, pp. 279–282, 1988. 59

[118] J. Mamin, D. Rugar, J. Stern, R. Fontana, Jr., and P. Kasiraj, "Magnetic force microscopy of thin permalloy films," *Appl. Phys. Lett.*, vol. 55, no. 3, pp. 318–320, 1989. 61

[119] T. Göddenhenrich, U. Hartmann, and C. Heidon, "Generation and imaging of domains with the magnetic force microscope," *Ultramicroscopy*, vol. 42-44, pp. 256–261, 1992. 61

[120] R. Cowburn, "Property variation with shape in magnetic nanoelements," *J. Phys. D: Appl. Phys.*, vol. 33, pp. R1–R16, 2000. 88

[121] L. O'Brien, D. Petit, H. Zeng, E. Lewis, J. Sampaio, A. Jausovec, D. Read, and R. Cowburn, "Near-field interaction netween domain walls in adjacent permalloy nanowires," *Physical Review Letters*, vol. 103, p. 077206, 2009. 89

[122] A. Imre, G. Csaba, L. Ji, A. Orlov, G. H. Bernstein, and W. Porod, "Majority logic gate for magnetic quantum-dot cellular automata," *Science*, vol. 311, pp. 205–208, 2006. 90

[123] Z. Budrikis, J. P. Morgan, J. Akerman, A. Stein, R. L. Stamps, P. Politi, S. Langridge, and C. H. Marrows, "Disorder strength and field-driven ground state domain formation in artificial spin ice: experiment, simulation and theory," *arXiv:1111.6491v1.* 98, 99

[124] R. Joseph and E. Schlömann, "Demagnetizing field in nonellipsoidal bodies," *J. Appl. Phys.*, vol. 36, pp. 1579–1593, 1965. 112

[125] S. Lepadatu, J. Wu, and Y. Xu, "Current-induced magnetization switching in asymmetric necked wires," *Appl. Phys. Lett.*, vol. 91, p. 062512, 2007. 114

[126] K. A. Reinhardt and W. Kern, eds., *Handbook of silicon wafer cleaning technology.* Material Science and Process Technology Series, William Andrew, 2 ed., 2008. 130

[127] P. Politi and M. G. Pini, "Dipolar interactions between two-dimensional magnetic particles," *Phys. Rev. B*, vol. 66, p. 214414, 2002. 137

[128] P. Eames and E. Dan Dahlberg, "Characterization of domain states in submicron sized permalloy particles with perpendicular anisotropy," *Journal of Applied Physics*, vol. 91, pp. 7986–7988, 2002. 137

[129] S. Daunheimer, O. Petrova, O. Tchernyshyov, and J. Cumings, "Reducing disorder in artificial kagome ice," *Phys. Rev. Lett.*, vol. 107, p. 167201, 2011. 149